The Telecommunications and Data Acquisition Progress Report 42-124

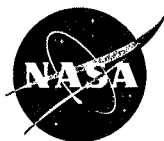## October–December 1995

Joseph H. Yuen

Editor

February 15, 1996

The Telecommunications and Data Acquisition Progress Report 42-124

October–December 1995

Joseph H. Yuen
Editor

February 15, 1996

Note From the Editor

As previously announced, this is the last issue of *The Telecommunications and Data Acquisition Progress Report* for which printed copies will be produced. Since issue 42-121, published on May 15, 1995, *The TDA Progress Report* has been available to all its readers on the World Wide Web at

http://tda.jpl.nasa.gov/progress_report

as well as in printed form. Beginning with the next issue, 42-125, due to be published on May 15, 1996, *The TDA Progress Report* will be published entirely electronically at the above-mentioned URL. *The TDA Progress Report* is linked to numerous home pages; among them is the JPL home page at

http://www.jpl.nasa.gov

Page intentionally left blank

Preface

This quarterly publication provides archival reports on developments in programs managed by JPL's Telecommunications and Mission Operations Directorate (TMOD), which now includes the former Telecommunications and Data Acquisition (TDA) Office. In space communications, radio navigation, radio science, and ground-based radio and radar astronomy, it reports on activities of the Deep Space Network (DSN) in planning, supporting research and technology, implementation, and operations. Also included are standards activity at JPL for space data and information systems and reimbursable DSN work performed for other space agencies through NASA. The preceding work is all performed for NASA's Office of Space Communications (OSC).

TMOD also performs work funded by other NASA program offices through and with the cooperation of OSC. The first of these is the Orbital Debris Radar Program funded by the Office of Space Systems Development. It exists at Goldstone only and makes use of the planetary radar capability when the antennas are configured as science instruments making direct observations of the planets, their satellites, and asteroids of our solar system. The Office of Space Sciences funds the data reduction and science analyses of data obtained by the Goldstone Solar System Radar. The antennas at all three complexes are also configured for radio astronomy research and, as such, conduct experiments funded by the National Science Foundation in the U.S. and other agencies at the overseas complexes. These experiments are either in microwave spectroscopy or very long baseline interferometry.

Finally, tasks funded under the JPL Director's Discretionary Fund and the Caltech President's Fund that involve TMOD are included.

This and each succeeding issue of *The Telecommunications and Data Acquisition Progress Report* will present material in some, but not necessarily all, of the aforementioned programs.

Page intentionally left blank

Contents

OSC TASKS
DSN Advanced Systems
TRACKING AND GROUND-BASED NAVIGATION

COMMUNICATIONS, SPACECRAFT–GROUND

DSN Systems Implementation
NETWORK UPGRADE AND SUSTAINING

The Effect of Aperture Averaging Upon Tropospheric Delay Fluctuations Seen With a DSN Antenna

R. Linfield
Tracking Systems and Applications Section

The spectrum of tropospheric delay fluctuations expected for a DSN antenna at time scales <100 s has been calculated. A new feature included in these calculations is the effect of aperture averaging, which causes a reduction in delay fluctuations on time scales less than the antenna wind speed crossing time, $\approx 5\text{--}10$ s. On time scales less than a few seconds, the Allan deviation $\sigma_y(\Delta t) \propto (\Delta t)^{+1}$, rather than $\sigma_y(\Delta t) \propto (\Delta t)^{-1/6}$ without aperture averaging. Due to thermal radiometer noise, calibration of tropospheric delay fluctuations with water vapor radiometers will not be possible on time scales less than ≈ 10 s. However, the tropospheric fluctuation level will be small enough that radio science measurements with a spacecraft on time scales less than a few seconds will be limited by the stability of frequency standards and/or other nontropospheric effects.

I. Introduction

Radio science experiments with a spacecraft use a one- or two-way radio link between a DSN antenna and the spacecraft. The received amplitude and phase are used to measure quantities such as gravitational radiation, refractivity profiles of the atmosphere of the planet or planetary satellite near the spacecraft, or the structure of a planetary ring system. Any perturbations on the link that are caused by the media between the DSN antenna and the spacecraft will corrupt the accuracy of the radio science measurement (unless the purpose of the experiment is to study that medium, e.g., the solar plasma). As the link frequency used for radio science experiments has increased, the relative magnitude of tropospheric and solar plasma phase fluctuations has changed dramatically, because plasma is dispersive at microwave frequencies and the troposphere is not. At S-band (2.3 GHz), solar plasma phase fluctuations dominate, while at Ka-band (32 GHz), tropospheric phase fluctuations will dominate except at small sun–spacecraft angular separations.

Knowledge of the tropospheric fluctuation spectrum will be useful in planning and analyzing radio science experiments. Comparison of fluctuation levels measured by very long baseline interferometry (VLBI) and water vapor radiometers (WVRs) has demonstrated that tropospheric delay/phase fluctuations at microwave frequencies are dominated by fluctuations in water vapor density [1].[1] The spectrum

---

[1] C. D. Edwards, "Water Vapor Radiometer Line-of-Sight Calibration Capabilities," JPL Interoffice Memorandum 335.1-90-015 (internal document), Jet Propulsion Laboratory, Pasadena, California, March 30, 1990.

of tropospheric fluctuations has been measured by VLBI on time scales >20 s [2] and by WVRs on time scales ≥200 s [3]. A model for these fluctuations has been developed [4]. Previous calculations using this model (e.g., [5]) have assumed a zero thickness "pencil beam" for a DSN antenna. However, on time scales less than ≈10 s, the nonzero diameter of a DSN antenna will modify this pencil beam spectrum. The method for calculating this "aperture averaging" effect is presented in Section II, and results are given in Section III. A short summary is given in Section IV.

II. Calculation of Aperture Averaging

Both theoretical arguments [6] and observational data [2,4,7] support the idea that tropospheric refractivity fluctuations obey a Kolmogorov power law. The refractivity structure function $D_n(r)$ on scales up to at least a few tens of kilometers is

$$D_n(r) \equiv \left\langle [N(\vec{x} + \vec{r}) - N(\vec{x})]^2 \right\rangle = C_n^2 r^{2/3} \tag{1}$$

where $N(\vec{x})$ is the refractivity at location $\vec{x}$ ($N \equiv n - 1$, where n is the index of refraction), and C_n is the refractivity structure constant. Over time scales up to thousands of seconds, time variations in line-of-sight tropospheric delay can be successfully represented by a "frozen flow" model, in which spatial variations are convected past the observer by the wind.

The height dependence of C_n is poorly constrained by data. It was modeled by [4] as constant up to a 1-km height and zero above that. This "slab height" was subsequently revised to 2 km.[2] Recent WVR data from Goldstone [3] show that the observed fluctuations agree with the predictions of this 2-km slab model on time scales >400 s but are lower than model predictions on shorter time scales. This result is most easily explained by a thickness of the turbulent layer that is significantly larger than 2 km, although the data are not adequate to solve for a specific value for this thickness. The effect of a finite thickness h of the medium is that fluctuations in the vertical dimension saturate on time scales $> h/v_w$, where v_w is the wind speed. For time scales $\Delta t << h/v_w$, the delay structure function $D_\tau \propto (\Delta t)^{5/3}$, and for time scales $\Delta t >> h/v_w$, $D_\tau \propto (\Delta t)^{2/3}$ [4]. The time scales covered in this article are all $<< h/v_w$. WVR measurements of fluctuations on time scales of 200 s [3] were used to derive the mean C_n, once h was chosen. For $h = 4$ km, $C_n = 3.0 \times 10^{-8}$ m$^{-1/3}$; these values were used for all calculations presented in this article. Over the course of a year, the structure constant at Goldstone exhibits variations of at least a factor of 2 about its mean value [3].

The tropospheric delay for a pencil beam looking from location $\vec{x}$ at elevation angle θ and azimuth AZ is

$$\tau_{pencil}(\vec{x}, \theta, AZ) = \frac{1}{\sin\theta} \int_0^\infty N\left[\vec{x} + \vec{r}(\theta, AZ, z)\right] dz \tag{2}$$

where $\vec{r}(\theta, AZ, z)$ is the vector from the surface to height z in direction (θ, AZ). For a DSN antenna of diameter d, the delay is averaged over the circular aperture, to give

$$\tau_{DSN}(\vec{x}, \theta, AZ) = \frac{4}{\pi d^2} \int_0^{2\pi} \int_0^{d/2} \xi \tau_{pencil}\left[\vec{x} + \vec{r}(\xi, \phi), \theta, AZ\right] d\xi d\phi \tag{3}$$

where $\vec{r}(\xi, \phi)$ is the vector in the plane of the aperture, starting from the center, of length ξ and at angle ϕ (the direction chosen for $\phi = 0$ does not affect the result). Equation (3) assumes that the near-field

---

[2] R. N. Treuhaft, personal communication, Jet Propulsion Laboratory, Pasadena, California, 1995.

2

DSN beam profile is uniform across its circular cross section. The true profile will be tapered towards the edges. As presented in Section III, a change of a factor of two in antenna diameter causes a change in the resulting fluctuation level by a factor of ≈ 2. Therefore, neglect of beam tapering should cause an error of <20 percent in the results reported here.

A convenient way of calculating and expressing the tropospheric fluctuation spectrum is Allan variance $\sigma_y^2(\Delta t)$, defined for a delay process $\tau(t)$ as [8]

$$\sigma_y^2(\Delta t) \equiv \frac{\left\langle [\tau(t + 2\Delta t) - 2\tau(t + \Delta t) + \tau(t)]^2 \right\rangle}{2(\Delta t)^2} \tag{4}$$

Expanding Eq. (4) and assuming that averaged quantities are independent of time and position gives, for the tropospheric delay fluctuations measured by a DSN antenna,

$$\sigma_y^2(\Delta t) = \frac{3\left\langle \tau_{DSN}^2(t) \right\rangle}{(\Delta t)^2} - \frac{4\left\langle \tau_{DSN}(t + \Delta t)\tau_{DSN}(t) \right\rangle}{(\Delta t)^2} + \frac{\left\langle \tau_{DSN}(t + 2\Delta t)\tau_{DSN}(t) \right\rangle}{(\Delta t)^2} \tag{5}$$

We can evaluate this expression with Eq. (3) and the frozen-flow assumption. Taking the middle term in Eq. (5) as an example,

$$\langle \tau_{DSN}(t + \Delta t)\tau_{DSN}(t) \rangle = \frac{16}{\pi^2 d^4} \int_0^{2\pi} \int_0^{2\pi} \int_0^{d/2} \int_0^{d/2} \xi\xi' \left\langle \tau_{pencil} \left[\vec{x} + \vec{v}_w \Delta t + \vec{r}(\xi, \phi) \right] \tau_{pencil} \left[\vec{x} + \vec{r}(\xi', \phi') \right] \right\rangle$$

$$\times d\xi d\xi' d\phi d\phi'$$

It has been assumed that averaged quantities are position independent, so that

$$\left\langle \tau_{pencil}(\vec{x}_1, \theta, AZ)\tau_{pencil}(\vec{x}_2, \theta, AZ) \right\rangle = \left\langle \tau_{pencil}^2(\vec{x}, \theta, AZ) \right\rangle - \frac{1}{2}\left\langle [\tau_{pencil}(\vec{x}_1, \theta, AZ) - \tau_{pencil}(\vec{x}_2, \theta, AZ)]^2 \right\rangle$$

$$= \left\langle \tau_{pencil}^2(\vec{x}, \theta, AZ) \right\rangle - \frac{1}{2}D_\tau\left(|\vec{x}_1 - \vec{x}_2| \right)$$

where D_τ is the pencil-beam delay structure function, defined as

$$D_\tau(r) \equiv \left\langle [\tau_{pencil}(\vec{x} + \vec{r}, \theta, AZ) - \tau_{pencil}(\vec{x}, \theta, AZ)]^2 \right\rangle$$

In evaluating Eq. (5), the $\left\langle \tau_{pencil}^2(\vec{x}) \right\rangle$ terms add to zero, and $\sigma_y^2(\Delta t)$ can be expressed as a four-dimensional integral of three D_τ terms:

$$\sigma_y^2(\Delta t) = \frac{16}{\pi^2 d^4 (\Delta t)^2} \int_0^{2\pi} d\phi \int_0^{2\pi} d\phi' \int_0^{d/2} \xi d\xi \int_0^{d/2} \xi' d\xi \left[-\frac{3}{2} D_\tau(A) + 2D_\tau(B) - \frac{1}{2} D_\tau(C) \right]$$

$$A = |\vec{r}(\xi, \phi) - \vec{r}(\xi', \phi')|$$

$$B = |\vec{v}_w \Delta t + \vec{r}(\xi, \phi) - \vec{r}(\xi', \phi')|$$

$$C = |2\vec{v}_w \Delta t + \vec{r}(\xi, \phi) - \vec{r}(\xi', \phi')|$$

(6)

The horizontal distance scales are d and $v_w \Delta t$. As a result, $\sigma_y(\Delta t)$ will be suppressed, relative to its $d = 0$ value, for values of Δt smaller than a few times the wind speed crossing time of $t_{cross} = d/v_w$. For a typical wind speed in the lower few kilometers of 8 m/s and for $d = 34$ m, $t_{cross} \approx 5$ s. For $\Delta t << t_{cross}$, $\sigma_y(\Delta t)$ will be much lower than its $d = 0$ value, due to the averaging of many small-scale delay fluctuations over the much larger DSN aperture.

For any DSN tracking scenario at an observing frequency high enough (≥ 8 GHz) for tropospheric delay fluctuations to dominate over those from plasma, the Earth's troposphere will lie entirely within the near field of the antenna. The effective tropospheric volume sampled by the DSN antenna will then be cylindrical. For tracking of planetary spacecraft, the antenna will move at a nearly sidereal rate. This tracking will cause an effective velocity v_{eff} through the troposphere, at height z and elevation angle θ, of

$$v_{eff} = \frac{\Omega z}{\sin \theta}$$

The Earth's rotation rate is Ω. For $z = 2$ km (half the turbulent slab height), $v_{eff} = 0.15/\sin \theta$ m/s. This is much less than the wind speed of 8 m/s used in the calculations. Sidereal tracking, therefore, will not significantly modify the results presented in this article.

The Fresnel length scale l for observations at a wavelength λ with phase perturbations occurring at a distance L is $l \approx \sqrt{\lambda L}$. For $\lambda = 1$ cm and $L = 2$ km (the middle of the turbulent troposphere), $l \approx 4$ m. On smaller scales, geometric optics is not completely valid. The results for time scales <4 m/s/$v_w = 0.5$ s should, therefore, be regarded as approximate.

III. Results

Equation (6) was evaluated numerically, for a range of time intervals, and for both 34-m- and 70-m-diameter antennas. A wind speed of 8 m/s was assumed. The results for antennas pointed in the zenith direction are shown in Fig. 1. Values of $\sigma_y(\Delta t)$ for a pencil beam antenna are shown for comparison.

For time intervals shorter than 10 s, the Allan deviation for measurements made with a DSN antenna are less than those made with a pencil beam. For time intervals less than ≈ 2 s, $\sigma_y(\Delta t) \propto (\Delta t)^k$, where $k \approx +1$. This proportionality can be roughly understood as follows: The effect of fluctuations over a time interval Δt are confined to a region of size $\approx v_w \Delta t$. For $v_w \Delta t << d$, there are $N_{regions} \sim (d/(v_w \Delta t))^2$ such regions over the antenna aperture. Averaging the delay fluctuations of these regions will cause a reduction by a factor of $\sim \sqrt{N_{regions}} \sim d/(v_w \Delta t)$. The slope of the pencil beam $\sigma_y(\Delta t)$ is $\approx -1/6$, so the slope of the DSN $\sigma_y(\Delta t)$ will be $\approx +5/6$.

As Δt decreases, the amount of computer time needed to calculate $\sigma_y(\Delta t)$ increases rapidly. For small Δt, the terms A, B, and C in Eq. (6) are nearly equal, and high numerical precision is needed in order
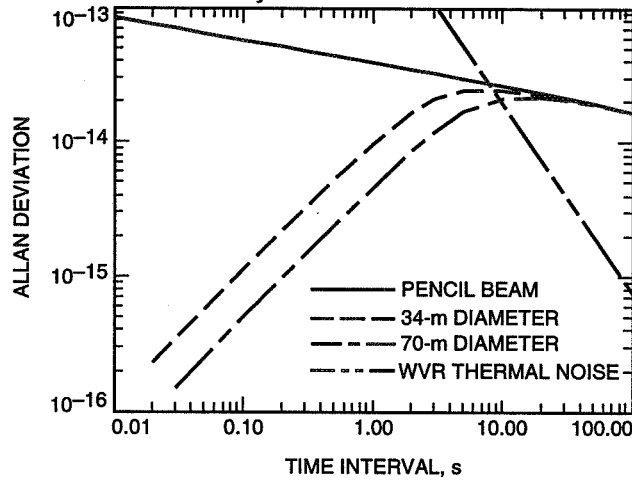
Fig. 1. The Allan deviation calculated for a pencil beam antenna and for antenna diameters of 34 and 70 m is shown as a function of time interval for typical Goldstone conditions and the zenith direction. The Allan deviation at other elevation angles will be somewhat larger, increasing by a factor of 1.8 at a 10-deg elevation angle. The thermal noise from a WVR with the characteristics expected for the Cassini radio science calibration system is included.

to determine the differences in the D_τ terms. Furthermore, all derivatives of D_n and all but the first derivative of D_τ become singular at zero separation, so that numerical integration methods have difficulty.

Calculations for Δt as small as 0.02 s were possible in the zenith direction, because $D_\tau(r)$ could be evaluated separately, with an empirically fitted analytical formula used for D_τ in Eq. (6) to reduce the number of dimensions in the integration from 6 to 4. Calculations at other elevation angles were limited to a narrower range of time intervals (1–100 s). These calculations showed that $\sigma_y(\Delta t)$ increases slowly with decreasing elevation angle. Relative to its value at the zenith, $\sigma_y(\Delta t)$ was 1.16 times larger at a 30-deg elevation angle and 1.82 times larger at a 10-deg elevation angle.

All $\sigma_y(\Delta t)$ values in Fig. 1 are linearly proportional to the structure constant, C_n. Therefore, the actual $\sigma_y(\Delta t)$ values at a DSN site will range up and down from those in Fig. 1 by a factor of at least 2, depending upon the season, time of day, and weather conditions. Winter nights tend to have the lowest C_n values, with summer days having the largest values.

Tropospheric delay fluctuations at microwave frequencies can be calibrated by WVRs, which measure thermal emission from water vapor in the vicinity of its 22-GHz spectral line [9]. However, on short time scales, the thermal noise from a WVR becomes the limiting error source. The main vapor-sensing channel of current WVRs is at a frequency near 21.5 or 23.8 GHz, where a 1-K brightness temperature corresponds to $\approx$6 mm/c = 2 × 10^{-11} s of path delay (c is the speed of light). The thermal path delay equivalent noise in a WVR measurement of integration time t_{int} for a total system temperature T_{sys} and bandwidth BW is

$$N(t_{int}) = \frac{T_{sys}}{\sqrt{BW\ t_{int}}} \cdot \frac{2 \times 10^{-11}\ \text{s}}{1\text{K}} = \frac{2 \times 10^{-13} T_{100}}{BW_{100}^{0.5}\ t_{int_s}^{0.5}}\ \text{s} \tag{7}$$

where $T_{100} \equiv T_{sys}/100$ K, $BW_{100} \equiv BW/100$ MHz, and $t_{int_s} \equiv t_{int}/1$ s.

To set a firm lower limit on the effect of WVR thermal noise, we assume that $\Delta t = t_{int}$ (i.e., we give up all information on time scales shorter than Δt). Future uncooled WVRs currently under design are expected to have $T_{sys} \approx 300$ K and $BW \approx 400$ MHz.[3] The Allan deviation from thermal WVR noise for $\Delta t_s = \Delta t/1$ s (note that $\sigma_y(\Delta t) = N(t_{int})\sqrt{3}/\Delta t$ for thermal noise) then is

$$\sigma_y(\Delta t) \approx \frac{5 \times 10^{-13}}{\Delta t_s^{1.5}} \quad \text{(WVR thermal noise)} \tag{8}$$

This WVR thermal noise curve is plotted in Fig. 1. If we require $\sigma_y(\Delta t)$ from WVR thermal noise to be at least 3 times smaller than the tropospheric $\sigma_y(\Delta t)$ in order to achieve useful calibration, then, for any elevation angle ≥ 10 deg, the minimum time interval Δt_{min} for WVR calibration is

$$\Delta t_{min} \approx 10 \text{ s}$$

Because the slope of the tropospheric $\sigma_y(\Delta t)$ is small at $\Delta t \sim 10$ s and the slope of the WVR thermal noise $\sigma_y(\Delta t)$ is steep, the minimum useful calibration interval is relatively insensitive to the values of T_{sys} and BW. On time scales less than ≈ 10 s, tropospheric fluctuations cannot be calibrated with any known technique.

IV. Summary

The effect of aperture averaging upon radio science measurements is that tropospheric fluctuations will not be important on short time scales. For occultation measurements of Saturn's rings with Cassini, the shortest time scale of interest is the desired physical resolution (≈ 100 m) divided by the spacecraft orbital velocity (≈ 10 km/s), or ~ 0.01 s.[4] These measurements will use an onboard oscillator with $\sigma_y(\Delta t) \geq 10^{-13}$. Even if future flight oscillators were a factor of 10 more stable than the one on Cassini, the troposphere would be more stable than the oscillator for $\Delta t < 1$ s. The tropospheric fluctuations on $\Delta t < 10$ s appear to form a fundamental lower limit for radio science measurements using an Earth antenna, because WVR thermal noise precludes calibration of the fluctuations.

Acknowledgments

References

[1] G. Elgered, J. L. Davis, T. A. Herring, and I. I. Shapiro, "Geodesy by Radio Interferometry: Water Vapor Radiometry for Estimation of the Wet Delay," *J. Geophy. Res.*, vol. 96, no. B4, pp. 6541–6555, 1991.

---

[3] A. B. Tanner, personal communication, Jet Propulsion Laboratory, Pasadena, California, November 27, 1995.

[4] N. Rappaport, personal communication, Jet Propulsion Laboratory, Pasadena, California, November 21, 1995.

[2] R. P. Linfield, S. J. Keihm, L. P. Teitelbaum, S. J. Walter, M. J. Mahoney, R. N. Treuhaft, and L. J. Skjerve, "A Test of Water Vapor Radiometer-Based Troposphere Calibration Using Very Long Baseline Interferometry Observations on a 21-km Baseline," *Radio Science*, 1996 (in press).

[3] S. J. Keihm, "Water Vapor Radiometer Measurements of the Tropospheric Delay Fluctuations at Goldstone Over a Full Year," *The Telecommunications and Data Acquisition Progress Report 42-122, April–June 1995*, Jet Propulsion Laboratory, Pasadena, California, pp. 1–11, August 15, 1995.

[4] R. N. Treuhaft and G. E. Lanyi, "The Effect of Dynamic Wet Troposphere on Radio Interferometric Measurements," *Radio Science*, vol. 22, no. 22, pp. 251–265, 1987.

[5] R. P. Linfield and J. Z. Wilcox, "Radio Metric Errors Due to Mismatch and Offset Between a DSN Antenna Beam and the Beam of a Troposphere Calibration Instrument," *The Telecommunications and Data Acquisition Progress Report 42-114, April–June 1993*, Jet Propulsion Laboratory, Pasadena, California, pp. 1–13, August 15, 1993.

[6] V. I. Tatarski, *Wave Propogation in a Turbulent Medium*, New York: Dover, 1961.

[7] A. E. E. Rogers, A. T. Moffet, D. C. Backer, and J. M. Moran, "Coherence Limits in VLBI Observations at 3-mm Wavelength," *Radio Science*, vol. 19, pp. 1552–1560, 1984.

[8] D. W. Allan, "Statistics of Atomic Frequency Standards," *Proc. IEEE*, vol. 54, no. 2, pp. 221–230, 1966.

[9] G. Elgered, "Tropospheric Radio Path Delay From Ground-Based Microwave Radiometry," Chapter 5, *Atmospheric Remote Sensing by Microwave Radiometry*, edited by M. Janssen, New York: Wiley & Sons, 1993.

An Overview of the GOLD Experiment Between the ETS-VI Satellite and the Table Mountain Facility

K. E. Wilson

Communications Systems and Research Section

The Ground/Orbiter Lasercomm Demonstration is a demonstration of optical communications between the Japanese Engineering Test Satellite (ETS-VI) and an optical ground transmitting and receiving station at the Table Mountain Facility in Wrightwood, California. Laser transmissions to the satellite are performed for approximately 4 hours every third night when the satellite is at apogee above Table Mountain. The experiment requires the coordination of resources at the Communications Research Laboratory (CRL), JPL, the National Aeronautics and Space Development Agency (NASDA) Tsukuba tracking station, and NASA's Deep Space Network at Goldstone, California, to generate and transmit real-time commands and receive telemetry from the ETS-VI. Transmissions to the ETS-VI began in November 1995 and are scheduled to last into the middle of January 1996, when the satellite is expected to be eclipsed by the Earth's shadow for a major part of its orbit. The eclipse is expected to last for about 2 months, and during this period there will be limited electrical power available on board the satellite. NASDA plans to restrict experiments with the ETS-VI during this period, and no laser transmissions are planned. Posteclipse experiments are currently being negotiated. GOLD is a joint NASA–CRL experiment that is being conducted by JPL in coordination with CRL and NASDA.

I. Introduction

The Ground/Orbiter Lasercomm Demonstration (GOLD) is a joint NASA/Communications Research Laboratory (CRL) optical communications experiment to evaluate one-way and two-way optical communications under a range of atmospheric conditions and to demonstrate optical ranging. GOLD's objectives and goals are outlined below.

The objectives are to

(1) Demonstrate two-way spatial acquisition/tracking of laser beams with a spacecraft

(2) Accomplish one-way and two-way optical data transfer to a spacecraft and measure bit-error rates

(3) Accumulate 10 elapsed hours of transmission/reception experience and 30 Gbytes over a 6-month period

(4) Compare downlink atmospheric transmission losses with similar data from the Table Mountain Facility's (TMF's) atmospheric visibility monitoring (AVM) observatory

The goals are to

(1) Gather atmospheric transmission statistics from an actual space-to-ground link and compare them with corresponding statistics from the AVM system

(2) Build a database for optical link acquisition/reacquisition times

(3) Validate optical communications-link performance prediction tools

(4) Demonstrate optical ranging to 10-m accuracy

GOLD experiments will use the 0.6-m and 1.2-m telescopes located at NASA's TMF to communicate with the Japanese Engineering Test Satellite (ETS-VI). The experiment concept is depicted in Fig. 1. An argon-ion laser coupled to the 0.6-m telescope transmits a 1.024-Mbps Manchester-coded pseudorandom noise (PN) sequence to the spacecraft. The ETS-VI in turn uses its GaAs laser to transmit a similar PN sequence to the 1.2-m ground receiver located approximately 60-m from the transmitter site.

830-nm DOWNLINK

514.5-nm UPLINK
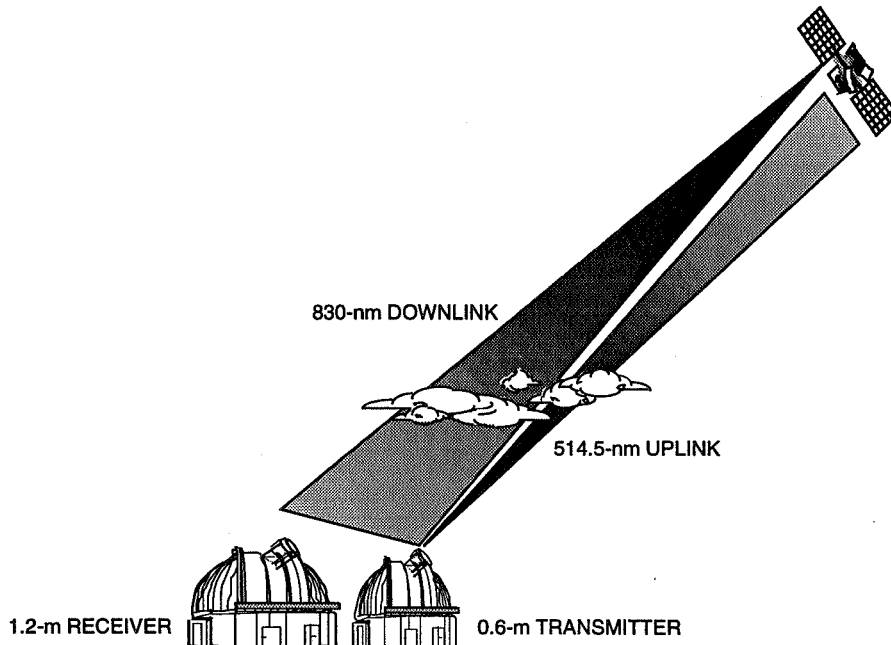
1.2-m RECEIVER   0.6-m TRANSMITTER

Fig. 1. Conceptual drawing of GOLD. The transmitter at TMF uplinks a 514.5-nm communications signal to the ETS-VI. The satellite downlinks a 830-nm 1-Mbps signal.

The ETS-VI was launched into orbit on August 28, 1994. It was originally intended to be in a geostationary orbit above Japan, but difficulty with one of its motors has resulted in the satellite now being in a geotransfer orbit. To make maximum use of the spacecraft's subsystems in its current orbit, researchers at CRL have encouraged both NASA and European Space Agency (ESA) experimenters to use the optical communications subsystem on board the ETS-VI. In response to this, the National Aeronautics and Space Development Agency (NASDA) has refined the satellite's orbit to facilitate the use of the laser communications equipment (LCE) by experimenters at JPL. Yet, because the satellite's elliptical orbit takes the satellite through the Van Allen belts, its power generation capabilities have been degraded and its expected life reduced. Between mid-January and mid-March 1996, the satellite will go into a 2-month-long eclipse. During this time, very little power will be generated on the spacecraft, and only low-power experiments will be feasible. It is unclear whether optical communications falls into this category of experiments. Posteclipse experiments are not scheduled as yet because of the large uncertainty in whether the satellite batteries will survive the long eclipse.

This article describes the work on the GOLD project to date. The three phases of the GOLD experiment are described in Section II, along with a brief description of the satellite predict generation. The data link between CRL and TMF that is used to confirm the acquisition of the uplink beam and to communicate with CRL experimenters is also described in Section II. The transmitter and receiver optics and electronics are described in Sections III and IV, respectively, and the AVM station that measures the atmospheric transmission at optical wavelengths is described briefly in Section V. Samples of the data collected to date are presented and discussed in Section VI. Conclusions are in Section VII.

II. GOLD Preparation and Operations Phase

A. GOLD Operations and Experiment Phases

The ETS-VI satellite is in a recurrent orbit that makes it visible every 3 days at night from TMF. The GOLD schedule given in Table 1 extends over the period from October 30, 1995, to January 13, 1996. The table shows the laser communications and associated Deep Space Network (DSN) satellite control times. The DSN begins satellite control 2 hours before the laser transmission times and ends 90 minutes after laser transmission.

Table 1 shows the transmission times of the GOLD experiments. The experiment is broken into three phases over the period from November 1995 to January 1996. Phase 1 is a beacon uplink with a 1.024-Mbps downlink detection. The goals of this phase are to

(1) Complete integrated system testing

(2) Measure the uplink optical beam divergence at the satellite

(3) Evaluate the benefits of spatial diversity of the uplink beacon, i.e., single- and dual-beam beacon transmissions

(4) Determine the appropriate uplink power levels to maintain spacecraft closed-loop tracking of the ground station

(5) Evaluate the spacecraft's ability to point to the TMF ground station, and develop appropriate ground-station acquisition strategies

(6) Establish operations procedures for the phases discussed below

Table 1. Laser transmission times for the GOLD experiment.

Date	Start, time UT	End, time UT	Duration, h:min
30 October 1995	11:55	15:00	2:05
2 November 1995	11:45	15:00	3:15
5 November 1995	11:30	14:50	3:20
8 November 1995	11:20	14:40	3:20
11 November 1995	11:15	14:30	3:15
14 November 1995	11:05	14:10	3:05
17 November 1995	11:05	14:10	3:05
20 November 1995	10:45	14:00	3:15
26 November 1995	10:35	13:30	2:55
29 November 1995	9:52	13:55	4:01
2 December 1995	9:36	13:50	4:14
5 December 1995	9:20	13:47	4:27
8 December 1995	9:04	13:43	4:39
11 December 1995	8:48	13:40	4:52
14 December 1995	8:35	13:35	5:00
17 December 1995	8:25	13:24	4:59
20 December 1995	8:14	13:13	4:59
23 December 1995	8:04	13:03	4:59
29 December 1995	7:44	12:41	4:57
4 January 1996	7:24	12:20	4:56
7 January 1996	7:14	12:09	4:56
10 January 1996	7:04	11:59	4:55
13 January 1996	6:54	11:48	4:54

Phase 2 extends over the month of December 1995, and the goals are to demonstrate two-way optical communications, measure the bit-error rate (BER) on the uplink, and evaluate the spacecraft's ability to regenerate an uplinked data sequence.

Phase 3 extends from January 4, 1995, to January 13, 1996. The primary goal during this period is to use the spacecraft's uplink signal regeneration capabilities to measure the one-way light-time to the spacecraft. These data will be processed through JPL's orbit determination program (ODP) to generate an element set to predict the spacecraft ephemeris.

Table 2 gives a brief description of the results of each night's operations as of the time of writing. Once the required LCE gimbal angle relative to the satellite's orientation was established on November 11, 1995, the uplink was acquired within seconds of transmission on subsequent nights.

B. Satellite Predicts Generation

The satellite predicts for the TMF telescopes are generated from a satellite osculating-element set that is faxed to JPL from NASDA's Tsukuba tracking facility. Ephemeris files are generated at JPL for the transmitter and receiver telescopes, separately with offsets to account for the point ahead angle. The files are electronically transmitted to TMF and are loaded into the telescope control program (TCP). The TCP uses a spline-fitting routine to interpolate between the ephemerides to generate a "smooth" telescope-pointing file to track the ETS-VI satellite.

Table 2. Brief description of results for each night's operations.

Date	Description
30 October 1995	Heavy cloud cover precluded transmission
2 November 1995	Transmitted laser beacon to satellite; no uplink detected
5 November 1995	Transmitted laser beacon to satellite; no uplink detected
8 November 1995	First detection of uplink beacon
	Spacecraft gimball was being scanned
	Downlink detected and recorded
11 November 1995	Uplink detected for 45 min; became sporatic thereafter
	Spacecraft has difficulty tracking the ground station
	Downlink detected and recorded
14 November 1995	Uplink detected, and downlink data recorded
17 November 1995	Spacecraft detector gains adjusted to prevent saturation
	Satellite acquired within seconds of initiating beacon
	Uplink detected for 3 h
20 November 1995	0.6-m telescope malfunction
23 November 1995	Thanksgiving holiday
26 November 1995	Heavy cloud cover over TMF; no transmission

C. Data Links

GOLD requires the simultaneous real-time coordination of experimenters at NASDA, CRL, and the DSN to accomplish the laser transmission from TMF. The command and data flow diagram is shown in Fig. 2. In addition, during the early part of the experiment, the Federal Aviation Administration's (FAA's) Air Traffic Control Center in Palmdale, California, is assisting in aircraft avoidance strategies until an aircraft detection radar system at TMF is installed.

Commands to control the satellite's attitude during the experiment are generated at NASDA. CRL generates commands to control the LCE and sends them to NASDA. These commands are then transmitted from NASDA to DSS 27 at Goldstone, which relays them to the satellite.

The data link between CRL, JPL, and TMF provides near-real-time feedback on the measured onboard laser communications equipment sensors to the experimenters at TMF. The delay between the spacecraft transmission and the TMF reception is approximately 15 s. Spacecraft attitude control system (ACS) data are transmitted along with LCE data via S-band (2.3 GHz) telemetry to DSS 27. The DSN transmits these data to the NASDA Space Center at Tsukuba, where they are demodulated. The LCE data are transmitted to CRL for processing. CRL in turn transmits an ASCII data stream showing time, charge-coupled device (CCD) level, quadrant detector (QD) level, spacecraft laser-diode bias current, and coarse and fine tracking-sensor errors via integrated digital network services (ISDN) link to JPL. Because there are no ISDN links to Wrightwood, a 56-kbps telephone link is used to transmit the data from JPL to TMF.

III. The Transmitter

The transmitter consists of an argon-ion laser coupled to the 0.6-m telescope at TMF. The telescope is located in Building TM-12 at TMF, and its surveyed position is as follows:

Parameter	Position
Longitude	117° 40' 52.55"
Latitude	34° 22' 53.49"
Altitude	2.286 km

The telescope is used in the coude mode, which allows light to be coupled from large, high-power lasers into the telescope. The uplink laser is a prism-tuned coherent Innova-100 argon-ion laser that delivers a maximum 14.5-W linearly polarizer laser-light output power at 514.5 nm. At maximum power, the laser output is multimode. The laser is typically operated at an output power of about 13 W to achieve good beam quality. Coalignment of the laser beam with the telescope axis was achieved by adjusting the position of the telescope's secondary mirror until the focus was brought to a position on the optical bench. At this setting, the telescope's focal ratio was f/41, i.e., a focal length of 26.4 m.

A schematic of the optical train is shown in Fig. 3. A Conoptics electro-optic modulator impresses the uplink data stream on the optical carrier. The modulator consists of four potassium–dihydrogen–phosphate crystals and a polarizer. A data formatter—a Firebird 6000 bit-error rate tester (BERT) is used to generate a basic data pattern that is amplified—generates 0- to 1-V square-wave modulation that is amplified to the modulator's half-wave voltage in the driver, with 0 V corresponding to maximum transmission through the modulator.

After modulation, the beam is incident on a concave/convex lens pair that sets the beam divergence out of the telescope. This is nominally set at 20 μrad. A beam splitter separates the beam into two
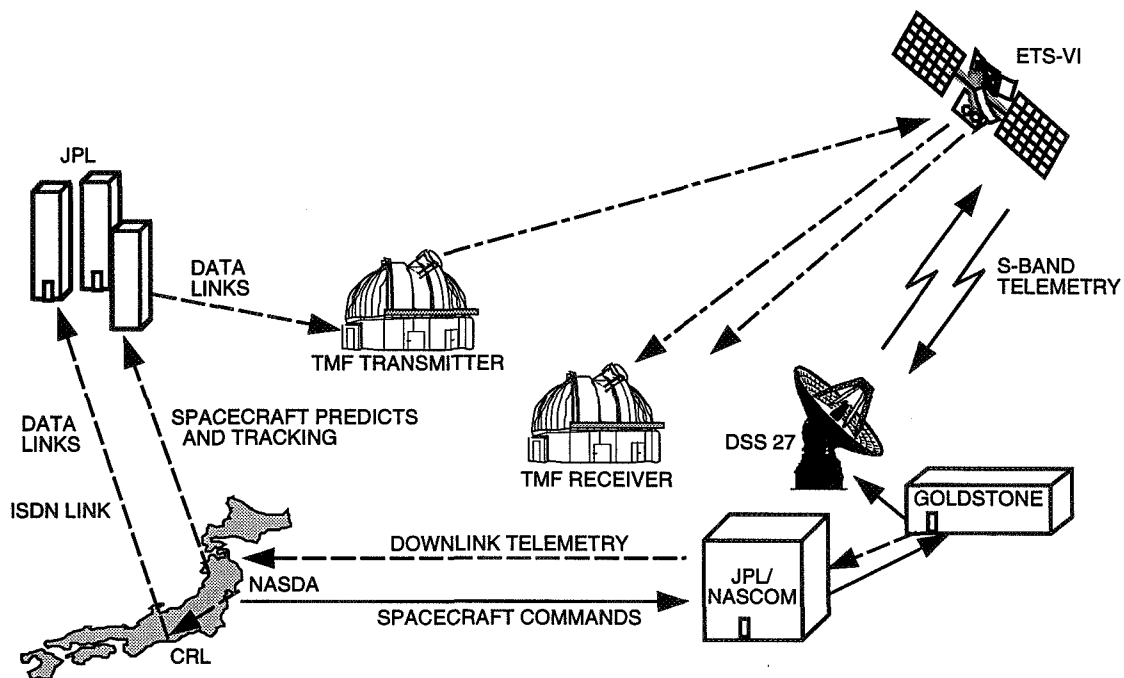

Fig. 2. Real-time coordination of several organizations is needed to accomplish the GOLD experiment. NASDA transfer commands to the DSN, which uplinks them to the ETS-VI. The spacecraft attitude and LCE sensor status are downlinked via S-band telemetry to Goldstone. The telemetry is demodulated by NASDA and forwarded to CRL for processing. During the optical uplink, CRL transmits LCE sensor data to JPL and TMF.
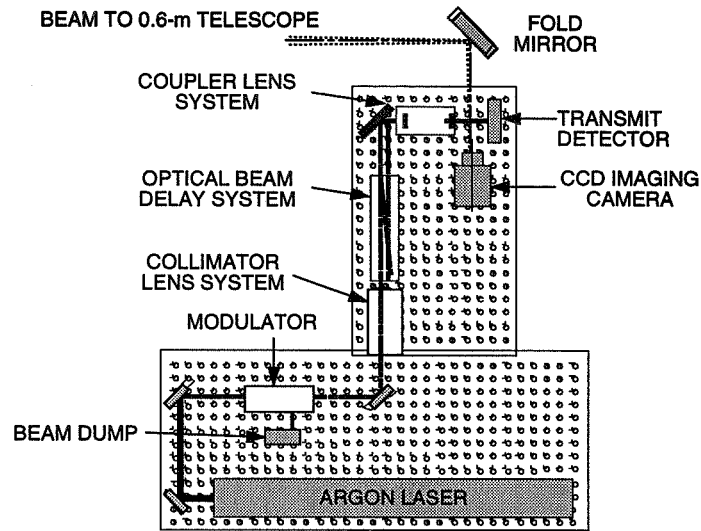
Fig. 3. Schematic of the optical train for the GOLD experiment showing the laser, the modulator, and the optical beam delay system used to provide temporal and spatial diversity of the optical beams transmitted to the satellite. Also shown are the detector used to monitor the modulated wave form and the CCD camera used to image the satellite.

equal parts, one of which goes through a 25-cm optical delay line with a path length difference greater than the laser's coherence length; $\lambda^2/\Delta\lambda$ is 10 cm. Both beams are reflected from a high-power dichroic beam splitter and are brought to a focus at the iris that is located at the f/41 focus of the telescope. From there the beams diverge and are reflected by the third coude flat and into the telescope. The beams are made incident on opposite sides of the 0.6-m telescope's primary mirror, a distance greater than the size of an atmospheric coherence cell. The use of spatial and temporal diversity mitigates the effects of atmospheric scintillation on the uplink beacon, thereby allowing the satellite's tracking system to better track the uplink beacon.

The CCD was a Pulnix camera and image intensifier with sensitivity down to 10^{-6} lux. This high-sensitivity camera has enabled us to track the satellite around apogee, where its brightness has varied from that of a magnitude 12 to a magnitude 14 star, depending on the phase angle of the solar panels. The avalanche photodiode (APD) transmitter detector monitors the modulation of the transmitted signal. In the ranging phase of the GOLD experiment, this detector will monitor the modulation sequence sent to the satellite, and these data will be transmitted to the receiver facility to initiate the timing sequence.

IV. The Receiver Facility

The optical receiver weighs approximately 30 kg and is mounted at the flange of the 1.2-m (f/29.5) telescope's bent Cassegrain focus. It consists of two CCD cameras and a 3-mm diameter low-noise APD (see Fig. 4). The cameras are a wide-field Cohu with an image intensifier for satellite acquisition and tracking and a Spectra Source CCD for atmospheric seeing measurements. These detectors are coaligned on an optical bench assembly to ensure that the downlink transmission is incident on both the tracking and communications detectors.

Satellite acquisition at the receiver is accomplished in a series of steps. It begins with calibration of the telescope's pointing direction relative to a 0.25-m Meade and a 0.4-m guiding telescope attached to the telescope's frame. A bright calibration star is acquired in the wider-field Meade and is transferred to the satellite CCD tracking detector in the smaller 1.2-m telescope field. Because the blind point accuracy of
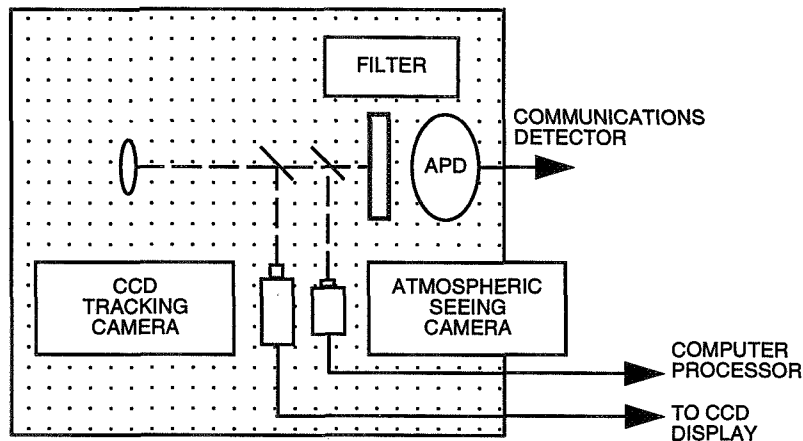
14

Fig. 4. Schematic of the optical receiver located at the focus of the 1.2-m telescope. CCD detectors in the optical train track the satellite and measure atmospheric seeing. The APD detects the 1.024-Mbps optical downlink data stream.

the telescope depends on separation between the calibration star and the satellite positions, the telescope is moved to a star in the vicinity of the satellite and the pointing offsets are noted for calibration. Near apogee, the satellite brightness ranges from the 12th to the 14th magnitude. Because of the large dynamic range between the third- to fifth-magnitude calibration stars and the satellite, an optical density no.-2 filter is placed in an electronically switchable holder located in front of the tracking camera. The filter is placed in the optical beam during the calibration and is switched out to acquire the satellite.

Atmospheric seeing measurements provide essential data for evaluating the optical link performance. The predictions of theoretical models that incorporate scintillation effects into the link performance will be compared with experimental results to validate the models. The data are taken at 15-min intervals and are reduced and transferred to the data analyst at the end of each night's run.

Downlink data-recovery electronics starts with the APD amplifier and signal conditioner. Depending on the mode of operation, the downlinked data are recovered through a bit synchronizer to recover the clock and then stored on a digital data recorder. This is shown in Fig. 5. When operating in the ranging or regeneration modes, before storage, the data are correlated with the transmitted data from the BERT located in the transmitter facility.

V. AVM Observatory

The atmospheric attenuation during the experiment is measured using the AVM observatory located at TMF. The AVM measures and records the intensity of selected stars over the course of the experiment. Star intensities are measured using three Johnson standard [V (100-nm wide centered at 560 nm), R (200-nm wide centered at 700 nm), and I (200-nm wide centered at 860 nm)] astronomical filters and three 10-nm-wide interference filters centered at the 532-nm, 860-nm, and 1064.2-nm wavelengths. The attenuation measurements made at 532 nm and 860 nm are used to estimate the atmospheric transmission at the uplink (514.5-nm) and downlink (830-nm) laser wavelengths. Transmission data at these wavelengths are calibrated using data taken through the astronomical V and I filters.

VI. Data Recovery and Data Processing

Data recovery from the satellite is accomplished using both S-band and optical downlinks. The uplink signal power is sampled at the CCD and QD at 1 Hz and transmitted on S-band telemetry. A 1-h
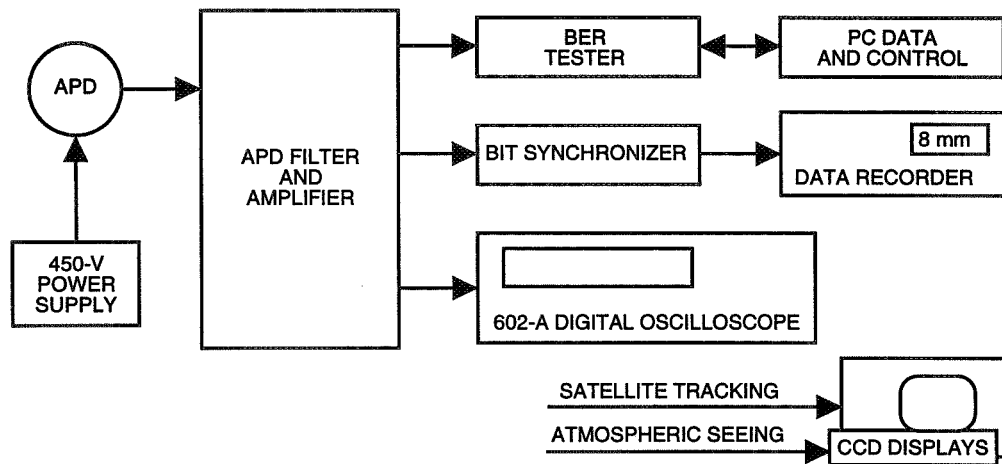
Fig. 5. Schematic of downlink data recovery. The APD output is bit synchronized and recorded for later processing. The 602-A digital oscilloscope monitors the low-pass-filtered downlink signal for long-term signal amplitude variations.
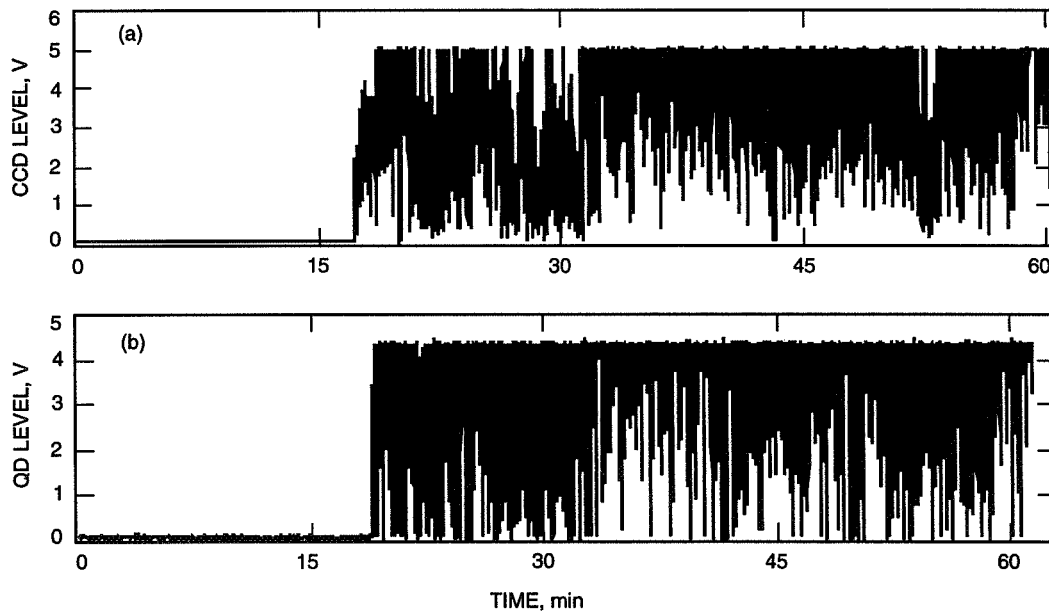

Fig. 6. A 1-hour sample of the uplink beacon as measured by the onboard CCD and QDs: (a) satellite coarse-tracking CCD sensor and (b) satellite fine-tracking QD sensor. The data show that the uplink signal is strong enough to saturate these detectors. In subsequent experiments, improved tracking performance was achieved by reducing both the transmitted intensity and the detector gain.

section of the uplink laser signal measured on the November-14 pass is shown in Fig. 6. The data clearly show saturation of the uplink power measurement on both the CCD and the QD. The coarse-pointing tracking system that is servoed around the CCD camera acquires the uplink first. The detected signal is then centered in the camera's field of view and tracked by the fine-tracking loop servoed around the QD's output. The delay between acquisition and tracking is on the order of minutes and can be clearly discerned in the two traces presented in Fig. 6. The dropouts seen in the data file are due to a combination of scintillation on the uplink beam and satellite and LCE pointing.

The LCE can impress three different data types on the downlink optical carrier. The first is the PN mode, in which an onboard PN sequence is transmitted to the ground station. This is shown in Fig. 7,

where the random bit flips of the modulation that make up the 1.024-Mbps PN data stream are clearly evident. The second is the telemetry mode, where the LCE data are transmitted at 128 kbps (with redundant transmission and Manchester modulation up to the 1.024-Mbps channel rate). Included in this data stream are the laser diode levels, the CCD and QD signal levels, the fine- and coarse-tracking levels, the APD communication detector signal levels, and the measured uplink BER data. A sample of this data stream is shown in Fig. 8. The data show bit flips occurring in multiples of eight, consistent with the ×8 multiplication of the 128-kbps data stream to achieve the 1.024-Mbps data rate.

The third mode, the regeneration mode, is shown in Fig. 9. In this mode, a 1-MHz square-wave uplink is detected by the communications detector and then retransmitted back to the ground station. Figure 9 clearly shows the regenerated 1-MHz uplink. It also shows the signal fades at a frequency inconsistent with atmospheric effects. We believe that these effects are caused by distortion in the modulated uplink beam. The causes of this distortion are being investigated. This regeneration feature will be used to perform the turnaround optical ranging experiments.

VII. Conclusions

GOLD is an international cooperative experiment that has demonstrated two-way optical communications between a satellite at a geostationary distance and an optical ground receiver. GOLD's thrust is to measure and understand the performance of the two-way optical link under a variety of atmospheric attenuation and turbulence conditions. The data accumulated from this experiment will enable better definition of the performance of optical communications systems for mission designers. Satellite ranging by detection and retransmission of an uplinked code is a time-tested approach in rf communications systems. A key goal of GOLD is to demonstrate this capability at optical frequencies for the first time.

To date we have amassed several gigabytes of data and videotapes of the optical links, along with measurements on the uplink scintillation. These data will be processed and the findings reported in future articles.
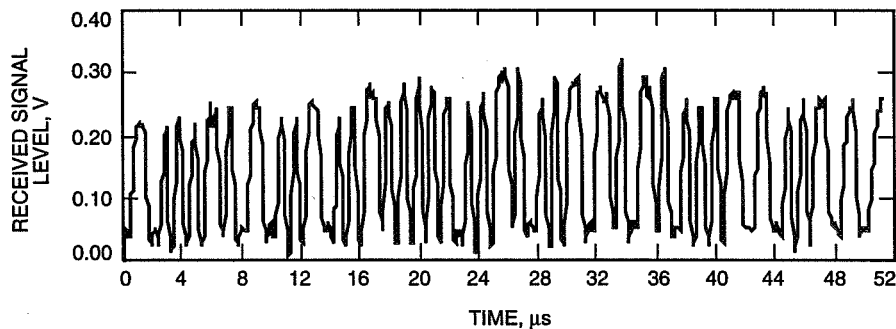

Fig. 7. Sample of 1.024-Mbps Manchester-coded PN sequence downlink telemetry from the LCE showing random bit flips.
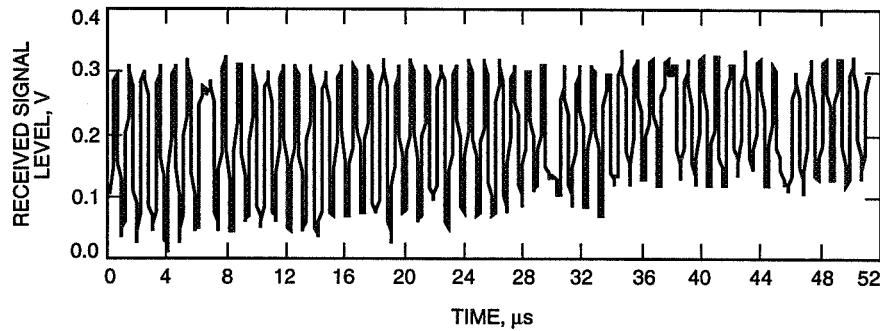
Fig. 8. Downlinked satellite telemetry at 128 kbps. The data show bit flips in multiples of eight consistent with 8X repetition of the bit pattern.
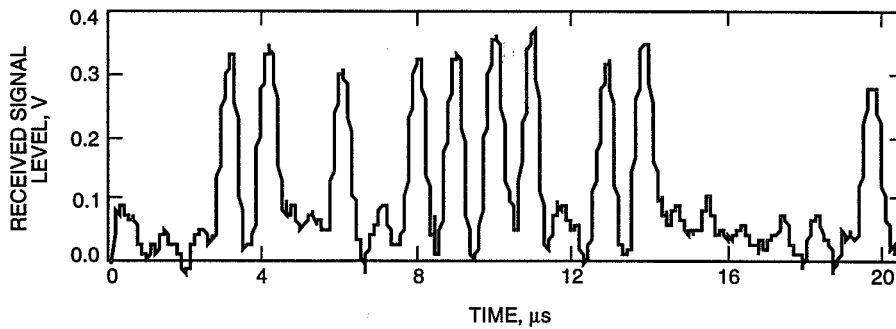

Fig. 9. Section of a 1-MHz square-wave regenerated from a 1-MHz uplink to the satellite.

Acknowledgments

Preliminary Analysis of Fluctuations in the Received Uplink-Beacon-Power Data Obtained From the GOLD Experiments

M. Jeganathan, K. E. Wilson, and J. R. Lesh
Communications Systems and Research Section

Uplink data from recent free-space optical communication experiments carried out between the Table Mountain Facility and the Japanese Engineering Test Satellite are used to study fluctuations caused by beam propagation through the atmosphere. The influence of atmospheric scintillation, beam wander and jitter, and multiple uplink beams on the statistics of power received by the satellite is analyzed and compared to experimental data. Preliminary analysis indicates the received signal obeys an approximate lognormal distribution, as predicted by the weak-turbulence model, but further characterization of other sources of fluctuations is necessary for accurate link predictions.

I. Introduction

An optical communication link between an Earth-orbiting satellite and a ground-based receiver involves propagation of a laser beam through the atmosphere. Spatial and temporal variations in the index of refraction of the air that forms the atmosphere severely degrade the quality of the beam. These variations, typically lasting on the order of one thousandth of a second at optical and near-infrared (NIR) frequencies, in the index of refraction result in random changes in the amplitude and phase of the arriving wave. The amplitude and phase fluctuations manifest themselves in effects such as scintillation, beam broadening, and beam motion or wander. Scintillation can be thought of as interference between partial waves propagating through different paths (or turbulent cells), which results in fades (destructive interference) or surges (constructive interference) at the receiver. Deep fades causing signal loss or strong surges causing saturation of the quad-detector can force loss of track. On the uplink, with the exception of heavy cloud cover, atmospheric scintillation is usually the limiting factor in an optical link. For downlink, however, the large size of the receiver's aperture typically compensates for scintillation by averaging over fades and surges. Beam motion, primarily on the uplink, can often be considered as atmospheric-induced jitter in the pointing of the laser beam. Such motion of narrow beams can cause deep fades in the signal due to the Gaussian nature of the spatial beam profile.

In this article, we use data from the recent Ground/Orbiter Lasercomm Demonstration (GOLD) experiments to study the atmosphere-induced fluctuations in signal power on the uplink. The experiment's objective is to establish a 1-Mbps optical communication link between the laser communication experiment (LCE) package on board the Japanese Engineering Test Satellite (ETS-VI) and the Table Mountain Facility (TMF) near the Jet Propulsion Laboratory (JPL). The link is established by first transmitting a

beacon from TMF to ETS-VI using a priori knowledge of the satellite's orbit. The beacon is subsequently acquired and tracked by the LCE package on the satellite. Once the tracking loop is activated on the LCE, an onboard laser is turned on for downlink. The downlink beam is then picked up by the receiver at TMF to complete the link. Once the link is established, both the downlink laser and uplink beacon can be modulated for transmission of data. Here, we shall restrict our analysis to scintillation-induced signal fluctuations on uplink and ignore the communication aspect of the experiment.

In the following analysis, we compare the statistics of the power received by the detectors on board the satellite when a continuous wave (CW) beacon is transmitted from TMF to the probability distribution function (pdf) predicted by existing models for atmospheric propagation. In Section II, we begin with a brief summary of the theory that takes into account atmospheric scintillation, jitter, and multiple uplink beams. Section III provides the specifics of the experiments and a typical link budget for the uplink. The experimental data are presented in Section IV. The final section discusses the observed results in comparison with theoretical predictions and offers potential sources of discrepancy between the theory and the experiment.

II. Theory

Consider a communication channel between a ground station and an orbiting satellite that is specific to GOLD, as shown in Fig. 1. A detailed discussion of the influence of the atmosphere on the statistics of the channel during beacon uplink follows. Figure 2 shows a system-level representation of the optical channel. We will show that the power, P_R, received by the photodetector on the satellite is the product of three quantities:

$$P_R = P_0 I S$$

where P_0 is the power received in the absence of a turbulent atmosphere, I is a random variable with a beta-distribution caused by atmospheric and pointing jitter, and S typically is a lognormal random variable due to scintillation. The maximum receivable power, P_0, at the satellite is assumed to have zero variance. Thus, fluctuations due to the laser and detector noise are assumed to be negligible compared to scintillation and beam jitter. In the following sections, the major contributions to the observed statistics of the received power are described.
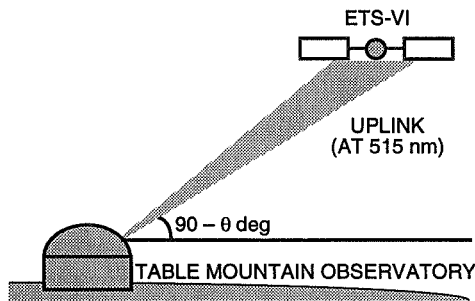

Fig. 1. Geometry of a ground-to-orbiter laser communication link showing transmission from TMF to ETS-VI.
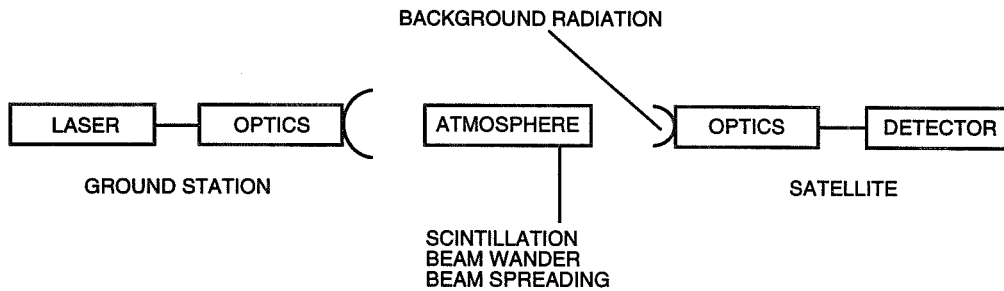
Fig. 2. Components and channels in an optical communication system.

A. Free-Space Propagation

For an optical transmitter with continuous wave (CW) laser power of P_T W, the power received by the detector on board the satellite in the absence of atmospheric turbulence is primarily governed by free-space-propagation loss and optical absorption. Taking into account optical losses at the transmitter and receiver and atmospheric absorption, we find that the received power is given by

$$P_0 = \eta_{roe}\eta_{toe}\eta_0^{\sec\theta}\frac{4}{\pi}\frac{A_R P_T}{(Z\Theta_{bd})^2}$$

where Z is the communication range in meters; Θ_{bd} is the laser beam divergence in radians; θ is the zenith angle to the receiver looking from the transmitter station; η_{toe} is the transmitter optical efficiency; η_{roe} is the receiver optical efficiency; η_0 is the atmospheric transmission at zenith; and A_R is the area of the receiver's aperture in square meters. The exponent sec θ is often referred to as the air mass. We may to a good approximation assume that all quantities in the above equation are constant over the duration of the experiment, which typically lasts a few hours.

B. Light Wave Propagation in Turbulent and Random Media

Wave propagation through lossless random media, like the atmosphere, is often characterized by the structure constant C_n^2, which is a measure of the variance of the index of refraction, n, due to inhomogeneities in the medium [1]. For modeling the atmosphere, one often needs to know the altitude variation of the structure constant and its dependence on weather conditions. Though modeling the atmosphere is a difficult task, there exist several empirical and parametric models for the altitude variation in the structure constant of the atmosphere. The most common of these is the theoretically based Hufnagel model, in which the dominant turbulence arises from winds in the 5- to 20-km altitude range [2]. The altitude of TMF (2.2 km above sea level) is well outside the range of validity of the Hufnagel model (over 5-km above sea level). The validity of the improved Hufnagel–Valley model [3], on the other hand, extends down to the ground. This model, however, predicts a larger than observed turbulence at TMF by overestimating the low-altitude contribution. We, therefore, use the experimentally based Air Force Geophysical Laboratory (AFGL) CLEAR I night model [4]. The AFGL CLEAR I night model is based on the average of a large number of measurements of the atmospheric properties in the New Mexico Desert. The model provides the functional dependence of C_n^2 on altitude down to 1.23 km above mean sea level:

$$\log_{10} C_n^2 = A + Bh + Ch^2 + D\exp\left\{-0.5\left[\frac{h-E}{F}\right]^2\right\}$$

where h is the altitude in km above mean sea level. The constants $A, B, C, D, E,$ and F are defined for three different ranges of altitude and listed in Chapter 2 of [3]. Most quantities of interest are usually expressed as weighted integrals of the index of refraction structure constant, as described below.

Consider, for example, observation of a star with a large aperture telescope. As noted earlier, the large aperture negates the effect of scintillation by averaging over constructive and destructive interferences. Since light from a distant object can be well approximated by plane waves, the only prominent effect of the turbulent atmosphere is thus the change in the angle of arrival of the plane wave. The random arrival angle limits the resolution of the telescope. In fact, the resolution of the telescope is equivalent to the resolution of an aperture, r_0 (called the coherence length of the atmosphere), determined by the atmospheric structure constant and wavelength of light [5]:

$$ r_0 = \left[0.42 k^2 \sec \theta \int_{h_0}^{Z} C_n^2(h) dh \right]^{-3/5} $$

where k is the wave vector $(2\pi/\lambda)$ of the plane wave; h is the height above sea level; and h_0 is the altitude of the location of the telescope. From basic principles of optics, an aperture with diameter r_0 has a full-width-half-maximum (FWHM) angular resolution of

$$ angular\ resolution\ = \frac{\lambda}{r_0} $$

For a wavelength of 0.5 μm, the coherence length r_0 is on the order of 10 cm. In experimental observations, it is convenient to define "seeing" as the FWHM of the angular spread of the star. For r_0 of 10 cm, the seeing is approximately 1 arcsec, or 5 μrad. It must be noted that though subarcsecond seeing conditions are possible at TMF, a more representative value for the seeing at TMF is 2–3 arcsec, or an r_0 of a little under 5 cm.

Given the AFGL CLEAR I model for the altitude dependence of the structure constant, the above equation for r_0 gives a single value for the atmospheric coherence length irrespective of the meteorological conditions. To better model the existing local weather conditions, we scale the structure constant function by a multiplicative constant so that the predicted value of r_0 matches the r_0 derived from measured seeing. The scaled C_n^2 is then used to determine other atmospheric-related quantities, such as scintillation variation and beam wander. For this purpose, the seeing was measured several times during a single run of the GOLD experiment.

C. Beam Motion and Jitter

To account for intensity fluctuations due to pointing inaccuracies and beam wander, we assume a Gaussian intensity profile for the uplink laser beam. That is, the normalized intensity pattern takes the form

$$ I\left(\delta_x, \delta_y\right) = \exp\left[-4 \left(\frac{\delta_x + \delta_y}{\Theta_{bd}} \right)^2 \right] $$

where δ_x and δ_y are the angular deviation or error in the pointing. If the transmitter and receiver are on-axis and there is no pointing offset $(\delta_x = \delta_y = 0)$, the receiver would see a power P_0 from the transmitter. Because of pointing jitter and atmospheric-induced beam motion, however, δ_x and δ_y are random variables (RVs) and not constants. We assume δ_x and δ_y to be identically and normally distributed with zero mean and variance σ_j^2. The variance σ_j^2 is the sum of the variance of atmospheric-induced and transmitter-induced pointing errors. The variance of the atmospheric-induced beam motion is again given by a weighted integral of the structure constant [5, Chapter 6], but as a first-order approximation, we assume it to be equal to the seeing. The transmitter-induced jitter is more difficult to ascertain, but is typically small relative to atmospheric effects.

The new random variable I can be shown to have the following cumulative probability distribution function (CDF) [6]:

$$P_I(I \leq i) = F_I(i) = i^\beta \quad \text{for} \quad 0 < i < 1$$

where

$$\beta = \frac{1}{8} \left(\frac{\Theta_{bd}}{\sigma_j} \right)^2$$

is a measure of the pointing accuracy with respect to the beamwidth. We immediately see that the mean and variance of I are given by

$$< I > = \frac{\beta}{\beta + 1}$$

and

$$< I^2 > - < I >^2 = \frac{\beta}{(\beta + 1)^2} \frac{1}{\beta + 2}$$

respectively. It is obvious that a large value of β is desirable. In fact, for large values of β, the mean approaches the optimum value of 1 and the variance tends to 0 as $1/\beta^2$. For small values of $\beta, (\beta << 1)$, on the other hand, both the mean and variance are proportional to β.

To achieve a large value of β, either the angular beamwidth must be increased or the beam jitter must be decreased. With little control over the atmospheric-turbulence-induced beam wander, one is often limited in practice to increasing the beam divergence for obtaining a particular value of β. But the received power is inversely proportional to the square of the beam divergence. An optimum value of β, therefore, exists and depends on atmospheric conditions. The statistical analysis of the effect of a constant pointing offset is complicated by the loss of circular symmetry, and one may be forced to resort to numerical or Monte-Carlo simulations for a complete analysis. Thus, for simplicity, we will account for constant pointing offset only through an exponential loss factor, which is a reasonable assumption if the offset is much smaller than the beam divergence.

D. Atmospheric Scintillation

The pdf of the normalized received intensity, S, at a point receiver due to scintillation can take several forms. For weak turbulence, the pdf takes on a lognormal distribution. This can be understood from the fact that S is proportional to

$$S \propto |\exp(\chi + i\phi)|^2$$

where χ and ϕ are the amplitude and phase of the wave, respectively, and both are normally distributed random variables. The quantity 2χ is often referred to as the log-irradiance. For strong turbulence over long paths, the intensity fluctuations are severe and the distribution is exponential. Andrews and Phillips have shown that the scintillation takes the form of an I-K (i.e., containing I and K Bessel functions) distribution, which reduces to the two limits given above for weak and strong turbulence [7,8]. Since the GOLD experiments were performed at a relatively high altitude (2.2 km for TMF) and the source of most

turbulence is at or near sea level, we assume a weak turbulence model and use the lognormal distribution for S. That is,

$$f_S(s) = \frac{1}{\sqrt{2\pi\sigma_l^2}} \frac{1}{s} \exp\left[-\frac{1}{2\sigma_l^2}\left(\ln s - l_m\right)^2\right]$$

where $l_m = -\sigma_l^2/2$ is the mean of the log-irradiance distribution. The S, being a normalized quantity, has a mean of 1. The variance of the log-irradiance is determined from the following weighted integral of the index of refraction structure constant [9,10]:

$$\sigma_l^2 = 2.24k^{7/6}\left(\sec\theta\right)^{11/6} \int_{h_0}^{Z} C_n^2(h)h^{5/6}\, dh$$

where k, h, and h_0 are as defined before. Experiments have shown that σ_l^2 does not arbitrarily increase with increasing atmospheric turbulence [11]. In fact, the scintillation variance reaches a saturation value of approximately $0.25\sigma_l^2 = 0.3$ and even decreases for high levels of turbulence. The variance of S itself is given by

$$\sigma_S^2 = \exp(\sigma_l^2) - 1$$

Note that it is customary to characterize the lognormal distribution of S using the mean and variance of the log-irradiance. Thus, neither the mean nor the variance of S is immediately apparent from $f_S(s)$. Given $y = \exp(x)$, where x is a Gaussian RV, and thus y is a lognormal RV, we use the following convention: By log-variance of y, we mean the variance of x.

Combining the effect of atmospheric scintillation and beam-pointing errors, the received power can be written as

$$P_R = \eta_{toe}\eta_{toe}\eta_0^{\sec\theta} \frac{4}{\pi} \frac{A_R P_T}{(Z\Theta_{bd})^2} I S$$

We emphasize that in the above equation I and S are RVs. The pdf of the received signal resulting from the product of a lognormal and beta-distributed random variable can be derived analytically. This, however, involves the use of cumbersome integral functions. Through Monte-Carlo simulations, Kiasaleh has shown that, for a scintillation variance larger than 0.2, the pdf of the product of S and I can be approximated by a lognormal distribution [12]. We will, therefore, assume the received power P_R to be lognormally distributed to arrive at an analytical expression for the final result.

The voltage readout, V, of the detection system on board the satellite is the product of the received power and the transimpedance gain, G, of the detector–amplifier combination. That is, $V = G\, P_R$. In principle, the statistics of the detector and amplifier must be taken into account for accurate analysis. For the case at hand, scintillation and jitter are dominant, and we therefore assume the statistics of V to be identical to P_R. The pdf of V, being lognormal, is

$$f_V(\nu) = \frac{1}{\sqrt{2\pi\sigma^2}} \frac{1}{\nu} \exp\left[-\frac{1}{2\sigma^2}\left(\ln\nu - \ln\nu_0\right)^2\right]$$

To determine the value of ν_0 and σ, we use the properties of independent RVs. That is, $\langle V \rangle = GP_0 \langle I \rangle \langle S \rangle$ and $\langle V^2 \rangle = (GP_0)^2 \langle I^2 \rangle \langle S^2 \rangle$. Moreover, from the properties of the lognormal distribution, $\ln \nu_0 = -0.5\sigma^2 + \ln \langle V \rangle$ and $\sigma^2 = \ln \langle V^2 \rangle - \ln \langle V \rangle^2$. From these expressions, we find that

$$\sigma^2 = \sigma_I^2 + \ln \frac{(1+\beta)^2}{(2+\beta)\beta}$$

and

$$\ln \nu_0 = \ln [GP_0] - \frac{1}{2}\sigma_I^2 - \frac{1}{2} \ln \frac{(1+\beta)^3}{(2+\beta)\beta^2}$$

The photodetector/amplifier gain factor G has units of volts per watt. The mean and variance of the received signal are not independent, as they both depend on β and σ_I^2. For example, an increase in atmospheric turbulence resulting in a larger scintillation variance will decrease the mean.

E. Effect of Multiple Uplink Beams

The adverse effect of scintillation can be reduced by the use of multiple uplink beams, each incoherent with the rest and separated by a distance larger than the atmospheric coherence diameter, r_0. For such a case, the signal arriving at the detector is the sum of the signal from each uplink beam with independent identically distributed (i.i.d.) statistics. That is,

$$S = \frac{1}{N} \sum_{n=1}^{N} S_n$$

where N is the number of independent beams, and the random variables S_n are lognormally distributed. We assume that the total uplink power remains constant and, thus, each beam has $1/N$th of total power. From the properties of sums of i.i.d. random variables, we find that S is a convolution of N lognormal distributions. Analytic expressions for the convolution of lognormal functions are unavailable, and thus we resort to numerical techniques using characteristic functions and fast Fourier transforms (FFTs). Note that for a large N, according to the central limit theorem (CLT), the distribution of S approaches a Gaussian.

To illustrate the benefits of launching multiple beams during uplink, we choose, as an example, a mean of $100/N$ and a log-variance of 0.6 for each S_n. Figure 3 shows the expected pdf when total laser power is equally distributed in 1, 2, 4, 8, or 16 beams. Several features are worth noting. First, the means for all the distributions are the same. Second, the location of the peak of the pdf approaches the mean of S when N is increased. Finally, the pdf is concentrated around the mean for large values of N. In short, though the mean varies little with an increasing number of beams, the variance drops significantly with additional beams. In fact, for the example in the figure, the standard deviations are 88, 64, 45, 32, and 23 for 1, 2, 4, 8, and 16 beams, respectively. That is, the standard deviation is approximately one-half with 4 beams and one-quarter with 16 beams.

In the presence of strong scintillation, dividing the laser power into several beams is essential for avoiding deep fades and surges. The number of beams needed to achieve a given bit-error rate (BER) will depend on the strength of the scintillation. One can, in principle, increase the number of beams arbitrarily to improve signal statistics at the receiver. Practical considerations, such as efficiency of dividing the laser power, modulation timing accuracy, and, most importantly, the available space, however, will typically limit the number of beams to less than 10.
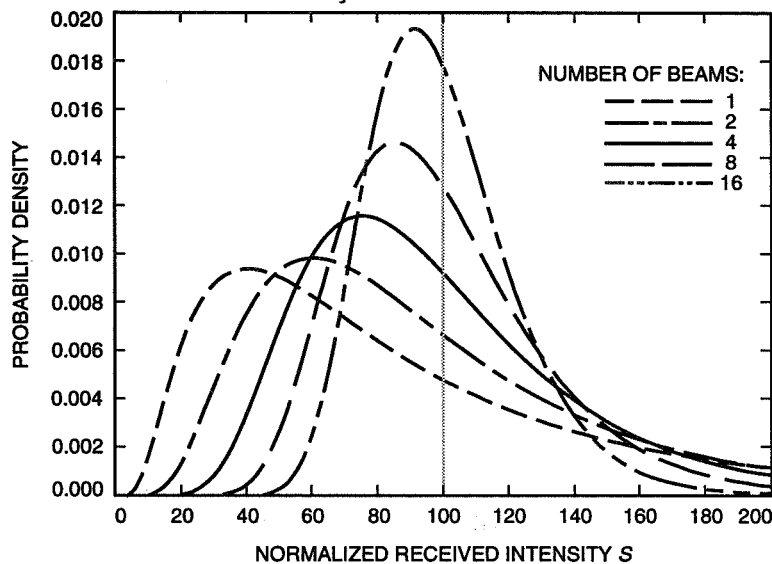
Fig. 3. The pdf of the received signal intensity, S, showing the improvement in variance with multiple uplink beams.

Part of the objective of GOLD is to understand the effects of multibeam propagation through the atmosphere. In the GOLD experiments, light from the laser is split into two and the path length of one of the beams is increased by a distance greater than the coherence length of the laser. The two beams are then launched into the coudé so as to emerge from the primary separated by a distance of 20 cm (which is much greater than r_0). Thus, the actual variance of the received signal will be less than that predicted by the single-beam model.

III. Link Budget

Table 1 shows the link budget for transmission of a single high-power CW beam from TMF up to the satellite on November 17, 1995. The link budget is for the quad-photodetector (QPD) on the satellite. All data concerning the laser communication package on the satellite are provided by the Communication Research Laboratory (CRL) in Japan. Parameters pertaining to the TMF transmitter were determined experimentally. Atmospheric-related parameters were estimated from "seeing" conditions, as described earlier. We assume that the beam wander is dominated by atmospheric-induced motion and that it is equal to the seeing. Finally, background radiation from Earth reaching the detector is negligible, as the experiments are conducted at night from TMF. Values of parameters such as range, elevation, and seeing represent average values for the duration of the experiment. The atmospheric scintillation contribution to the log-variance is 0.52 in the above calculation. The remainder of the contribution to the variance is from atmosphere-induced beam wander. The effect of two beams on the expected variance is discussed in the next section.

IV. Experimental Data and Analysis

Figure 4 shows the QPD signal versus time for an approximately 100-min time period when two CW beams (each with ~6.6 W of power) were sent up to the satellite. The data were collected on the 17th of November 1995. The QPD signal was sampled every second and sent down through RF telemetry. Furthermore, the QPD has a gain value of 0.22 V/nW in the "low" gain setting, a gain value of 4.60 V/nW in the "high" gain setting, and few other intermediate settings. During the time corresponding to Fig. 4, the gain was set to low. Figure 5 shows the histogram of the signal shown in Fig. 4. The most likely

Table 1. Link budget for a single beacon uplink from TMF to ETS-VI.

Parameter	Value	Equivalent value, dB/dBm
Range (satellite to TMF distance)	37,850 km	—
Zenith angle	43.8 deg	—
Seeing	6 μrad	—
Transmitter information		
Laser wavelength	514.5 nm	—
Laser power	13,200 mW	41.21 dBm
Optical transmission[a]	0.75	−2.22 dB
Beam divergence	20 μrad	—
Pointing loss	4 μrad	−0.09 dB
Pointing jitter	0 μrad	—
Free space/atmosphere		
Propagation loss	—	−56.53 dB
Estimated atmospheric transmission at zenith	0.80	—
Atmospheric loss (at zenith angle)	—	−1.34 dB
Receiver information		
Aperture diameter	7.50-cm	−23.55 dB
Optical transmission	0.15	−8.24 dB
Received power (no turbulence)	10.49 nW	−49.79 dBm
Sensitivity ("high" gain)	631.0 pW	−62.00 dBm
Margin	16.62	12.21 dB
Reduction due to scintillation	0.77	−1.11 dB
Reduction due to jitter	0.71	−1.48 dB
New received power	5.7 nW	−52.38 dBm
New margin	9.0	8.89 dB
Net log-variance, σ^2	0.69	—
Probability of detection with above sensitivity	99.6 percent	—
Scintillation fades greater than 3 dB	33.7 percent	—

[a] Estimate based on losses in optical train components and reflectivity of telescope mirrors.

value of the QPD signal was approximately 1.2 V. The clustering of points around the maximum value of 4.5 V indicates saturation of the detector due to scintillation-induced surges, while clustering near the minimum value of 0 V indicates the beam was outside the field of view of the QPD due to tracking errors. The fact that the statistics of the received signal are not lognormal but rather a convolution of two lognormal distributions makes analyzing the data difficult because of the lack of an analytic expression for the convolution. The histogram data may nonetheless be fit to a lognormal function to obtain an approximate value for the mean and log-variance. To do so, the histogram data were fit to a scaled lognormal distribution, $A\ f(\nu)$, in an indirect way. The lognormal distribution can be written as a second-order polynomial by appropriate transformation of variables. Let $w = \ln f(\nu)$ and $u = \ln \nu$. By taking the log of the lognormal distribution function, we have
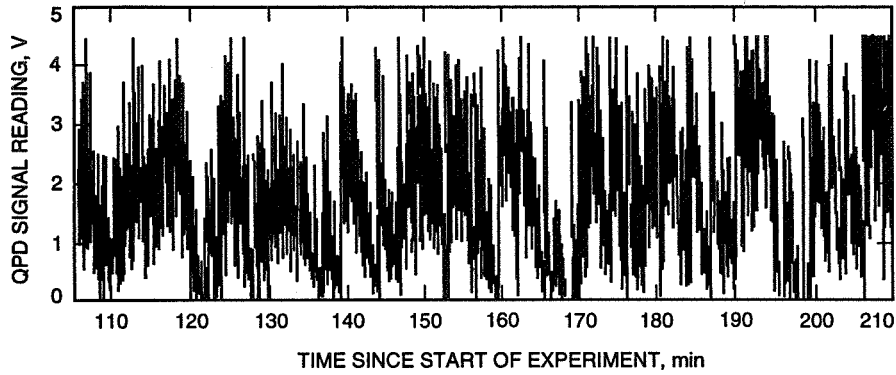
$$w = au^2 + bu + c$$

Fig. 4. The QPD signal reading versus time in minutes since the start of the experiment (10:40 UTC) on November 17, 1995.
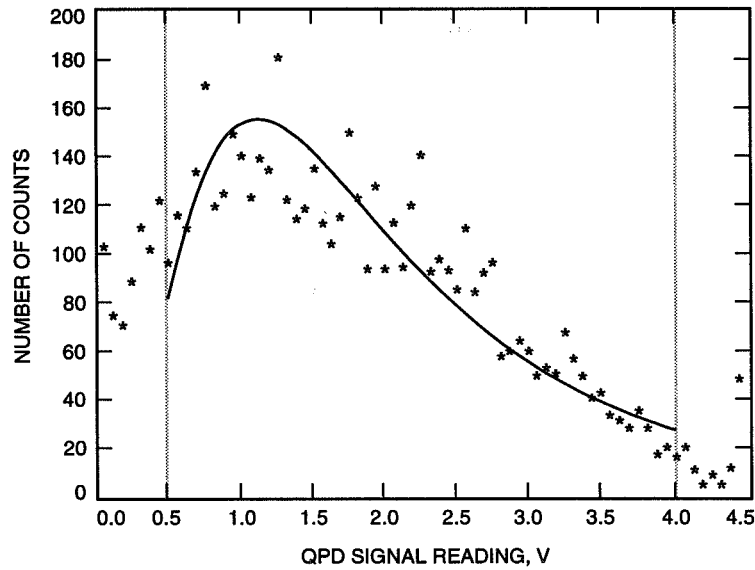
Fig. 5. Histograms of the QPD signal reading. The asterisks show the number of times a given signal level was observed in the time interval of interest. The solid line is a fit of the histogram data to a log-normal function.

The amplitude, mean, and variance of the lognormal distribution can be inferred from the parameters a, b, and c in a straightforward manner, the results of which are given below:

$$\sigma = \frac{1}{\sqrt{-2a}}$$

$$\ln \nu_0 = \sigma^2 (1 + b)$$

$$\ln A = c + \frac{(\ln \nu_0)^2}{2\sigma^2} + \frac{1}{2} \ln(2\pi\sigma^2)$$

Using least-square methods, the log of the raw data can, therefore, be easily fit to a polynomial to determine the mean and variance of the lognormal distribution. This technique eliminates the need

to take several partial derivatives of the lognormal distribution and simplifies the fitting algorithm. The fit is shown along with the original data in Fig. 5. Data points near saturation and data points around the minimum signal level resulting from pointing errors were not considered. The resulting fit had a mean of $\nu_0 = 1.81$ V and $\sigma^2 = 0.49$. These numbers account for contributions from both scintillation and beam motion/jitter. In the presence of multiple beams, it is more convenient to use the actual mean and standard deviation of the distribution as opposed to indirect measures such as log-variance. From $\ln < V > = 0.5\sigma^2 + \ln \nu_0$, we find that the mean of the fit is $< V > = 2.3$ V. It is also useful to define a normalized standard deviation, $SD = (< V^2 > - < V >^2)^{1/2} / < V >$ for the distribution. It is easy to show that $SD = (\exp(\sigma^2) - 1)^{1/2}$, and therefore the standard deviation is 0.80 for the fit.

V. Comparison of Theory and Experiment

Figure 6 shows the predicted (with one and two beams) and experimentally observed pdf's for the QPD signal. Figure 6 also lists the mean and standard deviation for each of the theoretical and experimental curves. For two beams, the theory predicts the standard deviation of the signal to be 0.71, while it is 0.80 for the experimental fit. The difference arises mainly from the uncertainty in the transmitter pointing jitter and the unaccounted satellite tracking errors (discussed later). The electronics on board the satellite are susceptible to Earth's radiation belts, and the resulting noise can increase signal variation as well. Additional data from the planned experiments with a single uplink beam will enable better comparison to theory.
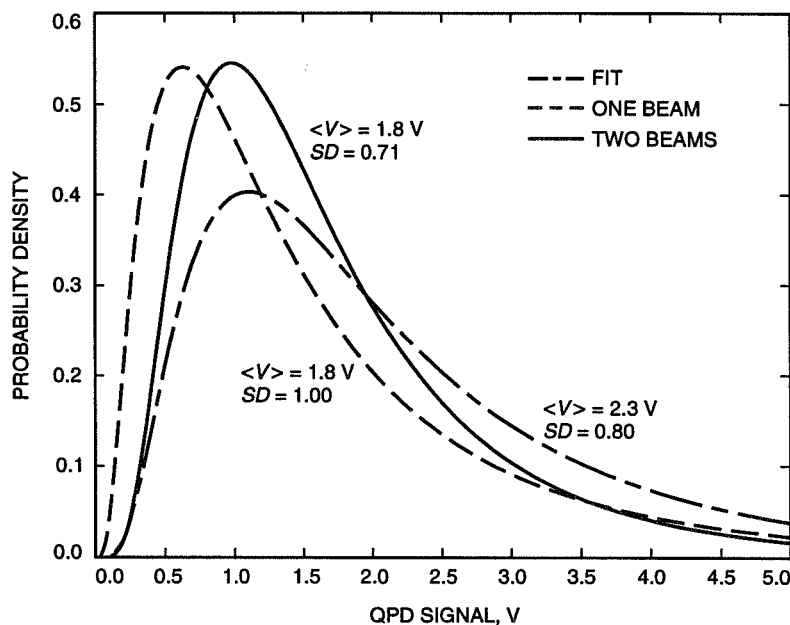
Fig. 6. Expected and observed pdf of the QPD signal, showing the experimental lognormal fit of Fig. 5, the theoretical pdf for a single uplink beam, and the expected pdf in the presence of two uplink beams.

The discrepancy between the predicted and observed mean values, on the other hand, is just over 1.5 dB. It is interesting to note that the theoretical and observed most-likely value of the QPD voltage reading is almost identical. The agreement between theory and experiment for the mean value is surprisingly good given the various unknown factors that are currently being investigated. Recent experiments suggest a reduction in the sensitivity of the detector with time due to temperature increases. The effect of excessive exposure to Earth's radiation belts on the QPD and charge-coupled device (CCD) sensitivity is

still unclear. Some of the difference can be attributed to uncertainties in the optical loss of the transmitter system, which was estimated from the number of elements in the optical train. Also, the atmospheric transmission value at the uplink wavelength needs to be updated from the planned recalibration of the atmospheric visibility monitoring (AVM) data. Moreover, neither the transmitter pointing offset nor the beam divergence is accurately known.

As is apparent from Fig. 4, there is a slow (on the order of minutes) decay in the signal level followed by a sharp jump to a high value. This is due to drift in the tracking of the beacon by the satellite, which is not included in the analysis. The tracking errors cause the out-of-focus beam to fall partially outside the area of the QPD and, hence, cause a reduction in the detected signal. The slow decays in received signal power partly explain the large variance in the observed signal. Faster sampling of the beacon signal from the communication detector should provide additional data about temporal statistics of scintillation. Downlink signal statistics will provide information on satellite vibrations, pointing accuracy, and pointing drift that will further enable us to better isolate atmospheric scintillation effects.

Acknowledgments

References

[1] J. W. Goodman, *Statistical Optics*, New York: John Wiley and Sons, 1985.

[2] R. E. Hufnagel, "Variations of Atmospheric Turbulence," *Digest of Topical Meeting on Optical Propagation Through Turbulence*, Paper WA1, Optical Society of America, Washington, DC, 1974.

[3] G. C. Valley, "Isoplanatic Degradation of Tilt Correction and Short-Term Imaging Systems," *Appl. Opt.*, vol. 19, 1980.

[4] F. G. Smith, ed., *Atmospheric Propagation of Radiation*, vol. 2, Bellingham, Washington: SPIE Optical Engineering Press, 1993.

[5] W. L. Wolfe and G. J. Zissis, eds., *The Infrared Handbook*, revised edition, Ann Arbor, Michigan: Environmental Research Institute of Michigan, 1989.

[6] K. Kiesaleh and T.-Y. Yan, "A Statistical Model for Evaluating GOPEX Uplink Performance," *The Telecommunications and Data Acquisition Progress Report 42-111, July–September 1992*, Jet Propulsion Laboratory, Pasadena, California, pp. 325–332, November 15, 1992.

[7] L. C. Andrews and R. L. Phillips, "I-K Distribution as a Universal Propagation Model of Laser Beams in Atmospheric Turbulence," *Journal of the Optical Society of America*, vol. 2, pp. 160–163, 1985.

[8] L. C. Andrews, R. L. Phillips, and B. K. Shivamogg, "Relations of the Parameters of the I-K Distribution for Irradiance Fluctuations to Physical Parameters of the Turbulence," *Appl. Opt.*, vol. 27, pp. 2150–2156, 1985.

[9] V. I. Tatarskii, *Wave Propagation in Turbulent Medium*, New York: McGraw-Hill, 1961.

[10] A. Ishimaru, *Wave Propagation and Scattering in Random Media*, vol. 2, New York: Academic Press, 1978.

[11] S. F. Clifford, G. R. Ochs, and R. S. Lawrence, "Saturation of Optical Scintillation by Strong Turbulence," *Journal of the Optical Society of America*, vol. 64, no. 148, 1974.

[12] K. Kiesaleh, "On the Probability Density Function of Signal Intensity in Free-Space Optical Communications Systems Impaired by Pointing Jitter and Turbulence," *Opt. Eng.*, vol. 33, pp. 3748–3757, 1994.

Optimum Combining of Residual Carrier Array Signals in Correlated Noises

H. H. Tan
Communications Systems and Research Section
and
University of California, Irvine

R. Liang and P.-H. Suen[1]

An array feed combining system for the recovery of signal-to-noise ratio (SNR) loss due to antenna reflector deformation has been implemented and is currently being evaluated on the Jet Propulsion Laboratory 34-m DSS-13 antenna. The current signal-combining system operates under the assumption that the white Gaussian noise processes in the received signals from different array elements are mutually uncorrelated. However, experimental data at DSS 13 indicate that these noise processes are indeed mutually correlated. The objective of this work is to develop a signal-combining system optimized to account for the mutual correlations between these noise processes. The set of optimum combining weight coefficients that maximizes the combined signal SNR in the correlated noises environment is determined. These optimum weights depend on unknown signal and noise covariance parameters. A maximum-likelihood approach is developed to estimate these unknown parameters to obtain estimates of the optimum weight coefficients based on residual carrier signal samples. The actual combined signal SNR using the estimated weight coefficients is derived and shown to converge to the maximum achievable SNR as the number of signal samples increases. These results are also verified by simulation. A numerical example shows a significant improvement in SNR performance can be obtained, especially when the amount of correlation increases.

I. Introduction

An array feed-combining system has been proposed for the recovery of signal-to-noise ratio (SNR) losses caused by large antenna reflector deformations at Ka-band (32-GHz) frequencies in the Deep Space Network [1]. In this system, a focal plane feed array is used to collect the defocused signal fields that result from these deformations. All the signal power captured by the feed array is then recovered using real-time signal-processing and signal-combining techniques. The optimum combiner weights that maximize the combined signal SNR were derived in [1] under the assumption that the white Gaussian noise processes in the received signals from different array elements are mutually uncorrelated. These optimum weights depend on unknown signal and noise parameters that need to be estimated. The work in [1] proposed to estimate the optimum weights from the observed residual carrier received-signal samples

---

[1] Students at the University of California, Irvine.

using a maximum-likelihood (ML) approach. The actual combined-signal SNR in an uncorrelated noises environment when the estimated weights are used in place of the optimum weight coefficients was also derived in [1].

A seven-element array feed combiner system is currently being evaluated at the JPL DSS-13 34-m antenna. Although the work in [1] assumed mutually uncorrelated noise processes, experimental data [2] indicate that the noise processes in the received signals from different feed elements are indeed correlated, with correlation coefficients of the order of 0.01 under clear sky conditions. Since the noise in each of the array feed element signals consists of receiver white noise plus noise due to background radiation, it has been conjectured that this small correlation is caused by near-field atmospheric background noise. Recent data gathered at DSS 13 in more adverse weather conditions, however, indicate both increases and decreases in the observed amount of correlation. This experimental work is still in progress. Larger correlations may also result from undesired radiation source emissions gathered by the antenna side lobes. Moreover, our recent work [5] has shown that the array feed combining system derived in [1], which is suboptimal in the correlated noises environment, actually can have a better performance in the presence of correlated noises. Therefore, it is important to develop optimum signal-combining techniques that account for the mutual correlation between the noises in the signals from different array elements. That is the objective of this work.

As a first step towards this objective, in Section II we provide a derivation of the set of optimum combining weight coefficients that maximizes the combined-signal SNR in this correlated noises environment. These optimum weights depend on unknown signal amplitude and phase parameters as well as noise variance and correlation parameters. An ML approach is then developed in Section III to estimate these unknown parameters and arrive at an ML estimate of the optimum weight coefficients based on residual carrier received-signal samples. The actual combined-signal SNR is derived in Section IV when the estimated weights are used in place of the optimum weights, with the details given in Appendices A and B. The SNR performance is shown to converge to the maximum achievable SNR as the number of signal samples used in the estimates increases. These results are also verified by simulation. Numerical examples are given in Section V with a particular choice of noise covariance matrix and signal parameters and show a significant improvement in SNR performance compared to the previous signal-combining system developed in [1], especially when the amount of correlation increases.

II. Array Feed Signals and Optimal Combining Weights

Consider a K-element array and the NASA Deep Space Network standard residual carrier modulation with binary phase shift keyed (PSK) modulated square-wave subcarrier [4]. The received signal from each array element is downconverted to baseband and sampled. Similar to the combining system proposed in [1], only the residual carrier portion of the received signal spectrum will be used to estimate the unknown parameters in the combiner weights. The full-spectrum modulated signals from the array elements, which contain both the modulated sidebands as well as the residual carrier spectrum, are subsequently combined. As in [1], assume that the higher bandwidth primitive baseband signal samples are lowpass filtered by averaging successive blocks of M_B samples to yield a full-spectrum signal stream B for each array element. Additive white Gaussian noise is assumed to be present in the primitive baseband signal sequences from each of the array elements. The white Gaussian noises in the primitive baseband samples from different array elements are assumed to be mutually correlated. *Specifically, the noise samples corresponding to different array elements are assumed to be mutually correlated at any given time instant, but uncorrelated at different time instants.* Let

$$y_k(i_B) = V_k[\cos \delta + js(i_B) \sin \delta] + n_k(i_B), \quad i_B = 1, 2, \cdots \tag{1}$$

denote the stream B signal samples from the kth array element. The complex signal parameters $V_k, 1 \leq k \leq K$, represent the unknown signal amplitude and phase parameters induced by the antenna reflector

deformation. Moreover, δ is the modulation index, $s(i_B) = \pm 1$ is the transmitted data, and $\{n_k(i_B)\}$ is the zero-mean white Gaussian noise corruption in the stream B signal samples from the kth array element. The primitive baseband signal samples are also more narrowly lowpass filtered by averaging successive blocks of M_A samples to yield a residual carrier signal stream A for each array element. Clearly, $M_A > M_B$ and $\eta = M_A/M_B$ is the ratio of the bandwidth of stream B to stream A. Let

$$u_k(i_A) = V_k \cos \delta + m_k(i_A), \quad i_A = 1, 2, \cdots \tag{2}$$

denote the stream A signal samples from the kth array element. Here $\{m_k(i_A)\}$ is the zero-mean white Gaussian noise corruption in the stream A signal samples from the kth array element. Let A^*, A^T, and $A^\dagger$ denote the complex conjugate, the transpose, and the complex conjugate transpose of the matrix A, respectively. In order to specify the correlations between the white noise sequences corresponding to different array elements, consider the noise vectors $\underline{n}(i_B) = (n_1(i_B) \cdots n_K(i_B))^T$ and $\underline{m}(i_A) = (m_1(i_A) \cdots m_K(i_A))^T$. Then $\{\underline{n}(i_B)\}$ and $\{\underline{m}(i_A)\}$ are each sequences of independent identically distributed (i.i.d.) zero-mean complex Gaussian random vectors of dimension K. The respective covariance matrices $\underline{R}_B = \{r_{Bkj}\} = \mathbf{E}[\underline{n}(i_B)\underline{n}(i_B)^\dagger]$ and $\underline{R}_A = \{r_{Akj}\} = \mathbf{E}[\underline{m}(i_A)\underline{m}(i_A)^\dagger]$ of $\underline{n}(i_B)$ and $\underline{m}(i_A)$ specify the mutual correlations between the white noises in the signal streams from different array elements. For example, r_{Bkj} is the correlation between the noise variables $n_k(i_B)$ and $n_j(i_B)$. Because of the different averaging rates in streams A and B on the primitive baseband signals, it follows that $\underline{R}_B = \eta\underline{R}_A$. Finally, these different averaging rates also imply that $\underline{m}(i_A)$ is independent of $\underline{n}(i_B)$ provided that $i_A < i_B$ and the samples averaged to yield $\underline{m}(i_A)$ occurred prior to the samples averaged to yield $\underline{n}(i_B)$.

Application of the complex combining-weight coefficients $W_k, 1 \le k \le K$ yields the combiner output sequence $z_c(i_B) = s_c(i_B) + n_c(i_B)$, where

$$s_c(i_B) = \sum_{k=1}^{K} W_k V_k e^{js(i_B)\delta} \tag{3}$$

and

$$n_c(i_B) = \sum_{k=1}^{K} W_k n_k(i_B) \tag{4}$$

are the signal and noise components, respectively. Define $\underline{W} = (W_1 \cdots W_K)^T$ to be the vector of combining-weight coefficients. The objective is to determine the optimum weight vector $\underline{W}$ that maximizes the SNR of the combiner output defined by

$$\gamma(\underline{W}) = \frac{|\mathbf{E}[z_c(i_B)]|^2}{\mathbf{Var}[z_c(i_B)]} = \frac{|s_c(i_B)|^2}{\mathbf{Var}[n_c(i_B)]} \tag{5}$$

The optimum weight vector and the maximum achievable SNR have been derived previously in [3]. For the sake of completeness, we provide a derivation below that is slightly different from that in [3]. Define $\underline{V} = (V_1 \cdots V_K)^T$ to be the vector of complex signal parameters. Then, from Eqs. (3) and (4), we have $|s_c(i_B)|^2 = |\underline{W}^T\underline{V}|^2$ and $\mathbf{Var}[n_c(i_B)] = \underline{W}^T\underline{R}_B\underline{W}^*$, substitution of which in Eq. (5) yields

$$\gamma(\underline{W}) = \frac{|\underline{W}^T\underline{V}|^2}{\underline{W}^T\underline{R}_B\underline{W}^*} \tag{6}$$

Since $\underline{R}_B$ is a positive definite Hermitian matrix, there is a unitary matrix $\underline{Q}$ such that

$$\underline{R}_B = \underline{Q}^\dagger \underline{D}^2 \underline{Q} \tag{7}$$

where $\underline{D}$ is a real-valued $K \times K$ diagonal matrix with the kth diagonal term given by $\sqrt{r_{Bkk}}$. Using Eq. (7), we have

$$\underline{W}^T \underline{R}_B \underline{W}^* = \left(\underline{W}^T \underline{Q}^\dagger \underline{D} \right) \left(\underline{D} \underline{Q} \underline{W}^* \right)$$

$$= \left(\underline{D} \underline{Q} \underline{W}^* \right)^\dagger \left(\underline{D} \underline{Q} \underline{W}^* \right) = \| \underline{D} \underline{Q} \underline{W}^* \|^2 \tag{8}$$

Moreover, since $\underline{Q}$ is the inverse of the matrix $\underline{Q}^\dagger$,

$$\left[\left(\underline{D} \underline{Q}^* \right)^T \right]^{-1} = \left[\underline{Q}^\dagger \underline{D} \right]^{-1} = \underline{D}^{-1} \underline{Q} \tag{9}$$

Hence, by using Eq. (9), we can write

$$\underline{W}^T \underline{V} = \underline{W}^T \left(\underline{D} \underline{Q}^* \right)^T \left[\left(\underline{D} \underline{Q}^* \right)^T \right]^{-1} \underline{V}$$

$$= \left(\underline{D} \underline{Q} \underline{W}^* \right)^\dagger \left(\underline{D}^{-1} \underline{Q} \underline{V} \right) \tag{10}$$

So substituting Eqs. (8) and (10) in Eq. (6) and applying the Schwartz inequality gets

$$\gamma(\underline{W}) = \frac{\left| \left(\underline{D} \underline{Q} \underline{W}^* \right)^\dagger \left(\underline{D}^{-1} \underline{Q} \underline{V} \right) \right|^2}{\| \underline{D} \underline{Q} \underline{W}^* \|^2}$$

$$\leq \frac{\| \underline{D} \underline{Q} \underline{W}^* \|^2 \| \underline{D}^{-1} \underline{Q} \underline{V} \|^2}{\| \underline{D} \underline{Q} \underline{W}^* \|^2}$$

$$= \| \underline{D}^{-1} \underline{Q} \underline{V} \|^2 \triangleq \gamma_{MAX} \tag{11}$$

Moreover, equality holds in Eq. (11) if and only if for some complex-valued constant α, $\underline{D} \underline{Q} \underline{W}^* = \alpha \left(\underline{D}^{-1} \underline{Q} \underline{V} \right)$. So, by using Eq. (7), the set of optimum weight vectors $\underline{W}_{OPT}$ that achieves $\gamma(\underline{W}_{OPT}) = \gamma_{MAX}$ is given by

$$\underline{W}_{OPT} = \alpha \left(\underline{Q}^\dagger \underline{D}^{-2} \underline{Q} \right)^* \underline{V}^* = \alpha \left(\underline{R}_B^* \right)^{-1} \underline{V}^* = \frac{\alpha}{\eta} \left(\underline{R}_A^* \right)^{-1} \underline{V}^* \tag{12}$$

where α is an arbitrary complex-valued constant. Moreover, it follows from Eqs. (7) and (11) that the optimum SNR γ_{MAX} can be written as

$$\gamma_{MAX} = \left(\underline{D}^{-1}\underline{Q}\underline{V}\right)^{\dagger}\left(\underline{D}^{-1}\underline{Q}\underline{V}\right) = \underline{V}^{\dagger}\underline{R}_B^{-1}\underline{V} \tag{13}$$

Note that, in the uncorrelated noises case, $\underline{R}_B^{-1} = \underline{D}^{-2}$. So the set of optimum weight vectors, Eq. (12), in this case is given by $\underline{W}_{OPT} = \alpha\underline{D}^{-2}\underline{V}^*$, and the optimum SNR is given by

$$\gamma_{MAX} = \|\underline{D}^{-1}\underline{V}\|^2 = \sum_{k=1}^{K}\frac{|V_k|^2}{r_{Bkk}} \triangleq \gamma \tag{14}$$

which is the sum of the array element output SNRs. These results for the uncorrelated noises case agree with previous results derived in [1].

III. Parameter Estimation

The signal parameter vector $\underline{V}$ and the noise covariance matrix $\underline{R}_A$ are not known and need to be estimated to obtain an estimate of one of the optimum weight vectors, $\underline{W}_{OPT}$, given by Eq. (12). Assuming that these unknown parameters are not random, we propose to use ML estimates based on the stream A residual carrier-signal vector samples $\{\underline{u}(i_A)\}$, where $\underline{u}(i_A) = (u_1(i_A)\cdots u_K(i_A))^T$. Instead of estimating $\underline{V}$ directly, consider estimating $\underline{X} = \underline{V}\cos\delta$. Note from Eq. (2) that $\{\underline{u}(i_A)\}$ is an i.i.d. sequence of complex Gaussian random vectors with mean $\underline{X}$ and covariance matrix $\underline{R}_A$. It then follows from multivariate statistical analysis [6,7] that, based on observations $\{\underline{u}(i_A - 1), \cdots, \underline{u}(i_A - L)\}$,

$$\underline{\hat{X}}_{ML}(i_A) = \frac{1}{L}\sum_{l=i_A-L}^{i_A-1}\underline{u}(l) \tag{15}$$

and

$$\underline{\hat{R}}_{A,ML}(i_A) = \frac{1}{L}\sum_{l=i_A-L}^{i_A-1}\left[\underline{u}(l) - \underline{\hat{X}}_{ML}(i_A)\right]\left[\underline{u}(l) - \underline{\hat{X}}_{ML}(i_A)\right]^{\dagger} \tag{16}$$

are the respective ML estimates of $\underline{X}$ and $\underline{R}_A$. By the invariant property of ML estimators,

$$\underline{\hat{V}}_{ML}(i_A) = \frac{1}{\cos\delta}\underline{\hat{X}}_{ML}(i_A) \tag{17}$$

is then the ML estimate of $\underline{V}$ and

$$\underline{\hat{W}}_{OPT}(i_A) = \frac{\alpha}{\eta}\left(\underline{\hat{R}}_{A,ML}^*(i_A)\right)^{-1}\underline{\hat{V}}_{ML}^*(i_A) \tag{18}$$

is the ML estimate of $\underline{W}_{OPT}$ given by Eq. (12).

It is well known [6,7] that $\underline{\hat{X}}_{ML}(i_A)$ is a complex Gaussian random vector with mean $\underline{X}$ and covariance matrix $(1/L)\underline{R}_A$. Furthermore, $\underline{\hat{X}}_{ML}(i_A)$ and $\underline{\hat{R}}_{ML}(i_A)$ are statistically independent, and $L\underline{\hat{R}}_{ML}(i_A)$ has the same distribution as the random matrix

$$\underline{A} = \sum_{i=1}^{L-1} \underline{Z}_i \underline{Z}_i^\dagger \tag{19}$$

where $\underline{Z}_i$ is a sequence of i.i.d. zero-mean complex Gaussian random vectors with covariance matrix $\underline{R}_A$. This type of distribution is called a complex Wishart distribution with parameters $\underline{R}_A$ and $(L-1)$, and $\underline{A}$ in Eq. (19) is said to have a $CW(\underline{R}_A, L-1)$ distribution [7]. It has been shown in [8] that, for $L > K+1$,

$$\mathbf{E}[\underline{A}^{-1}] = \frac{1}{(L-1) - K} \underline{R}_A^{-1} \tag{20}$$

for a $K \times K$ $CW(\underline{R}_A, L-1)$ distributed random matrix $\underline{A}$. Since $(\underline{A}^*)^{-1} = (\underline{A}^{-1})^*$, it then follows from using the property of Eq. (20) for the complex Wishart matrix $L\hat{\underline{R}}_{ML}(i_A)$ along with Eqs. (12), (17), and (18) that, for $L > K+1$,

$$\mathbf{E}\left[\hat{\underline{W}}_{OPT}(i_A)\right] = \frac{\alpha}{\eta} \mathbf{E}\left[\left(\hat{\underline{R}}_{A,ML}^*(i_A)\right)^{-1}\right] \mathbf{E}\left[\hat{\underline{V}}_{ML}^*(i_A)\right]$$

$$= \frac{\alpha L}{\eta(L-K-1)} \underline{R}_A^{*-1} \underline{V}^*$$

$$= \frac{L}{L-K-1} \underline{W}_{OPT} \tag{21}$$

Hence, the ML estimate $\hat{\underline{W}}_{OPT}(i_A)$ of the optimum weight vector $\underline{W}_{OPT}$ is actually a biased estimate. This is not a problem, since it is clear from Eq. (12) that the optimum weight vectors are not unique and any complex scaled version of an optimum weight vector is also optimum. So the constant α in Eq. (18) can be set arbitrarily. We shall set $\alpha = (L - K - 1)/L$ for the purpose of normalization and also assume that $L > K + 1$. The ML estimate of the optimum weight vector that will be used here is, therefore,

$$\hat{\underline{W}}_{ML}(i_A) = \frac{L-K-1}{L\eta} \left(\hat{\underline{R}}_{A,ML}^*(i_A)\right)^{-1} \hat{\underline{V}}_{ML}^*(i_A)$$

$$= \frac{L-K-1}{L\eta \cos \delta} \left(\hat{\underline{R}}_{A,ML}^*(i_A)\right)^{-1} \hat{\underline{X}}_{ML}^*(i_A) \tag{22}$$

with mean

$$\underline{W}_O \triangleq \mathbf{E}\left[\hat{\underline{W}}_{ML}(i_A)\right] = \frac{1}{\eta} \underline{R}_A^{*-1} \underline{V}^* = \underline{R}_B^{*-1} \underline{V}^* \tag{23}$$

that is also an optimum weight vector.

Note that $\hat{\underline{V}}_{ML}(i_A)$ and $\hat{\underline{R}}_{A,ML}(i_A)$ are both consistent estimates, i.e., they both converge with probability one to their respective expected values $\underline{V}$ and $\underline{R}_A$ in the limit as L tends to infinity. So it follows that $\hat{\underline{W}}_{ML}(i_A)$ also converges with probability one to the optimum weight vector $\underline{W}_O$ in the limit as the number L of samples tends to infinity. The analysis in Appendix C shows that this convergence also holds in the mean-square sense. These properties indicate that we may expect the actual combiner output SNR

using the estimated weight vector $\underline{\hat{W}}_{ML}(i_A)$ to also converge to the maximum achievable SNR γ_{MAX} as L tends to infinity. That result will be shown in the next section, which derives an explicit expression for the actual combiner output SNR for finite L.

As in [1], these weight coefficient estimates are used in a sliding-window structure to produce the following combiner output sequence:

$$z_c(i_B) = \underline{\hat{W}}_{ML}^T(\tilde{i}_A)\underline{y}(i_B) \tag{24}$$

where $\tilde{i}_A$ is the largest integer less than i_B, so that the residual carrier-signal vector samples $\{\underline{u}(\tilde{i}_A - 1), \cdots, \underline{u}(\tilde{i}_A - L)\}$ used for estimating $\underline{\hat{W}}_{ML}(\tilde{i}_A)$ occur before the full-spectrum signal vector sample $\underline{y}(i_B) = (y_1(i_B), \cdots, y_K(i_B))^T$. This ensures that the noise vector $\underline{n}(i_B)$ in $\underline{y}(i_B)$ is statistically independent of $\{\underline{u}(\tilde{i}_A - 1), \cdots, \underline{u}(\tilde{i}_A - L)\}$, and hence the statistical independence between $\underline{\hat{W}}_{ML}(\tilde{i}_A)$ and $\underline{n}(i_B)$.

IV. SNR Performance Analysis

The combiner output, Eq. (24), can be written as

$$z_c(i_B) \doteq s_c(i_B) + n_c(i_B) \tag{25}$$

where

$$s_c(i_B) = \underline{\hat{W}}_{ML}^T(\tilde{i}_A)\underline{V}e^{js(i_B)\delta} \tag{26}$$

and

$$n_c(i_B) = \underline{\hat{W}}_{ML}^T(\tilde{i}_A)\underline{n}(i_B) \tag{27}$$

are the signal and noise components, respectively. In the following analysis, $\underline{V}$, $\underline{R}_B$, and $s(i_B)$ are assumed to be nonrandom parameters. As noted above, $\underline{\hat{W}}_{ML}(\tilde{i}_A)$ and $\underline{n}(i_B)$ are statistically independent. Since the components of $\underline{n}(i_B)$ are all of zero mean, it follows from Eqs. (26) and (27) that $n_c(i_B)$ also has zero mean and moreover is uncorrelated with $s_c(i_B)$. Thus, it follows from Eq. (25) that the actual SNR γ_{ML} of the combiner output can be written as

$$\gamma_{ML} = \frac{|\mathbf{E}[z_c(i_B)]|^2}{\mathbf{Var}[z(i_B)]} = \frac{|\mathbf{E}[s_c(i_B)]|^2}{\mathbf{Var}[s_c(i_B)] + \mathbf{Var}[n_c(i_B)]} \tag{28}$$

Now, it follows from Eqs. (26) and (23) that

$$|\mathbf{E}[s_c(i_B)]|^2 = |\mathbf{E}[\underline{\hat{W}}_{ML}^T(\tilde{i}_A)]\underline{V}|^2 = |\underline{W}_O^T\underline{V}|^2 = |\underline{V}^\dagger\underline{R}_B^{-1}\underline{V}|^2 = \hat{\gamma}_{MAX}^2 \tag{29}$$

where γ_{MAX} is the maximum achievable SNR given by Eq. (13). The explicit expression, Eq. (A-9), for $\mathbf{Var}[s_c(i_B)]$ is derived in Appendix A. Moreover, the derivation in Appendix B yields the expression,

Eq. (B-5), for $\text{Var}\,[n_c(i_B)]$. So, by using Eqs. (29), (A-9), and (B-5) in Eq. (28), one arrives at the following expression for the actual combiner output SNR performance:

$$\gamma_{ML} = \frac{\gamma_{MAX}^2}{\gamma_{MAX}(1 + C_1) + C_2} \qquad (30)$$

where

$$C_1 = \frac{LK - K^2 - K + 1}{(L-K)(L-K-2)} + \frac{(L-K-1)(L-1)}{(L-K)(L-K-2)} \left(\frac{1}{L\eta\cos^2\delta}\right) + \frac{1}{L-K-2}\gamma_{MAX}$$

$$C_2 = \frac{K(L-1)(L-K-1)}{L(L-K)(L-K-2)} \frac{1}{\eta\cos^2\delta} \qquad (31)$$

Since both C_1 and C_2 converge to zero as L tends to infinity, it follows from Eq. (30) that the actual combiner output SNR γ_{ML} converges to the maximum possible achievable SNR, γ_{MAX}, as the number of signal samples, L, used in the estimates tends to infinity.

V. Numerical Example

We consider here a numerical example using a $K = 7$ element array feed. In this example, a modulation index, $\delta = 80$ deg, and a primitive sample period of $T_0 = 2.5 \times 10^{-8}$ s are assumed. The full-spectrum modulation signal is assumed to be of bandwidth 2×10^6 Hz, which yields $M_B = 20$. Moreover, the ratio of the full-spectrum bandwidth to the residual-carrier bandwidth is $\eta = M_A/M_B = 200$. A nominal P_T/N_0 of 65 dB-Hz is considered with a corresponding $\gamma = (P_T/N_0)M_B T_0$ (recall that γ, which is given by Eq. (14), is the sum of the array element SNRs). The white Gaussian noise processes in the received signals from different array feed elements are assumed to be correlated. Moreover, the correlation magnitudes are assumed to be inversely proportional to the distances between feed centers (this assumption has not been verified for the array feed system at DSS 13). In the numerical examples below, the following noise covariance matrix is considered:

$$\underline{R}_B =$$

$$\begin{bmatrix}
1 & \rho_{max}e^{-j(\frac{4\pi}{7}+\phi)} & \rho_{max}e^{-j(\frac{10\pi}{7}+\phi)} & \rho_{max}e^{-j(\frac{6\pi}{7}+\phi)} & \rho_{max}e^{-j(\frac{2\pi}{7}+\phi)} & \rho_{max}e^{-j(\frac{12\pi}{7}+\phi)} & \rho_{max}e^{-j(\frac{8\pi}{7}+\phi)} \\
\rho_{max}e^{j(\frac{4\pi}{7}+\phi)} & 1 & \rho_{max}e^{-j(\frac{6\pi}{7}+\phi)} & \frac{\rho_{max}}{\sqrt{3}}e^{-j(\frac{2\pi}{7}+\phi)} & \frac{\rho_{max}}{2}e^{j(\frac{2\pi}{7}-\phi)} & \frac{\rho_{max}}{\sqrt{3}}e^{-j(\frac{8\pi}{7}+\phi)} & \rho_{max}e^{-j(\frac{4\pi}{7}+\phi)} \\
\rho_{max}e^{j(\frac{10\pi}{7}+\phi)} & \rho_{max}e^{j(\frac{6\pi}{7}+\phi)} & 1 & \rho_{max}e^{j(\frac{4\pi}{7}-\phi)} & \frac{\rho_{max}}{\sqrt{3}}e^{j(\frac{8\pi}{7}-\phi)} & \frac{\rho_{max}}{2}e^{-j(\frac{2\pi}{7}+\phi)} & \frac{\rho_{max}}{\sqrt{3}}e^{j(\frac{2\pi}{7}-\phi)} \\
\rho_{max}e^{j(\frac{6\pi}{7}+\phi)} & \frac{\rho_{max}}{\sqrt{3}}e^{j(\frac{2\pi}{7}+\phi)} & \rho_{max}e^{-j(\frac{4\pi}{7}-\phi)} & 1 & \rho_{max}e^{j(\frac{4\pi}{7}-\phi)} & \frac{\rho_{max}}{\sqrt{3}}e^{-j(\frac{6\pi}{7}+\phi)} & \frac{\rho_{max}}{2}e^{-j(\frac{2\pi}{7}+\phi)} \\
\rho_{max}e^{j(\frac{2\pi}{7}+\phi)} & \frac{\rho_{max}}{2}e^{-j(\frac{2\pi}{7}-\phi)} & \frac{\rho_{max}}{\sqrt{3}}e^{-j(\frac{8\pi}{7}-\phi)} & \rho_{max}e^{-j(\frac{4\pi}{7}-\phi)} & 1 & \rho_{max}e^{-j(\frac{10\pi}{7}+\phi)} & \frac{\rho_{max}}{\sqrt{3}}e^{-j(\frac{6\pi}{7}+\phi)} \\
\rho_{max}e^{j(\frac{12\pi}{7}+\phi)} & \frac{\rho_{max}}{\sqrt{3}}e^{j(\frac{8\pi}{7}+\phi)} & \frac{\rho_{max}}{2}e^{j(\frac{2\pi}{7}+\phi)} & \frac{\rho_{max}}{\sqrt{3}}e^{j(\frac{6\pi}{7}+\phi)} & \rho_{max}e^{j(\frac{10\pi}{7}+\phi)} & 1 & \rho_{max}e^{j(\frac{4\pi}{7}-\phi)} \\
\rho_{max}e^{j(\frac{8\pi}{7}+\phi)} & \rho_{max}e^{j(\frac{4\pi}{7}+\phi)} & \frac{\rho_{max}}{\sqrt{3}}e^{-j(\frac{2\pi}{7}-\phi)} & \frac{\rho_{max}}{2}e^{j(\frac{2\pi}{7}+\phi)} & \frac{\rho_{max}}{\sqrt{3}}e^{j(\frac{6\pi}{7}+\phi)} & \rho_{max}e^{-j(\frac{4\pi}{7}-\phi)} & 1
\end{bmatrix}$$

$$(32)$$

Figure 1 shows the $K = 7$ element feed array geometry and the relative distances between feed centers. The main feed is labeled feed 1 and is surrounded by the six others. In the correlation matrix, Eq. (32),
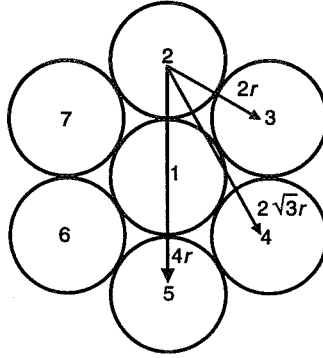
**Fig. 1. Feed array geometry
for K = 7 feeds.**

the noise power in the feed-element stream B received signal samples are all assumed to be equal and normalized to one ($r_{Bkk} = 1$ for all k). The maximum possible noise correlation (and also correlation coefficient) magnitude is denoted by ρ_{max}. The corresponding noise correlation magnitudes in this matrix are identical and reflect an inverse dependence on distances between feed centers. The noise correlation magnitudes between nearest neighbor feed pairs are equal to the maximum correlation magnitude ρ_{max} (for example, between the main feed, feed 1, and any of the outer feeds). As can be seen from Fig. 1, the next nearest neighbor feed pairs (for example, feed 2 and feed 4) are of a distance equal to $\sqrt{3}$ times the distance between nearest neighbor feed pairs, and hence have a noise correlation magnitude equal to $\rho_{max}/\sqrt{3}$. Finally, the furthest feed pairs (for example, feed 2 and feed 5) are of a distance equal to twice the distance between closest feed pairs, and so have a noise correlation magnitude equal to $\rho_{max}/2$. The parameter ϕ in Eq. (32) specifies the noise correlation phases. The rationale for assigning these phases will be described below. Since the noise power in each feed element is equal to one, the sum of the feed element SNRs is equal to the total received power, and so $\gamma = P_T$. For the complex signal parameters vector, $\underline{V}$, we shall use

$$\underline{V} = \left[\sqrt{\gamma\beta} \ \sqrt{\gamma\frac{(1-\beta)}{6}}e^{j\frac{4\pi}{7}} \ \sqrt{\gamma\frac{(1-\beta)}{6}}e^{j\frac{10\pi}{7}} \ \sqrt{\gamma\frac{(1-\beta)}{6}}e^{j\frac{6\pi}{7}} \ \sqrt{\gamma\frac{(1-\beta)}{6}}e^{j\frac{2\pi}{7}} \ \sqrt{\gamma\frac{(1-\beta)}{6}}e^{j\frac{12\pi}{7}} \ \sqrt{\gamma\frac{(1-\beta)}{6}}e^{j\frac{8\pi}{7}}\right]^T$$

(33)

where $0 \leq \beta \leq 1$ represents the fraction of total received signal power in the main antenna feed (feed 1) as defined in [9]. The remaining total received signal power is then evenly distributed among the other six feed elements (this assumption does not appear to be generally valid for severely distorted antenna reflectors). The signal phases in Eq. (33) were chosen arbitrarily. The parameter ϕ in Eq. (32) specifies the relation between the noise correlation phases and the signal parameter phases as follows: Let V_k denote the kth component of the vector $\underline{V}$ given by Eq. (33). Then for $k > j$, $\phi = $ [phase of r_{Bkj}] $-$ [(phase of V_k) $-$ (phase of V_j)]. Moreover, since $\underline{R}_B$ is a Hemitian matrix, $-\phi = $ [phase of r_{Bkj}] $-$ [(phase of V_k) $-$ (phase of V_j)] when $j > k$. That is, ϕ represents the difference between the phase of the noise correlations and the phase differences between the corresponding signal components in $\underline{V}$. The significance of this will be discussed below.

In the numerical examples below, the signal combining scheme given by Eq. (24) will be referred to as the correlated noises algorithm. The signal-combining scheme from [1] will, on the other hand, be referred to as the uncorrelated noises algorithm. A comparison of the SNR performance of these two signal combining schemes will be made below, assuming the noise covariance matrix given by Eq. (32) and the signal parameter vector given by Eq. (33). Our previous work in [5] determined the SNR performance of the uncorrelated noises algorithm in the environment where the noise processes in the feed element received

signals are indeed correlated. For a given signal vector $\underline{V}$ and set of noise correlation magnitudes, the results in [5] show that the best-case performance of the uncorrelated noises algorithm occurs when each of the noise correlations between feed pairs has a phase that is exactly 180 deg from the phase difference between the corresponding signal components in $\underline{V}$. For the correlation matrix, Eq. (32), this "best case" scenario for the uncorrelated noises algorithm occurs when the parameter $\phi = 180$ deg. Moreover, the worst-case performance was shown in [5] to occur when each of the noise correlations between feed pairs has a phase that is exactly equal to the phase difference between the corresponding signal components in $\underline{V}$. This "worst-case" scenario for the uncorrelated noises algorithm occurs when the parameter $\phi = 0$ deg for the correlation matrix, Eq. (32). The numerical examples below will consider these two extreme cases only. The performance comparisons between these two algorithms can then be made under both the most-favorable and the least-favorable situations for the uncorrelated noises algorithm.

The SNR performances will be compared in terms of the combining gain, which is the ratio of the actual SNR performance to the sum of the SNRs of the array feed element received signals (γ_{ML}/γ for the correlated noises algorithm). Note that γ is also the maximum achievable SNR in the uncorrelated noises environment. Hence, the combining gain represents the SNR gain relative to the best possible performance in the uncorrelated noises environment. We shall, therefore, refer to an SNR gain when the combining gain is positive (in dB) and to an SNR loss otherwise. The SNR performance analysis given in Section IV showed that the combining gain γ_{ML}/γ of the correlated noises algorithm converges to the maximum possible combining gain, γ_{MAX}/γ, in the limit as the number of samples, L, approaches infinity. Figure 2 plots this maximum possible combining gain as the phase parameter ϕ in Eq. (32) is varied between 0 and 180 deg for values of ρ_{max} equal to 0.1, 0.15, and 0.2, and when $\beta = 0.7$. These results show that the best- and worst-case scenarios for the correlated noises algorithm are the same as those for the uncorrelated noises algorithm. These results show that
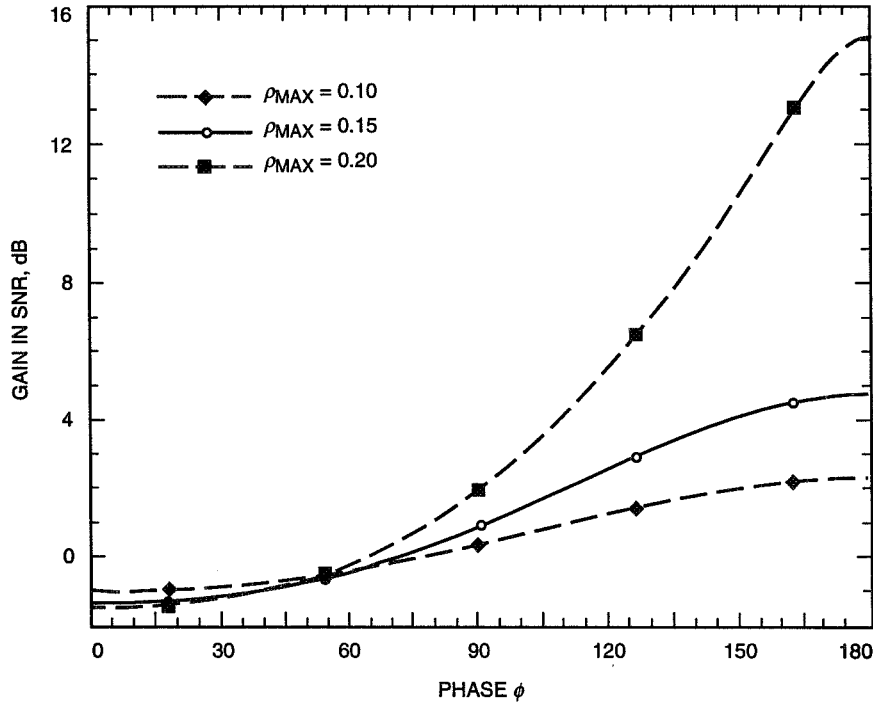

Fig. 2. Maximum possible combining gain versus ϕ with $\beta = 0.7$

the maximum possible combining gain is positive for a majority of the ϕ phase values. Moreover, the maximum possible combining gains increase with increasing ρ_{max}. Simulations were also performed to validate the analytical result, Eq. (30), that yields the combining gain for the correlated noises algorithm. Table 1 compares the simulated combining gain to the analytical result for the best-case $\underline{R}_B$ matrix (with $\phi = 180$ deg) at various values of ρ_{max} and L. Table 2 displays the corresponding comparisons for the worst-case $\underline{R}_B$ (with $\phi = 0$ deg). The simulated combining gain from these two tables can be seen to be within 3 percent of the analytical results. This appears to validate the analysis.

Table 1. Correlated algorithm simulated combining gain for best-case $\underline{R}_B$.

		SNR Gain, dB	
L	ρ_{max}	Simulation	Analytical
500	0.050	0.85896	0.80340
500	0.100	2.24048	2.17891
500	0.150	4.75655	4.67706
500	0.175	7.25759	7.14633
500	0.200	15.06133	14.60054
5000	0.050	0.88286	0.87982
5000	0.100	2.26456	2.25971
5000	0.150	4.78108	4.77260
5000	0.175	7.28267	7.26961
5000	0.200	15.08713	15.03570
10^6	0.050	0.86770	0.88821
10^6	0.100	2.24674	2.26859
10^6	0.150	4.76168	4.78312
10^6	0.175	7.26309	7.28324
10^6	0.200	15.06514	15.08578

In Fig. 3, the combining gains of both algorithms are plotted versus the number of samples, L, for $\beta = 0.7$ (70 percent of the power in the main feed), using the best-case $\underline{R}_B$ and with ρ_{max} having values of 0.05, 0.1, and 0.15. We notice that for a fixed ρ_{max}, the correlated noises algorithm (CNA in the figures) actually has a smaller combining gain than the uncorrelated noises algorithm (UNA in the figures) for small values of L below a threshold value. In the examples considered, this threshold value increases with decreasing ρ_{max} and is always less than about $L = 500$. Note that although the ML estimator is asymptotically optimal as $L \to \infty$, it is not necessarily the best estimator for small values of L. Hence, the correlated noises algorithm may not have the best possible performance at small values of L. The convergence of the combining gain to the optimum theoretically achievable value was proved in the last section. These examples show that convergence to within 0.1 dB of the limiting value occurs at about $L = 1000$ samples. Figure 4 shows the respective combining gains as a function of β, the fraction of total received signal power in the main feed, for $L = 5000$ samples and values of ρ_{max} equal to 0.05, 0.1, 0.15, and 0.2. We can see that the performance of the correlated noises algorithm is much less sensitive to β in this example than that of the uncorrelated noises algorithm. The performance superiority of the correlated noises algorithm also increases significantly with increasing β. The respective combining gains versus ρ_{max} with $L = 5000$ and β taking on values of 0.7, 0.8, and 0.9 are shown in Fig. 5. This figure shows that the performance improvement of the correlated noises algorithm over the uncorrelated noises algorithm increases significantly with increasing ρ_{max}. The results in these three figures indicate that there can be

Table 2. Correlated algorithm simulated combining gain for worst-case $\underline{R}_B$.

		SNR Gain, dB	
L	ρ_{max}	Simulation	Analytical
500	0.050	−0.63659	−0.68802
500	0.100	−1.05467	−1.10542
500	0.150	−1.33373	−1.38419
500	0.175	−1.43041	−1.48083
500	0.200	−1.50179	−1.55220
5000	0.050	−0.61306	−0.61410
5000	0.100	−1.03140	−1.03182
5000	0.150	−1.31079	−1.31072
5000	0.175	−1.40765	−1.40738
5000	0.200	−1.47920	−1.47877
10^6	0.050	−0.62206	−0.60598
10^6	0.100	−1.03724	−1.02373
10^6	0.150	−1.31348	−1.30265
10^6	0.175	−1.40878	−1.39931
10^6	0.200	−1.47881	−1.47070
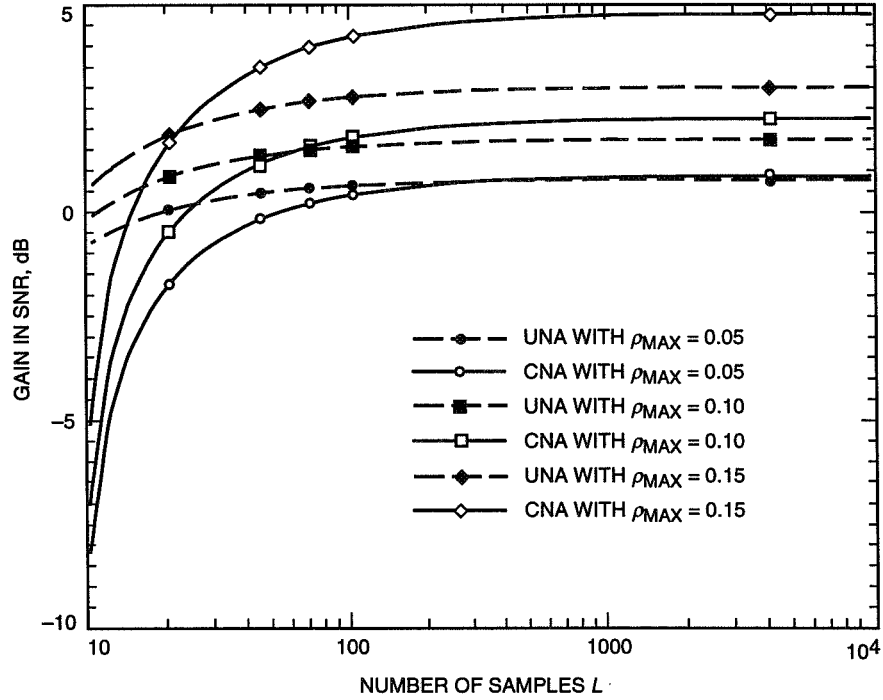
Fig. 3. Combining gain versus L with $\beta = 0.7$ for best-case $\underline{R}_B$.
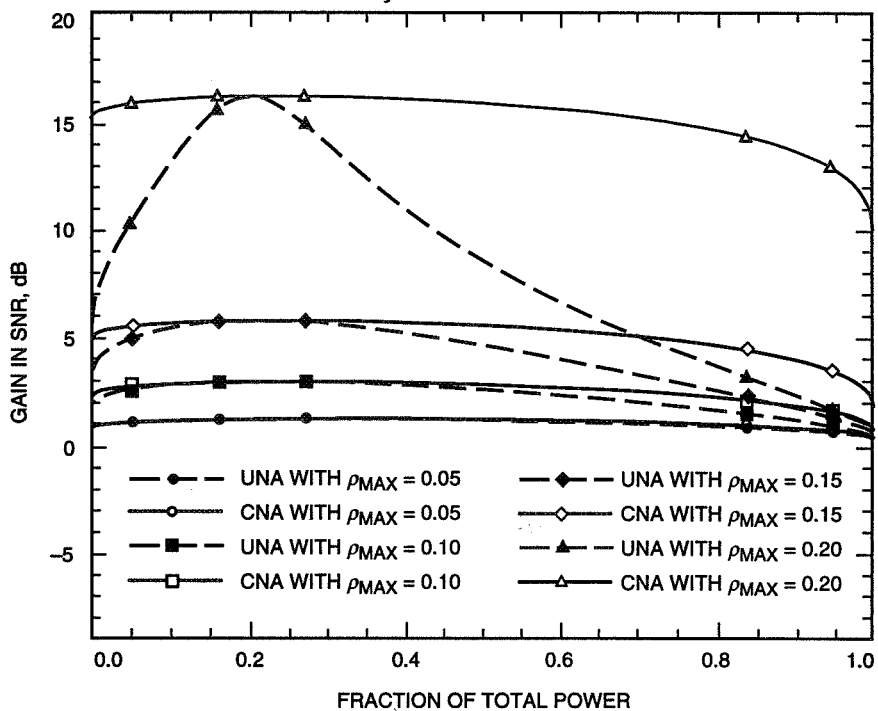
Fig. 4 Combining gain versus β with L = 5000 for best-case R_B.
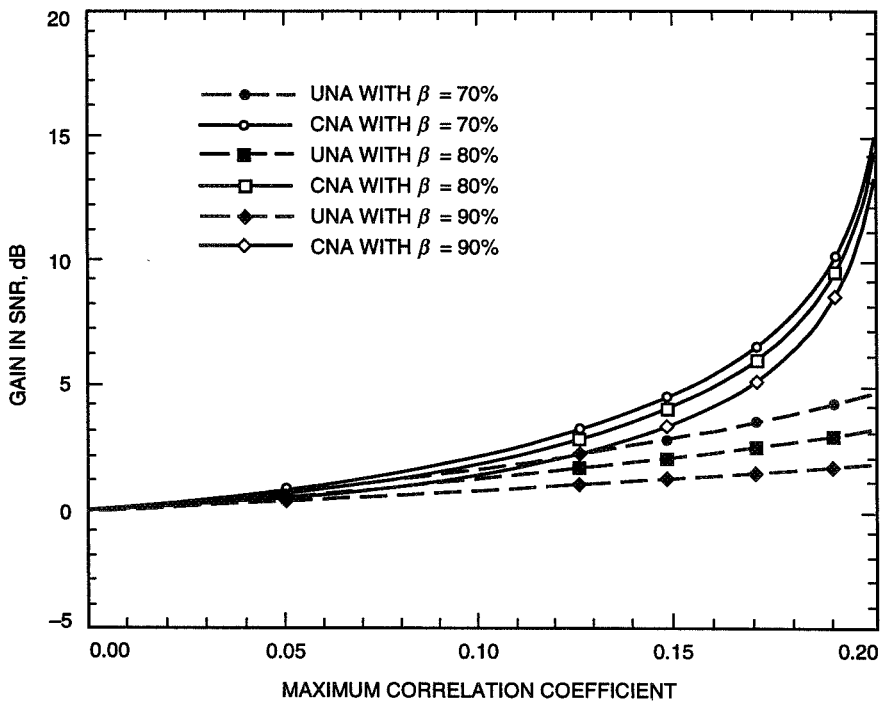
Fig. 5. Combining gain versus ρ_{max} with L = 5000 for best-case R_B.

a substantial SNR gain in this best-case scenario, particularly for the correlated noises algorithm at larger values of ρ_{max}. We also note that the value of ρ_{max} cannot exceed 0.2 in order to preserve the positive definiteness of $\underline{R}_B$.

Figures 6 through 8 repeat Figs. 3 through 5, respectively, using the worst-case scenario $\underline{R}_B$ matrix instead, while keeping the other parameters unchanged. These examples show that this worst-case scenario can result in an SNR loss, and the loss nominally increases with increasing ρ_{max}. Figure 6 again shows that convergence of the combining gain for the correlated noises algorithm to within 0.1 dB of its limiting value occurs at about $L = 1000$ samples. The small sample performance of the correlated algorithm again lags that of the uncorrelated algorithm. Similarly to Fig. 4, Fig. 7 shows that the performance superiority of the correlated noises algorithm increases with increasing β. However, as β approaches one, the SNR loss of the correlated noises algorithm turns around and starts to decrease with increasing ρ_{max}. At large values of β close to one, the correlated noises algorithm can in fact have an SNR gain even when the uncorrelated noises algorithm still has an SNR loss. Finally, Fig. 8 shows that the SNR loss of the correlated noises algorithm in this unfavorable situation deteriorates much slower than that of the uncorrelated noises algorithm as ρ_{max} increases.
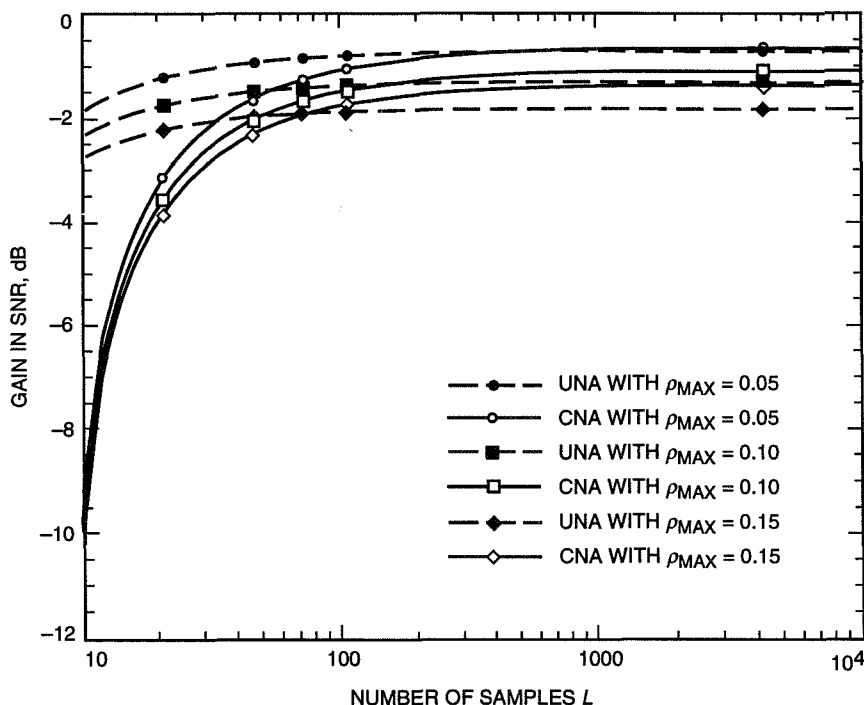

Fig. 6. Combining gain versus L with β = 0.7 for worst-case $\underline{R}_B$.

VI. Conclusion

The correlated noises signal-combining scheme developed in this article has been shown to be asymptotically optimal as the number of residual carrier-signal samples used in the estimates of the optimum weight coefficients increases. The numerical examples considered here show that convergence of the combining algorithm's SNR performance to the optimum achievable SNR performance level to within 0.1 dB occurs at about $L = 1000$ signal samples. Hence, real-time operation is possible, although the inversion of a complex-valued K-dimensional matrix is required at every update of the weight coefficient estimates. The numerical examples considered here consistently demonstrate a significant performance superiority
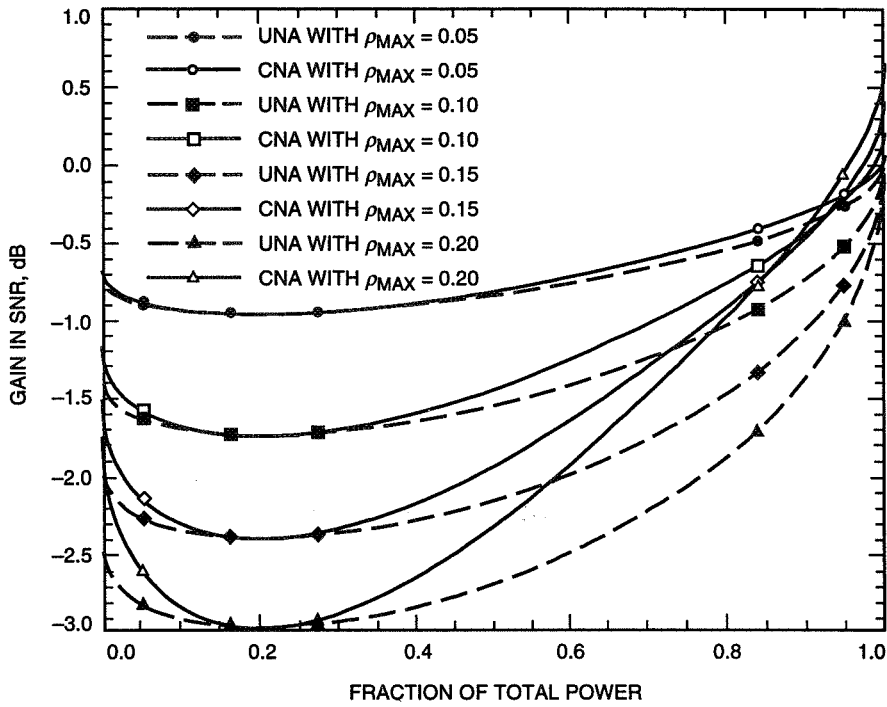
Fig. 7. Combining gain versus β with L = 5000 for worst-case $\underline{R}_B$.
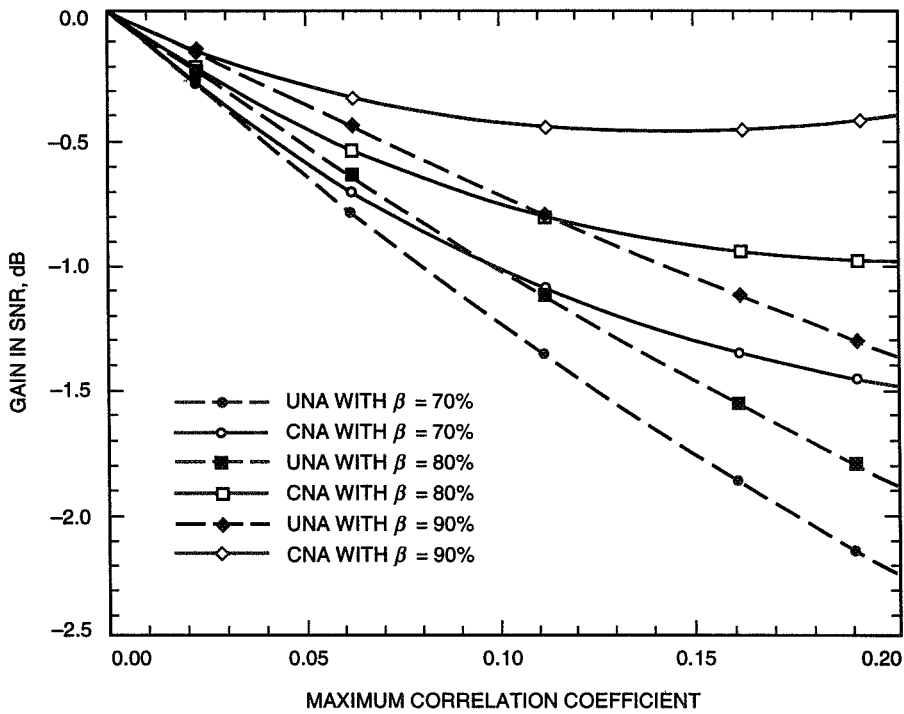

Fig. 8. Combining gain versus ρ_{max} with L = 5000 for worst-case $\underline{R}_B$.

of the correlated noises combining scheme over the uncorrelated noises signal-combining algorithm. It appears to be the combining system of choice in the presence of significant correlations between the noise processes in different array feed received signals. A degree of caution should be exercised in extrapolating the expected amount of SNR gain or loss from the numerical examples considered in Section V. The best-case and worst-case performances in these examples should not be viewed as being typical. Moreover, these two cases also should not be viewed as being best- and worst-case performances in general.

References

[1] V. A. Vilnrotter, E. R. Rodemich, and S. J. Dolinar, Jr., "Real-Time Combining of Residual Carrier Array Signals Using ML Weight Estimates," *IEEE Transactions Communications*, vol. COM-40, no. 3, pp. 604–615, March 1992.

[2] B. A. Iijima, V. A. Vilnrotter, and D. Fort, "Correlator Data Analysis for the Array Feed Compensation System," *The Telecommunications and Data Acquisition Progress Report 42-117, January–March 1994*, Jet Propulsion Laboratory, Pasadena, California, pp. 110–118, May 15, 1994.

[3] S. P. Applebaum, "Adaptive Arrays," *IEEE Transactions on Antennas and Propagation*, vol. AP-24, pp. 585–598, September 1976.

[4] J. H. Yuen, *Deep Space Telecommunications Systems Engineering*, Chapter 5, New York: Plenum, 1983.

[5] H. H. Tan, "Performance of Residual Carrier Array-Feed Combining in Correlated Noise," *The Telecommunications and Data Acquisition Progress Report 42-121, January–March 1995*, Jet Propulsion Laboratory, Pasadena, California, pp. 131–147, May 15, 1995.
http://edms-www.jpl.nasa.gov/tda/progress_report/42-121/121H.pdf

[6] N. R. Goodman, "Statistical Analysis Based on a Certain Multivariate Complex Gaussian Distribution (An Introduction)," *Annals of Mathematical Statistics*, vol. 34, pp. 152–177, 1963.

[7] T. W. Anderson, *An Introduction to Multivariate Statistical Analysis*, 2nd ed., New York: Wiley, 1984.

[8] J. Tague and C. Caldwell, "Expectations of Useful Complex Wishart Forms," *Multidimensional Systems and Signal Processing*, no. 5, pp. 263–279, July 1994.

[9] V. Vilnrotter, "Channel Assignments for Improved Gain in Baseband Array Feed Compensation Systems," *IEEE Transactions Communications*, vol. COM-42, no. 5, pp. 2127–2133, May 1994.

Appendix A

Combiner Output Signal Variance

An explicit expression for $\mathrm{Var}\,[s_c(i_B)]$ is derived in this appendix. For convenience in the following analysis, let us use $\hat{\underline{W}}_{ML}$ as the shortened notation for $\hat{\underline{W}}_{ML}(\tilde{i}_A)$, $\hat{\underline{X}}_{ML}$ for $\hat{\underline{X}}_{ML}(\tilde{i}_A)$, and $\hat{\underline{R}}_{A,ML}$ for $\hat{\underline{R}}_{A,ML}(\tilde{i}_A)$. Using Eqs. (26) and (22), we can write

$$
\mathrm{Var}\,[s_c(i_B)] = \mathrm{Var}\left[\hat{\underline{W}}_{ML}^T \underline{V} e^{js(i_B)\delta}\right]
$$

$$
= \mathbf{E}\left[\left(\hat{\underline{W}}_{ML}^\dagger \underline{V}^*\right)\left(\hat{\underline{W}}_{ML}^T \underline{V}\right)\right] - |\underline{W}_O^T \underline{V}|^2
$$

$$
= \underline{V}^\dagger \mathbf{E}\left[\hat{\underline{W}}_{ML}^* \hat{\underline{W}}_{ML}^T\right]\underline{V} - |\underline{W}_O^T \underline{V}|^2
$$

$$
= \underline{V}^\dagger \mathbf{E}\left[\frac{(L-K-1)^2}{L^2\eta^2\cos^2\delta}\hat{\underline{R}}_{A,ML}^{-1}\hat{\underline{X}}_{ML}\hat{\underline{X}}_{ML}^\dagger\hat{\underline{R}}_{A,ML}^{-1}\right]\underline{V} - |\underline{W}_O^T \underline{V}|^2 \qquad \text{(A-1)}
$$

Since $\hat{\underline{R}}_{A,ML}$ is independent of $\hat{\underline{X}}_{ML}$, we can write

$$
\mathbf{E}\left[\hat{\underline{R}}_{A,ML}^{-1}\hat{\underline{X}}_{ML}\hat{\underline{X}}_{ML}^\dagger\hat{\underline{R}}_{A,ML}^{-1}\right] = \mathbf{E}\left[\mathbf{E}\left[\hat{\underline{R}}_{A,ML}^{-1}\hat{\underline{X}}_{ML}\hat{\underline{X}}_{ML}^\dagger\hat{\underline{R}}_{A,ML}^{-1}\mid\hat{\underline{R}}_{A,ML}\right]\right]
$$

$$
= \mathbf{E}\left[\hat{\underline{R}}_{A,ML}^{-1}\mathbf{E}\left[\hat{\underline{X}}_{ML}\hat{\underline{X}}_{ML}^\dagger\mid\hat{\underline{R}}_{A,ML}\right]\hat{\underline{R}}_{A,ML}^{-1}\right]
$$

$$
= \mathbf{E}\left[\hat{\underline{R}}_{A,ML}^{-1}\mathbf{E}\left[\hat{\underline{X}}_{ML}\hat{\underline{X}}_{ML}^\dagger\right]\hat{\underline{R}}_{A,ML}^{-1}\right] \qquad \text{(A-2)}
$$

Moreover, since $\hat{\underline{X}}_{ML}(i_A)$ is a complex Gaussian random vector with mean $\underline{X}$ and covariance matrix $(1/L)\underline{R}_A$, we have

$$
\mathbf{E}\left[\hat{\underline{X}}_{ML}\hat{\underline{X}}_{ML}^\dagger\right] = \frac{1}{L}\underline{R}_A + \underline{X}\underline{X}^\dagger \qquad \text{(A-3)}
$$

Therefore, it follows from Eqs. (A-1), (A-2), and (A-3) that

$$
\mathrm{Var}[s_c(i_B)] = \frac{(L-K-1)^2}{L^2\eta^2\cos^2\delta}\underline{V}^\dagger\mathbf{E}\left[\hat{\underline{R}}_{A,ML}^{-1}\left(\frac{1}{L}\underline{R}_A + \underline{X}\underline{X}^\dagger\right)\hat{\underline{R}}_{A,ML}^{-1}\right]\underline{V} - |\underline{W}_O^T\underline{V}|^2
$$

$$
= \frac{(L-K-1)^2}{\eta^2\cos^2\delta}\underline{V}^\dagger\mathbf{E}\left[\left(L\hat{\underline{R}}_{A,ML}\right)^{-1}\left(\frac{1}{L}\underline{R}_A + \underline{X}\underline{X}^\dagger\right)\left(L\hat{\underline{R}}_{A,ML}\right)^{-1}\right]\underline{V} - |\underline{W}_O^T\underline{V}|^2 \qquad \text{(A-4)}
$$

Let $\text{Tr}(\underline{A})$ denote the trace of a square matrix $\underline{A}$ and let $\underline{I}_K$ denote the $K \times K$ identity matrix. Recall that $L\hat{\underline{R}}_{A,ML}$ is a $K \times K$ $CW(\underline{R}_A, L-1)$ distributed random matrix. It has been shown in [8] that if $\underline{A}$ is a $K \times K$ $CW(\underline{R}_A, L-1)$ random matrix and $\underline{C}$ is any constant $K \times K$ matrix, then

$$\text{E}\left[\underline{A}^{-1}\underline{C}\,\underline{A}^{-1}\right] = \frac{1}{(L-K)(L-K-2)}\underline{R}_A^{-1}\underline{C}\,\underline{R}_A^{-1} + \frac{1}{(L-K)(L-K-1)(L-K-2)}\text{Tr}\left(\underline{C}\,\underline{R}_A^{-1}\right)\underline{R}_A^{-1}$$

(A-5)

for $L > K$. So, using Eq. (A-5) in Eq. (A-4) gets

$$\begin{aligned}
\text{Var}\left[s_c(i_B)\right] = &\frac{(L-K-1)}{(L-K)(L-K-2)\eta^2\cos^2\delta}\underline{V}^\dagger\left\{[(L-1)-K]\left(\frac{1}{L}\underline{R}_A^{-1} + \underline{R}_A^{-1}\underline{X}\underline{X}^\dagger\underline{R}_A^{-1}\right)\right.\\
&\left.+ \text{Tr}\left(\frac{1}{L}\underline{I}_K + \underline{X}\underline{X}^\dagger\underline{R}_A^{-1}\right)\underline{R}_A^{-1}\right\}\underline{V} - |\underline{W}_O^T\underline{V}|^2\\[2mm]
= &\frac{(L-K-1)^2}{(L-K)(L-K-2)\eta^2\cos^2\delta}\left[\frac{1}{L}\left(\underline{V}^\dagger\underline{R}_A^{-1}\underline{V}\right) + \underline{V}^\dagger\underline{R}_A^{-1}\underline{X}\underline{X}^\dagger\underline{R}_A^{-1}\underline{V}\right]\\[2mm]
&+ \frac{(L-K-1)}{(L-K)(L-K-2)\eta^2\cos^2\delta}\underline{V}^\dagger\text{Tr}\left(\frac{1}{L}\underline{I}_K + \underline{X}\underline{X}^\dagger\underline{R}_A^{-1}\right)\underline{R}_A^{-1}\underline{V} - |\underline{W}_O^T\underline{V}|^2 \quad \text{(A-6)}
\end{aligned}$$

Since $\underline{X} = \underline{V}\cos\delta$, and $\underline{R}_B = \eta\underline{R}_A$, it follows from Eq. (29) that

$$\frac{1}{\eta^2\cos^2\delta}\left(\underline{V}^\dagger\underline{R}_A^{-1}\underline{X}\underline{X}^\dagger\underline{R}_A^{-1}\underline{V}\right) = |\underline{V}^\dagger\underline{R}_B^{-1}\underline{V}|^2 = |\underline{W}_O^T\underline{V}|^2 = \gamma_{MAX}^2 \quad \text{(A-7)}$$

Since $\underline{R}_A^{-1}$ is Hermitian, $\text{Tr}(\underline{X}\underline{X}^\dagger\underline{R}_A^{-1}) = \underline{X}^\dagger\underline{R}_A^{-1}\underline{X}$. So we have, by using Eq. (A-7),

$$\begin{aligned}
\frac{1}{\eta^2\cos^2\delta}\underline{V}^\dagger\text{Tr}\left(\frac{1}{L}\underline{I}_K + \underline{X}\underline{X}^\dagger\underline{R}_A^{-1}\right)\underline{R}_A^{-1}\underline{V} &= \frac{1}{\eta^2\cos^2\delta}\left[\frac{K}{L} + \underline{X}^\dagger\underline{R}_A^{-1}\underline{X}\right]\underline{V}^\dagger\underline{R}_A^{-1}\underline{V}\\[2mm]
&= \frac{K}{L\eta^2\cos^2\delta}\left(\underline{V}^\dagger\underline{R}_A^{-1}\underline{V}\right) + \underline{V}^\dagger\underline{R}_B^{-1}\underline{V}\underline{V}^\dagger\underline{R}_B^{-1}\underline{V}\\[2mm]
&= \frac{K}{L\eta\cos^2\delta}\gamma_{MAX} + \gamma_{MAX}^2 \quad \text{(A-8)}
\end{aligned}$$

Finally, using Eqs. (A-7) and (A-8) in Eq. (A-6) yields the following expression for $\text{Var}[s_c(i_B)]$:

$$\text{Var}\left[s_c(i_B)\right] = \frac{(L-K-1)(L-1)}{(L-K)(L-K-2)}\left(\frac{\gamma_{MAX}}{L\eta\cos^2\delta}\right) + \frac{1}{L-K-2}\gamma_{MAX}^2 \quad \text{(A-9)}$$

Note that $\text{Var}[s_c(i_B)]$ approaches zero in the limit as L tends to infinity. This is because the estimate $\hat{\underline{W}}_{ML}(i_A)$ converges with probability one to the optimum weight vector $\underline{W}_O$ given by Eq. (23) as L tends to infinity.

Appendix B

Combiner Output Noise Variance

Consider next an explicit expression for $\mathbf{Var}[n_c(i_B)]$. We shall also employ here the shortened notations $\hat{\underline{W}}_{ML}$, $\hat{\underline{X}}_{ML}$, $\hat{\underline{R}}_{A,ML}$, as in Appendix A. Moreover, we shall use the shortened notation $\underline{n}$ for $\underline{n}(i_B)$. Since $\hat{\underline{W}}_{ML}$ is independent of $\underline{n}$, a derivation similar to that establishing Eq. (A-2) can be used along with Eq. (22) to get

$$\mathbf{Var}\left[n_c(i_B)\right] = \mathbf{E}\left[\hat{\underline{W}}_{ML}^T \underline{n}\,\underline{n}^\dagger \hat{\underline{W}}_{ML}^*\right]$$

$$= \mathbf{E}\left[\hat{\underline{W}}_{ML}^T \underline{R}_B \hat{\underline{W}}_{ML}^*\right]$$

$$= \frac{(L-K-1)^2}{L^2}\frac{1}{\eta\cos^2\delta}\mathbf{E}\left[\hat{\underline{X}}_{ML}^\dagger \hat{\underline{R}}_{A,ML}^{-1} \underline{R}_A \hat{\underline{R}}_{A,ML}^{-1} \hat{\underline{X}}_{ML}\right] \tag{B-1}$$

Since $\hat{\underline{R}}_{A,ML}$ is independent of $\hat{\underline{X}}_{ML}$, using the same approach on the expected value in Eq. (B-1) gets

$$\mathbf{Var}\left[n_c(i_B)\right] = \frac{(L-K-1)^2}{\eta\cos^2\delta}\mathbf{E}\left[\hat{\underline{X}}_{ML}^\dagger \mathbf{E}\left[\left(L\hat{\underline{R}}_{A,ML}\right)^{-1} \underline{R}_A \left(L\hat{\underline{R}}_{A,ML}\right)^{-1}\right] \hat{\underline{X}}_{ML}\right] \tag{B-2}$$

Next, using the property of Eq. (A-5) for the $K \times K$ $CW(\underline{R}_A, L-1)$ distributed random matrix $L\hat{\underline{R}}_{A,ML}$ in Eq. (B-2) results in the following expression:

$$\mathbf{Var}\left[n_c(i_B)\right] = \frac{(L-K-1)}{\eta\cos^2\delta}\mathbf{E}\left[\hat{\underline{X}}_{ML}^\dagger \frac{[(L-1)-K]\underline{R}_A^{-1} + K\underline{R}_A^{-1}}{(L-K)(L-K-2)} \hat{\underline{X}}_{ML}\right]$$

$$= \frac{(L-K-1)(L-1)}{\eta\cos^2\delta(L-K)(L-K-2)}\mathbf{E}\left[\hat{\underline{X}}_{ML}^\dagger \underline{R}_A^{-1} \hat{\underline{X}}_{ML}\right] \tag{B-3}$$

It follows from Eq. (A-3) that

$$\mathbf{E}\left[\hat{\underline{X}}_{ML}^\dagger \underline{R}_A^{-1} \hat{\underline{X}}_{ML}\right] = \mathbf{E}\left[\mathbf{Tr}\left(\underline{R}_A^{-1} \hat{\underline{X}}_{ML}\hat{\underline{X}}_{ML}^\dagger\right)\right]$$

$$= \mathbf{Tr}\left(\underline{R}_A^{-1}\mathbf{E}\left[\hat{\underline{X}}_{ML}\hat{\underline{X}}_{ML}^\dagger\right]\right)$$

$$= \mathbf{Tr}\left(\underline{R}_A^{-1}\left[\frac{1}{L}\underline{R}_A + \underline{X}\underline{X}^\dagger\right]\right)$$

$$= \frac{K}{L} + \underline{X}^\dagger \underline{R}_A^{-1} \underline{X} \tag{B-4}$$

Finally, using Eq. (B-4) in Eqs. (B-3) and (13) yields

$$\mathbf{Var}\,[n_c(i_B)] = \left[1 + \frac{LK - K^2 - K + 1}{(L-K)(L-K-2)}\right]\gamma_{MAX} + \frac{(L-1)(L-K-1)}{(L-K)(L-K-2)\eta\cos^2\delta}\frac{K}{L} \qquad \text{(B-5)}$$

Appendix C
Mean-Square Convergence of Estimated Weights

We employ the shortened notations $\underline{\hat{W}}_{ML}$, $\underline{\hat{X}}_{ML}$, and $\underline{\hat{R}}_{A,ML}$, similar to the usage in the previous appendices. Since

$$\|\,\underline{\hat{W}}_{ML} - \underline{W}_O\,\|^2 = \mathbf{Tr}\left[\left(\underline{\hat{W}}_{ML} - \underline{W}_O\right)\left(\underline{\hat{W}}_{ML} - \underline{W}_O\right)^\dagger\right]$$

and

$$\mathbf{E}\left[\left(\underline{\hat{W}}_{ML} - \underline{W}_O\right)\left(\underline{\hat{W}}_{ML} - \underline{W}_O\right)^\dagger\right] = \mathbf{E}\left[\underline{\hat{W}}_{ML}\underline{\hat{W}}^\dagger_{ML}\right] - \underline{W}_O\underline{W}^\dagger_O$$

we need only establish that $\mathbf{E}[\underline{\hat{W}}_{ML}\underline{\hat{W}}^\dagger_{ML}] \longrightarrow \underline{W}_O\underline{W}^\dagger_O$ as $L \longrightarrow \infty$ to prove the mean-square convergence of $\underline{\hat{W}}_{ML}$ to $\underline{W}_O$. Using Eqs. (17) and (18), we can write

$$\mathbf{E}\left[\underline{\hat{W}}_{ML}\underline{\hat{W}}^\dagger_{ML}\right] = \frac{(L-1-K)^2}{L^2\eta^2\cos^2\delta}\mathbf{E}\left[\left(\underline{\hat{R}}^*_{A,ML}\right)^{-1}\underline{\hat{X}}^*_{ML}\underline{\hat{X}}^T_{ML}\left(\underline{\hat{R}}^*_{A,ML}\right)^{-1}\right] \qquad \text{(C-1)}$$

It then follows from using Eqs. (A-2) and (A-3) in Eq. (C-1) that

$$\mathbf{E}\left[\underline{\hat{W}}_{ML}\underline{\hat{W}}^\dagger_{ML}\right] = \frac{(L-1-K)^2}{\eta^2\cos^2\delta}\mathbf{E}\left[\left(L\underline{\hat{R}}^*_{A,ML}\right)^{-1}\left(\frac{1}{L}\underline{R}^*_A + \underline{X}^*\underline{X}^T\right)\left(L\underline{\hat{R}}^*_{A,ML}\right)^{-1}\right] \qquad \text{(C-2)}$$

So, by using the property of Eq. (A-5) for the $CW(\underline{R}_A, L-1)$ distributed random matrix $L\underline{\hat{R}}_{A,ML}$ in Eq. (C-2), we can write

$$\mathbf{E}\left[\underline{\hat{W}}_{ML}\underline{\hat{W}}^\dagger_{ML}\right] =$$

$$\frac{L-1-K}{\eta^2\cos^2\delta}\left\{\frac{(L-1-K)\left[\frac{1}{L}(\underline{R}^*_A)^{-1} + (\underline{R}^*_A)^{-1}\underline{X}^*\underline{X}^T(\underline{R}^*_A)^{-1}\right] + \left[\frac{K}{L} + \underline{X}^T(\underline{R}^*_A)^{-1}\underline{X}^*\right](\underline{R}^*_A)^{-1}}{(L-K)(L-K-2)}\right\}$$

Therefore, $\mathbf{E}[\underline{\hat{W}}_{ML}\underline{\hat{W}}^\dagger_{ML}] \longrightarrow (\underline{R}^*_A)^{-1}\underline{X}^*\underline{X}^T(\underline{R}^*_A)^{-1}/\eta^2\cos^2\delta = \underline{W}_O\underline{W}^\dagger_O$ as $L \longrightarrow \infty$, thereby establishing the mean-square convergence of $\underline{\hat{W}}_{ML}$ to $\underline{W}_O$.

Channel Capacity of an Array System for Gaussian Channels With Applications to Combining and Noise Cancellation

K.-M. Cheung and V. Vilnrotter
Communications Systems and Research Section

A closed-form expression for the capacity of an array of correlated Gaussian channels is derived. It is shown that when signal and noise are independent, the array of observables can be replaced with a single observable without diminishing the capacity of the array channel. Examples are provided to illustrate the dependence of channel capacity on noise correlation for two- and three-channel arrays.

I. Introduction

In this article, we formulate the framework to evaluate the channel capacity of an array system. We define the channel capacity of an array channel as the maximum of the mutual information between a single input source and an array of n output observables over all distributions on the input that satisfy certain constraints (e.g., power, bandwidth, discrete or continuous, etc.). We derive a closed-form general formula to the channel capacity of an array of n Gaussian channels. This formula applies to correlated and uncorrelated noise, as long as the Gaussian assumption holds and the second-order statistics (covariance) of the signal and noise sources can be characterized. This formula allows one to find the channel capacity of various array constellations and orientations in the presence of correlated and uncorrelated noise. Some of the interesting results that we observed are as follows:

(1) When the noise sources are uncorrelated, the array channel capacity is equivalent to the channel capacity of a single Gaussian channel with a signal-to-noise ratio (SNR) equal to the sum of the SNRs of the individual channels.

(2) The array channel capacity is lower bounded by the channel capacity of the channel with the highest SNR.

II. Problem Formulation

We consider transmitting a single complex source through n channels, as illustrated in Fig. 1. Let $\sigma_{X,ij} \triangleq EX_iX_j^*, \sigma_{Z,ij} \triangleq EZ_iZ_j^*$, and $\sigma_{Y,ij} \triangleq EY_iY_j^*$ for $1 \leq i,j \leq n$. Notice that $\sigma_{X,1}^2, \sigma_{X,2}^2, \cdots, \sigma_{X,n}^2$ are the signal powers as seen by the receivers; $\sigma_{Z,1}^2, \sigma_{Z,2}^2, \cdots, \sigma_{Z,n}^2$ are the noise variances; and $\sigma_{Y,1}^2, \sigma_{Y,2}^2, \cdots, \sigma_{Y,n}^2$ are the channel output variances. The array channel capacity is given by
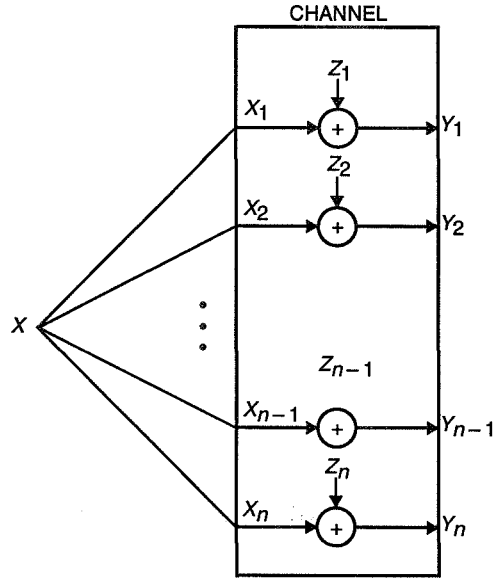
Fig. 1. Array channel model.

$$C_{array} \triangleq \max_{p(x)} I(Y_1, Y_2, \cdots, Y_n; X)$$

$$= \max_{p(x)} \{H(Y_1, Y_2, \cdots, Y_n) - H(Y_1, Y_2, \cdots, Y_n | X)\}$$

$$= \max_{p(x)} \{H(Y_1, Y_2, \cdots, Y_n) - H(Z_1, Z_2, \cdots, Z_n)\} \tag{1}$$

where we further assume a power constraint on X, and where the X_i are obtained from X by a deterministic operation on each i. The interpretation of this model is that signals in the various channels can have different magnitudes and phases, but that the differential delays between the waveforms are negligible, having been removed by delay compensation. Thus, the signal path differences between the various channels either are negligibly small, as in the case of array-feed or phased-array applications, or have been properly equalized, as in the case of antenna arrays.

III. Capacity of an Array of Gaussian Channels

In the following derivation, we will use some results from Cover and Thomas [1]. Since $\underline{Z}^T = (Z_1, Z_2, \cdots, Z_n)$ is a complex Gaussian random vector, $H(\underline{Z})$ is given by [1, Theorem 9.4.1]

$$H(\underline{Z}) = \frac{1}{2} \log_2(2\pi e)^n |\Theta_Z| \quad \text{bits/channel use} \tag{2}$$

where Θ_Z is the covariance matrix of $\underline{Z}$, and $|\Theta_Z|$ is its determinant. From Theorem 9.6.5 of [1] and under the assumption that the input source is power constrained to P, the input source X that maximizes $H(Y_1, Y_2, \cdots, Y_n)$ has a Gaussian distribution. The maximum mutual information and, therefore, the array channel capacity are achieved with a Gaussian source, and the output observables $Y_1, Y_2, \cdots, Y_n$ are correlated complex Gaussian variables. Using Theorem 9.4.1 of [1], $H(Y_1, Y_2, \cdots, Y_n)$ is given by

$$H(Y_1, Y_2, \cdots, Y_n) = \frac{1}{2} \log_2 (2\pi e)^n |\Theta_Y| \quad \text{bits/channel use} \tag{3}$$

where Θ_Y is the covariance matrix of $Y_1, Y_2, \cdots, Y_n$. The array channel capacity is

$$C_{array} = \frac{1}{2} \log_2 \frac{|\Theta_Y|}{|\Theta_Z|} \quad \text{bits/channel use} \tag{4}$$

This formula can also be found in [1, Eq. (10.98)]. Notice that this formula makes no assumption on the pairwise correlation between the signal X_i and the noise Z_j.

Next, we consider the problem from the viewpoint of communications theory and assume that the additive complex Gaussian noise $\underline{Z}$ is independent of the signal X. For the Gaussian channel, we let $\Theta_X = \underline{S} \, \underline{S}^\dagger$, where $S^T = (S_1, S_2, \cdots, S_n)$ is a deterministic vector with $\sum_{i=1}^{n} |S_i|^2 = P$, and $\dagger$ is defined as the conjugate transpose of a vector (that is, $S^\dagger = S^{*T}$). Now the covariance matrix of the observables can be expressed as

$$\Theta_Y = \Theta_X + \Theta_Z = \underline{S} \, \underline{S}^\dagger + \Theta_Z \tag{5}$$

since, in this case, $ES_i Z_j^* = 0$ for $1 \leq i, j \leq n$. With the above notation, Eq. (4) can be evaluated as

$$C_{array} = \frac{1}{2} \log_2 \frac{|\underline{S} \, \underline{S}^\dagger + \Theta_Z|}{|\Theta_Z|} \quad \text{bits/channel use} \tag{6}$$

emphasizing the independent signal and noise components of the observable covariance matrix. Using a corollary to Theorem A.3.2 in [3], the ratio of determinants in Eq. (6) can be written as a quadratic form of the inverse noise covariance matrix and the signal vector as

$$\frac{|\underline{S} \, \underline{S}^\dagger + \Theta_Z|}{|\Theta_Z|} = 1 + \underline{S}^\dagger \Theta_Z^{-1} \underline{S} \tag{7}$$

and, hence, the array capacity may be equivalently expressed as

$$C_{array} = \frac{1}{2} \log_2 (1 + \underline{S}^\dagger \Theta_Z^{-1} \underline{S}) \quad \text{bits/channel use} \tag{8}$$

While Eqs. (6) and (8) are mathematically equivalent, Eq. (8) is particularly important for the following reasons: First, it provides useful insights into the behavior of array capacity and, second, it suggests a simple receiver structure for processing the array observables.

IV. Receiver Structure for an Array of Gaussian Channels

Let $\underline{w}^T = (w_1, w_2, \cdots, w_n)$ be a complex weight vector. It follows that the SNR of the scalar output $v = \underline{w}^T \underline{Y}$ ($\underline{Y}^T = (Y_1, Y_2, \cdots, Y_n)$) is given by

$$SNR = \frac{|\underline{w}^T \underline{S}|^2}{E(|\underline{w}^T \underline{Z}|^2)}$$

$$= \frac{\underline{w}^T \underline{S} \; \underline{S}^\dagger \underline{w}^*}{\underline{w} \Theta_Z \underline{w}^*} \tag{9}$$

This expression holds for any weight vector. As shown in the Appendix, the weight vector $\underline{w}$ that maximizes the SNR is given by

$$\underline{w}_{opt} = a(\Theta_Z^{-1} \underline{S})^* \tag{10}$$

where a is an arbitrary complex constant. Substituting Eq. (10) into Eq. (9) yields the optimal SNR

$$SNR_{max} = \underline{S}^\dagger \Theta_Z^{-1} \underline{S} \tag{11}$$

which is seen to be the same as the quadratic form in Eq. (8). Thus, the quadratic form in Eq. (8) is equivalent to the maximum of the SNR obtained from an optimally weighted sum of the array observables. The array receiver structure implied by this observation is shown in Fig. 2.
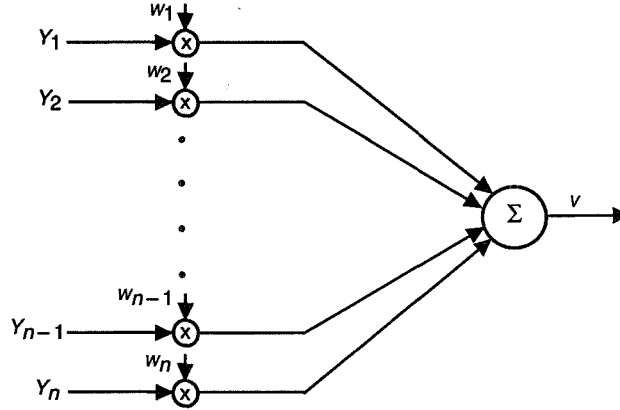
Fig. 2. Receiver structure derived from Eq. (8).

It is well known that a Gaussian source achieves capacity for a Gaussian channel [1]. Since the output of the receiver in Fig. 2 is a weighted sum of the X_i plus Gaussian noise, it is a Gaussian random variable for any value of the source X: hence, the output is a Gaussian channel. Since the array capacity in Eq. (8) depends only on the maximum SNR of the output variable v, it follows that the capacity of the scalar channel of Fig. 2 equals the capacity of the array channel of Fig. 1. This is an important observation since it enables the conversion of an n-dimensional vector observable to a single-dimensional scalar observable without decreasing the capacity of the channel.

Writing Eq. (8) in terms of Eq. (11) emphasizes the point that the channel capacity of the array depends only on the maximum SNR that can be achieved by a weighted sum of the array observables:

$$C_{array} = \frac{1}{2} \log_2(1 + SNR_{max}) \tag{12}$$

It follows that the maximum of the mutual information between v and X can also be stated directly as

$$\max_{p(x)} \{H(v) - H(v|X)\} = C_v = C_{array} \qquad (13)$$

which is simply the capacity C_v of the scalar channel.

When the components of the noise vector $\underline{Z}$ are uncorrelated, both the covariance matrix Θ_Z and its inverse Θ_Z^{-1} become diagonal matrices, with the diagonal element of the inverse matrix equal to the inverse of the corresponding diagonal element of the covariance matrix. With the ith diagonal element of Θ_Z equal to $\sigma_{Z,i}^{-2}$, the maximized SNR becomes

$$SNR_{max} = \underline{S}^\dagger \Theta_Z^{-1} \underline{S} = \sum_{i=1}^{n} \frac{|S_i|^2}{\sigma_{Z,i}^2} \qquad (14)$$

where the right-hand side of Eq. (14) is recognized as the sum of the individual channel SNRs. The array capacity follows directly as

$$C_{array} = \frac{1}{2} \log_2 \left(1 + \sum_{i=1}^{n} \frac{|S_i|^2}{\sigma_{Z,i}^2} \right) \quad \text{bits/channel use} \qquad (15)$$

Thus, the capacity of an array of Gaussian channels with uncorrelated noise is equivalent to that of a single Gaussian channel, with an SNR equal to the sum of the individual channel SNRs.

For the correlated noise case, the observation of the noise in any channel provides useful information about the noise in every other channel. This concept is called "noise cancellation" in the adaptive signal-processing literature.

V. Examples

Some examples of simple array channels that allow closed-form analytic solutions and provide insights into the problem are considered.

A. Two-Channel Array

Consider a two-channel array with signal vector $\underline{S} = (S_1, S_2)$ and noise covariance matrix

$$\Theta_Z = \begin{bmatrix} \sigma_{Z,1}^2 & \rho \sigma_{Z,1} \sigma_{Z,2} \\ \rho^* \sigma_{Z,1} \sigma_{Z,2} & \sigma_{Z,2}^2 \end{bmatrix} \qquad (16)$$

where $EZ_1 Z_2^* = \rho \sigma_{Z,1} \sigma_{Z,2}, E|Z_1|^2 = \sigma_{Z,1}^2$, and $E|Z_2|^2 = \sigma_{Z,2}^2$. The determinant of the noise covariance matrix is $|\Theta_Z| = \sigma_{Z,1}^2 \sigma_{Z,2}^2 (1 - |\rho|^2)$; its inverse is given by

$$\Theta_Z^{-1} = \frac{1}{1 - |\rho|^2} \begin{bmatrix} \dfrac{1}{\sigma_{Z,1}^2} & \dfrac{-\rho}{\sigma_{Z,1} \sigma_{Z,2}} \\ \dfrac{-\rho^*}{\sigma_{Z,1} \sigma_{Z,2}} & \dfrac{1}{\sigma_{Z,2}^2} \end{bmatrix} \qquad (17)$$

and the resulting array channel capacity is

$$C_{array} = \frac{1}{2} \log_2 \left(1 + \frac{1}{1 - |\rho|^2} \left(\frac{|S_1|^2}{\sigma_{Z,1}^2} + \frac{|S_2|^2}{\sigma_{Z,2}^2} - \frac{2Re(\rho S_1^* S_2)}{\sigma_{Z,1} \sigma_{Z,2}} \right) \right) \tag{18}$$

As the magnitude of the correlation coefficient approaches 1, the array capacity grows without bound except for the special case when $|S_1|/\sigma_{Z,1} = |S_2|/\sigma_{Z,2}$ and the phase of ρ cancels the phase of $S_1^* S_2$. This corresponds to the singular detection case in communications theory where the signal is recovered without error in the absence of noise. If the noise is uncorrelated ($\rho = 0$), the array capacity depends only on the sum of the channel SNRs, as noted above. If the noise is correlated but the signal is 0 in one of the channels (for example, $|S_2| = 0$), the array capacity reduces to

$$C_{array} = \frac{1}{2} \log_2 \left(1 + \frac{|S_1|^2}{\sigma_{Z,1}^2 (1 - |\rho|^2)} \right), \quad |S_2| = 0 \tag{19}$$

This "noise-cancellation" result is independent of the phase of the correlation coefficient, implying that the complex noise samples in the two channels need not be phase aligned for perfect cancellation—in effect, the optimum weights defined in Eq. (10) ensure that the noise phases are properly aligned. The array capacity for the two-channel noise-cancellation case corresponding to Eq. (19) is shown in Fig. 3 for several SNRs.
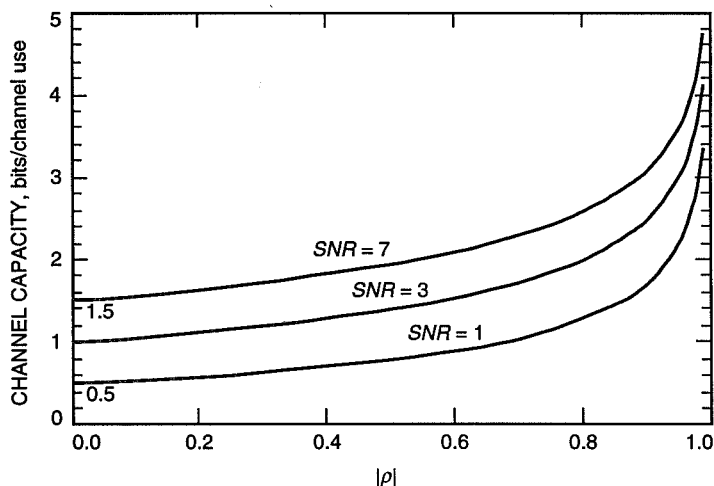
Fig. 3. Array channel for the two-channel case, $|S_2| = 0$.

B. Three-Channel Examples

Next, we consider some three-channel examples, but only for the case of real signals and noise (in other words, here we ignore phase effects). We consider the triangular and the linear constellations as shown in Fig. 4, each having an array of three elements. We assume that the correlation coefficient of Z_i and Z_j, which is denoted by ρ_{ij}, is geometrically related to the distance d_{ij} of array elements i and j as follows:

$$\rho_{ij} = \rho^{|d_{ij}|} \tag{20}$$

where $\max\{-1, a\} \le \rho \le \min\{1, b\}$, and a and b define the range $[a, b] \subseteq [-1, 1]$ such that the covariance matrix Θ_Z is legal, that is, Θ_Z is non-negative definite and $|\Theta_Z| \ge 0$. Also,
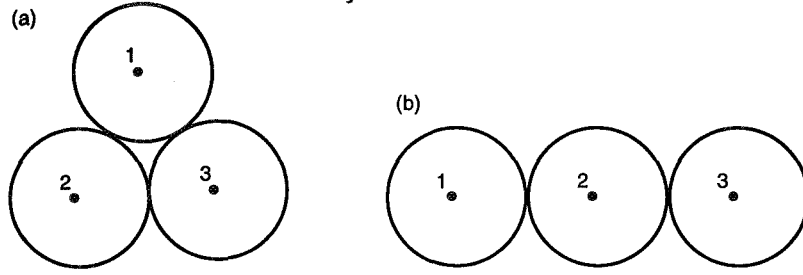
Fig. 4. Array configurations of three elements: (a) triangular configuration and (b) linear configuration.

$$EZ_iZ_j = \rho_{ij}\sigma_{Z,i}\sigma_{Z,j} \tag{21}$$

The covariance matrices Θ_Z^1 and Θ_Z^2 of the triangular and linear constellations, therefore, are given by

$$\Theta_Z^1 = \begin{bmatrix} \sigma_{Z,1}^2 & \rho\sigma_{Z,1}\sigma_{Z,2} & \rho\sigma_{Z,1}\sigma_{Z,3} \\ \rho\sigma_{Z,1}\sigma_{Z,2} & \sigma_{Z,2}^2 & \rho\sigma_{Z,2}\sigma_{Z,2} \\ \rho\sigma_{Z,1}\sigma_{Z,3} & \rho\sigma_{Z,2}\sigma_{Z,3} & \sigma_{Z,3}^2 \end{bmatrix} \tag{22}$$

and

$$\Theta_Z^2 = \begin{bmatrix} \sigma_{Z,1}^2 & \rho\sigma_{Z,1}\sigma_{Z,2} & \rho^2\sigma_{Z,1}\sigma_{Z,3} \\ \rho\sigma_{Z,1}\sigma_{Z,2} & \sigma_{Z,2}^2 & \rho\sigma_{Z,2}\sigma_{Z,2} \\ \rho^2\sigma_{Z,1}\sigma_{Z,3} & \rho\sigma_{Z,2}\sigma_{Z,3} & \sigma_{Z,3}^2 \end{bmatrix} \tag{23}$$

By substituting Θ_Z^1 and Θ_Z^2 into Eq. (8), we can evaluate the array channel capacities of the above array constellations as a function of ρ. We consider two cases: channels having different SNRs and channels having the same SNR.

1. Channels Having Different SNRs. Let $\sigma_{X,1}^2 = 1, \sigma_{X,2}^2 = 1$, and $\sigma_{X,3}^2 = 9$; let $\sigma_{Z,1}^2 = 0.16, \sigma_{Z,2}^2 = 0.49$, and $\sigma_{Z,3}^2 = 1.44$. The array channel capacities of the two constellations as a function of ρ are given in Fig. 5. We observe that the array channel capacities approach infinity when ρ approaches -0.5 and 1.0 for the triangular constellation (when $|\Theta_Z^1| = 0$) and when ρ approaches -1.0 and 1.0 for the linear constellation (when $|\Theta_Z^2| = 0$). The channel capacities of both constellations are the same (3.2 bits/channel use) at $\rho = 0$, and they are lower bounded at 2.75 bits/channel use for this example. Thus, the maximum degradation due to noise correlation is only 0.45 bits/channel use.

2. Channels Having the Same SNR. Let $\sigma_{X,1}^2 = 1.0, \sigma_{X,2}^2 = 1.0$, and $\sigma_{X,3}^2 = 0.25$; let $\sigma_{Z,1}^2 = 0.16, \sigma_{Z,2}^2 = 0.16$, and $\sigma_{Z,3}^2 = 0.04$. The array channel capacities of the two constellations as a function of ρ are given in Fig. 6. Again we observe that the array channel capacities approach infinity when ρ approaches -0.5 for the triangular constellation and when ρ approaches -1.0 for the linear constellation. However, both channel capacities approach 1.43 bits/channel use for the real signal and noise case, the channel capacity of a single channel, when ρ approaches 1.0. This is apparent from the fact that the receiver actually sees three scaled copies of the received signal plus noise, and this is equivalent to looking at one channel alone.

The observations described in the two examples conform to our intuition, and the general formula given in Eq. (8) predicts all these observations.
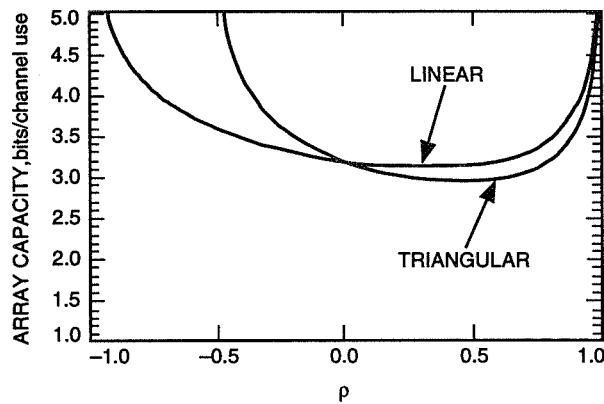
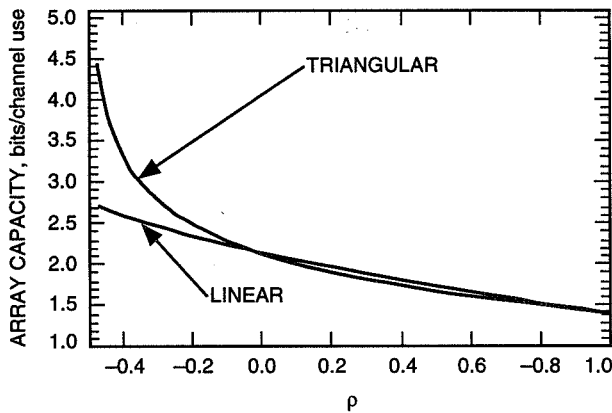**Fig. 5. Array capacity of Gaussian channels: different SNRs.**

Fig. 6. Array capacity of Gaussian channels: same SNR.

VI. Summary

The capacity of an array of n Gaussian channels has been derived. The array channel was modeled as n observations of a single source, in the presence of additive Gaussian noise. It was shown that an optimally weighted sum of the array outputs achieves the same channel capacity as the array channel. Several examples of two- and three-channel arrays were discussed, and graphs of channel capacities were provided to illustrate array capacity as a function of noise correlation as well as display examples of singular behavior.

References

[1] T. Cover and J. Thomas, *Elements of Information Theory*, New York: Wiley Interscience, 1991.

[2] V. Vilnrotter, E. Rodemich, and S. Dolinar, "Real-Time Combining of Residual Carrier Array Signals Using ML Weight Estimates," *IEEE Trans. Comm.*, vol. 40, no. 3, pp. 604–615, March 1992.

[3] T. Anderson, *An Introduction to Multivariate Statistical Analysis*, New York: Wiley, 1958.

[4] L. E. Brennan and L. S. Reed, "Theory of Adaptive Radar," *Array Processing Applications to Radar*, ed. S. Haykin, Stroudsburg, Pennsylvania: Dowden, Hutchinson and Ross, Inc., 1980.

[5] S. P. Applebaum, "Adaptive Arrays," *Array Processing Applications to Radar*, ed. S. Haykin, Stroudsburg, Pennsylvania: Dowden, Hutchinson and Ross, Inc., 1980.

[6] H. H. Tan, R. Liang, and P.-H. Suen, "Optimum Combining of Residual Carrier Array Signals in Correlated Noises," *The Telecommunications and Data Acquisition Progress Report 42-124, October–December 1995*, Jet Propulsion Laboratory, Pasadena, California, pp. 33–52, February 15, 1996. http://edms-www.jpl.nasa.gov/tda/progress_report/42-124/124K.pdf

Appendix

Derivation of Optimum Combining Weights

The following is a simple derivation of the optimum combining weights that maximize the SNR. Other derivations can be found in the adaptive signal processing literature [4,5] and in this issue [6].

We start with a derivation for the uncorrelated noise case (diagonal covariance matrix). It is shown in [2], using the Cauchy–Schwarz inequality, that for the uncorrelated case the optimum combining weight vector $\underline{U}$ is proportional to

$$\underline{U} = (\Theta_D^{-1}\underline{V})^*$$

where $\underline{V}$ is a signal vector, Θ_D is a diagonal matrix with components $\sigma_{Z,i}^2$, and Θ_D^{-1} is its inverse. When the weight vector $\underline{U}$ is applied, the combined SNR is maximized, achieving its upper bound,

$$SNR_{max} = \underline{V}^\dagger \Theta_D^{-1} \underline{V}$$

Next, consider a correlated Gaussian noise vector with covariance matrix Θ_Z, and let D be a unitary matrix that diagonalizes Θ_Z. With $D^\dagger$ the conjugate transpose of D, D^{-1} its inverse, and $D^\dagger = D^{-1}$ (unitary), we can write the diagonal covariance in terms of Θ_Z and D as

$$\Theta_D = D\Theta_Z D^T$$

Thus, D rotates vectors from the uncorrelated into the correlated reference frame, without changing their length, while its inverse rotates them in the opposite direction. Let $\underline{S} = D^{-1}\underline{V}$ be a signal vector, and let $\underline{W} = D^{-1}\underline{U}$ be a weight vector in the correlated frame. The optimum weights can be written in terms of Θ_Z and $\underline{S}$ as

$$\underline{U} = (\Theta_D^{-1}\underline{V})^* = (D^*\Theta_Z^*D^\dagger)^{-1}\underline{V}^*$$

$$= (\Theta_Z^*D^\dagger)^{-1}D^{*-1}\underline{V}^*$$

$$= (D^\dagger)^{-1}\Theta_Z^{*-1}(D^{*-1}\underline{V}^*)$$

$$= D(\Theta_Z^{-1}\underline{S})^*$$

This is the optimal weight vector in the uncorrelated frame, in terms of Θ_Z^{-1} and $\underline{S}$. Applying the inverse rotation operator D^{-1}, we obtain the optimum weight vector in the correlated frame as

$$\underline{W} = D^{-1}\underline{U} = D^{-1}D(\Theta_Z^{-1}\underline{S})^* = (\Theta_Z^{-1}\underline{S})^*$$

Soft-Output Decoding Algorithms in Iterative Decoding of Turbo Codes

S. Benedetto and G. Montorsi
Politecnico di Torino, Torino, Italy

D. Divsalar and F. Pollara
Communications Systems and Research Section

In this article, we present two versions of a simplified maximum a posteriori decoding algorithm. The algorithms work in a sliding window form, like the Viterbi algorithm, and can thus be used to decode continuously transmitted sequences obtained by parallel concatenated codes, without requiring code trellis termination. A heuristic explanation is also given of how to embed the maximum a posteriori algorithms into the iterative decoding of parallel concatenated codes (turbo codes). The performances of the two algorithms are compared on the basis of a powerful rate 1/3 parallel concatenated code. Basic circuits to implement the simplified a posteriori decoding algorithm using lookup tables, and two further approximations (linear and threshold), with a very small penalty, to eliminate the need for lookup tables are proposed.

I. Introduction and Motivations

The broad framework of this analysis encompasses digital transmission systems where the received signal is a sequence of wave forms whose correlation extends well beyond T, the signaling period. There can be many reasons for this correlation, such as coding, intersymbol interference, or correlated fading. It is well known [1] that the optimum receiver in such situations cannot perform its decisions on a symbol-by-symbol basis, so that deciding on a particular information symbol u_k involves processing a portion of the received signal T_d seconds long, with $T_d > T$. The decision rule can be either optimum with respect to a sequence of symbols, $u_k^n \triangleq (u_k, u_{k+1}, \cdots, u_{k+n-1})$, or with respect to the individual symbol, u_k.

The most widely applied algorithm for the first kind of decision rule is the Viterbi algorithm. In its optimum formulation, it would require waiting for decisions until the whole sequence has been received. In practical implementations, this drawback is overcome by anticipating decisions (single or in batches) on a regular basis with a fixed delay, D. A choice of D five to six times the memory of the received data is widely recognized as a good compromise between performance, complexity, and decision delay.

Optimum symbol decision algorithms must base their decisions on the maximum a posteriori (MAP) probability. They have been known since the early seventies [2,3], although much less popular than the Viterbi algorithm and almost never applied in practical systems. There is a very good reason for this neglect in that they yield performance in terms of symbol error probability only slightly superior to the Viterbi algorithm, yet they present a much higher complexity. Only recently, the interest in these

63

algorithms has seen a revival in connection with the problem of decoding concatenated coding schemes. Concatenated coding schemes (a class in which we include product codes, multilevel codes, generalized concatenated codes, and serial and parallel concatenated codes) were first proposed by Forney [4] as a means of achieving large coding gains by combining two or more relatively simple "constituent" codes. The resulting concatenated coding scheme is a powerful code endowed with a structure that permits an easy decoding, like "stage decoding" [5] or "iterated stage decoding" [6].

To work properly, all these decoding algorithms cannot limit themselves to passing the symbols decoded by the inner decoder to the outer decoder. They need to exchange some kind of soft information. Actually, as proved by Forney [4], the optimum output of the inner decoder should be in the form of the sequence of the probability distributions over the inner code alphabet conditioned on the received signal, the a posteriori probability (APP) distribution. There have been several attempts to achieve, or at least to approach, this goal. Some of them are based on modifications of the Viterbi algorithm so as to obtain, at the decoder output, in addition to the "hard"-decoded symbols, some reliability information. This has led to the concept of "augmented-output," or the list-decoding Viterbi algorithm [7], and to the soft-output Viterbi algorithm (SOVA) [8]. These solutions are clearly suboptimal, as they are unable to supply the required APP. A different approach consisted in revisiting the original symbol MAP decoding algorithms [2,3] with the aim of simplifying them to a form suitable for implementation [9–12].

In this article, we are interested in soft-decoding algorithms as the main building block of iterative stage decoding of parallel concatenated codes. This has become a "hot" topic for research after the successful proposal of the so-called turbo codes [6]. They are (see Fig. 1) parallel concatenated convolutional codes (PCCC) whose encoder is formed by two (or more) constituent systematic encoders joined through an interleaver. The input information bits feed the first encoder and, after having been interleaved by the interleaver, enter the second encoder. The codeword of the parallel concatenated code consists of the input bits to the first encoder followed by the parity check bits of both encoders. Generalizations to more than one interleaver are possible and fruitful [13].
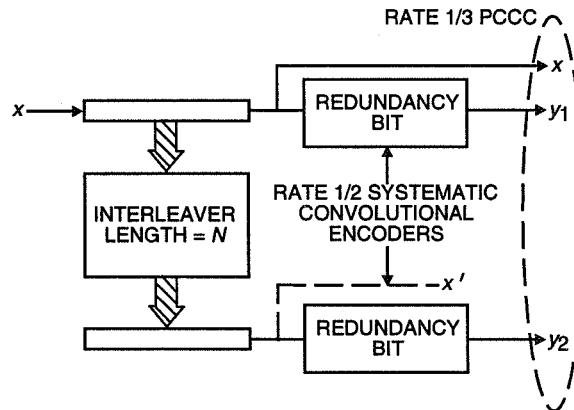
Fig. 1. Parallel concatenated convolutional code.

The suboptimal iterative decoder is modular and consists of a number of equal component blocks formed by concatenating soft decoders of the constituent codes (CC) separated by the interleavers used at the encoder side. By increasing the number of decoding modules and, thus, the number of decoding iterations, bit-error probabilities as low as 10^{-5} at $E_b/N_0 = 0.0$ dB for rate $1/4$ PCCC have been shown by simulation [13]. A version of turbo codes employing two eight-state convolutional codes as constituent codes, an interleaver of 32×32 bits, and an iterative decoder performing two and one-half iterations with a complexity of the order of five times the maximum-likelihood (ML) Viterbi decoding of each constituent code is presently available on a chip yielding a measured bit-error probability of 0.9×10^{-6} at $E_b/N_0 = 3$ dB [14].

In recent articles [15,17], upper bounds to the ML bit-error probability of PCCCs have been proposed. As a by-product, it has been shown by simulation that iterative decoding can approach quite closely the ML performance. The iterative decoding algorithm was a simplification of the algorithm proposed in [3], whose regular steps and limited complexity seem quite suitable to very large-scale integration (VLSI) implementation. Simplified versions of the algorithm [3] have been proposed and analyzed in [12] in the context of a block decoding strategy that requires trellis termination after each block of bits. Similar simplification also was used in [16] for hardware implememtation of the MAP algorithm.

In this article, we will describe two versions of a simplified MAP decoding algorithm that can be used as building blocks of the iterative decoder to decode PCCCs. A distinctive feature of the algorithms is that they work in a "sliding window" form, like the Viterbi algorithm, and thus can be used to decode "continuously transmitted" PCCCs, without requiring trellis termination and a block-equivalent structure of the code. The simplest among the two algorithms will be compared with the optimum block-decoding algorithm proposed in [3]. The comparison will be given in terms of bit-error probability when the algorithms are embedded into iterative decoding schemes for PCCCs. We will choose, for comparison, a very powerful PCCC scheme suitable for deep-space applications [18–20] and, thus, working at a very low signal-to-noise ratio.

II. System Context and Notations

As previously outlined, our final aim is to find suitable soft-output decoding algorithms for iterated staged decoding of parallel concatenated codes employed in a continuous transmission. The core of such algorithms is a procedure to derive the sequence of probability distributions over the information symbols' alphabet based on the received signal and constrained on the code structure. Thus, we will start by this procedure and only later will we extend the description to the more general setting.

Readers acquainted with the literature on soft-output decoding algorithms know that one burden in understanding and comparing the different algorithms is the spread and, sometimes, mess of notations involved. For this reason, we will carefully define the system and notations and then stick consistently to them for the description of all algorithms.

For the first part of the article, we will refer to the system of Fig. 2. The information sequence $\mathbf{u}$, composed of symbols drawn from an alphabet $U = \{u_1, \cdots, u_I\}$ and emitted by the source, enter an encoder that generates code sequences $\mathbf{c}$. Both source and code sequences are defined over a time index set K (a finite or infinite set of integers). Denoting the code alphabet $C = \{c_1, \cdots, c_M\}$, the code $\mathcal{C}$ can be written as a subset of the Cartesian product of C by itself K times, i.e.,

$$\mathcal{C} \subseteq C^K$$

The code symbols c_k (the index k will always refer to time throughout the article) enter the modulator, which performs a one-to-one mapping of them with its signals, or channel input symbols x_k, belonging to the set $X = \{x_1, \cdots, x_M\}$.[1]

The channel symbols x_k are transmitted over a stationary memoryless channel with output symbols y_k. The channel is characterized by the transitions probability distribution (discrete or continuous, according to the channel model) $P(y|x)$. The channel output sequence is fed to the symbol-by-symbol soft-output demodulator, which produces a sequence of probability distributions $\gamma_k(c)$ over C conditioned on the received signal, according to the memoryless transformation

---

[1] For simplicity of notation, we have assumed that the cardinality of the modulator equals that of the code alphabet. In general, each coded symbol can be mapped in more than one channel symbol, as in the case of multilevel codes or trellis codes with parallel transitions. The extension is straightforward.
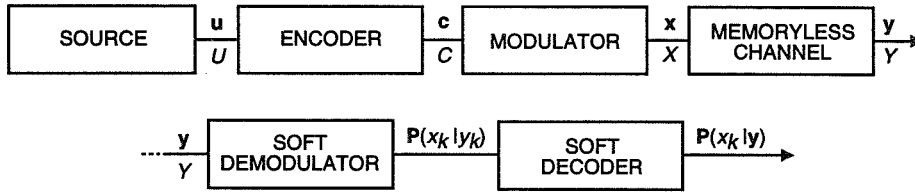
Fig. 2. The transmission system.

$$\gamma_k(c) \triangleq P(x_k = x(c), y_k) = P(y_k|x_k = x(c))P_k(c) \triangleq \gamma_k(x) \tag{1}$$

where we have assumed to know the sequence of the a priori probability distributions of the channel input symbols $(P_k(x) : k \in K)$ and made use of the one-to-one mapping $C \to X$.

The sequence of probability distributions $\gamma_k(c)$ obtained by the modulator on a symbol-by-symbol basis is then supplied to the soft-output symbol decoder, which processes the distributions in order to obtain the probability distributions $P_k(u|\mathbf{y})$. They are defined as

$$P_k(u|\mathbf{y}) \triangleq P(u_k = u|\mathbf{y}) \tag{2}$$

The probability distributions $P_k(u|\mathbf{y})$ are referred to in the literature as symbol-by-symbol a posteriori probabilities (APP) and represent the optimum symbol-by-symbol soft output.

From here on, we will limit ourselves to the case of time-invariant convolutional codes with N states, use the following notations with reference to Fig. 3, and assume that the (integer) time instant we are interested in is the kth:

(1) S_i is the generic state at time k, belonging to the set $\mathcal{S} = \{S_1, \cdots, S_N\}$

(2) $S_i^-(u')$ is one of the precursors of S_i, and precisely the one defined by the information symbol u' emitted during the transition $S_i^-(u') \to S_i$.[2]

(3) $S_i^+(u)$ is one of the successors of S_i, and precisely the one defined by the information symbol u emitted during the transition $S_i \to S_i^+(u)$.

(4) To each transition in the trellis, a signal x is associated, which depends on the state from which the transition originates and on the information symbol u determining that transition. When necessary, we will make this dependence explicit by writing $x(u', S_i)$ when the transition ends in S_i and $x(S_i, u)$ when the transition originates from S_i.

III. The BCJR Algorithm

In this section, we will restate in our new notations, without derivation, the algorithm described in [3], which is the optimum algorithm to produce the sequence of APP. We will call this algorithm the

---

[2] The state S_i and the symbol u' uniquely specify the precursor $S_i^-(u')$ in the case of the class of recursive convolutional encoders, like the ones we are interested in (when the largest degree of feedback polynomial represents the memory of a convolutional encoder). The extension to the case of feed-forward encoders and other nonconventional recursive convolutional encoders is straightforward.

66
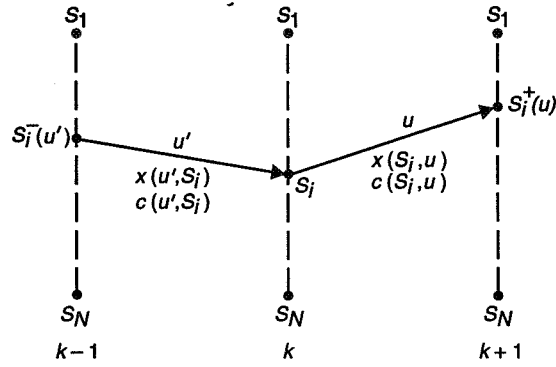
Fig. 3. The meaning of notations.

BCJR algorithm from the authors' initials.[3] We consider first the original version of the algorithm, which applies to the case of a finite index set $K = \{1, \cdots, n\}$ and requires the knowledge of the whole received sequence $\mathbf{y} = (y_1, \cdots, y_n)$ to work. In the following, the notations $\mathbf{u}, \mathbf{c}, \mathbf{x}$, and $\mathbf{y}$ will refer to sequences n-symbols long, and the integer time variable k will assume the values $1, \cdots, n$. As for the previous assumption, the encoder admits a trellis representation with N states, so that the code sequences $\mathbf{c}$ (and the corresponding transmitted signal sequences $\mathbf{x}$) can be represented as paths in the trellis and uniquely associated with a state sequence $\mathbf{s} = (s_0, \cdots, s_n)$ whose first and last states, s_0 and s_n, are assumed to be known by the decoder.[4]

Defining the a posteriori transition probabilities from state S_i at time k as

$$\sigma_k(S_i, u) \triangleq P(u_k = u, s_{k-1} = S_i | \mathbf{y}) \tag{3}$$

the APP $P(u|\mathbf{y})$ we want to compute can be obtained as

$$P_k(u|\mathbf{y}) = \sum_{S_i} \sigma_k(S_i, u) \tag{4}$$

Thus, the problem of evaluating the APP is equivalent to that of obtaining the a posteriori transition probabilities defined in Eq. (3). In [3], it was proven that the APP can be computed as

$$\sigma_k(S_i, u) = h_\sigma \alpha_{k-1}(S_i) \gamma_k(x(S_i, u)) \beta_k(S_i^+(u)) \tag{5}$$

where

---

[3] The algorithm is usually referred to in the recent literature as the "Bahl algorithm"; we prefer to credit all the authors: L. R. Bahl, J. Cocke, F. Jelinek, and J. Raviv.

[4] Lower-case s_k denotes the states of a sequence at time k, whereas upper-case S_i represents one particular state belonging to the set $\mathcal{S}$.

- h_σ is such that

$$\sum_{S_i, u} \sigma_k(S_i, u) = 1$$

- $\gamma_k(x(S_i, u))$ are the joint probabilities already defined in Eq. (1), i.e.,

$$\gamma_k(x) \triangleq P(y_k, x_k = x) = P(y_k | x_k = x) \cdot P(x_k = x) \qquad (6)$$

The γ's can be calculated from the knowledge of the a priori probabilities of the channel input symbols x and of the transition probabilities of the channel $P(y_k | x_k = x)$. For each time k, there are M different values of γ to be computed, which are then associated to the trellis transitions to form a sort of branch metrics. This information is supplied by the symbol-by-symbol soft-output demodulator.

- $\alpha_k(S_i)$ are the probabilities of the states of the trellis at time k conditioned on the past received signals, namely,

$$\alpha_k(S_i) \triangleq P(s_k = S_i | y_1^k) \qquad (7)$$

where y_1^k denotes the sequence $y_1, y_2, \cdots, y_k$. They can be obtained by the forward recursion[5]

$$\alpha_k(S_i) = h_\alpha \sum_u \alpha_{k-1}(S_i^-(u)) \gamma_k(x(u, S_i)) \qquad (8)$$

with h_α a constant determined through the constraint

$$\sum_{S_i} \alpha_k(S_i) = 1$$

and where the recursion is initialized as

$$\alpha_0(S_i) = \begin{cases} 1 & \text{if } S_i = s_0 \\ 0 & \text{otherwise} \end{cases} \qquad (9)$$

- $\beta_k(S_i)$ are the probabilities of the trellis states at time k conditioned on the future received signals $P(s_k = S_i | y_{k+1}^n)$. They can be obtained by the backward recursion

$$\beta_k(S_i) = h_\beta \sum_u \beta_{k+1}(S_i^+(u)) \gamma_{k+1}(x(S_i, u)) \qquad (10)$$

---

[5] For feed-forward encoders and nonconventional recursive convolutional encoders like $G(D) = [1, (1 + D + D^2)/(1 + D)]$ in Eq. (8), the summation should be over all possible precursors $S_i^-(u)$ that lead to the state S_i, and $x(u, S_i)$ should be replaced by $x(S_i^-(u), u)$. Then such modifications are also required for Eqs. (18) and (26). In Eqs. (22), (29), and (32), the maximum should be over all $S_i^-(u)$ that lead to S_i. The $c(u, S_i)$ should be replaced by $c(S_i^-(u), u)$.

with h_β a constant obtainable through the constraint

$$\sum_{S_i} \beta_k(S_i) = 1$$

and where the recursion is initialized as

$$\beta_n(S_i) = \begin{cases} 1 & \text{if } S_i = s_n \\ 0 & \text{otherwise} \end{cases} \tag{11}$$

We can now formulate the BCJR algorithm by the following steps:

(1) Initialize α_0 and β_n according to Eqs. (9) and (11).

(2) As soon as each term y_k of the sequence **y** is received, the demodulator supplies to the decoder the "branch metrics" γ_k of Eq. (6), and the decoder computes the probabilities α_k according to Eq. (8). The obtained values of $\alpha_k(S_i)$ as well as the γ_k are stored for all k, S_i, and x.

(3) When the entire sequence **y** has been received, the decoder recursively computes the probabilities β_k according to the recursion of Eq. (10) and uses them together with the stored α's and γ's to compute the a posteriori transition probabilities $\sigma_k(S_i, u)$ according to Eq. (5) and, finally, the APP $P_k(u|\mathbf{y})$ from Eq. (4).

A few comments on the computational complexity of the finite-sequence BCJR algorithm can be found in [3].

IV. The Sliding Window BCJR (SW-BCJR)

As previous description made clear, the BCJR algorithm requires that the whole sequence has been received before starting the decoding process. In this aspect, it is similar to the Viterbi algorithm in its optimum version. To apply it in a PCCC, we need to subdivide the information sequence into blocks,[6] decode them by terminating the trellises of both CCs,[7] and then decode the received sequence block by block. Beyond the rigidity, this solution also reduces the overall code rate.

A more flexible decoding strategy is offered by a modification of the BCJR algorithm in which the decoder operates on a fixed memory span, and decisions are forced with a given delay D. We call this new, and suboptimal, algorithm the sliding window BCJR (SW-BCJR) algorithm. We will describe two versions of the sliding window BCJR algorithm that differ in the way they overcome the problem of initializing the backward recursion without having to wait for the entire sequence. We will describe the two algorithms using the previous step description suitably modified. Of the previous assumptions, we retain only that of the knowledge of the initial state s_0, and thus assume the transmission of semi-infinite code sequences, where the time span K ranges from 1 to ∞.

---

[6] The presence of the interleaver naturally points toward a block length equal to the interleaver length.

[7] The termination of trellises in a PCCC has been considered a hard problem by several authors. As shown in [13], it is, indeed, quite an easy task.

A. The First Version of the Sliding Window BCJR Algorithm (SW1-BCJR)

Here are the steps:

(1) Initialize α_0 according to Eq. (9).

(2) Forward recursion at time k: Upon receiving y_k, the demodulator supplies to the decoder the M distinct branch metrics, and the decoder computes the probabilities $\alpha_k(S_i)$ according to Eqs. (6) and (8). The obtained values of $\alpha_k(S_i)$ are stored for all S_i, as well as the $\gamma_k(x)$.

(3) Initialization of the backward recursion ($k > D$):

$$\beta_k(S_j) = \alpha_k(S_j), \quad \forall S_j \tag{12}$$

(4) Backward recursion: It is performed according to Eq. (10) from time $k - 1$ back to time $k - D$.

(5) The a posteriori transition probabilities at time $k - D$ are computed according to

$$\sigma_{k-D}(S_i, u) = h_\sigma \cdot \alpha_{k-D-1}(S_i)\gamma_{k-D}(x(S_i, u))\beta_{k-D}(S_i^+(u)) \tag{13}$$

(6) The APP at time $k - D$ is computed as

$$P_{k-D}(u|\mathbf{y}) = \sum_{S_i} \sigma_{k-D}(S_i, u) \tag{14}$$

For a convolutional code with parameters (k_0, n_0), number of states N, and cardinality of the code alphabet $M = 2^{n_0}$, the SW1-BCJR algorithm requires storage of $N \times D$ values of α's and $M \times D$ values of the probabilities $\gamma_k(x)$ generated by the soft demodulator. Moreover, to update the α's and β's for each time instant, the algorithm needs to perform $M \times 2^{k_0}$ multiplications and N additions of 2^{k_0} numbers. To output the set of APP at each time instant, we need a D-times long backward recursion. Thus, the computational complexity requires overall

- $(D + 1)M \times 2^{k_0}$ multiplications

- $(D + 1)M$ additions of 2^{k_0} numbers each

As a comparison,[8] the Viterbi algorithm would require, in the same situation, $M \times 2^{k_0}$ additions and $M \times 2^{k_0}$-way comparisons, plus the trace-back operations, to get the decoded bits.

B. The Second, Simplified Version of the Sliding Window BCJR Algorithm (SW2-BCJR)

A simplification of the sliding window BCJR that significantly reduces the memory requirements consists of the following steps:

---

[8] Though, indeed, not fair, as the Viterbi algorithm does not provide the information we need.

(1) Initialize α_0 according to Eq. (9).

(2) Forward recursion $(k > D)$: If $k > D$, the probabilities $\alpha_{k-D-1}(S_i)$ are computed according to Eq. (8).

(3) Initialization of the backward recursion $(k > D)$:

$$\beta_k(S_j) = \frac{1}{N}, \quad \forall S_j \tag{15}$$

(4) Backward recursion $(k > D)$: It is performed according to Eq. (10) from time $k-1$ back to time $k - D$.

(5) The a posteriori transition probabilities at time $k - D$ are computed according to

$$\sigma_{k-D}(S_i, u) = h_\sigma \cdot \alpha_{k-D-1}(S_i)\gamma_{k-D}(x(S_i, u))\beta_{k-D}(S_i^+(u)) \tag{16}$$

(6) The APP at time $k - D$ is computed as

$$P_{k-D}(u|\mathbf{y}) = \sum_{S_i} \sigma_{k-D}(S_i, u) \tag{17}$$

This version of the sliding window BCJR algorithm does not require storage of the $N \times D$ values of α's as they are updated with a delay of D steps. As a consequence, only N values of α's and $M \times D$ values of the probabilities $\gamma_k(x)$ generated by the soft demodulator must be stored. The computational complexity is the same as the previous version of the algorithm. However, since the initialization of the β recursion is less accurate, a larger value of D should be set in order to obtain the same accuracy on the output values $P_{k-D}(u|\mathbf{y})$. This observation will receive quantitative evidence in the section devoted to simulation results.

V. Additive Algorithms

A. The Log-BCJR

The BCJR algorithm and its sliding window versions have been stated in multiplicative form. Owing to the monotonicity of the logarithm function, they can be converted into an additive form passing to the logarithms. Let us define the following logarithmic quantities:

$$\Gamma_k(x) \triangleq \log[\gamma(x)]$$

$$A_k(S_i) \triangleq \log[\alpha_k(S_i)]$$

$$B_k'(S_i) \triangleq \log[\beta_k(S_i)]$$

$$\Sigma_k(S_i, u) \triangleq \log[\sigma_k(S_i, u)]$$

These definitions lead to the following A and B recursions, derived from Eqs. (8), (10), and (5):

$$A_k(S_i) = \log \left[\sum_u \exp \left\{ A_{k-1}(S_i^-(u)) + \Gamma_k(x(u, S_i)) \right\} \right] + H_A \tag{18}$$

$$B_k(S_i) = \log \left[\sum_u \exp \left\{ \Gamma_{k+1} \left(x(S_i, u) \right) + B_{k+1} \left(S_i^+(u) \right) \right\} \right] + H_B \tag{19}$$

$$\Sigma_k(S_i, u) = A_{k-1}(S_i) + \Gamma_k(x(S_i, u)) + B_k(S_i^+(u)) + H_\Sigma \tag{20}$$

with the following initializations:

$$A_0(S_i) = \begin{cases} 0 & \text{if } S_i = s_0 \\ -\infty & \text{otherwise} \end{cases}$$

$$B_1(S_i) = \begin{cases} 0 & \text{if } S_i = s_n \\ -\infty & \text{otherwise} \end{cases}$$

B. Simplified Versions of the Log-BCJR

The problem in the recursions defined for the log-BCJR consists of the evaluation of the logarithm of a sum of exponentials:

$$\log \left[\sum_i \exp\{A_i\} \right]$$

An accurate estimate of this expression can be obtained by extracting the term with the highest exponential,

$$A_M = \max_i A_i$$

so that

$$\log \left[\sum_i \exp\{A_i\} \right] = A_M + \log \left(1 + \sum_{A_i \neq A_M} \exp\{A_i - A_M\} \right) \tag{21}$$

and by computing the second term of the right-hand side (RHS) of Eq. (21) using lookup tables. Further simplifications and the required circuits for implementation are discussed in the Appendix.

However, when $A_M \gg A_i$, the second term can be neglected. This approximation leads to the additive logarithmic-BCJR (AL-BCJR) algorithm:

$$A_k(S_i) = \max_u \left[A_{k-1}(S_i^-(u)) + \Gamma_k(x(u, S_i)) \right] + H_A \tag{22}$$

$$B_k(S_i) = \max_u \left[B_{k+1}(S_i^+(u)) + \Gamma_{k+1}(x(S_i, u)) \right] + H_B \tag{23}$$

$$\Sigma_k(S_i, u) = A_{k-1}(S_i) + \Gamma_k(x(S_i, u)) + B_k(S_i^+(u)) + H_\Sigma \tag{24}$$

with the same initialization of the log-BCJR.

Both versions of the SW-BCJR algorithm described in the previous section can be used, with obvious modifications, to transform the block log-BCJR and the AL-BCJR into their sliding window versions, leading to the SW-log-BCJR and the SWAL1-BCJR and SWAL2-BCJR algorithms.

VI. Explicit Algorithms for Some Particular Cases

In this section, we will make explicit the quantities considered in the previous algorithms' descriptions by making assumptions on the code type, modulation format, and channel.

A. Rate 1/*n* Binary Systematic Convolutional Encoder

In this section, we particularize the previous equations in the case of a rate $1/n$ binary systematic encoder associated to n binary-pulse amplitude modulation (PAM) signals or binary phase shift keying (PSK) signals.

The channel symbols x and the output symbols from the encoder can be represented as vectors of n binary components:

$$\tilde{c} \triangleq [c_1, \cdots, c_n] c_i \in \{0, 1\}$$

$$\tilde{x} \triangleq [x_1, \cdots, x_n] x_i \in \{A, -A\}$$

$$\tilde{x}_k \triangleq [x_{k1}, \cdots, x_{kn}]$$

$$\tilde{y}_k \triangleq [y_{k1}, \cdots, y_{kn}]$$

where the notations have been modified to show the vector nature of the symbols. The joint probabilities $\gamma_k(\tilde{x})$, over a memoryless channel, can be split as

$$\gamma_k(\tilde{x}) = \prod_{m=1}^n P(y_{km}|x_{km} = x_m) P(x_{km} = x_m) \tag{25}$$

Since in this case the encoded symbols are n-tuple of binary symbols, it is useful to redefine the input probabilities, γ, in terms of the likelihood ratios:

$$\lambda_{km} \triangleq \frac{P(y_{km}|x_{km} = A)}{P(y_{km}|x_{km} = -A)}$$

$$\lambda_{km}^A \triangleq \frac{P(x_{km} = A)}{P(x_{km} = -A)}$$

so that, from Eq. (25),

$$\gamma_k(\tilde{x}) = \prod_{m=1}^{n} \frac{(\lambda_{km})^{c_m}}{1 + \lambda_{km}} \frac{(\lambda_{km}^A)^{c_n}}{1 + \lambda_{km}^A} = h_\gamma \prod_{m=1}^{n} \left[\lambda_{km} \cdot \lambda_{km}^A \right]^{c_m}$$

where h_γ takes into account all terms independent of $\tilde{x}$.

The BCJR can be restated as follows:

$$\alpha_k(S_i) = h_\gamma h_\alpha \sum_u \alpha_{k-1}(S_i^-(u)) \prod_{m=1}^{n} \left[\lambda_{km} \cdot \lambda_{km}^A \right]^{c_m(u,S_i)} \tag{26}$$

$$\beta_k(S_i) = h_\gamma h_\beta \sum_u \beta_{k+1}(S_i^+(u)) \prod_{m=1}^{n} \left[\lambda_{(k+1)m} \cdot \lambda_{(k+1)m}^A \right]^{c_m(S_i,u)} \tag{27}$$

$$\sigma_k(S_i, u) = h_\gamma h_\sigma \alpha_{k-1}(S_i) \prod_{m=1}^{n} \left[\lambda_{km} \cdot \lambda_{km}^A \right]^{c_m(u,S_i)} \beta_k(S_i^+(u)) \tag{28}$$

whereas its simplification, the AL-BCJR algorithm, becomes

$$A_k(S_i) = \max_u \left\{ A_{k-1}(S_i^-(u)) + \sum_{m=1}^{n} c_m(u, S_i) \left(\Lambda_{km} + \Lambda_{km}^A \right) \right\} + H_A \tag{29}$$

$$B_k(S_i) = \max_u \left\{ B_{k+1}(S_i^+(u)) + \sum_{m=1}^{n} c_m(S_i, u) \left(\Lambda_{km} + \Lambda_{km}^A \right) \right\} + H_B \tag{30}$$

$$\Sigma_k(S_i, u) = A_{k-1}(S_i) + \sum_{m=1}^{n} c_m(S_i, u) \left(\Lambda_{km} + \Lambda_{km}^A \right) + B_k(S_i^+(u)) \tag{31}$$

where Λ stands for the logarithm of the corresponding quantity λ.

B. The Additive White Gaussian Noise Channel

When the channel is the additive white Gaussian noise (AWGN) channel, we obtain the explicit expression of the log–likelihood ratios Λ_{ki} as

$$\Lambda_{ki} \triangleq \log \left[\frac{P(y_{ki}|x_{ki} = A)}{P(y_{ki}|x_{ki} = -A)} \right]$$

$$= \log \left[\frac{\frac{1}{\sqrt{2\pi\sigma^2}} \exp\{-\frac{1}{2\sigma^2}(y_{ki} - A)^2\}}{\frac{1}{\sqrt{2\pi\sigma^2}} \exp\{-\frac{1}{2\sigma^2}(y_{ki} + A)^2\}} \right] = \frac{2A}{\sigma^2} y_{ki}$$

Hence, the AL-BCJR algorithm assumes the following form:

$$A_k(S_i) = \max_u \left\{ A_{k-1}(S_i^-(u)) + \sum_{m=1}^{n} c_m(u, S_i) \left(\frac{2A}{\sigma^2} y_{km} + \Lambda_{km}^A \right) \right\} + H_A \tag{32}$$

$$B_k(S_i) = \max_u \left\{ B_{k+1}(S_i^+(u)) + \sum_{m=1}^{n} c_m(S_i, u) \left(\frac{2A}{\sigma^2} y_{km} + \Lambda_{km}^A \right) \right\} + H_B \tag{33}$$

$$\Sigma_k(S_i, u) = A_{k-1}(S_i) + \sum_{m=1}^{n} c_m(S_i, u) \left(\frac{2A}{\sigma^2} y_{km} + \Lambda_{km}^A \right) + B_k(S_i^+(u)) \tag{34}$$

In the examples presented in Section VIII, we will consider turbo codes with rate 1/2 component convolutional codes transmitted as binary PAM or binary PSK over an AWGN channel.

VII. Iterative Decoding of Parallel Concatenated Convolutional Codes

In this section, we will show how the MAP algorithms previously described can be embedded into the iterative decoding procedure of parallel concatenated codes. We will derive the iterative decoding algorithm through suitable approximations performed on maximum-likelihood decoding. The description will be based on the fairly general parallel concatenated code shown in Fig. 4, which employs three encoders and three interleavers (denoted by π in the figure).

Let u_k be the binary random variable taking values in $\{0, 1\}$, representing the sequence of information bits $\mathbf{u} = (u_1, \cdots, u_n)$. The optimum decision algorithm on the kth bit u_k is based on the conditional log–likelihood ratio L_k:

$$L_k = \log \frac{P(u_k = 1|\mathbf{y})}{P(u_k = 0|\mathbf{y})}$$

$$= \log \frac{\sum_{\mathbf{u}:u_k=1} P(\mathbf{y}|\mathbf{u}) \prod_{j \neq k} P(u_j)}{\sum_{\mathbf{u}:u_k=0} P(\mathbf{y}|\mathbf{u}) \prod_{j \neq k} P(u_j)} + \log \frac{P(u_k = 1)}{P(u_k = 0)}$$

$$= \log \frac{\sum_{\mathbf{u}:u_k=1} P(\mathbf{y}|\mathbf{x}(\mathbf{u})) \prod_{j \neq k} P(u_j)}{\sum_{\mathbf{u}:u_k=0} P(\mathbf{y}|\mathbf{x}(\mathbf{u})) \prod_{j \neq k} P(u_j)} + \log \frac{P(u_k = 1)}{P(u_k = 0)} \tag{35}$$

where, in Eq. (35), $P(u_j)$ are the a priori probabilities.
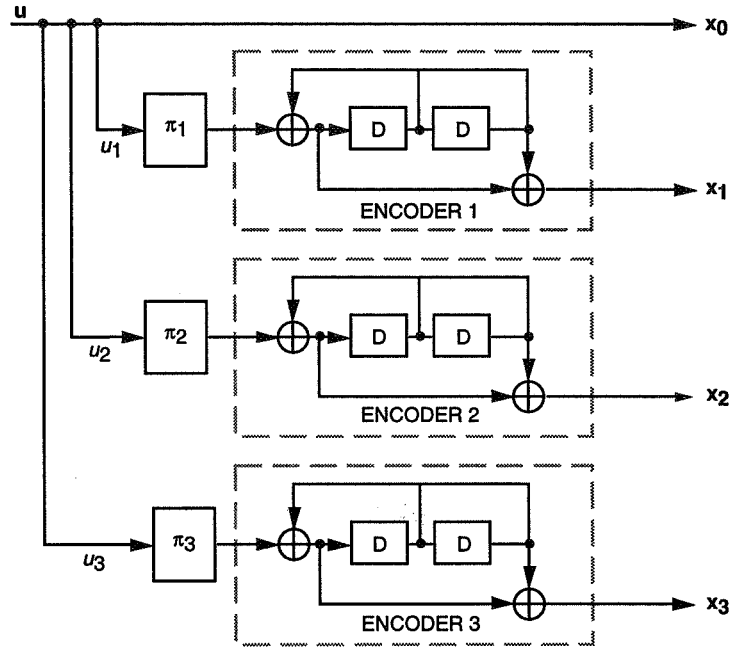
Fig. 4. Parallel concatenation of three convolutional codes.

If the rate k_o/n_o constituent code is not equivalent to a punctured rate $1/n'_o$ code or if turbo trellis-coded modulation is used, we can first use the symbol MAP algorithm as described in the previous sections to compute the log–likelihood ratio of a symbol $\mathbf{u} = u_1, u_2, \cdots, u_{k_o}$, given the observation $\mathbf{y}$ as

$$\lambda(\mathbf{u}) = \log \frac{P(\mathbf{u}|\mathbf{y})}{P(\mathbf{0}|\mathbf{y})}$$

where $\mathbf{0}$ corresponds to the all-zero symbol. Then we obtain the log–likelihood ratios of the jth bit within the symbol by

$$L(u_j) = \log \frac{\sum_{\mathbf{u}:u_j=1} e^{\lambda(\mathbf{u})}}{\sum_{\mathbf{u}:u_j=0} e^{\lambda(\mathbf{u})}}$$

In this way, the turbo decoder operates on bits, and bit, rather than symbol, interleaving is used.

To explain the basic decoding concept, we restrict ourselves to three codes, but extension to several codes is straightforward. In order to simplify the notation, consider the combination of the permuter (interleaver) and the constituent encoder connected to it as a block code with input $\mathbf{u}$ and outputs $\mathbf{x}_i$, $i = 0, 1, 2, 3(\mathbf{x}_0 = \mathbf{u})$ and the corresponding received sequences as $\mathbf{y}_i$, $i = 0, 1, 2, 3$. The optimum bit decision metric on each bit is (for data with uniform a priori probabilities)

$$L_k = \log \frac{\sum_{\mathbf{u}:u_k=1} P(\mathbf{y}_0|\mathbf{u})P(\mathbf{y}_1|\mathbf{u})P(\mathbf{y}_2|\mathbf{u})P(\mathbf{y}_3|\mathbf{u})}{\sum_{\mathbf{u}:u_k=0} P(\mathbf{y}_0|\mathbf{u})P(\mathbf{y}_1|\mathbf{u})P(\mathbf{y}_2|\mathbf{u})P(\mathbf{y}_3|\mathbf{u})} \tag{36}$$

but, in practice, we cannot compute Eq. (36) for large n because the permutations π_2, π_3 imply that $\mathbf{y}_2$ and $\mathbf{y}_3$ are no longer simple convolutional encodings of $\mathbf{u}$. Suppose that we evaluate $P(\mathbf{y}_i|\mathbf{u})$, $i = 0, 2, 3$ in Eq. (36) using Bayes' rule and using the following approximation:

$$P(\mathbf{u}|\mathbf{y}_i) \approx \prod_{k=1}^{n} \tilde{P}_i(u_k) \tag{37}$$

Note that $P(\mathbf{u}|\mathbf{y}_i)$ is not separable in general. However, for $i = 0$, $P(\mathbf{u}|\mathbf{y}_0)$ is separable; hence, Eq. (37) holds with equality. So we need an algorithm that approximates a nonseparable distribution $P(\mathbf{u}|\mathbf{y}_i) \triangleq P$ with a separable distribution $\prod_{k=1}^{n} \tilde{P}_i(u_k) \triangleq Q$. The best approximation can be obtained using the Kullback cross-entropy minimizer, which minimizes the cross-entropy $H(Q,P) = E\{\log(Q/P)\}$ between the input P and the output Q.

The MAP algorithm approximates a nonseparable distribution with a separable one; however it is not clear how good it is compared with the Kullback cross-entropy minimizer. Here we use the MAP algorithm for such an approximation. In the iterative decoding, as the reliability of the $\{u_k\}$ improves, intuitively one expects that the cross-entropy between the input and the output of the MAP algorithm will decrease, so that the approximation will improve. If such an approximation, i.e., Eq. (37), can be obtained, we can use it in Eq. (36) for $i = 2$ and $i = 3$ (by Bayes' rule) to complete the algorithm.

Define $\tilde{L}_{ik}$ by

$$\tilde{P}_i(u_k) = \frac{e^{u_k \tilde{L}_{ik}}}{1 + e^{\tilde{L}_{ik}}} \tag{38}$$

where $u_k \in \{0,1\}$. To obtain $\{\tilde{P}_i\}$ or, equivalently, $\{\tilde{L}_{ik}\}$, we use Eqs. (37) and (38) for $i = 0,2,3$ (by Bayes' rule) to express Eq. (36) as

$$L_k = f(\mathbf{y}_1, \tilde{\mathbf{L}}_0, \tilde{\mathbf{L}}_2, \tilde{\mathbf{L}}_3, k) + \tilde{L}_{0k} + \tilde{L}_{2k} + \tilde{L}_{3k} \tag{39}$$

where $\tilde{L}_{0k} = 2Ay_{0k}/\sigma^2$ (for binary modulation) and

$$f(\mathbf{y}_1, \tilde{\mathbf{L}}_0, \tilde{\mathbf{L}}_2, \tilde{\mathbf{L}}_3, k) = \log \frac{\sum_{\mathbf{u}:u_k=1} P(\mathbf{y}_1|\mathbf{u}) \prod_{j \neq k} e^{u_j(\tilde{L}_{0j} + \tilde{L}_{2j} + \tilde{L}_{3j})}}{\sum_{\mathbf{u}:u_k=0} P(\mathbf{y}_1|\mathbf{u}) \prod_{j \neq k} e^{u_j(\tilde{L}_{0j} + \tilde{L}_{2j} + \tilde{L}_{3j})}} \tag{40}$$

We can use Eqs. (37) and (38) again, but this time for $i = 0,1,3$, to express Eq. (36) as

$$L_k = f(\mathbf{y}_2, \tilde{\mathbf{L}}_0, \tilde{\mathbf{L}}_1, \tilde{\mathbf{L}}_3, k) + \tilde{L}_{0k} + \tilde{L}_{1k} + \tilde{L}_{3k} \tag{41}$$

and similarly,

$$L_k = f(\mathbf{y}_3, \tilde{\mathbf{L}}_0, \tilde{\mathbf{L}}_1, \tilde{\mathbf{L}}_2, k) + \tilde{L}_{0k} + \tilde{L}_{1k} + \tilde{L}_{2k} \tag{42}$$

A solution to Eqs. (39), (41), and (42) is

$$\left. \begin{aligned} \tilde{L}_{1k} &= f(\mathbf{y}_1, \tilde{\mathbf{L}}_0, \tilde{\mathbf{L}}_2, \tilde{\mathbf{L}}_3, k) \\[2mm] \tilde{L}_{2k} &= f(\mathbf{y}_2, \tilde{\mathbf{L}}_0, \tilde{\mathbf{L}}_1, \tilde{\mathbf{L}}_3, k) \\[2mm] \tilde{L}_{3k} &= f(\mathbf{y}_3, \tilde{\mathbf{L}}_0, \tilde{\mathbf{L}}_1, \tilde{\mathbf{L}}_2, k) \end{aligned} \right\} \tag{43}$$

for $k = 1, 2, \cdots, n$, provided that a solution to Eq. (43) does indeed exist. The final decision is then based on

$$L_k = \tilde{L}_{0k} + \tilde{L}_{1k} + \tilde{L}_{2k} + \tilde{L}_{3k} \qquad (44)$$

which is passed through a hard limiter with zero threshold. We attempted to solve the nonlinear equations in Eq. (43) for $\tilde{\mathbf{L}}_1$, $\tilde{\mathbf{L}}_2$, and $\tilde{\mathbf{L}}_3$ by using the iterative procedure

$$\tilde{L}_{1k}^{(m+1)} = \alpha_1^{(m)} f(\mathbf{y}_1, \tilde{\mathbf{L}}_0, \tilde{\mathbf{L}}_2^{(m)}, \tilde{\mathbf{L}}_3^{(m)}, k) \qquad (45)$$

for $k = 1, 2, \cdots, n$, iterating on m. Similar recursions hold for $\tilde{L}_{2k}^{(m)}$ and $\tilde{L}_{3k}^{(m)}$.

We start the recursion with the initial condition $\tilde{\mathbf{L}}_1^{(0)} = \tilde{\mathbf{L}}_2^{(0)} = \tilde{\mathbf{L}}_3^{(0)} = \tilde{\mathbf{L}}_0$. For the computation of $f(\cdot)$, we can use any MAP algorithm as described in the previous sections, with permuters (direct and inverse) where needed; call this the basic decoder D_i, $i = 1, 2, 3$. The $\tilde{L}_{ik}^{(m)}$, $i = 1, 2, 3$ represent the extrinsic information. The signal flow graph for extrinsic information is shown in Fig. 5 [13], which is a fully connected graph without self-loops. Parallel, serial, or hybrid implementations can be realized based on the signal flow graph of Fig. 5 (in this figure $\mathbf{y}_0$ is considered as part of $\mathbf{y}_1$). Based on our equations, each node's output is equal to internally generated reliability $\mathbf{L}$ minus the sum of all inputs to that node. The BCJR MAP algorithm always starts and ends at the all-zero state since we always terminate the trellis as described in [13]. We assumed $\pi_1 = I$ identity; however, any π_1 can be used.
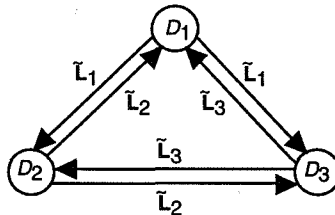
Fig. 5. Signal flow graph for
extrinsic information.

The overall decoder is composed of block decoders D_i connected in parallel, as in Fig. 6 (when the switches are in position P), which can be implemented as a pipeline or by feedback. A serial implementation is also shown in Fig. 6 (when the switches are in position S). Based on [13, Fig. 5], a serial implementation was proposed in [21]. For those applications where the systematic bits are not transmitted or for parallel concatenated trellis codes with high-level modulation, we should set $\tilde{L}_0 = 0$. Even in the presence of systematic bits, if desired, one can set $\tilde{L}_0 = 0$ and consider $\mathbf{y}_0$ as part of $\mathbf{y}_1$. If the systematic bits are distributed among encoders, we use the same distribution for $\mathbf{y}_0$ among the received observations for MAP decoders.

At this point, further approximation for iterative decoding is possible if one term corresponding to a sequence $\mathbf{u}$ dominates other terms in the summation in the numerator and denominator of Eq. (40). Then the summations in Eq. (40) can be replaced by "maximum" operations with the same indices, i.e., replacing $\sum_{\mathbf{u}:u_k=i}$ with $\max_{\mathbf{u}:u_k=i}$ for $i = 0, 1$. A similar approximation can be used for $\tilde{L}_{2k}$ and $\tilde{L}_{3k}$ in Eq. (43). This suboptimal decoder then corresponds to an iterative decoder that uses AL-BCJR rather than BCJR decoders. As discussed, such approximations have been used by replacing $\sum$ with max in the log-BCJR algorithm to obtain AL-BCJR. Clearly, all versions of SW-BCJR can replace BCJR (MAP) decoders in Fig. 6.

For turbo codes with only two constituent codes, Eq. (45) reduces to
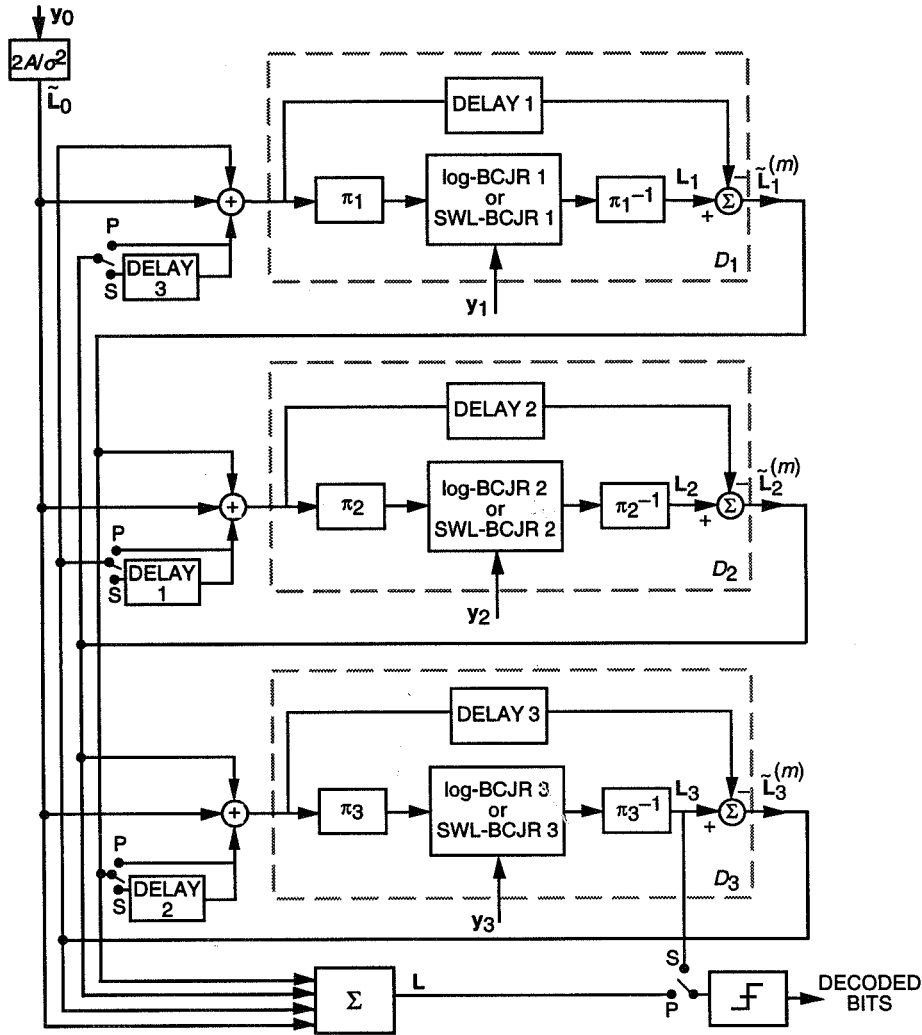
Fig. 6. Iterative decoder structure for three parallel concatenated codes.

$$\tilde{L}_{1k}^{(m+1)} = \alpha_1^{(m)} f(\mathbf{y}_1, \tilde{\mathbf{L}}_0, \tilde{\mathbf{L}}_2^{(m)}, k)$$

$$\tilde{L}_{2k}^{(m+1)} = \alpha_2^{(m)} f(\mathbf{y}_2, \tilde{\mathbf{L}}_0, \tilde{\mathbf{L}}_1^{(m)}, k)$$

for $k = 1, 2, \cdots, n$, and $m = 1, 2, \cdots$, where, for each iteration, $\alpha_1^{(m)}$ and $\alpha_2^{(m)}$ can be optimized (simulated annealing) or set to 1 for simplicity. The decoding configuration for two codes is shown in Fig. 7. In this special case, since the paths in Fig. 7 are disjointed, the decoder structure can be reduced to a serial mode structure if desired. If we optimize $\alpha_1^{(m)}$ and $\alpha_2^{(m)}$, our method for two codes is similar to the decoding method proposed in [6], which requires estimates of the variances of $\tilde{L}_{1k}$ and $\tilde{L}_{2k}$ for each iteration in the presence of errors. It is interesting to note that the concept of extrinsic information introduced in [6] was also presented as "partial factor" in [22]. However, the effectiveness of turbo codes lies in the use of recursive convolutional codes and random permutations. This results in time-shift-varying codes resembling random codes.

In the results presented in the next section, we will use a parallel concatenated code with only two constituent codes.
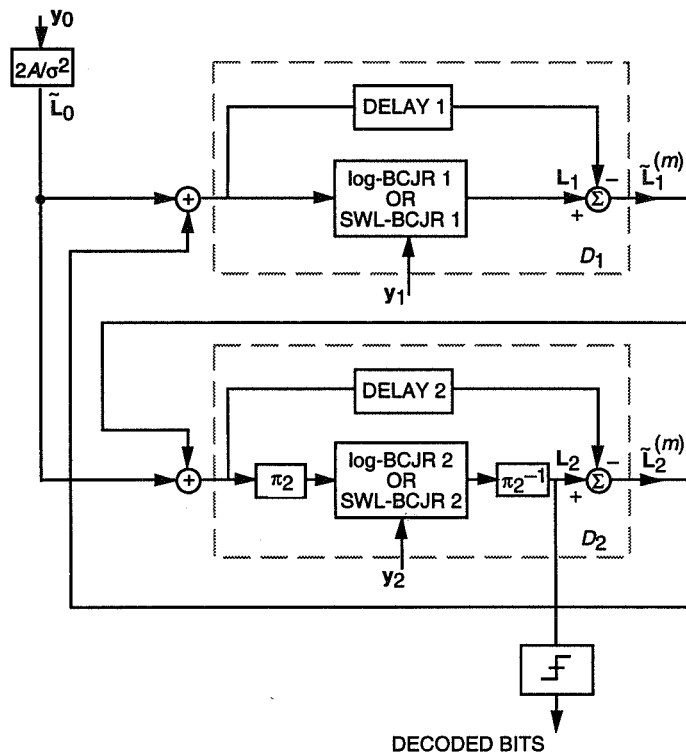
Fig. 7. Iterative decoder structure for two parallel concatenated codes.

VIII. Simulation Results

In this section, we will present some simulation results obtained applying the iterative decoding algorithm described in Section VII, which, in turn, uses the optimum BCJR and the suboptimal, but simpler, SWAL2-BCJR as embedded MAP algorithms. All simulations refer to a rate 1/3 PCCC with two equal, recursive convolutional constituent codes with 16 states and generator matrix

$$G(D) = \left[1, \frac{1 + D + D^3 + D^4}{1 + D^3 + D^4} \right]$$

and an interleaver of length 16,384 designed according to the procedure described in [13], using an S-random permutation with $S = 40$. Each simulation run examined at least 25,000,000 bits.

In Fig. 8, we plot the bit-error probabilities as a function of the number of iterations of the decoding procedure using the optimum block BCJR algorithm for various values of the signal-to-noise ratio. It can be seen that the decoding algorithm converges down to BER $= 10^{-5}$ at signal-to-noise ratios of 0.2 dB with nine iterations. The same curves are plotted in Fig. 9 for the case of the suboptimum SWAL2-BCJR algorithm. In this case, 0.75 dB of signal-to-noise ratio is required for convergence to the same BER and with the same number of iterations.

In Fig. 10, the bit-error probability versus the signal-to-noise ratio is plotted for a fixed number (5) of iterations of the decoding algorithm and for both optimum BCJR and SWAL2-BCJR MAP decoding algorithms. It can be seen that the penalty incurred by the suboptimum algorithm amounts to about 0.5 dB. This figure is in agreement with a similar result obtained in [12], where all MAP
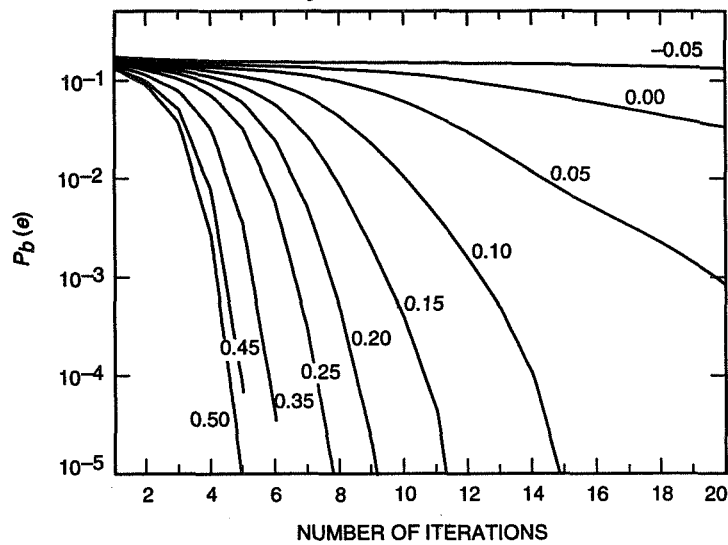
Fig. 8. Convergence of turbo coding: bit-error probability versus number of iterations for various E_b/N_0 using the SW2-BCJR algorithm.
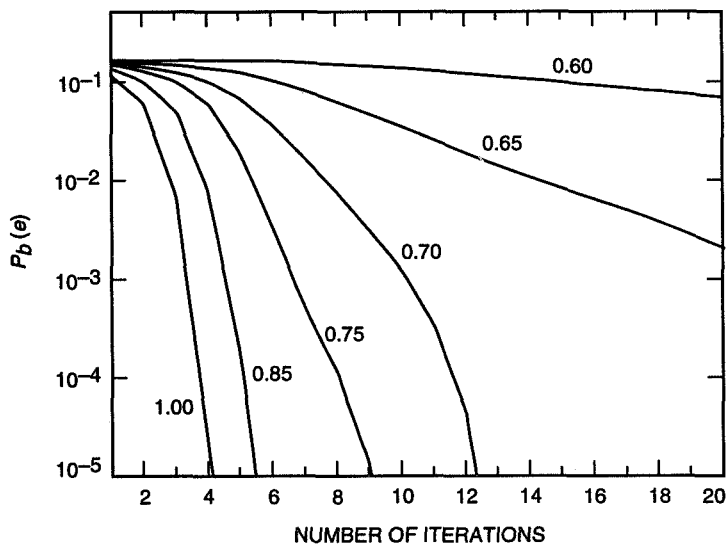
Fig. 9. Convergence of turbo coding: bit-error probability versus number of iterations for various E_b/N_0 using the SWAL2-BCJR algorithm.

algorithms were of the block type. The penalty is completely attributable to the approximation of the sum of exponentials described in Section V.B. To verify this, we have used a SW2-BCJR and compared its results with the optimum block BCJR, obtaining the same results.

Finally, in Figs. 11 and 12, we plot the number of iterations needed to obtain a given bit-error probability versus the bit signal-to-noise ratio, for the two algorithms. These curves provide information on the delay incurred to obtain a given reliability as a function of the bit signal-to-noise ratio.
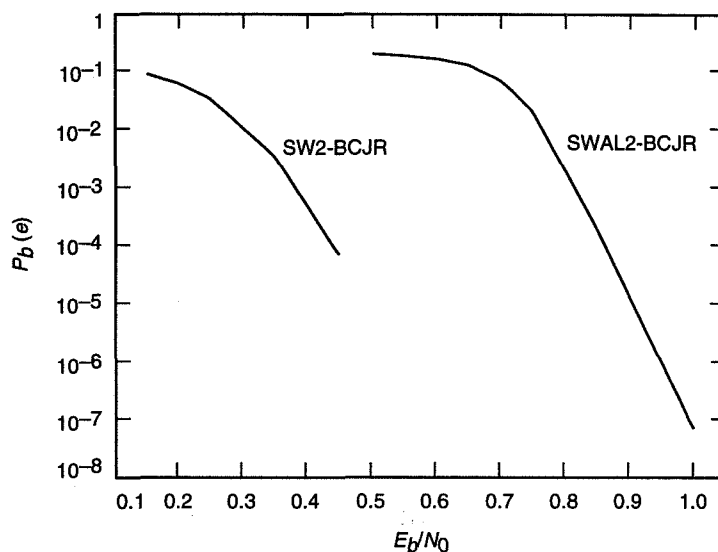
Fig. 10. Bit-error probability as a function of the bit signal-to-noise ratio using the SW2-BCJR and SWAL2-BCJR algorithms with five iterations.
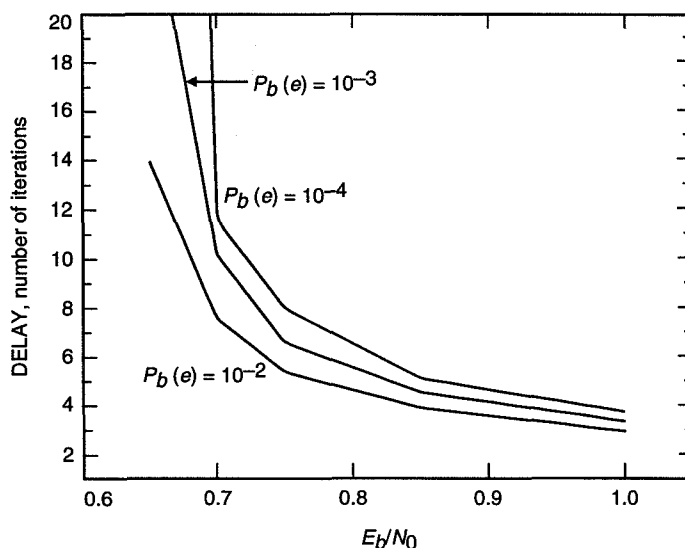
Fig. 11. Number of iterations to achieve several bit-error probabilities as a function of the bit signal-to-noise ratio using the SWAL2-BCJR algorithm.

IX. Conclusions

We have described two versions of a simplified maximum a posteriori decoding algorithm working in a sliding window form, like the Viterbi algorithm. The algorithms can be used as a building block to decode continuously transmitted sequences obtained by parallel concatenated codes, without requiring code trellis termination. A heuristic explanation of how to embed the maximum a posteriori algorithms into the iterative decoding of parallel concatenated codes was also presented. Finally, the performances of the two algorithms were compared on the basis of a powerful rate 1/3 parallel concatenated code.
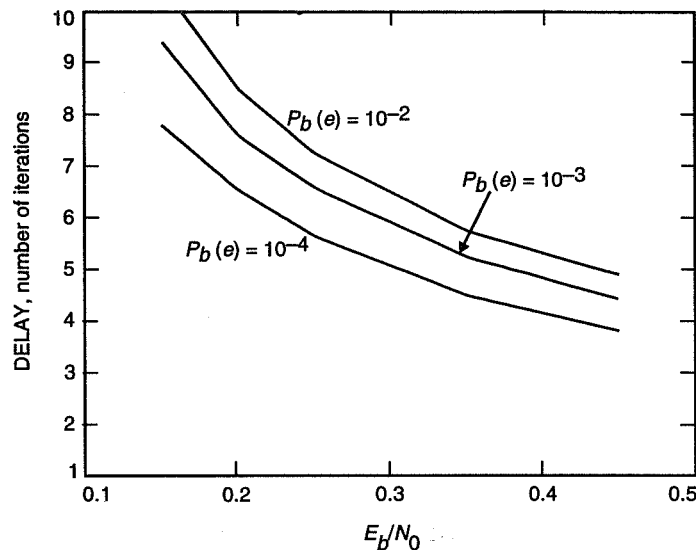
Fig. 12. Number ot iterations to achieve several bit-error probabilities as a function of the bit signal-to-noise ratio using the SW2-BCJR algorithm.

Acknowledgment

References

[1] S. Benedetto, E. Biglieri, and V. Castellani, *Digital Transmission Theory*, New York: Prentice-Hall, 1987.

[2] K. Abend and B. D. Fritchman, "Statistical Detection for Communication Channels With Intersymbol Interference," *Proceedings of IEEE*, vol. 58, no. 5, pp. 779–785, May 1970.

[3] L. R. Bahl, J. Cocke, F. Jelinek, and J. Raviv, "Optimal Decoding of Linear Codes for Minimizing Symbol Error Rate," *IEEE Transactions on Information Theory*, pp. 284–287, March 1974.

[4] G. D. Forney, Jr., *Concatenated Codes*, Cambridge, Massachusetts: Massachusetts Institute of Technology, 1966.

[5] V. V. Ginzburg, "Multidimensional Signals for a Continuous Channel," *Probl. Peredachi Inform.*, vol. 20, no. 1, pp. 28–46, January 1984.

[6] C. Berrou, A. Glavieux, and P. Thitimajshima, "Near Shannon Limit Error-Correcting Coding and Decoding: Turbo-Codes," *Proceedings of ICC'93*, Geneva, Switzerland, pp. 1064–1070, May 1993.

[7] N. Seshadri and C.-E. W. Sundberg, "Generalized Viterbi Algorithms for Error Detection With Convolutional Codes," *Proceedings of GLOBECOM'89*, vol. 3, Dallas, Texas, pp. 43.3.1–43.3.5, November 1989.

[8] J. Hagenauer and P. Hoeher, "A Viterbi Algorithm With Soft-Decision Outputs and Its Applications," *Proceedings of GLOBECOM'89*, Dallas, Texas, pp. 47.1.1–47.1.7, November 1989.

[9] Y. Li, B. Vucetic, and Y. Sato, "Optimum Soft-Output Detection for Channels With Intersymbol Interference," *Trans. on Information Theory*, vol. 41, no. 3, pp. 704–713, May 1995.

[10] S. S. Pietrobon and A. S. Barbulescu, "A Simplification of the Modified Bahl Algorithm for Systematic Convolutional Codes," *Proceedings of ISITA'94*, Sydney, Australia, pp. 1073–1077, November 1994.

[11] U. Hansson and T. Aulin, "Theoretical Performance Evaluation of Different Soft-Output Algorithms," *Proceedings of ISITA'94*, Sydney, Australia, pp. 875–880, November 1994.

[12] P. Robertson, E. Villebrun, and P. Hoeher, "A Comparison of Optimal and Sub-Optimal MAP Decoding Algorithms Operating in the Log Domain," *Proceedings of ICC'95*, Seattle, Washington, pp. 1009–1013, June 1995.

[13] D. Divsalar and F. Pollara, "Turbo Codes for PCS Applications," *Proceedings of ICC'95*, Seattle, Washington, pp. 54–59, June 1995.

[14] *CAS 5093 Turbo-Code Codec*, 3.7 ed., data sheet, Chateaubourg, France: Comatlas, August 1994.

[15] S. Benedetto and G. Montorsi, "Performance of Turbo Codes," *Electronics Letters*, vol. 31, no. 3, pp. 163–165, February 1995.

[16] S. S. Pietrobon, "Implementation and Performance of a Serial MAP Decoder for Use in an Iterative Turbo Decoder," *Proceedings of ISIT'95*, Whistler, British Columbia, Canada, pp. 471, September 1995.
Also http://audrey.levels.unisa.edu.au/itr-users/steven/turbo/ISIT95ovh2.ps.gz

[17] D. Divsalar, S. Dolinar, R. J. McEliece, and F. Pollara, "Transfer Function Bounds on the Performance of Turbo Codes," *The Telecommunications and Data Acquisition Progress Report 42-122, April–June 1995*, Jet Propulsion Laboratory, Pasadena, California, pp. 44–55, August 15, 1995.
http://edms-www.jpl.nasa.gov/tda/progress_report/42-122/122A.pdf

[18] S. Benedetto and G. Montorsi, " Design of Parallel Concatenated Convolutional Codes," to be published in *IEEE Transactions on Communications*, 1996.

[19] D. Divsalar and F. Pollara, "Multiple Turbo Codes," *Proceedings of IEEE MILCOM95*, San Diego, California, November 5–8, 1995.

[20] D. Divsalar and F. Pollara, "On the Design of Turbo Codes," *The Telecommunications and Data Acquisition Progress Report 42-123, July–September 1995*, Jet Propulsion Laboratory, Pasadena, California, pp. 99–121, November 15, 1995.
http://edms-www.jpl.nasa.gov/tda/progress_report/42-123/123D.pdf

[21] S. A. Barbulescu, "Iterative Decoding of Turbo Codes and Other Concatenated Codes," Ph.D. Dissertation, University of South Australia, August 1995.

[22] J. Lodge, R. Young, P. Hoeher, and J. Hagenauer, "Separable MAP 'Filters' for the Decoding of Product and Concatenated Codes," *Proceedings of ICC'93*, Geneva, Switzerland, pp. 1740–1745, May 1993.

Appendix

Circuits to Implement the MAP Algorithm for Decoding Rate 1/*n* Component Codes of a Turbo Code

In this appendix, we show the basic circuits required to implement a serial additive MAP algorithm for both block log-BCJR and SW-log-BCJR. Extension to a parallel implementation is straightforward. Figure A-1 shows the implementation[9] of Eq. (18) for the forward recursion using a lookup table for evaluation of $\log(1 + e^{-x})$, and subtraction of $\max_j\{A_k(S_j)\}$ from $A_k(S_i)$ is used for normalization to prevent buffer overflow.[10] The circuit for maximization can be implemented simply by using a comparator and selector with feedback operation. Figure A-2 shows the implementation of Eq. (19) for the backward recursion, which is similar to Fig. A-1. A circuit for computation of $\log(P_k(u|\mathbf{y}))$ from Eq. (4) using Eq. (20) for final computation of bit reliability is shown in Fig. A-3. In this figure, switch 1 is in position 1 and switch 2 is open at the start of operation. The circuit accepts $\Sigma_k(S_i, u)$ for $i = 1$, then switch 1 moves to position 2 for feedback operation. The circuit performs the operations for $i = 1, 2, \cdots, N$. When the circuit accepts $\Sigma_k(S_i, u)$ for $i = N$, switch 1 goes to position 1 and switch 2 is closed. This operation is done for $u = 1$ and $u = 0$. The difference between $\log(P_k(1|\mathbf{y}))$ and $\log(P_k(0|\mathbf{y}))$ represents the reliability value required for turbo decoding, i.e., the value of L_k in Eq. (35).
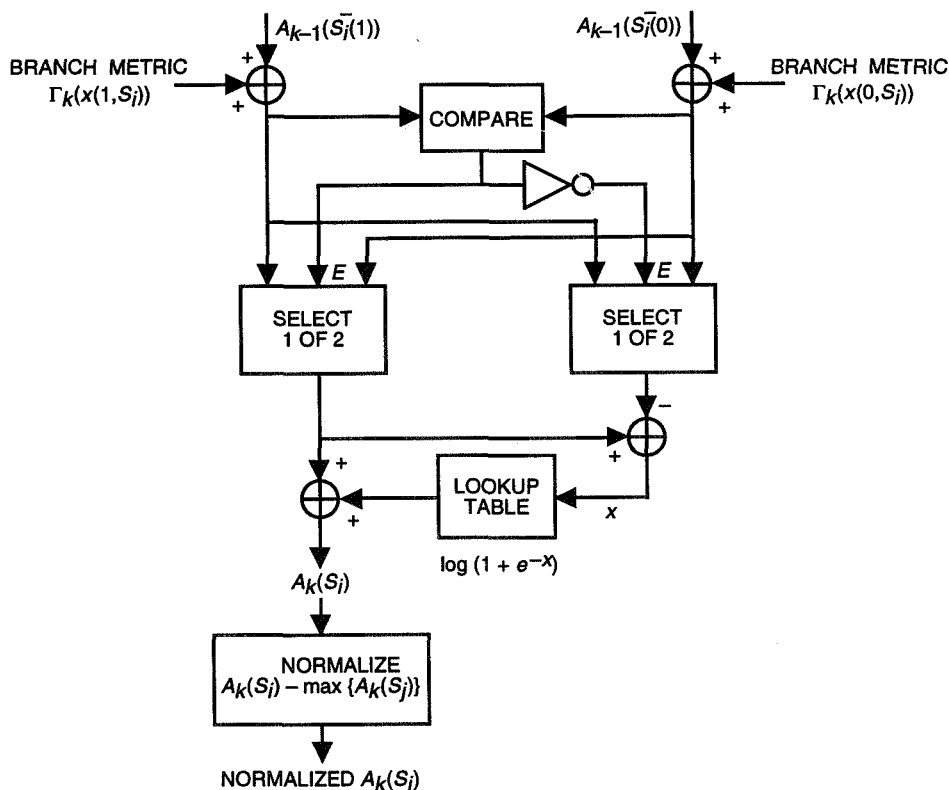
Fig. A-1. Basic structure for forward computation in the log-BCJR MAP algorithm.

---

[9] For feed-forward and nonconventional recursive convolutional codes, the notations in Fig. A-1 should be changed according to Footnotes 2 and 5.

[10] Simpler normalization can be achieved by monitoring the two most significant bits. When both of them are one, then we reset all the most significant bits to zero. This method increases the bit representation by an additional 2 bits.

$B_{k+1}(S_j^+(1))$ $B_{k+1}(S_j^+(0))$

BRANCH METRIC
$\Gamma_{k+1}(x(S_j,1))$

BRANCH METRIC
$\Gamma_{k+1}(x(S_j,1))$

COMPARE

E   E

SELECT
1 OF 2

SELECT
1 OF 2

LOOKUP
TABLE   x

$B_k(S_j)$

$\log(1 + e^{-x})$

NORMALIZE
$B_k(S_j) - \max\{B_k(S_j)\}$

NORMALIZED $B_k(S_j)$
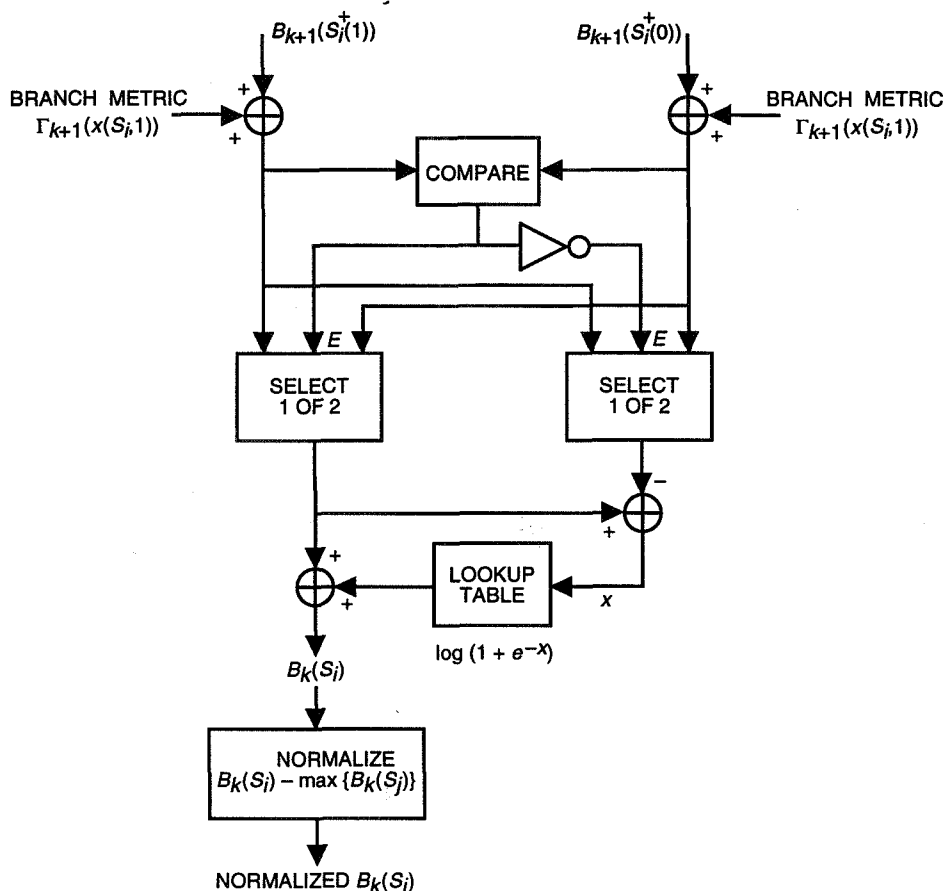
Fig. A-2. Basic structure for backward computation in the log-BCJR MAP algorithm.

We propose two simplifications to be used for computation of $\log(1 + e^{-x})$ without using a lookup table.

Approximation 1: We used the approximation $\log(1 + e^{-x}) \approx -ax + b$, $0 < x < b/a$ where $b = \log(2)$, and we selected $a = 0.3$ for the simulation. We observed about a 0.1-dB degradation compared with the full MAP algorithm for the code described in Section VIII. The parameter a should be optimized, and it may not necessarily be the same for the computation of Eq. (18), Eq. (19), and $\log(P_k(u|\mathbf{y}))$ from Eq. (4) using Eq. (20). We call this "linear" approximation.

Approximation 2: We take

$$\log(1 + e^{-x}) \approx \begin{cases} 0 & \text{if } x > \eta \\ c & \text{if } x < \eta \end{cases}$$

We selected $c = \log(2)$ and the threshold $\eta = 1.0$ for our simulation. We observed about a 0.2-dB degradation compared with the full MAP algorithm for the code described in Section VIII. This threshold should be optimized for a given SNR, and it may not necessarily be the same for the computation of Eq. (18), Eq. (19), and $\log(P_k(u|\mathbf{y}))$ from Eq. (4) using Eq. (20). If we use this approximation, the log-BCJR algorithm can be built based on addition, comparison, and selection operations without requiring a lookup table, which is similar to a Viterbi algorithm implementation. We call this "threshold" approximation. At most, 8- to 10-bit representation suffices for all operations (see also [12] and [16]).
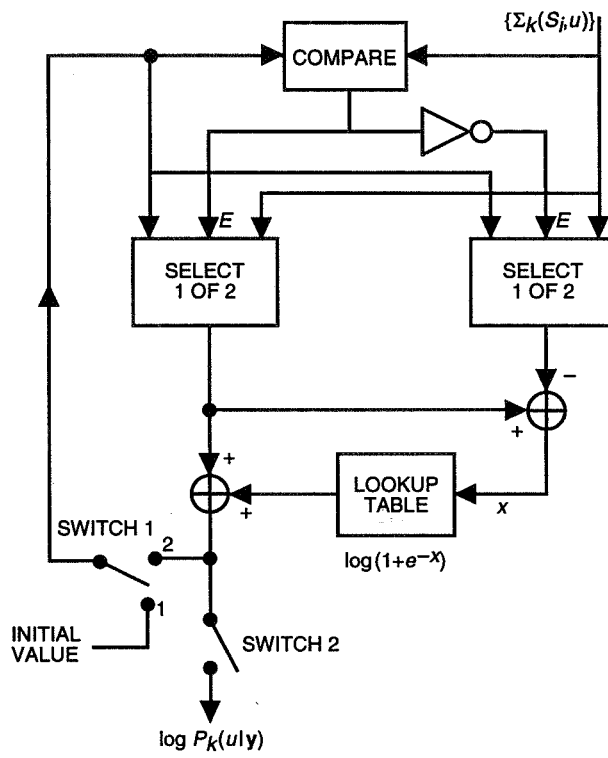
Fig. A-3. Basic structure for bit reliability computation in the log-BCJR MAP algorithm.

Progressive Transmission and Compression of Images

A. B. Kiely
Communications Systems and Research Section

We describe an image data compression strategy featuring progressive transmission. The method exploits subband coding and arithmetic coding for compression. We analyze the Laplacian probability density, which closely approximates the statistics of individual subbands, to determine a strategy for ordering the compressed subband data in a way that improves rate-distortion performance. Results are presented for a test image.

I. Introduction

An image data compression system that uses progressive transmission is one that allows a user to reconstruct successively higher fidelity versions of an image as data are received. The goal of progressive transmission is thus not only efficient overall compression, but efficient compression at every step.

If the data rate available for image transmission is unexpectedly low, or if the volume of compressed data exceeds expectations, the available rate will be used to its full extent, to provide nearly the highest-fidelity image possible given the rate constraint. Alternatively, if the available rate exceeds expectations, it will be possible to send higher-resolution images than originally planned. In this sense, progressive transmission strategies are robust with respect to the available data rate.

In situations where the reverse channel can be used, data compression can be combined with advanced communications strategies to increase the volume of data returned. The use of retransmission schemes is one example of such a strategy [8]. Progressive transmission gives another method, because it provides the ability to quickly view low- or medium-resolution previews of an image, making efficient browsing possible. A user can decide whether to continue the transmission of the full image or proceed to the next image. This makes more efficient use of the channel because images of less value are not transmitted at full resolution. This is particularly beneficial to deep-space missions with high data volume and severe rate constraints.

II. Progressive Transmission and Rate-Distortion Theory

For a given source and distortion metric, we are interested in the trade-off between the rate (usually measured in average number of bits/sample) and distortion. Some of the rate-distortion functions of interest include

(1) The rate-distortion limit. This is the theoretical minimum distortion as a function of the average number of bits used to describe the source [2]. This describes the optimum performance obtainable, ignoring constraints such as speed and complexity, and is computable only if the source statistics are known.

(2) The rate-distortion performance achievable by a particular technique.

(3) The rate-distortion performance "progressively" achievable by a particular progressive transmission technique. This is the performance obtained by measuring the rate and distortion of the reconstructed versions of the data at each stage of the transmission.

In theory, we can select a "target" rate-distortion limit point that represents the rate and distortion when all of the compressed data are transmitted. Ideally, using progressive transmission, at every point in the transmission we would like to be as close as possible to the rate-distortion limit. Unfortunately, it is not always possible to meet the target and have all of the points leading up to the target lie along the rate-distortion limit [4].

Equitz and Cover showed that it is possible to meet the rate-distortion limit progressively when solutions to the rate-distortion problem can be written as a Markov chain [4]. Such a source is called "successively refinable." Whether or not a source is successively refinable depends not only on the source statistics but also on the distortion metric selected. For example, a Laplacian source is successively refinable with respect to mean absolute error but, in general, not with respect to other metrics [4]. Even if a source is successively refinable, the optimal strategy for refinement may be unwieldy. Fortunately, even when a source is not successively refinable, the penalty for progressive transmission may be small.

An example follows: Under mean square error (MSE) distortion, a memoryless Gaussian source with variance σ^2 has a rate-distortion limit $MSE = \sigma^2 2^{-2R}$, where R is the rate in bits [2, p. 99]. In a practical source coding system, we might be willing to sacrifice performance in exchange for the simplicity of using, say, a 6-bit uniform scalar quantizer, where each quantizer interval is identified by a 6-bit codeword, and each codeword is compressed by arithmetic coding. For the Gaussian source, this produces a different rate-distortion curve parameterized by the quantizer step size. Both rate-distortion functions are shown in Fig. 1.

Suppose we wish to transmit 24 independent and identically distributed Gaussian samples quantized using the 6-bit uniform quantizer, and we select a target rate of 4 bits/sample, which corresponds to
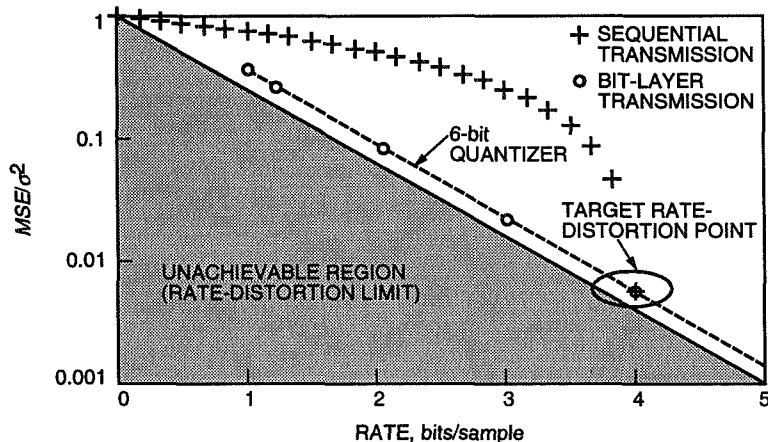
Fig. 1. Some rate-distortion functions associated with a quantized Gaussian source.

$MSE/\sigma^2 \approx 5.56 \times 10^{-3}$. Figure 1 shows the progressive rate-distortion performance obtained if we transmit the arithmetic encoded 6-bit quantized samples sequentially. Another option is to reorder the codeword bits before arithmetic coding so that the 24 most-significant bits of the samples are compressed and transmitted first, followed by the next most significant bit from each codeword, and so on. Figure 1 illustrates that although this bit-layer strategy ultimately achieves the same target rate-distortion point as sequential transmission, its progressive performance is superior.

Although in this article we focus on the MSE distortion measure, image quality is subjective and depends on the application. Neither a thousand words nor a single scalar metric can accurately describe the "quality" of an image.

III. Subband Coding

A progressive quantization and compression scheme, such as the technique illustrated in the example of Section II, can be used in combination with a decorrelating transform. In particular, we use a subband coding stage prior to quantization and compression. Unlike block-transform-based methods, such as the discrete cosine transform used in the Joint Photographic Experts Group (JPEG) algorithm, subband coding does not suffer from blockiness artifacts even when used in progressive transmission. For a general description of image compression via subband coding, see [9].

A two-band subband decomposition uses high-pass and low-pass digital filters to decompose a data sequence into high and low subbands, each containing half as many points as the original sequence. This is done independently on horizontal and vertical lines of the image. Because image signal energy is usually concentrated in the lower frequencies, the lowest subband may be repeatedly decomposed. Figure 2 illustrates a two-stage decomposition of the test image.

The filters used for the tests in this article[1] are eighth-order quadrature mirror filters from [1, p. 267]. Because quadrature mirror filters are orthogonal, the MSE introduced by quantization in the transform domain is equal to the MSE of the reconstructed image. We can use this fact to improve the progressive rate-distortion performance by carefully selecting the order in which blocks of information from each subband are transmitted. At each step, we transmit the set of compressed bits giving the largest reduction in MSE per bit. Nonorthogonal filters have the potential to offer improved performance for the same complexity [7]; however, when such filters are used, the analysis in the subsequent sections no longer applies.

The filters are implemented using circular convolution, i.e., each data block is periodically extended before filtering [6]. At the edges of data blocks, this often produces high-frequency components that are processed separately from the rest of the subband data because they are not as easily compressed. Since these components form a small fraction of the image, the penalty for inefficient compression is small. An elegant alternative to circular convolution is to use interpolation at the edges [10]. Since the improvement in rate-distortion performance is small, this alternative is not investigated in this article, though it could be implemented without significant change in the progressive transmission strategy described here.

Each subband generally has a probability density function (PDF) quite close to Laplacian.[2] Figure 3 illustrates an empirical PDF for one of the subbands of the test image. In the following sections, we will analyze a Laplacian source to determine a strategy for the transmission order of the subband data.

---

[1] For this article, we are more concerned with the overall compression and transmission strategy than with the selection of a particular filter.

[2] The lowest subband may be less well behaved and can often be compressed more efficiently after taking differences, although this process makes progressive transmission more difficult. Some performance improvement may be possible by revising the coding strategy used for the lowest subband.
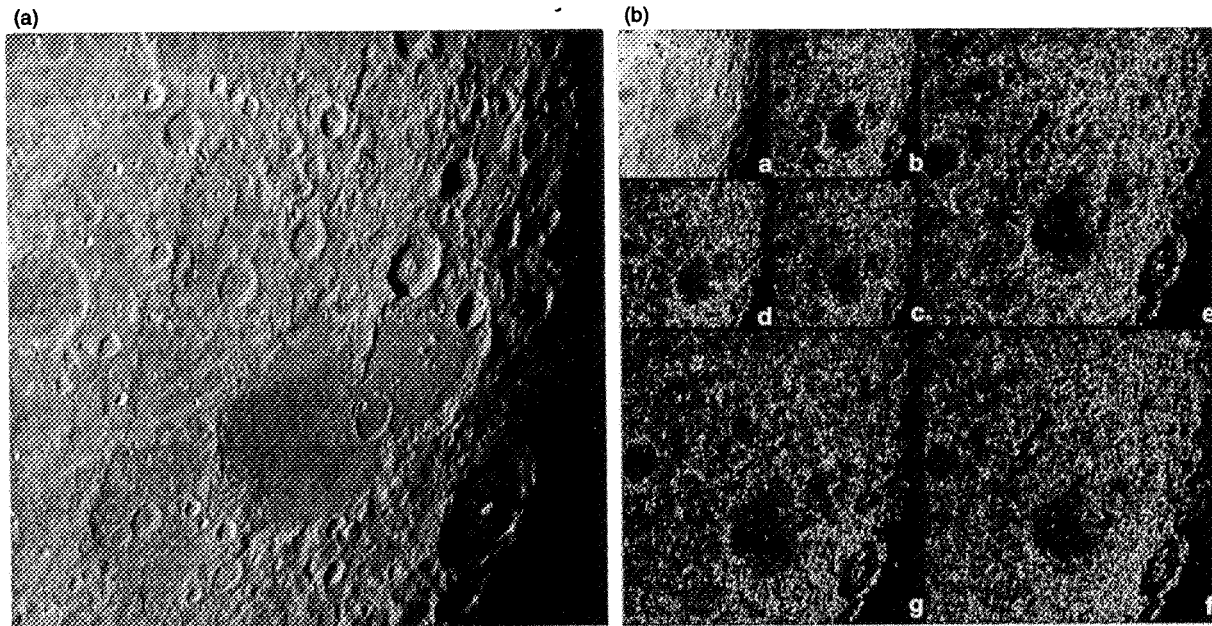
Fig. 2. Two-stage decomposition: (a) original image and (b) image decomposed into subbands labeled a–g (contrast enhanced).
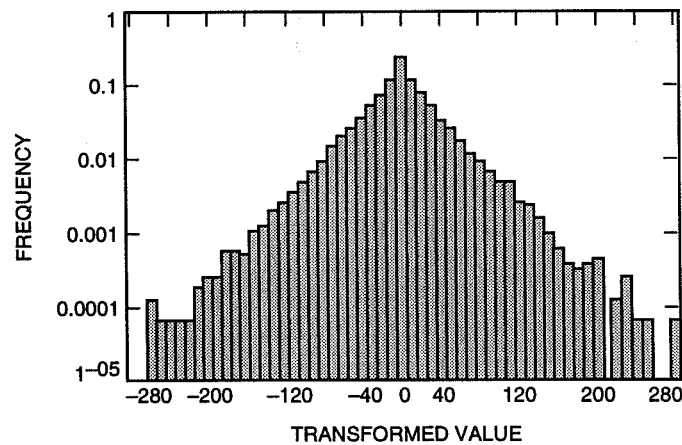
Fig. 3. Empirical PDF of the subband labeled "b" in Fig. 2.

IV. A Block-Oriented Progressive Transmission Scheme

A simple technique for progressive transmission using subband coding is to transmit the subbands in order from lowest to highest frequency [9]. Moderate quality images can be reconstructed even when only the lowest subband has been received, because signal energy in images is usually more concentrated in the lower frequencies. However, the ability to transmit each subband progressively provides an added dimension that can improve the progressive rate-distortion performance because we can switch between the subbands during transmission. In this section, we describe a progressive transmission method for an individual subband.

The progressive transmission scheme we use is bit-wise arithmetic coding [5]. A source sample is quantized, and each quantizer interval is identified by a b-bit codeword. Figure 4 illustrates the codeword
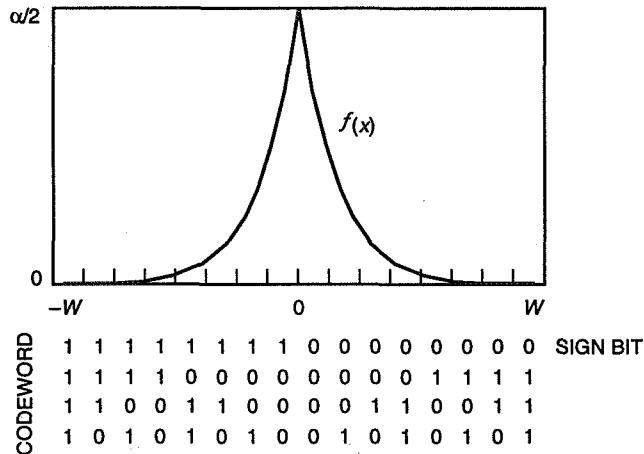
Fig. 4. Codeword assignment for a 4- bit quantizer.

assignment for a 4-bit uniform scalar quantizer along with the PDF $f(x)$ for a Laplacian source with variance $2/\alpha^2$. We can see that the bit assignment scheme is progressive—deleting i bits from the end of each codeword produces the same effect as using a lower resolution $b - i$ bit quantizer. The codeword assignment scheme also ensures that, for a Laplacian source, a zero is more likely in every bit position, with the exception of the "sign" bit.

The codewords corresponding to the quantized coefficients of a subband are grouped together. The ith bit layer, which consists of the ith bit from each codeword in the group, is compressed using the block-adaptive binary arithmetic encoder described in [5]. Each layer is compressed independently, i.e., the arithmetic encoder uses an estimate of the unconditional probability of a zero at each layer.

Slight modification of the quantizer can improve the progressive rate-distortion performance. Figure 5 shows three different quantizer options (illustrated for 3-bit quantizers). We can evaluate the rate and MSE distortion of each quantizer using the results of Appendix A. In each case, the quantizer range $[-W, W]$, step size Δ, and number of bits b are related by

$$\Delta = W2^{1-b}$$

A continuous rate-distortion performance curve for a quantizer can be obtained by fixing b and varying Δ. Figure 6 shows several such curves for the quantizer illustrated in Fig. 5(c). Decreasing Δ increases rate and lowers distortion until a minimum distortion point is reached. After this point, the distortion increases and the quantizer becomes inefficient. Ordinarily this inefficient region is not shown.

When we use a quantizer progressively, the range is fixed, but the number of bits b increases, reducing step size by half for each successive bit layer transmitted. The points in Fig. 6 illustrate progressive rate-distortion performance. We observe in the figure that as b becomes large, the distortion does not approach zero, but is dominated by the contribution from the overload regions. As this happens, the progressive rate-distortion performance flattens, as points are lying along the inefficient regions of the rate-distortion curves. This floor is easy to find and depends only on the range and the Laplacian parameter α. We find from Eq. (A-1) in Appendix A that

$$\lim_{b \to \infty} \frac{MSE}{\sigma^2} = e^{-\alpha W}$$
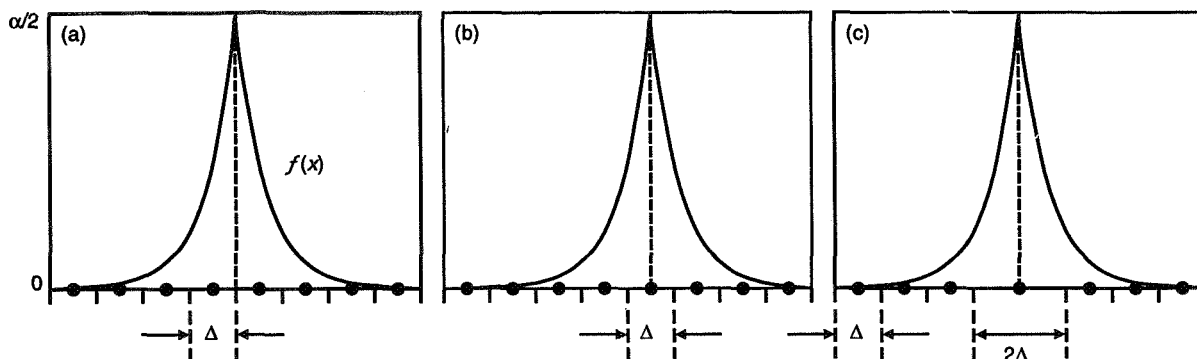
Fig. 5. Different quantizer options: (a) uniform symmetric with bin boundary at origin, (b) uniform with reconstruction
point at origin, and (c) almost uniform with enlarged center bin.
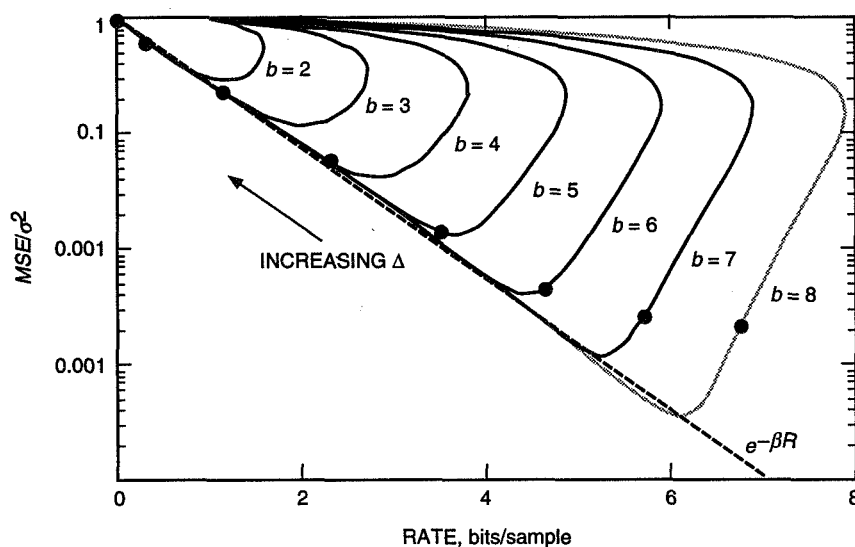
Fig. 6. Rate-distortion performance curves for the quantizer of Fig. 5(c).

when the reconstruction point of each interval is the interval midpoint.[3] In a real application, the range of possible values is limited by instrument dynamic range and the filters chosen, so the MSE floor can be avoided by making the quantizer range sufficiently large.

Figure 7 compares the performance of each quantizer option of Fig. 5. The rate-distortion curves shown correspond to 8-bit quantizers. The progressive performance points are obtained by transmitting bit-layers with a target rate of 6 bits/sample. In Appendix A, we derive rate-distortion functions used to compare the quantizers.

Quantizer (a), a symmetric uniform quantizer, has poor performance at low bit rates, because the sign bit is incompressible; hence, rates below 1 bit/sample are not achievable. Quantizer (b) is obtained by shifting quantizer (a) by $\Delta/2$, so that a reconstruction point is present at the origin, as done in [5]. When Δ is large, low rates are achievable, and the performance obtained by varying Δ is close to the rate-distortion limit. However, when this quantizer is used progressively and the step size is small, the entropy of the sign bit approaches 1. Thus, the progressive performance is generally poor at low bit rates.

---

[3] This quantity is reduced by half when the centroid of each quantizer interval is used (see Eq. (A-2) in Appendix A).
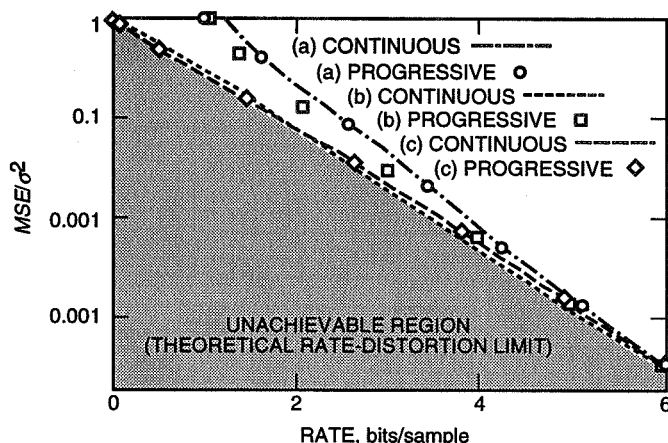
Fig. 7. Rate-distortion performance of different 8-bit quantizers. The continuous curves are obtained by varying the quantizer step size Δ while keeping the number of bits fixed. The progressive performance points are obtained by calculating the rate-distortion performance after the transmission of each bit layer.

To overcome these problems, we use quantizer (c) with range $[-W, W]$, which effectively combines the two center regions of quantizer (a), in combination with a different transmission order. We do not initially transmit the sign bit layer, but rather we begin by transmitting the next layer (after arithmetic coding). Then, for each codeword where a "1" appeared (i.e., each quantized value in the range $[-W, -W/2] \cup [W/2, W]$), the sign bit is transmitted. Then the next layer is transmitted, followed by the sign bits for each codeword representing a quantized value in the range $[-W/2, -W/4] \cup [W/4, W/2]$. This continues at each layer. Finally, if the quantized value lies in the range $[-W2^{1-b}, W2^{1-b}]$ (the two centermost quantization points), the sign bit is never transmitted. In progressive reconstruction, for any quantized value for which no sign bit was received, the origin is used as the reconstruction point. The advantage of this transmission order is that we delay the transmission of the sign bits, which are not easily compressible. Figure 7 shows that this technique offers improved progressive performance compared to quantizers (a) and (b) and is, in fact, close to the rate-distortion limit for a Laplacian source with MSE distortion, which is computed in Appendix B.

V. Ordering the Compressed Subband Data

In the previous section, we described a progressive transmission strategy that can be used for each subband. This strategy allows us to interrupt transmission of a subband to transmit data from another subband. In this section, we describe a method for choosing the order of transmission of subband data designed to improve the progressive rate-distortion performance.

At any point in transmission, we wish to transmit the next (compressed) layer of bits from the subband that gives the largest reduction in MSE per transmitted bit. Thus, we select the bit layer from the subband with a rate-distortion curve whose slope is minimum. Using the analytical expressions for rate and distortion of the quantizer (see the Appendices) is rather intractable, so we use the approximation

$$MSE \approx \sigma^2 e^{-\beta R} = \frac{2}{\alpha^2} e^{-\beta R}$$

where R is the rate in bits, and $\beta = 1.3$. This approximation is shown in Fig. 6. Using this approximation, omitting some algebraic details, we have the following subband selection strategy: Transmit the next bit layer from the subband with parameter α and rate R that minimizes $\ln \alpha + \beta R/2$.

To apply this strategy, we need to estimate the Laplacian parameter α for each subband or, equivalently, to estimate the mean absolute value $1/\alpha$. For each subband, we update the estimate at each bit layer transmitted. The estimate is created by keeping track of the frequency of sign bits transmitted at each bit layer, which is a quantity already computed in the compression stage.
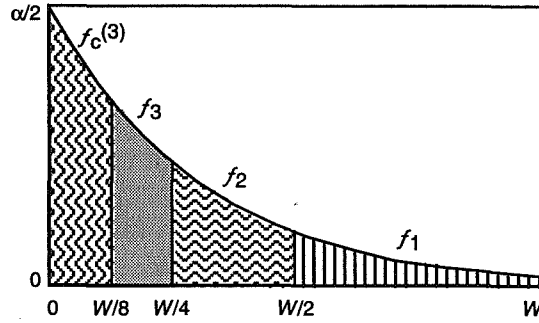
Fig. 8. Frequencies used to estimate the Laplacian parameter α at the third bit layer.

Let f_i denote the frequency of sign bits transmitted at the ith layer, and $f_c^{(i)}$ denote the frequency of the center region at the ith layer. This is illustrated in Fig. 8. For a Laplacian distribution with parameter α, at the ith bit layer, we expect

$$
f_j = \begin{cases} e^{-\alpha W/2}, & j = 1 \\ e^{-\alpha W 2^{-j}} - e^{-\alpha W 2^{1-j}}, & 1 < j \leq i \end{cases}
$$

$$
f_c^{(i)} = 1 - e^{-\alpha W 2^{-i}}
$$

which gives parameter estimates of

$$
\hat{\alpha}_j = \begin{cases} -\dfrac{2}{W} \ln f_1, & j = 1 \\ -\dfrac{2^j}{W} \ln \left[\dfrac{1 \pm \sqrt{1 - 4f_j}}{2} \right], & j > 1, f_j \leq 1/4 \\ \dfrac{2^j}{W} \ln 2, & j > 1, f_j > 1/4 \end{cases} \tag{1}
$$

$$
\hat{\alpha}_c^{(i)} = -\frac{2^i}{W} \ln \left(1 - f_c^{(i)} \right)
$$

where, in Eq. (1), we choose the estimator closest to $\hat{\alpha}_c^{(i)}$. For our overall estimate of the mean absolute value at the ith bit layer, we take the weighted average of the above estimators:

$$
\frac{1}{\hat{\alpha}} = \frac{f_c^{(i)}}{\hat{\alpha}_c^{(i)}} + \sum_{j=1}^{i} \frac{f_j}{\alpha_j} \tag{2}
$$

If any of the f_i's are zero, we can assign any finite value to the corresponding $\hat{\alpha}_i$, since it will have no weight in Eq. (2).

Since the quantizer range may be quite large compared to the variance of a subband, it is common for the first few bit layers to consist entirely of zeros. For each subband, we first transmit an integer identifying the number of leading all-zero bit layers. This ensures that $\hat{\alpha}$ is always well defined.

VI. Results

Curve (a) in Fig. 9 illustrates the progressive rate-distortion performance on the test image obtained using the subband selection strategy described in Section V combined with the parameter estimates from Eq. (2). In the figure, we compare this performance to the more traditional progressive transmission method (transmitting the subbands sequentially from lowest to highest frequency), shown as curve (b), and the optimum transmission order (that obtained by testing every possible transmission order of the subband data), curve (c). We also show the performance of the graphic-in-line-format (GIF) compression technique, a progressive transmission method that has recently become popular in Web browsing software.

In Fig. 10, we show four intermediate reconstructed images obtained in progressive transmission. The rate-distortion points corresponding to these four images are shown in Fig. 9.
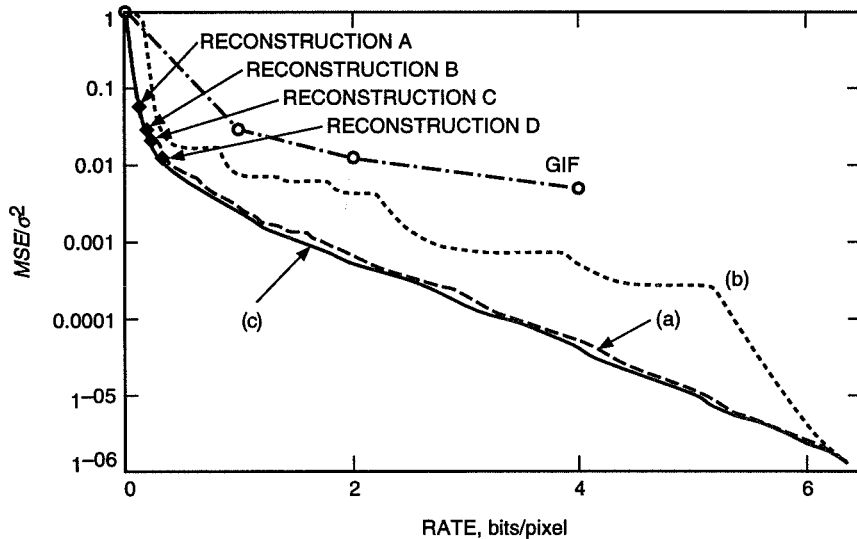
Fig. 9. Progressive rate-distortion performance on the test image using 12-bit quantizers on each subband. Curve (a) shows the performance obtained using the strategy described in Section V. Curve (b) is the performance obtained when we transmit the subbands in order from the lowest to the highest frequency. Curve (c) is the performance obtained if we choose the optimum subband bit layer at each step. The curve labled "GIF" corresponds to the performance obtained using the GIF progressive transmission technique. The images corresponding to the four labled reconstruction points are shown in Fig. 10.

VII. Conclusion

We have shown that careful selection of the quantization and compression strategy can significantly improve the progressive rate-distortion performance of a data compression system. The use of transforms such as subband coding can lead to further improvements, because they provide additional freedom in choosing the order in which the compressed data are transmitted.

When an effective progressive transmission scheme is used, the progressive rate-distortion performance may be good at every point in transmission. For image compression, this means that even if the rate
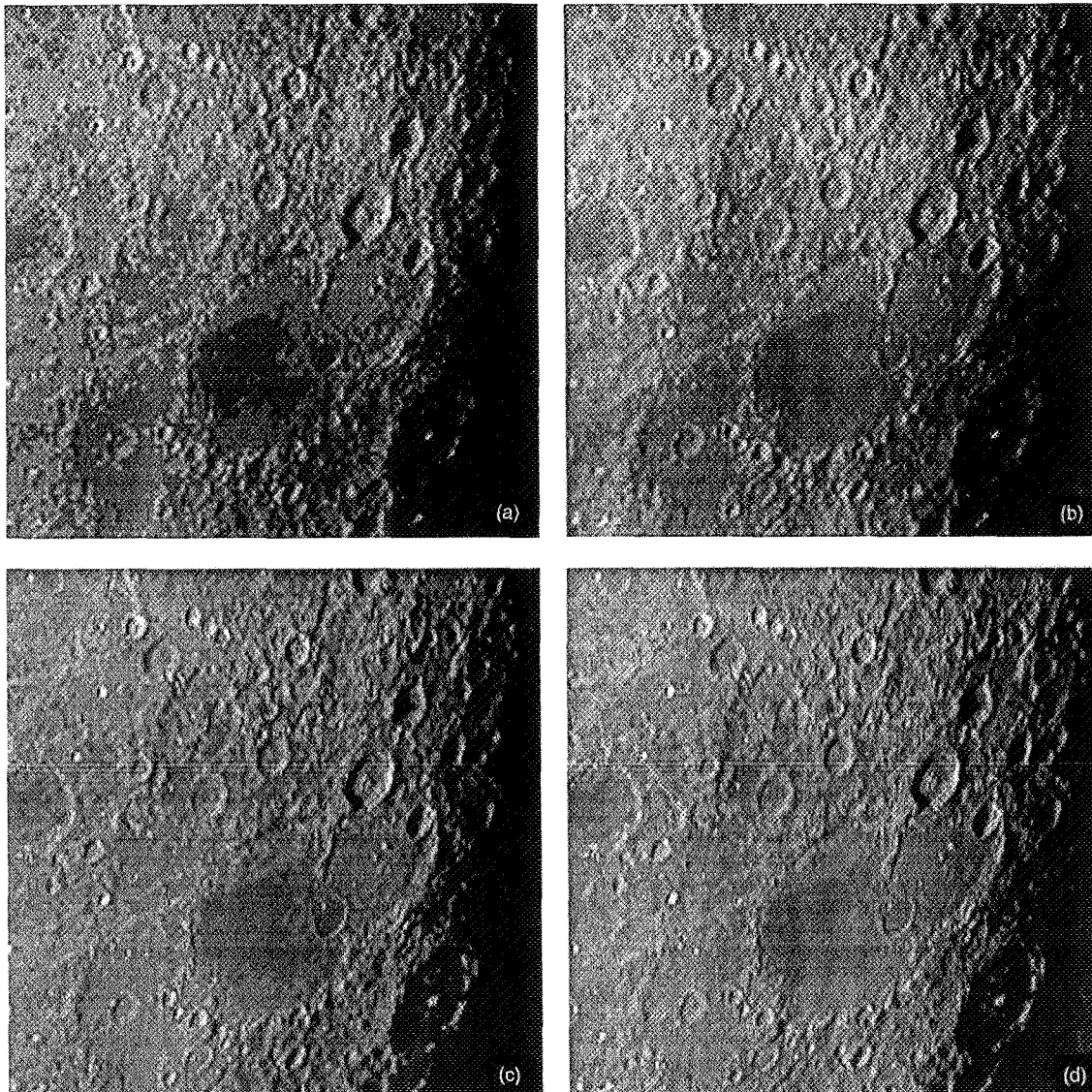
Fig. 10. Reconstructed images at various stages in the transmission. The savings compared to transmission of the original 8-bit image without compression are (a) 18.2, (b) 16.5, (c) 15.5, and (d) 13.9 dB, respectively.

constraints change during a mission, redesign of the compression strategy is not necessary. When the reverse channel can be used for browsing, the benefits of progressive transmission become even greater—we are not required to decide in advance the amount of resources devoted to a particular image.

It is interesting to consider the savings in dB that can be offered by lossy data compression. Suppose that 2:1 lossless compression is possible for the original image shown in Fig. 2. In this case, the lower-quality image of Fig. 10(d) could be obtained at a savings of approximately 10.9 dB. Alternatively, for the price of a single losslessly compressed image, we could obtain 12 images of quality comparable to that of Fig. 10(d).

References

[1] A. N. Akansu and R. A. Haddad, *Multiresolution Signal Processing*, San Diego, California: Academic Press, 1992.

[2] T. Berger, *Rate Distortion Theory: A Mathematical Basis for Data Compression*, Englewood Cliffs, New Jersey: Prentice-Hall, 1971.

[3] S. Dolinar, "Maximum-Entropy Probability Distributions Under L_p-Norm Constraints," *The Telecommunications and Data Acquisition Progress Report 42-104, October–December 1990*, Jet Propulsion Laboratory, Pasadena, California, pp. 74–87, February 15, 1991.

[4] W. H. R. Equitz and T. M. Cover, "Successive Refinement of Information," *IEEE Trans. Inform. Theory*. vol. 37, pp. 269–275, March 1991.

[5] A. B. Kiely, "Bit-Wise Arithmetic Coding for Data Compression," *The Telecommunications and Data Acquisition Progress Report 42-117, January–March 1994*, Jet Propulsion Laboratory, Pasadena, California, pp. 145–160, May 15, 1994.

[6] A. B. Kiely and F. Pollara, "A Seismic Data Compression System Using Subband Coding," *The Telecommunications and Data Acquisition Progress Report 42-121, January–March 1995*, Jet Propulsion Laboratory, Pasadena, California, pp. 242–251, May 15, 1995.
http://edms-www.jpl.nasa.gov/tda/progress_report/42-121/121J.pdf

[7] E. Majani, "Low-Complexity Wavelet Filter Design for Image Compression," *The Telecommunications and Data Acquisition Progress Report 42-119, July–September 1994*, Jet Propulsion Laboratory, Pasadena, California, pp. 181–200, December 15, 1994.
http://edms-www.jpl.nasa.gov/tda/progress_report/42-119/119E.pdf

[8] F. Pollara and L. Ekroot, "Analysis of Automatic Repeat Request Methods for Deep-Space Downlinks," *The Telecommunications and Data Acquisition Progress Report 42-122, April–June 1995*, Jet Propulsion Laboratory, Pasadena, California, pp. 66–83, August 15, 1995.
http://edms-www.jpl.nasa.gov/tda/progress_report/42-122/122L.pdf

[9] M. Rabbani and P. W. Jones, *Digital Image Compression Techniques*, Bellingham, Washington: SPIE Press, 1991.

[10] J. R. Williams and K. Amaratunga, *A Discrete Wavelet Transform Without Edge Effects Using Wavelet Extrapolation*, IESL Technical Report 95-02, Massachusetts Institute of Technology, Cambridge, Massachusetts, January 28, 1995.
http://www-iesl.mit.edu/pub_docs/Wavelets/15_FWT_poly-94.html

Appendix A

Performance of a Scalar Quantizer on a Laplacian Source

In this appendix, we analyze the rate-distortion performance of a Laplacian source with PDF $f(x)$ using a scalar quantizer that is nearly uniform. Consider the symmetric b-bit quantizer (with $2^b - 1$ intervals) shown in Fig. A-1. The reconstruction point of each interval may be the midpoint or the centroid of the interval.
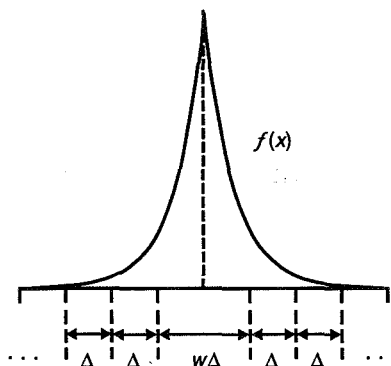
Fig. A-1. A symmetric scalar quantizer.

The normalized MSE obtained when this quantizer is used is

$$\frac{MSE}{\sigma^2} = \frac{\alpha^2}{2} \left[MSE_c + 2MSE_{ov} + 2 \sum_{i=0}^{2^{b-1}-3} MSE_i \right]$$

where MSE_c is the MSE contribution of the center region,

$$MSE_c = \frac{1}{\alpha^2} \left[2 - e^{-y} \left(y^2 + 2y + 2 \right) \right]$$

and $y = \alpha\Delta/2$. MSE_i is the MSE contribution of the region $[(w/2 + i)\Delta, (w/2 + i + 1)\Delta)$, $i = 0, 1, \cdots, 2^{b-1} - 3$,

$$MSE_i = \frac{e^{-y-si}}{2\alpha^2} \left[1 - e^{-s} + \frac{s^2}{1 - e^s} \right]$$

when the centroid is used, and

$$MSE_i = \frac{e^{-y-si}}{8\alpha^2} \left[(8 + s^2)(1 - e^{-s}) - 4s(1 + e^{-s}) \right]$$

when the midpoint is used, where $s = \alpha\Delta$. MSE_{ov} is the MSE of each overload region $\pm[(w/2 + 2^{b-1} - 2)\Delta, \infty)$,

$$MSE_{ov} = \frac{e^{s(2-M)}e^{-y}}{2\alpha^2}$$

when the centroid is used, and

$$MSE_{ov} = \left(\frac{s^2 - 4s + 8}{8\alpha^2}\right)e^{s(2-2^{b-1})}e^{-y}$$

when the midpoint is used.

Combining, we find that when midpoints are used,

$$\frac{MSE}{\sigma^2} = 1 - e^{-y}\left[\frac{1}{2}y(y+2) + \frac{1}{8}s(4-s) + \frac{s\left(1 - e^{s\left(2-2^{b-1}\right)}\right)}{e^s - 1}\right] \tag{A-1}$$

and when centroids are used,

$$\frac{MSE}{\sigma^2} = 1 - \frac{1}{2}e^{-y}\left[(y+1)^2 + \frac{s^2 e^s \left(1 - e^{s\left(2-2^{b-1}\right)}\right)}{(e^s - 1)^2}\right] \tag{A-2}$$

Next we compute the rate. The center region has probability $P_c = 1 - e^{-y}$; each overload region has probability $P_{ov} = (1/2)e^{-y}e^{s(2-2^{b-1})}$; and the region $[(w/2 + i)\Delta, (w/2 + i + 1)\Delta)$ has probability $(1/2)e^{-y-is}(1 - e^{-s})$. The entropy is

$$H = (e^{-y} - 1)\ln(1 - e^{-y}) + e^{-y}(y + \ln 2) + e^{-y}\left(1 - e^{s\left(2-2^{b-1}\right)}\right)\left[\frac{s}{e^s - 1} - \ln(1 - e^{-s})\right] \text{ nats}$$

Using the bit-wise transmission strategy described in Section IV, the sign bit has entropy of 1 bit but is not transmitted when the sample value lies in the center region; this contributes e^{-y} bits to the rate. If j denotes the bit layer index, with $j = 1$ corresponding to the least significant layer and $j = b$ the sign bit layer, then the probability that the jth bit is a 1 is

$$e^{s-y}\left(\frac{e^{-s2^{j-1}} + e^{-s2^{b-1}}}{1 + e^{-s2^{j-1}}}\right)$$

so the rate of bit-wise transmission is

$$R = e^{-y} + \sum_{j=0}^{b-2}\mathcal{H}_2\left[e^{s-y}\left(\frac{e^{-s2^j} + e^{-s2^{b-1}}}{1 + e^{-s2^j}}\right)\right] \text{ bits}$$

where $\mathcal{H}_2(x) \triangleq -\log_2 x - (1 - x)\log_2(1 - x)$ is the binary entropy function.

These expressions are used to compare the different quantizers in Section IV. We can also observe the losses resulting from the bit-wise transmission strategy and using the midpoint rather than the centroid of each quantizer interval. In fact, these losses are negligible, as can be seen by comparing the rate-distortion curves in Fig. 7.

Appendix B

Rate-Distortion Limit For a Laplacian Source With MSE Distortion

In this appendix, we derive the rate-distortion limit of a Laplacian source using a scalar quantizer with MSE distortion metric. A Laplacian source with parameter α has PDF $f(x) = (\alpha/2)e^{-\alpha|x|}$ and variance $\sigma^2 = 2/\alpha^2$. For a discussion of the mean absolute error distortion metric for this source, see [3].

The goal is to find the optimum (possibly infinite) scalar quantizer. Let the quantizer regions be $[t_i, t_{i+1})$, $i = \cdots, -1, 0, 1, 2, \cdots$. The MSE distortion of the quantizer is $MSE = \sum_{i=-\infty}^{\infty} MSE_i$, where MSE_i is the contribution to the MSE from the region $[t_i, t_{i+1})$ (assume $0 \leq t_i < t_{i+1}$; a similar analysis applies when this is not the case):

$$MSE_i = \int_{t_i}^{t_{i+1}} (x - c_i)^2 f(x)dx = \frac{e^{-\alpha t_i} - e^{-\alpha t_{i+1}}}{2\alpha^2} + \frac{(t_{i+1} - t_i)^2}{2(e^{\alpha t_i} - e^{\alpha t_{i+1}})} \qquad \text{(B-1)}$$

Here c_i is the centroid of the region (this choice minimizes MSE):

$$c_i = \frac{1}{P_i} \int_{t_i}^{t_{i+1}} xf(x)dx = \frac{1}{\alpha} + \frac{t_i e^{-\alpha t_i} - t_{i+1} e^{-\alpha t_{i+1}}}{e^{-\alpha t_i} - e^{-\alpha t_{i+1}}}$$

and $P_i = (1/2)(e^{-\alpha t_i} - e^{-\alpha t_{i+1}})$ is the probability of the region. The total entropy associated with the quantizer is $H = \sum_{i=-\infty}^{\infty} -P_i \ln P_i$, nats.

Consider what happens when we vary the threshold t_i:

$$\frac{\partial MSE}{\partial t_i} = \frac{(t_i - t_{i-1})}{2(e^{\alpha t_{i-1}} - e^{\alpha t_i})^2} \left[2e^{\alpha t_{i-1}} + e^{\alpha t_i}(\alpha t_i - \alpha t_{i-1} - 2) \right]$$

$$- \frac{(t_{i+1} - t_i)}{2(e^{\alpha t_i} - e^{\alpha t_{i+1}})^2} \left[-2e^{\alpha t_{i+1}} + e^{\alpha t_i}(\alpha t_{i+1} - \alpha t_i + 2) \right]$$

and

$$\frac{\partial H}{\partial t_i} = \frac{\alpha}{2e^{\alpha t_i}} \ln \left[\frac{e^{-\alpha t_i} - e^{-\alpha t_{i+1}}}{e^{-\alpha t_{i-1}} - e^{-\alpha t_i}} \right]$$

So by the chain rule, the slope of the rate-distortion curve (when varying t_i) is $\partial MSE/\partial H = (\partial MSE/\partial t_i)/\partial H/\partial t_i$. If the quantizer is locally uniform with step size Δ, i.e., $t_{i-1} = t_i - \Delta$, $t_{i+1} = t_i + \Delta$, then (omitting algebraic manipulations),

$$\frac{\partial MSE}{\partial H} = \frac{(2-s)e^s - 2 - s}{\alpha^2(e^s - 1)}$$

where $s = \alpha\Delta$. By the Kuhn–Tucker conditions, since this expression depends only on the normalized step size s, the optimal scalar quantizer is uniform (and infinite) on both sides of the origin and has the same step size on both sides.

Next, we need to determine the behavior of the quantizer near the origin. Suppose there is an arbitrary (possibly different) offset on each side of the origin. By symmetry, setting these two offsets equal will give a solution to the Kuhn–Tucker conditions. So we want to know the width of the center region relative to the normalized step size s.

Let the width of the center region be $w\Delta$. The center region has probability mass $1 - e^{-y}$, where $y = sw/2$, and makes MSE contribution

$$MSE_c = 2\int_0^{w\Delta/2} x^2 f(x)dx = \frac{1}{\alpha^2}\left[2 - \left(y^2 + 2y + 2\right)e^{-y}\right]$$

The right-hand side regions are $[(w/2 + i)\Delta, (w/2 + i + 1)\Delta)$, $i = 0, 1, 2, \cdots$. Using $t_i = (w/2 + i)\Delta$ and $t_{i+1} = (w/2 + i + 1)\Delta$ in Eq. (B-1) yields

$$MSE_i = \frac{e^{-si-y}}{2\alpha^2}\left[1 - e^{-s} + \frac{s^2}{1 - e^s}\right]$$

$$P_i = \frac{1}{2}e^{-si-y}(1 - e^{-s})$$

so the rate contribution is $R_i = -P_i \ln P_i = (1/2)e^{-si-y}(1 - e^{-s})\left[y + si + \ln 2 - \ln(1 - e^{-s})\right]$. The total MSE is

$$MSE = MSE_c + 2\sum_{i=0}^{\infty} MSE_i = \frac{1}{\alpha^2}\left\{2 + e^{-y}\left[\frac{s^2}{(1 - e^s)(1 - e^{-s})} - (y+1)^2\right]\right\}$$

(Alternatively, this can be derived from Eq. (A-2) in Appendix A taking the limit as $b \to \infty$.) The entropy is

$$H = -P_c \ln P_c + 2\sum_{i=0}^{\infty}(-P_i \ln P_i) = e^{-y}\left\{\frac{s}{e^s - 1} + \ln\left[\frac{2(e^y - 1)}{1 - e^{-s}}\right]\right\} - \ln(1 - e^{-y})$$

Given these expressions for MSE and entropy in terms of s and y, we apply the Kuhn–Tucker conditions once more. When s is fixed and y varies, the resulting rate-distortion curve has slope

$$\frac{1 - \dfrac{s^2 e^s}{(e^s - 1)^2} - y^2}{2 \left(\dfrac{s}{e^s - 1} + \ln \left[\dfrac{2(e^y - 1)}{1 - e^{-s}} \right] \right)}$$

When y is fixed and s varies, the resulting rate-distortion curve has slope

$$1 - s \left(\frac{1}{2} + \frac{1}{e^s - 1} \right)$$

By the Kuhn–Tucker conditions, these two quantities must be equal. We can use this fact to solve for y in terms of s numerically. We find that w varies between 1 (high rate limit) and 2 (low rate limit). The resulting rate-distortion limit is shown in Fig. 7.

Ka-Band Monopulse Antenna-Pointing Systems Analysis and Simulation

V. Y. Lo

Communications Systems and Research Section

NASA's Deep Space Network (DSN) has been using both 70-m and 34-m reflector antennas to communicate with spacecraft at S-band (2.3 GHz) and X-band (8.45 GHz). To improve the quality of telecommunication and to meet future mission requirements, JPL has been developing 34-m Ka-band (32-GHz) beam-waveguide antennas. Presently, antenna pointing operates in either the open-loop mode with blind pointing using navigation predicts or the closed-loop mode with conical scan (conscan). Pointing accuracy under normal conscan operating conditions is in the neighborhood of 5 mdeg. This is acceptable at S- and X-bands, but not enough at Ka-band. Due to the narrow beamwidth at Ka-band, it is important to improve pointing accuracy significantly (~2 mdeg). Monopulse antenna tracking is one scheme being developed to meet the stringent pointing-accuracy requirement at Ka-band. Other advantages of monopulse tracking include low sensitivity to signal amplitude fluctuations as well as single-pulse processing for acquisition and tracking. This article presents system modeling, signal processing, simulation, and implementation of Ka-band monopulse tracking feed for antennas in NASA/DSN ground stations.

I. Introduction

The design of the DSN monopulse pointing system consists of the reflector antenna, multimode corrugated horn feed, waveguide coupler, monopulse signal processor, and other associated RF electronics. A general block diagram is provided in Fig. 1. Starting at the main reflector, a tapered beam is formed. The HE11 mode in the corrugated horn is excited to radiate the sum pattern while the TE21 mode waveguide coupler generates the difference pattern [1]. With the assumption of perfect Ka-band-to-IF conversion, signal processing starts in the IF domain. A phase-locked loop recovers the carrier phase. This is used as a phase reference to coherently demodulate the elevation and azimuth difference channels. The sum and difference baseband signals are low-pass filtered and then followed by monopulse signal processing from which elevation and azimuth pointing errors are estimated. The error signals are used to drive the antenna servo controller for pointing corrections.

To predict the overall system performance, an antenna system model is needed. Mathematical models of the open-loop S-curve and pointing variance are presented in Section II. These models are validated by comparison with the difference pattern generated by a single-aperture multimode antenna. In Section III, a simplified servo loop model on the antenna controller and driver system is described. Higher-order complex multistate models are reserved for future upgrade. An end-to-end DSN block simulation
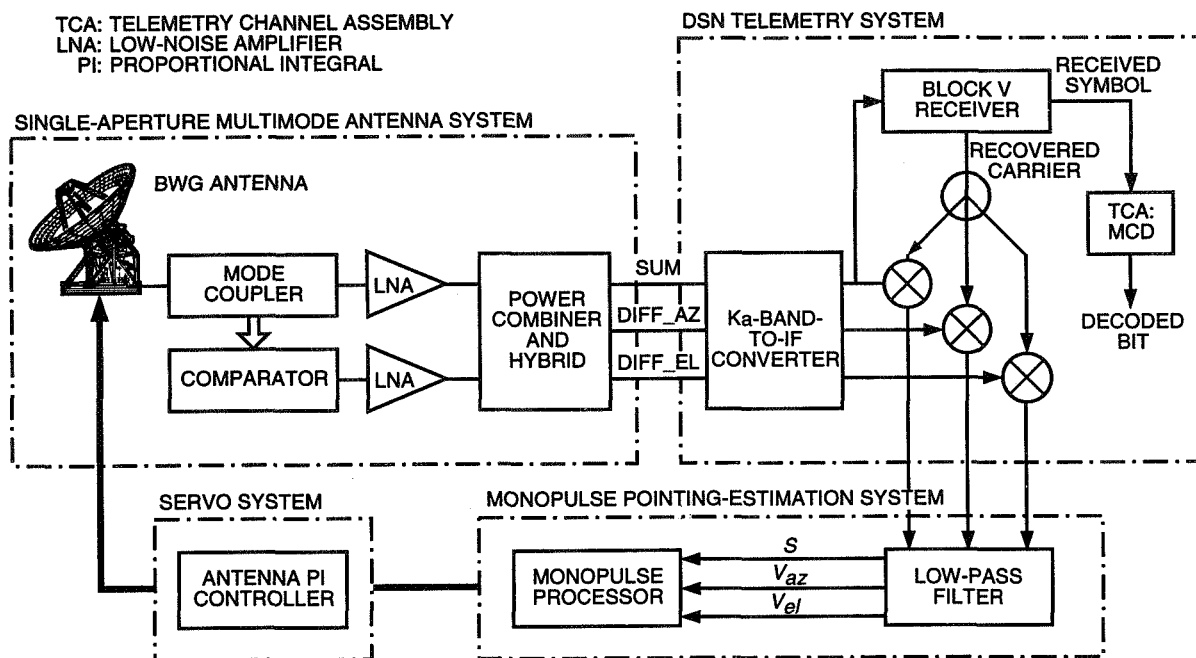
Fig. 1. Antenna-pointing system with monopulse signal processing.

program is presented in Section IV. The system includes the monopulse antenna block for a single-aperture multimode antenna, the digital receiver block for the Block V receiver (BVR), the decoder block for the maximum-likelihood convolutional decoder (MCD), the low-pass filter (LPF) and the monopulse processor blocks for pointing-error estimation, and the servo block for the antenna driver controller. Finally, in Section V, open- and closed-loop system performance in the presence of noise, cross-channel interference, amplitude and phase imbalance, and wind loading are investigated using this block simulation program.

II. System Model of Monopulse Antenna Pointing

Based on the physics of a corrugated horn and mode coupler, the classical four-horn monopulse antenna is shown to produce the same open-loop S-curve as the monopulse single-aperture multimode antenna.[1] In the presence of random noise, it can also be shown that the carrier-to-noise power spectral density ratio (CNR) is identical between the four-horn model and the single-aperture model with the same aperture size. Thus, the four-horn model produces the same system performance as a single-aperture multimode antenna under identical input signal conditions. The simple four-horn model can now be used for system simulation and analysis. Without loss of generality, we shall examine the azimuth pointing errors only.

From a complex signal analysis on a four-horn model [2,3],[2] the mean error voltage and its variance are shown to be

[1] S-curves from various models were compared under deterministic conditions in T. K. Wu, "Monopulse Antenna Study," JPL Interoffice Memorandum 3365-94-MP-001 (internal document), Jet Propulsion Laboratory, Pasadena, California, September 1994, and in V. Lo, "Single Aperture Multi-Mode Monopulse Antenna Pointing With Corrugated Horn," JPL Interoffice Memorandum 3393-94-VYL-015 (internal document), Jet Propulsion Laboratory, Pasadena, California, November 1994.

[2] The detailed mathematical derivation is shown in V. Y. Lo, "Monopulse Tracking Feed Link Study," JPL Interoffice Memorandum 339-92-134 (internal document), Jet Propulsion Laboratory, Pasadena, California, December 1992.

$$v_{az} = \frac{1}{2} \tan \left[\frac{\pi}{\lambda} d \sin \left(\theta_{az} \right) \right] \left[1 + \cos \left(\frac{2\pi}{\lambda} d \sin \left(\theta_{el} \right) \right) \right] \tag{1a}$$

$$\sigma_v^2 = \left| \frac{\delta_{az}}{S} \right|^2 \frac{1}{SNR_s} + \frac{1}{SNR_{az}} - 2 \left| \frac{\delta_{az}}{S} \right| \frac{1}{SNR_{az}} \tag{1b}$$

where

$v_{az}, \sigma_v^2 =$ the mean error voltage and its variance

$\theta_{az}, \theta_{el} =$ the azimuth and elevation pointing errors

$\delta_{az} =$ the azimuth difference signal

$d =$ the distance between adjacent horns

$|S|^2 =$ the signal power

$SNR_S = \dfrac{|S|^2}{\sigma_s^2} =$ the sum channel SNR

$SNR_{az} = \dfrac{|S|^2}{\sigma_{az}^2} =$ the azimuth channel carrier SNR

$SNR_c = \dfrac{|S|^2}{\rho \sigma_s \sigma_{az}} =$ the cross-channel SNR

$\rho =$ the correlation coefficient between the sum and azimuth channels

$\sigma_s^2, \sigma_{az}^2 =$ the variance of the sum and azimuth channels

For a high CNR and a small pointing error, the pointing error and its variance simplify to

$$\theta_{az} = \frac{v\lambda}{\pi d} \tag{2a}$$

$$\sigma_\theta^2 = \left(\frac{\lambda}{\pi d} \right)^2 \left(\frac{1}{SNR_{az}} \right) \tag{2b}$$

The 34-m Ka-band beam-waveguide (BWG) antenna parameters can now be substituted into Eqs. (1) and (2). For $d/\lambda = 1000$, the pointing-error voltage plot from Eq. (1a) is compared with S-curves generated from other physics and SPW [3] simulation models in Fig. 2. It shows that, at medium pointing errors, the mathematical model from Eq. (1a) matches the physics model of a single-aperture multimode antenna as well as the SPW-simulated S-curve of a four-horn monopulse antenna. Since a monopulse processor essentially performs integration on the input signal CNR to optimized pointing-error estimates, Eq. (2b) can be rewritten in terms of integration time T, $\sigma_\theta = (18 \times 10^{-3}) \left[1/\sqrt{(CNR \cdot T)} \right]$. The linearized standard deviation is plotted against the integration time for CNR values ranging from 10 to 30 dB-Hz

---

[3] Signal Processing WorkSystem (SPW) is the registered trademark of Alta Group, formerly Comdisco Systems, Inc.

(see Fig. 3). Based on the DSS-13 KABLE [4] link prediction, the carrier-to-noise power spectral-density ratio is expected to be greater than 10 dB-Hz. For a CNR value of 10 dB-Hz and a pointing error of 2 mdeg, integration time is 8 s. Given the possible range of CNR, 0.08 to 8 s represents the corresponding spread in integration time. For stable loop operation, the observation time of the estimator has to be short compared to the update time of the servo loop.
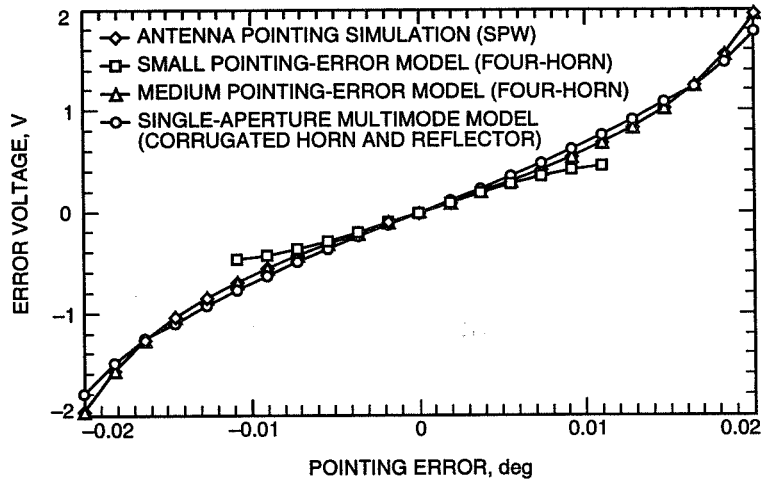
Fig. 2. Comparison of simulation, small/medium pointing-error
models, and the single-aperture multimode model.
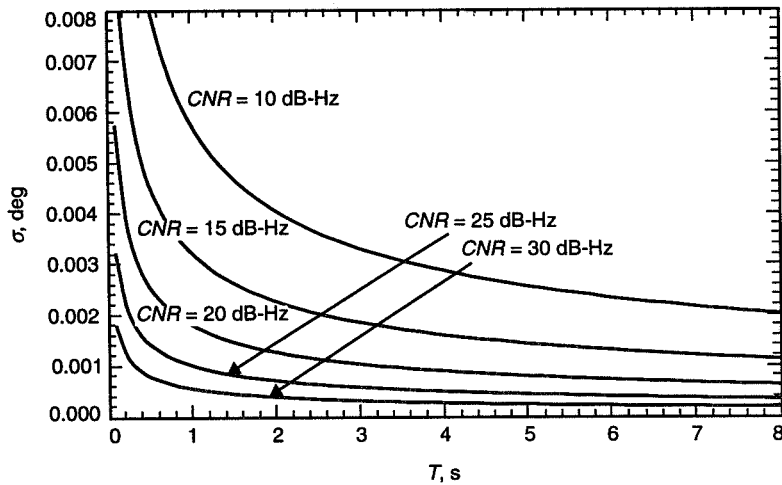
Fig. 3. Standard deviation of pointing error from the
linearized model.

III. Simplified Servo Loop Model of the DSN Ground Antenna

A model of the DSN BWG antenna servo control system [4] based on DSS 13 was developed to study pointing dynamics, channel cross-coupled dynamics, and wind disturbances. The state–space model of the antenna structure was obtained from its finite-element model. State reduction was applied separately on the antenna structure, elevation and azimuth drives, and rate-loop model. To a first-order approximation,

---

[4] The Ka-band link experiment (KABLE) was presented in *OSC Advanced Systems Review: TDA Systems Development* (internal document), Jet Propulsion Laboratory, Pasadena, California, June 1992.
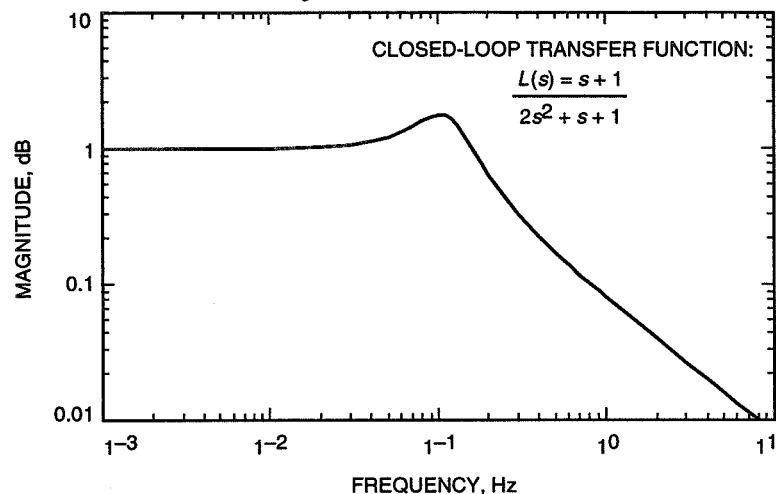
Fig. 4. Magnitude response of the servo loop model.

a proportional controller is used as a pointing-error estimator based on the observed differential error voltages. Such information is passed on to the elevation and azimuth drives to turn the antenna structure. This second-order servo loop model is shown in Fig. 4. The frequency response has a 3-dB roll-off at 0.2 Hz.

IV. End-to-End DSN Ground-Link Simulation

APSIM_MON is a simulation software [5] of the DSN BWG antenna supporting the Ka-band monopulse development effort. It is constructed on the platform of the SPW. The hierarchy simulation model for monopulse antenna pointing (ANT_MON) has been integrated with the advanced digital receiver model (DIG_RCVR) and the decoder model (CON_DEC) to form an end-to-end DSN telemetry system (see Fig. 5).[5] The proper encoded signal is available through the simulation signal generator (CC_SIG) model, which generates an encoded pseudonoise (PN) data sequence with different initial phase and frequency conditions. Parameters of the SNR, loop acquisition, and running averages of the bit error rate are monitored by the simulation monitor block (PERF_MONITOR).

The simulation model has been applied to analyze various design parameters. The following cases have specifically been investigated:

(1) Open-loop monopulse antenna pointing with and without random noise

(2) Closed-loop monopulse antenna pointing with and without random noise

(3) Effects of amplitude and phase imbalance between the sum and difference channels

(4) Effects of pointing errors on end-to-end telemetry link performance

---

[5] The SPW Costas-loop digital receiver model developed by J. Gevargiz for the BVR has been expanded to include residue carrier with square- and sine-wave subcarriers; see J. Gevargiz, "Acquisition, Tracking and Bit-Error-Rate Analysis of the Block V Receiver's BPSK Tracking Loop Including the Convolutional Coder and Decoder," JPL Interoffice Memorandum 3396-93-05 (internal document), Jet Propulsion Laboratory, Pasadena, California, March 1993, and V. Lo, "Antenna Pointing Simulation With Monopulse Processing (APSIM_MON)," JPL Interoffice Memorandum 3393-95-VYL-02 (internal document), Jet Propulsion Laboratory, Pasadena, California, April 1995.

CHANNEL

•GAUSSIAN
FADING
  •NAKAGAMI
  •RAYLEIGH
  •UNIFORM
  •RICE
  •LOG-NORMAL
SCINTILLATION
  •SOLAR

ANTENNA

•BWG (34-m/70-m)

POINTING ALGORITHM
•CONSCAN (ANT_CON)
•MONOPULSE (ANT_MON)

SERVO LOOP
•COMPENSATOR AND
  ESTIMATOR
•SERVO MOTOR,
  CONTROLLER

DISTURBANCES
•WIND LOADING
•GRAVITATION
•VIBRATION

**DIGITAL RECEIVER
(DIG_RCVR)**

•SUPPRESSED AND RESIDUE
  CARRIER, SUBCARRIER,
  AND SYMBOL
•SQUARE/SINE
•NARROW BANDWIDTH AND
  WINDOW
•DIGITAL PHASE-LOCKED
  LOOP AND NUMERICALLY
  CONTROLLED OSCILLATOR

**SIMULATION SIGNAL
GENERATOR
(CC_SIG)**

•PN DATA
•INITIAL CONDITIONS:
  INITIAL FREQUENCY/PHASE
  ERRORS
    CARRIER, SUBCARRIER
  INITIAL SYMBOL TIMING
•ENCODER
    CONVOLUTIONAL CODE
    REED–SOLOMON CODE

SIMULATION PARAMETERS
•BIT RATE
•SNR
•LOOP BANDWIDTH
    CARRIER, SUBCARRIER,
    AND SYMBOL
•WINDOW
    SUBCARRIER AND
    SYMBOL
•LOOP UPDATE RATE
    CARRIER, SUBCARRIER,
    AND SYMBOL

DECODER

•CONVOLUTIONAL CODE
  (CON_DEC)
•REED–SOLOMON CODE
  (RS_DEC)

**PERFORMANCE
MONITOR
(PERF_MONITOR)**

•ACQUISITION/LOCK
•BURST-ERRORS PROFILE
•BIT-ERROR PROBABILITY
  DYNAMIC SIGNAL DISPLAY

LEGEND:

☐ = TEST
SIMULATION
ASSEMBLY
(TSA)

▨ = DEEP SPACE COMMUN-
ICATIONS COMPLEX
(DSCC) ANTENNA AND
TELEMETRY SUBSYSTEM

■ = SYSTEM
PERFORMANCE
TEST (SPT)
MONITOR
AND CONTROL

— = LOCAL AREA
NETWORK (LAN)
(SHARED DATA)

Fig. 5. SPW simulation of the monopulse antenna-pointing system.

V. Summary of Simulation Results

For case (1), with variable pointing errors, the corresponding error voltages in the forward loop trace out the S-curve shown in Fig. 2. When Gaussian noise is added into the loop, a noisy pointing-error voltage is observed. The standard deviation of the linearized mathematical prediction based on the corrupt pointing-error voltage, Eq. (2), is shown in Fig. 3. Knowing the input SNR, these curves provide the integration time needed to meet a specific pointing-error variance.

For case (2), a simple second-order servo loop is used to model the antenna controller. The frequency response has a 3-dB roll-off at 0.2 Hz (see Fig. 4). Stability of the servo loop is investigated as a function of the low-pass filter bandwidths in the forward path. Various types of low-pass filters, including Butterworth, Bessel, and Chebyshev, with up to twenty orders are used in this evaluation. Deterministic step responses of the loop are simulated (see Fig. 6). The results show that the low-pass filter bandwidth has to be about two orders of magnitude higher than the servo-loop bandwidth for stable loop operations.
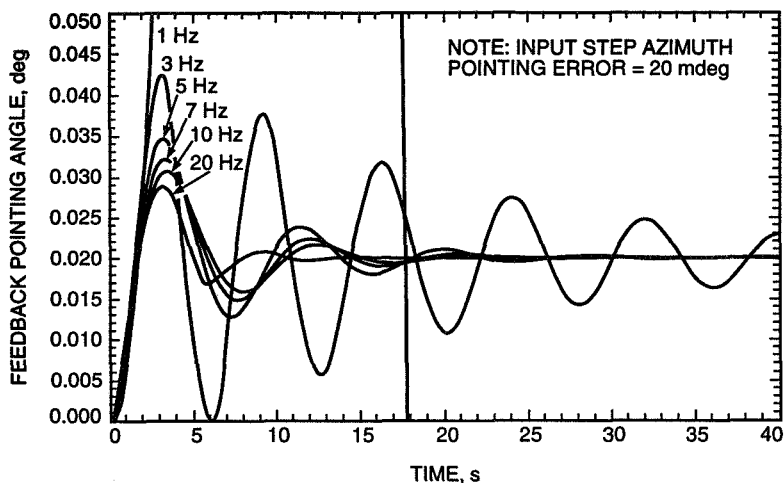
Fig. 6. Simulated closed-loop step response as a function of LPF bandwidth.
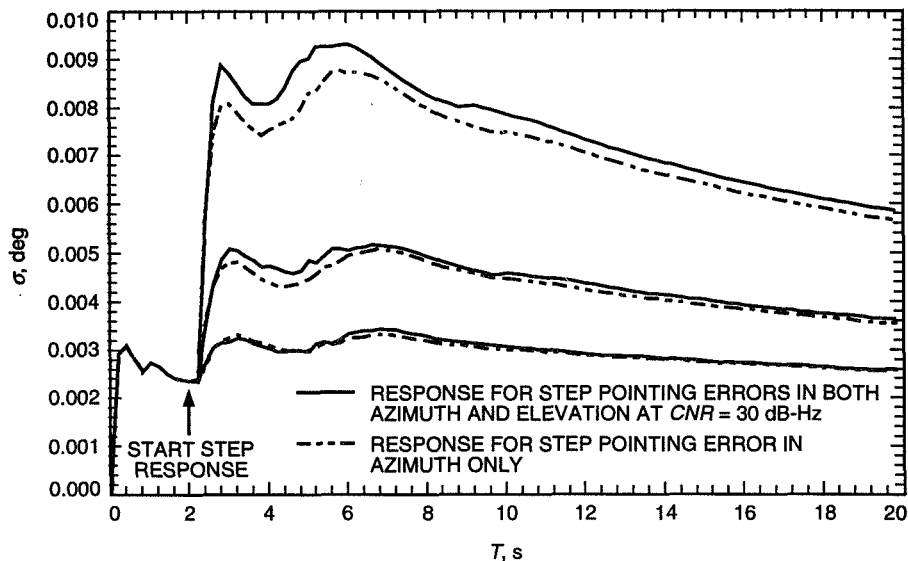
Fig. 7. Standard deviation of closed-loop pointing error of the azimuth channel induced by step perturbation in single and dual channels.

The same conclusion can also be reached from root locus and Nyquist stability analyses. In the presence of uncorrelated Gaussian noise, the simulated standard deviations of closed-loop step pointing error for single-channel and cross-channel interference are shown in Fig. 7. Coupling between the azimuth and elevation channels will increase the pointing error beyond this baseline.

For case (3), the amplitude imbalance between the sum and difference channels scales the voltage of the S-curve while the relative phase imbalance in electrical length manifests as a bias of the pointing error. The source of such imbalance may be due to amplifiers, hybrids, couplers, filters, etc. Both open- and closed-loop pointing-error variances are also modified by a multiplication factor of the squared amplitude imbalance. These results are summarized in Fig. 8, where a relative amplitude of 1 and a relative phase of 0 deg represent the baseline with no imbalance. Offsets corresponding to 0.1- and 1-dB pointing losses are marked by dotted lines in the figure for reference. Specifications on amplitude and phase mismatch between the difference and sum channels can now be established to meet pointing-loss tolerance.

110
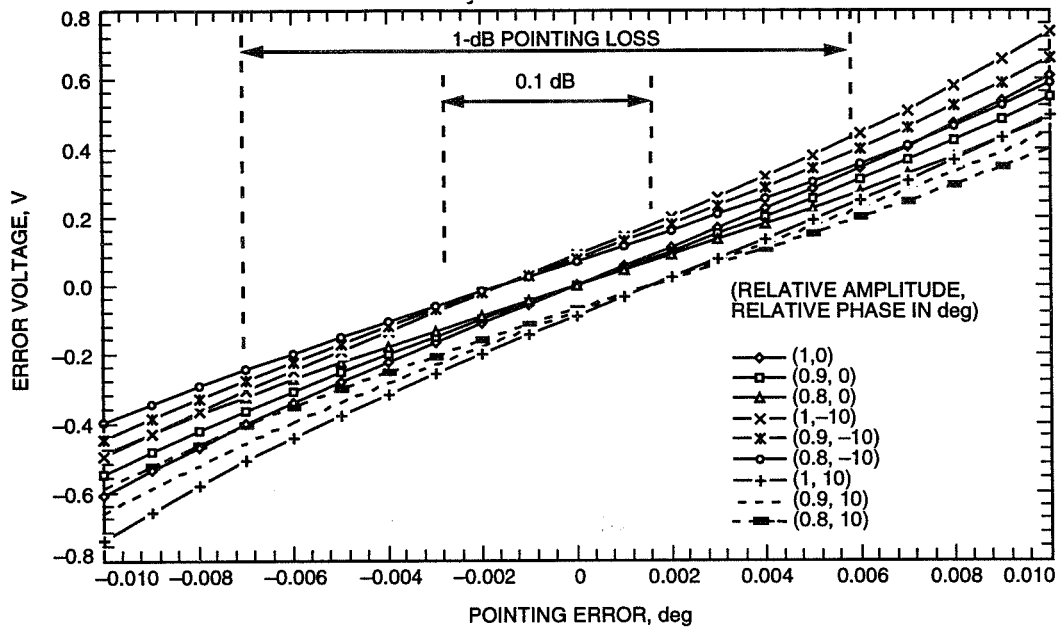
Fig. 8. Effects of cross-channel amplitude and phase distortion on the S-curve.
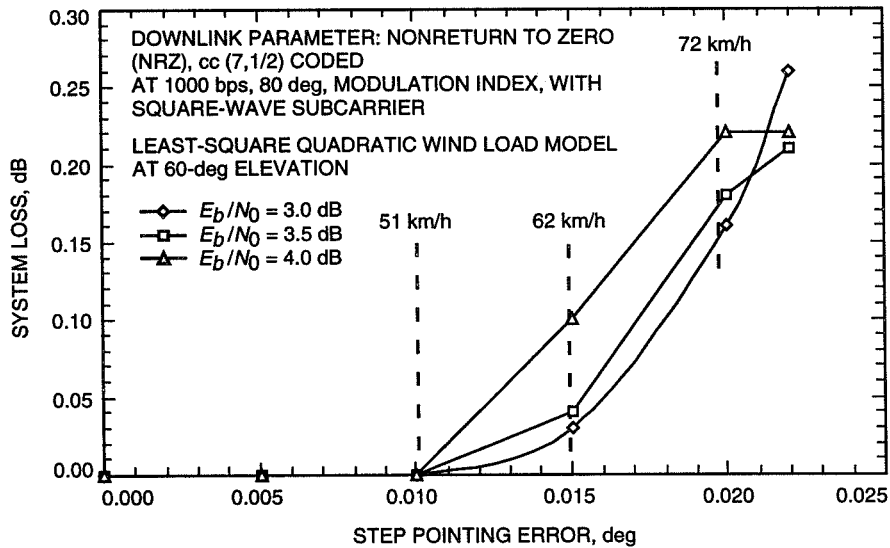
Fig. 9. System loss due to step pointing error.

Finally, the impact of pointing errors on the link quality driven by wind loading or gravitational effects can now be analyzed by observing the relative increase in bit errors after the onset of such disturbances. The loss in signal power relative to the unperturbed case can be obtained from the increase in bit-error probability. For example, a 1-kbps downlink with a (7,1/2) convolutional code at an 80-deg modulation index in a monopulse closed-loop pointing system with system loss from step pointing error induced by wind load is shown in Fig. 9. Unlike the antenna pointing loss from miscalibration, this peak pointing loss represents a dynamic process depending on the rate of change of the disturbance relative to the servo loop tracking rate. Similar to radio loss in carrier tracking, the results show that the telemetry link is more susceptible to small pointing errors at high SNR.

VI. Conclusion

A system model for monopulse antenna pointing has been presented. Under the framework of SPW simulation, a monopulse antenna block is constructed from this system model. Both open- and closed-loop responses in the presence of noise are investigated through simulation. Pointing performance is evaluated from the perspective of SNR degradation (system loss) on an end-to-end link due to wind loading. These simulation results provide the basis for design, implementation, and performance evaluation of the DSN Ka-band monopulse pointing system.

Acknowledgments

References

[1] P. J. Clarricoats and A. D. Olver, *Corrugated Horns for Microwave Antennas*, London: Peter Peregrinus Ltd., 1984.

[2] T. Inoue and T. Kaitsuka, "K-Band Tracking System for Domestic Satellite Communication System," *IEEE Trans. on Aerospace and Electronic Systems*, vol. AES-17, no. 4, pp. 561–570, July 1981.

[3] S. Sharenson, "Angle Estimation Accuracy With a Monopulse Radar in the Search Mode," *IRE Trans. on Aerospace and Navigation Electronics*, vol. ANE9, no. 3, pp. 175–179, September 1962.

[4] W. Gawronski and J. A. Mellstrom, "Modeling and Simulations of the DSS 13 Antenna Control System," *The Telecommunications and Data Acquisition Progress Report 42-106, April–June 1991*, Jet Propulsion Laboratory, Pasadena, California, pp. 205–248, August 15, 1991.

[5] V. Y. Lo and M. K. Sue, "Monopulse Signal Processing and Simulation for DSN Beam Waveguide Antenna," *Proc. ICSPAT*, vol. 2, Boston, Massachusetts, pp. 1603–1607, October 1995.

Modeling and Analysis of the DSS-14 Antenna Control System

W. Gawronski and R. Bartos
Communications Ground Systems Section

An improvement of pointing precision of the DSS-14 antenna is planned for the near future. In order to analyze the improvement limits and to design new controllers, a precise model of the antenna and the servo is developed, including a finite element model of the antenna structure and detailed models of the hydraulic drives and electronic parts. The DSS-14 antenna control system has two modes of operation: computer mode and precision mode. The principal goal of this investigation is to develop the model of the computer mode and to evaluate its performance. The DSS-14 antenna computer model consists of the antenna structure and drives in azimuth and elevation. For this model, the position servo loop is derived, and simulations of the closed-loop antenna dynamics are presented. The model is significantly different from that for the 34-m beam-waveguide antennas.

I. Introduction

The DSS-14 antenna control system model consists of the antenna structure, antenna drives in azimuth and elevation, and the position servo loop. Each drive, in turn, consists of gearboxes, hydraulic servo (active and passive valves, hydraulic lines, and hydraulic motors), and electronics boards (amplifiers and filters). The DSS-14 antenna control system model was developed by R. E. Hill [1,2]. In the present development, we obtain a more precise model that allows for accurate simulations of the antenna pointing errors and allows simulation of the intermediate variables, such as torques, currents, wheel rates, truss stresses, etc. We incorporate the finite element structural model with free rotation in azimuth and elevation, in a manner similar to the 34-m antenna models [3–5], that involves cross-coupling effects between azimuth and elevation, wind pressure on the dish, and pointing error model. The hydraulic part involves a recent development in modeling of the hydraulic components by R. Bartos [6–8].

The rate loop model consists of the elevation and azimuth drives and the antenna structure. Each drive consists of three major components: the electronics boards, hydraulic system, and gearbox. A model of each component is derived separately, then put together, forming the drive and rate loop models. Finally, the position loop is closed to obtain the position loop model.

II. Drive Model

A block diagram of the drive model is shown in Fig. 1, where N_t is the ratio between motor rate and tachometer (pinion) rate; r, rad/s, is the rate input to the drive; i, A, is the hydraulic active valve
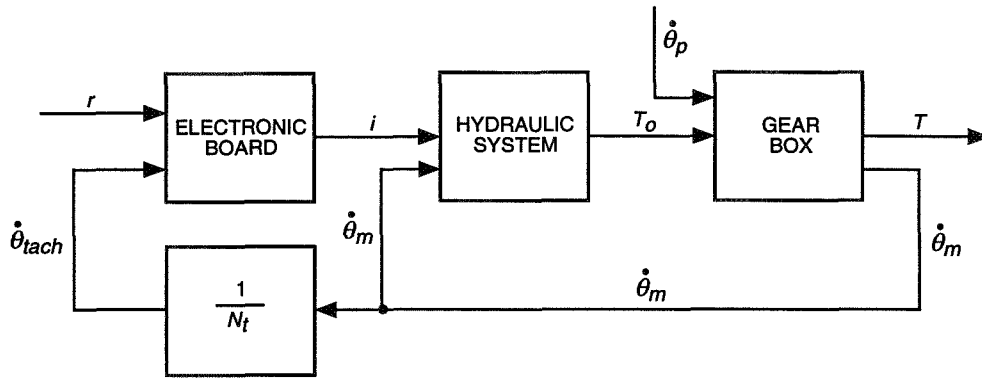
Fig. 1. Block diagram of the antenna drive.

solenoid current; T_o and T, N·m or lb in., are the gearbox and on-axis torques, respectively; and $\dot{\theta}_{tach}$ and $\dot{\theta}_m$, rad/s, are the pinion and motor rates, respectively. The state–space representation of the electronic board, hydraulic system, and gearbox are derived in the following sections.

A. Electronic Board

A schematic diagram for the electronic board is shown in Fig. 2. The inputs are the rate command r, rad/s, and the tachometer rate $\dot{\theta}_{tach}$, rad/s. The output is the solenoid valve current i. The scaling factors, k_r and k_t, convert the inputs into the command voltage, v_r, and tachometer voltage, v_t. The subsystem, G_t, is the tachometer circuit: it transforms the tachometer voltage, v_t, into the voltage, v_{to}. The subsystems with the transfer functions G_{r1} and G_{r2} are the rate amplifier circuits: they transform the command voltage, v_r, and the tachometer voltage, v_{to}, into the error voltage, v_s. The subsystem with the transfer function, G_s, is the valve driver amplifier circuit, with the error voltage, v_s, as the input and the valve current, i, as the output.
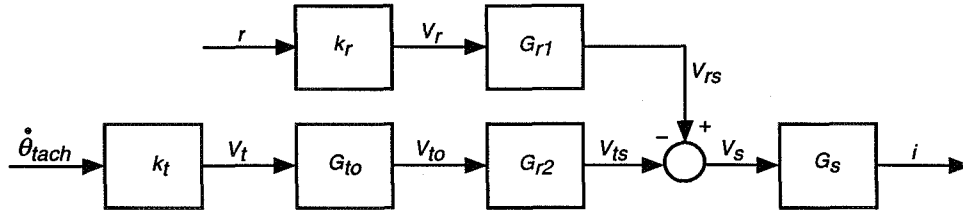
Fig. 2. Block diagram of the electronic board.

The following transfer functions of each of the four components are derived in the Appendix. The transfer function G_{to} for azimuth is

$$G_{to} = 0.151 \tag{1}$$

and, for elevation, is

$$G_{to} = 0.127 \tag{2}$$

The transfer functions G_{r1} (from v_r to v_s) and G_{r2} (from v_{to} to v_s) are

$$G_{r1} = 6.20 \ G_o \left.\vphantom{\begin{matrix}a\\b\end{matrix}}\right\} \tag{3}$$

$$G_{r2} = -4.65 \ G_o$$

where

$$G_o = \frac{1 + 0.400s}{1 + 4.205s} \tag{4}$$

is the transfer function of a lag compensator. The transfer function G_s is

$$G_s = 4.42 \times 10^{-5} \tag{5}$$

The scaling factors, k_r and k_t, are $k_r = 1212.6$ V/rad/s and $k_t = 2.5$ V/rad/s. Thus, the command transfer function from the rate command r to the solenoid current i_s is

$$G_r = k_r G_{r1} G_s = 0.3323 \ G_o \tag{6}$$

where G_o is defined in Eq. (4). The tachometer transfer function from the tachometer rate $\dot{\theta}_{tach}$ to the solenoid current i_s is

$$G_t = k_t G_{to} G_{r2} G_s \tag{7}$$

$$G_t = \begin{cases} -0.7750 \times 10^{-4} G_o & \text{for azimuth} \\ -0.6525 \times 10^{-4} G_o & \text{for elevation} \end{cases} \tag{8}$$

In order to check the correctness of the derivation, note that the ratio G_r/G_t should be equal to N_o, where N_o is the tachometer-to-axis ratio ($N_o = 4287.5$ for azimuth and $N_o = 5083.6$ for elevation). Indeed, from Eqs. (6) and (7), one obtains

$$\frac{G_r}{G_t} = \begin{cases} -4287.7 = N_o & \text{for azimuth} \\ -5092.7 \cong N_o & \text{for elevation} \end{cases} \tag{9}$$

Finally, the state–space representations of the transfer functions G_r and G_t (for azimuth and elevation) are easily obtained with the standard Matlab command in the form

$$\dot{x}_b = A_b x_b + B_{b1} r + B_{b2} \dot{\theta}_{tach} \left.\vphantom{\begin{matrix}a\\b\end{matrix}}\right\} \tag{10}$$

$$i = C_b x + D_{b1} r + D_{b2} \dot{\theta}_{tach}$$

The plot of the transfer function in azimuth (magnitude and phase) from r to i is shown in Fig. 3. The transfer function for elevation is identical. The plots of the transfer functions in azimuth and elevation from $\dot{\theta}_{tach}$ to i are shown in Fig. 4. The magnitudes drop in the frequency range from 0.01 to 0.1 Hz due to implementation of the filter G_o.
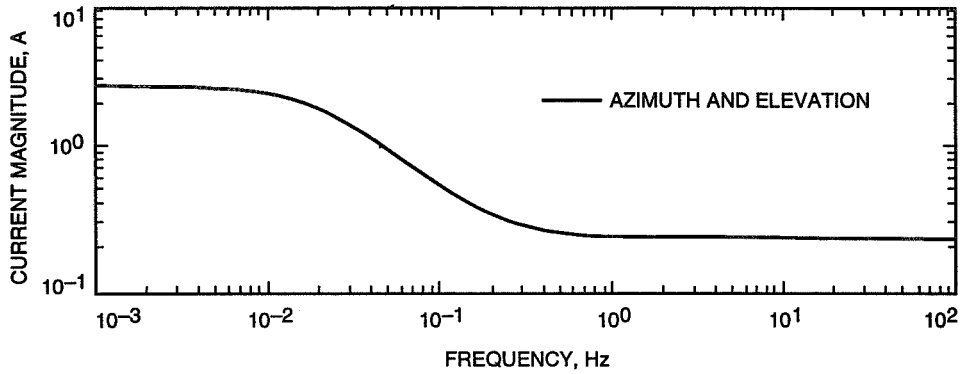
Fig. 3. Magnitude of the electronic board transfer function from the rate input to the board current.
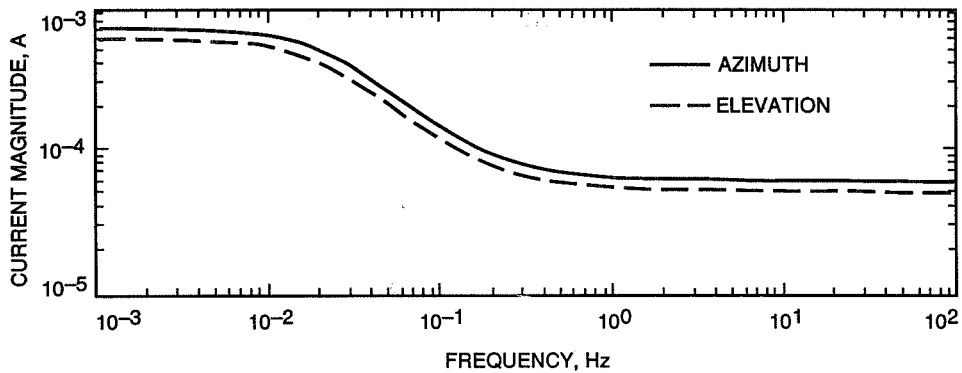
Fig. 4. Magnitude of the electronic board transfer function from the tachometer rate input to the board current.

B. Hydraulic System

The hydraulic servo system model was presented by R. E. Hill in [1] and [2]. Here we take a different approach, based on the recent investigations of hydraulic components by R. Bartos (see [6–8]). A block diagram of the DSS-14 hydraulic system is shown in Fig. 5. It consists of the hydraulic motor, shorting valve, hydraulic lines A and B, passive servo valves, and active servo valves. It has two inputs, servo valve current i and motor rate $\dot{\theta}_m$, and one output, motor torque T_o. The equations for each component are derived separately based on the work of Bartos [6–8]. Basically, these models are nonlinear ones; however, we linearize them in order to model the antenna linear regime of operation.

1. Active Servo Valve. This valve model has the input, i, A, and two outputs, q_{av}—the flow rate out of port a, cm³/s, or in.³/s, and q_{bv}, the flow rate out of port b, cm³/s, or in.³/s. From [6], one obtains

$$\ddot{q}_{av} + 2\zeta_o\omega_o\dot{q}_{av} + \omega_o^2 q_{av} = \omega_o^2 k_a i \tag{11a}$$

$$q_{bv} = -q_{av} \tag{11b}$$

where $\zeta_o = 0.8$ is the damping ratio, $\omega_o = 345.6$ rad/s is the valve natural frequency, and $k_a = 59,200 - 97,300$ cm³/s/A (23,300–38300 in.³/s/A) is the valve gain. The lower value is the Bartos estimate, while the upper value is the Hill estimate [2]. The values of the parameters are listed in Table 1.
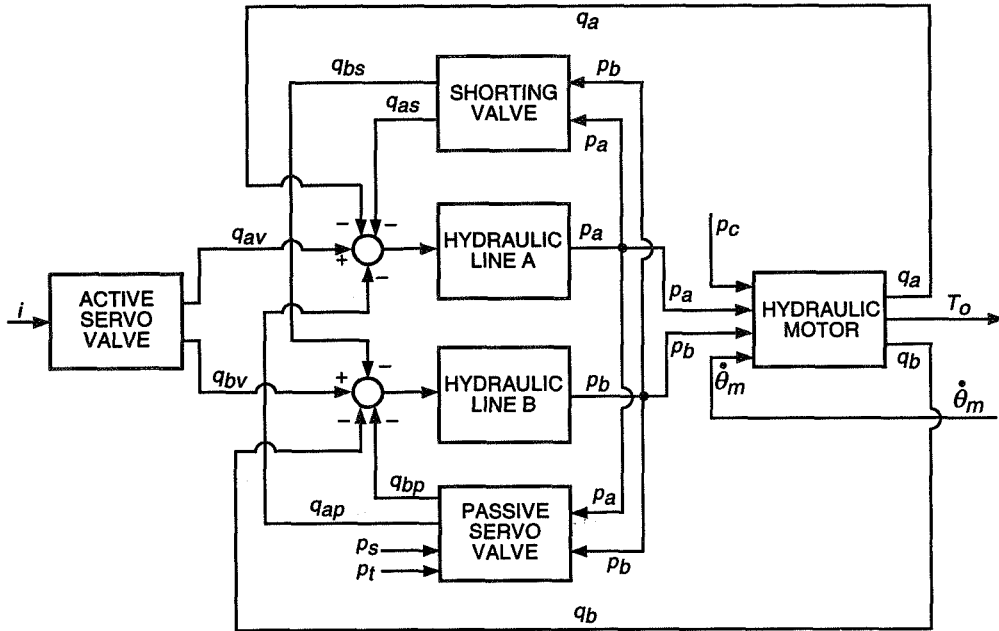
Fig. 5. Block diagram of the hydraulic drive.

Table 1. Parameters of the active servo valve (line A and line B).

Drive	ζ_o	ω_o, rad/s	k_a, cm^3/s/A	k_a, in.^{3}/s/A
Azimuth	0.6 to 0.8	345.56	59,200 to 97,300	23,300 to 38,300
Elevation	0.6 to 0.8	345.56	59,200 to 97,300	23,300 to 38,300

Introducing the new variable $q_v = q_{av} - q_{bv}$, one obtains from Eq. (11)

$$\ddot{q}_v + 2\zeta_o\omega_o\dot{q}_v + \omega_o^2 q_v = 2\omega_o^2 k_a i \tag{12}$$

The differential variable q_v and the other differential variables introduced allow one to further simplify the analysis without loss of accuracy and to get rid of the "parasitic" variables, such as tank pressure, supply pressure, and case pressure.

2. Shorting Valve. The pressures p_a and p_b, kPa (lb/in.^{2}), are the inputs to the shorting valve, and the flows q_{as} and q_{bs}, cm^3/s (in.^{3}/s), are its output (see Fig. 5). The linearized relationship between the inputs and outputs is as follows:

$$\left. \begin{array}{l} q_{as} = k_s(p_a - p_b) \\ \\ q_{bs} = -q_{as} \end{array} \right\} \tag{13}$$

where k_s is the valve gain, $k_s = 0.0007 - 0.007$ cm^3/s/kPa (0.0003–0.003 in.^{3}/s/psi), both in azimuth and elevation.

117

Introducing new differential variables $p = p_a - p_b$ and $q_s = q_{as} - q_{bs}$, one obtains Eq. (13) in the form

$$q_s = 2k_s p \tag{14}$$

3. Passive Servo Valve. This valve has four inputs: pressures p_a and p_b, supply pressure p_s, and tank pressure p_t. The last two are supplementary constant inputs that can be removed from the analysis. The valve has two outputs: flows q_{ap} and q_{bp}. Its linearized input–output relationship is as follows:

$$q_{ap} = k_{p1}(p_a - p_s) + k_{p2}(p_a - p_t) \tag{15a}$$

$$q_{bp} = k_{p1}(p_b - p_s) + k_{p2}(p_b - p_t) \tag{15b}$$

where the gains are $k_{p1} = 0.0055$ cm^3/kPa (0.00233 in.^{3}/psi) and $k_{p2} = k_{p1}$, the supply pressure is 17,240 kPa (2500 psi), and the tank pressure is 345 kPa (50 psi). These values are identical for azimuth and elevation.

Introducing $q_p = q_{ap} - q_{bp}$, and recalling that $p = p_a - p_b$, one obtains Eqs. (15a) and (15b) as follows:

$$q_p = (k_{p1} + k_{p2})p = 2k_p p \tag{16}$$

where, for simplicity of notation, we denote $k_p = k_{p1} = k_{p2}$.

4. Hydraulic Motor. The motor is described in [8]. From Fig. 5, it follows that the motor has four inputs and four outputs. The inputs are pressures p_a and p_b, case pressure p_c, and motor rate $\dot{\theta}_m$, rad/s. The outputs are flows q_a and q_b, leakage to the case q_c, and motor torque T_o, N·m (or lb in.). Following [8], one obtains the flow q_a from Eq. (59) of [8]:

$$q_a = q_{a1} + q_{a2} + q_{a3} \tag{17}$$

But, from Eq. (40) of [8],

$$q_{a1} = D\dot{\theta}_m \tag{18}$$

where $D = 6.3$ cm^3/rad (0.3836 in.^{3}/rad) is the motor "displacement." From Eq. (52) of [8], one obtains

$$q_{a2} = \frac{k_{a2}}{\mu}(p_a - p_c) \tag{19}$$

where $k_{a2} =$ from 6.35×10^{-5} to 18.3×10^{-5} cm^3 (from 2.5×10^{-5} to 7.2×10^{-5} in.^{3}) is the leakage constant (assumed to be 10^{-4} cm^3, or 4×10^{-5} in.^{3}); $\mu =$ from 2.8×10^{-4} to 2.8×10^{-3} kPa s (from 4×10^{-5} to 4×10^{-6} lb s/in.^{2}) is the absolute fluid viscosity (assumed to be 10^{-4} cm^3, or 4×10^{-5} in.^{3}); and $p_c = 221$ kPa (32 psi). From Eq. (58) of [8], one obtains the leakage from port A to port B, q_{a3}:

$$q_{a3} = \frac{k_{a3}}{\mu}(p_a - p_b) \tag{20}$$

where k_{a3} is the constant of proportionality determined through experiments. It is assumed to be equal to k_{a2}, $k_{a3} = k_{a2}$.

Combining Eqs. (17) through (20), one obtains

$$q_a = D\dot{\theta}_m + \frac{k_{a2} + k_{a3}}{\mu}p_a - \frac{k_{a3}}{\mu}p_b - \frac{k_{a2}}{\mu}p_c \qquad (21)$$

From [8], Eq. (60), one obtains the flow rate q_b:

$$q_b = q_{b1} + q_{b2} - q_{a3} \qquad (22)$$

It follows from [8], Eq. (41), that

$$q_{b1} = -q_{a1} = -D\dot{\theta}_m \qquad (23)$$

and from [8], Eq. (53), that

$$q_{b2} = \frac{k_{b2}}{\mu}(p_b - p_c) \qquad (24)$$

Combining Eqs. (22), (23), (24), and (20), one obtains

$$q_b = -D\dot{\theta} - \frac{k_{a3}}{\mu}p_a + \frac{k_{a3} + k_{b2}}{\mu}p_b - \frac{k_{b2}}{\mu}p_c \qquad (25)$$

The motor torque T_o is obtained from Eq. (28) of [8] by neglecting Coulomb friction and inertia torques (the latter are included in the gearbox model):

$$T_o = T_p + T_f \qquad (26)$$

where T_p is the torque generated by the motor and T_f is the viscous friction torque. The linearized Eq. (10) of [8] gives the torque generated by the motor:

$$T_p = D(p_a - p_b) \qquad (27)$$

and from Eq. (24) of [8], one obtains the viscous friction torque:

$$T_f = -k_v D\mu\dot{\theta} \qquad (28)$$

where $k_v = 0.0438$ is a dimensionless viscous friction coefficient. Combining Eqs. (26) through (28), one obtains

$$T_o = Dp_a - Dp_b - k_v D\mu\dot{\theta} \qquad (29)$$

119

Define $q = q_a - q_b$; then from Eqs. (21) and (25), one obtains

$$\left.\begin{array}{c} q = 2D\dot{\theta}_m + \dfrac{3k_{a2}}{\mu}p \\[4mm] T_o = Dp - k_v D\mu\dot{\theta}_m \end{array}\right\} \tag{30}$$

The motor parameters are given in Table 2.

Table 2. Parameters of the hydraulic motor (line A and line B).

Drive	μ, kPa s	μ, lb s/in.^{2}	D, cm^3/rad	D, in.^{3}/rad	k_v	k_{a2}, cm^3	k_{a2}, in.^{3}	p_c, kPa	p_c, psi
Azimuth	2.8×10^{-4} to 28×10^{-4}	0.4×10^{-6} to 4×10^{-6}	25.2	1.52	0.0438	4.1×10^{-4} to 11.8×10^{-4}	2.5×10^{-5} to 7.2×10^{-5}	220	32
Elevation	2.8×10^{-4} to 28×10^{-4}	0.4×10^{-6} to 4×10^{-6}	25.2	1.52	0.0438	4.1×10^{-4} to 11.8×10^{-4}	2.5×10^{-5} to 7.2×10^{-5}	220	32

5. Hydraulic Line. There are two lines: A and B. A model for line A is developed, and the model for line B is similar (index "a" should be replaced with "b"). Line A has four inputs, flows q_a, q_{av}, q_{apv}, and q_{asv}, and a single output, pressure p_a (refer to Fig. 5). From [7], one obtains the line-A model as an integrator, with the negative feedback signs as in Fig. 5:

$$\dot{p}_a = k_{la}(-q_a + q_{av} - q_{ap} - q_{as}) \tag{31a}$$

Similarly, the line-B model is obtained:

$$\dot{p}_b = k_{lb}(-q_b + q_{bv} - q_{bp} - q_{bs}) \tag{31b}$$

As before, defining $p = p_a - p_b$, one obtains

$$\dot{p} = k_l(-q + q_v - q_p - q_s) \tag{32}$$

In these equations, the gains are

$$k_l = \frac{\beta}{v_o} \tag{33}$$

where β is the effective bulk modulus (capacitance of the line), $\beta = 1.29 \times 10^6$ kPa (1.87×10^5 psi), and v_o is the total volume, $v_o = 27,200$ cm^3 (1660 in.^{3}), so that $k_l = 47.3$ kPa/cm^3 (113 psi/in.^{3}). The values are collected in Table 3.

Table 3. Parameters of line A and line B.

Drive	β, kPa	β, psi	v_o, cm^3	v_o, in.^{3}
		Line A		
Azimuth	1.29×10^6	1.87×10^5	27,200	1653.6
Elevation	1.29×10^6	1.87×10^5	24,500	1498.1
		Line B		
Azimuth	1.29×10^6	1.87×10^5	27,700	1690.4
Elevation	1.29×10^6	1.87×10^5	24,600	1499.9

6. Hydraulic System Model. The model of the hydraulic system is derived by combining its elements (active servo valve, shorting valve, passive valve, hydraulic lines, and hydraulic motors). By introducing the new differential variables, the block diagram in Fig. 5 is simplified to the one in Fig. 6. A detailed block diagram of the hydraulic system is shown in Fig. 7. Combining Eqs. (12), (14), (16), (32), and (30) (or, alternatively, using the block diagram in Fig. 7), and defining the new state vector $x_h = [x_1, x_2, x_3]^T$, with three states, $x_1 = \dot{q}_v, x_2 = q_v$, and $x_3 = p$, and defining the input current, i, motor rate $\dot{\theta}_m$, and the single-output motor torque, T_o, one obtains

$$\left. \begin{aligned} \dot{x}_h &= A_h x_h + B_{ho}\dot{\theta}_m + B_{hi}i \\[2mm] T_o &= C_h x_h + D_{ho}\dot{\theta}_m + D_{hi} \end{aligned} \right\} \tag{34a}$$

where
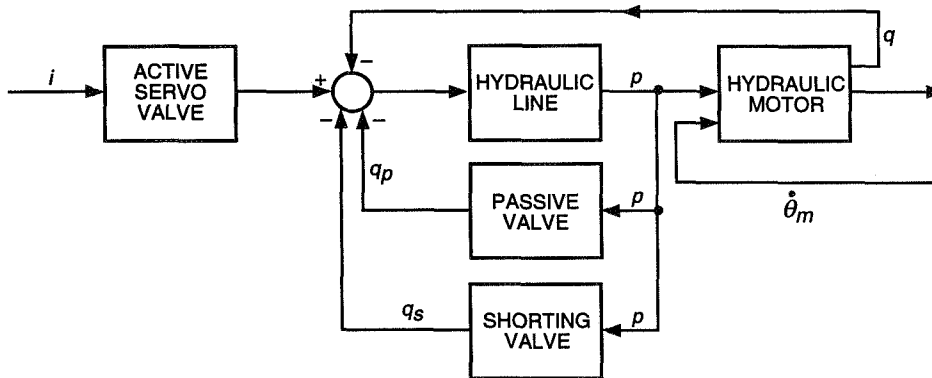
Fig. 6. Simplified block diagram of the hydraulic drive.
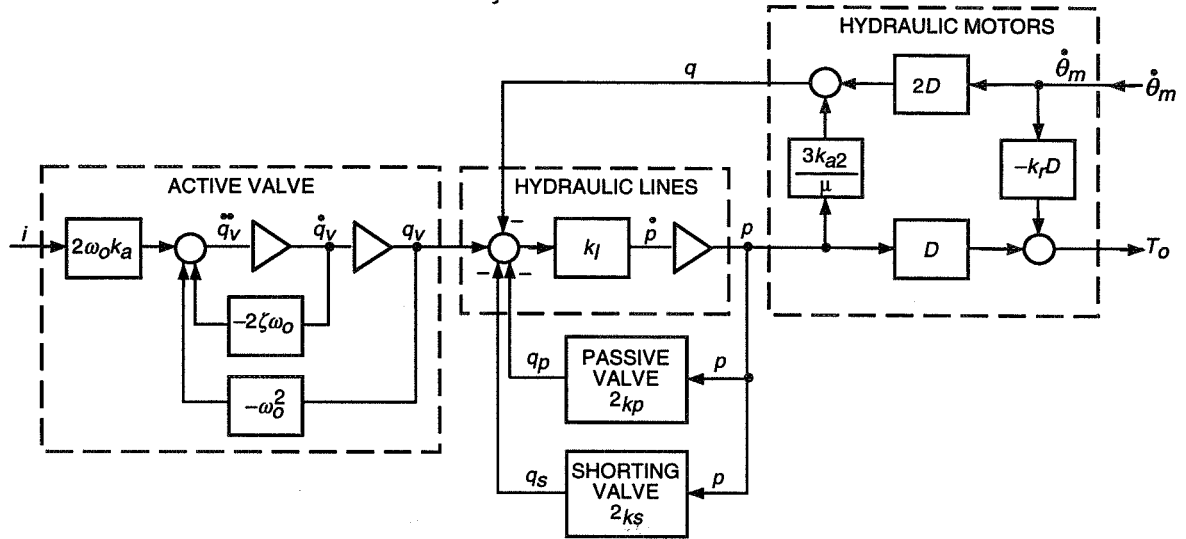
Fig. 7. Detailed block diagram of the hydraulic system.

$$A_h = \begin{bmatrix} -2\zeta_o\omega_o & -\omega_o^2 & 0 \\ 1 & 0 & 0 \\ 0 & k_l & k_l\left(-\dfrac{3k_{a2}}{\mu} - 2k_p - 2k_s\right) \end{bmatrix}$$

$$B_{hi} = \begin{bmatrix} 2\omega_o^2 k_a \\ 0 \\ 0 \end{bmatrix}$$

$$B_{ho} = \begin{bmatrix} 0 \\ 0 \\ -2k_l D \end{bmatrix} \qquad\qquad\qquad\qquad (34\text{b})$$

$$C_h = \begin{bmatrix} 0 \\ 0 \\ D \end{bmatrix}$$

$$D_{hi} = 0$$

$$D_{ho} = -k_v D\mu$$

The plots of the magnitudes of the transfer function in azimuth and elevation from i to T_o are shown in Fig. 8. The plots of the magnitudes of the transfer functions in azimuth and elevation from $\dot\theta_m$ to T_o are shown in Fig. 9.

C. Gearbox Model

The gearbox model was described in detail in [5], and its block diagram is given in Fig. 10. In this diagram, T_o is the motor torque, $\dot\theta_p$ is the antenna angular rate, ω_m is the motor rate, T is the gearbox
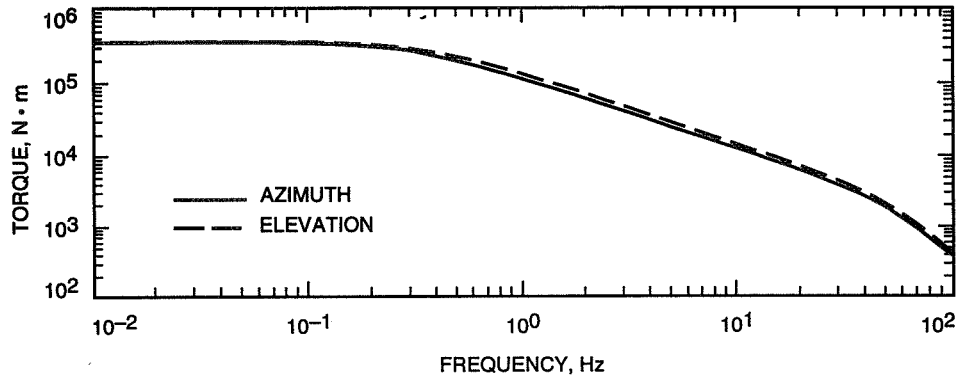
Fig. 8. Magnitude of the hydraulic drive transfer function from the solenoid current to the output torque.
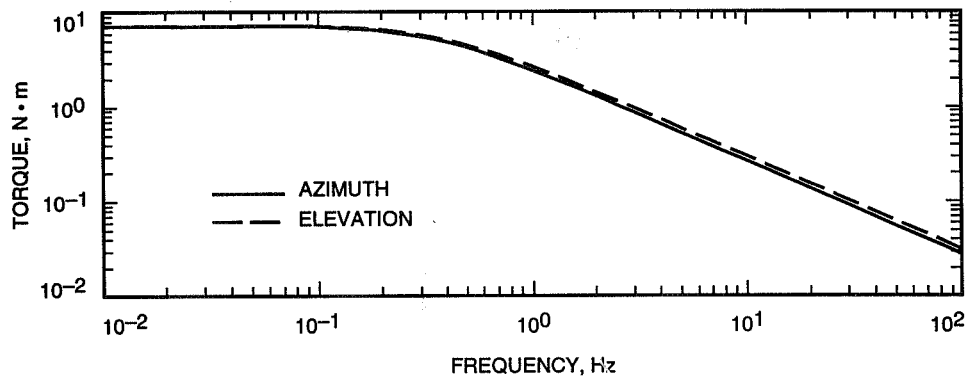
Fig. 9. Magnitude of the hydraulic drive transfer function from the motor rate to the output torque.
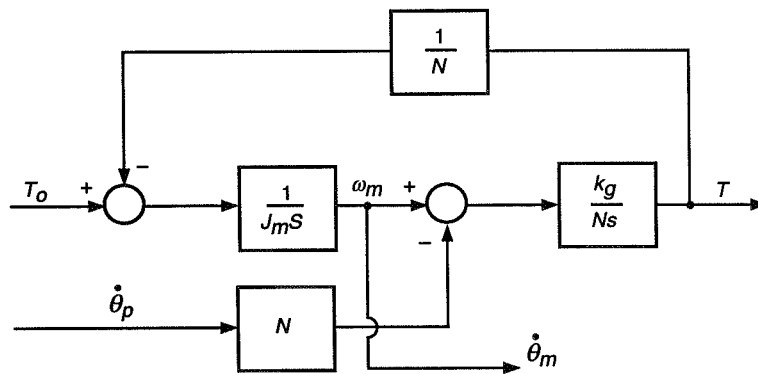
Fig. 10. Block diagram of the gearbox.

torque, J_m is the motor inertia, k_g is the gearbox (output) stiffness, and N is the gearbox ratio. This model has two inputs, the motor torque, T_o, and the wheel (pinion) angular rate, $\dot{\theta}_p$, and a single output, the gearbox torque, T.

The equations for this system are as follows:

$$\dot{J}_m \dot{\omega}_m = T_o - \frac{T}{N} \tag{35a}$$

$$T = k_g \left(\frac{\theta_m}{N} - \theta_p \right) \tag{35b}$$

Denoting the state variables $x_1 = \omega_m$ and $x_2 = T$, one obtains

$$\dot{x}_1 = \frac{-x_2}{N J_m} + \frac{T_o}{J_m} \tag{36a}$$

$$\dot{x}_2 = \frac{k_g x_1}{N} - k_g \dot{\theta}_p \tag{36b}$$

Defining the gearbox state as $x_g = [x_1 \quad x_2]^T$, input T_o and $\dot{\theta}_p$, and output T and ω_m, one obtains the gearbox state–space representation (A_g, B_g, C_g):

$$\left.\begin{aligned}
\dot{x}_g &= A_g x_g + B_{g1} T_o + B_{g2} \dot{\theta}_p \\[2mm]
T &= C_{g1} x_g \\[2mm]
\dot{\theta}_m &= C_{g2} x_g
\end{aligned}\right\} \tag{37a}$$

where

$$\left.\begin{aligned}
A_g &= \begin{bmatrix} 0 & \dfrac{-1}{N J_m} \\[3mm] \dfrac{k_g}{N} & 0 \end{bmatrix} \\[6mm]
B_{g1} &= \begin{bmatrix} \dfrac{1}{J_m} \\[3mm] 0 \end{bmatrix} \\[6mm]
B_{g2} &= \begin{bmatrix} 0 \\ -k_g \end{bmatrix} \\[4mm]
C_{g1} &= \begin{bmatrix} 0 & 1 \end{bmatrix} \\[3mm]
C_{g2} &= \begin{bmatrix} 1 & 0 \end{bmatrix}
\end{aligned}\right\} \tag{37b}$$

D. Drive Model

The drive model is obtained by combining the state–space representation of the electronic board, Eq. (10); the hydraulic system, Eq. (34); and the gearbox, Eq. (37), according to the block diagram in Fig. 1. Defining the drive state vector $x_d = [x_b^T, x_h^T, x_g^T]^T$, we obtain the state equations

$$\dot{x}_d = A_d x_d + B_{dr} r + B_{dt} \dot{\theta}_p \Bigg\}$$

$$T = C_d x_d$$

(38a)

where

$$A_d = \begin{bmatrix} A_b & 0 & \dfrac{B_{b2} C_{g2}}{N_t} \\ B_{hi} C_b & A_h & B_{ho} C_{g2} + \dfrac{B_{hi} D_{be} C_{g2}}{N_t} \\ B_{g1} D_{hi} C_b & B_{g1} C_h & A_g + B_{g1} D_{ho} C_{g2} + \dfrac{B_{g1} D_{hi} D_{b2} C_{g2}}{N_t} \end{bmatrix}$$

$$B_{dr} = \begin{bmatrix} B_{b1} \\ B_{hi} D_{b1} \\ B_{g1} D_{hi} D_{b1} \end{bmatrix}$$

(38b)

$$B_{dt} = \begin{bmatrix} 0 \\ 0 \\ B_{g2} \end{bmatrix}$$

$$C_d = \begin{bmatrix} 0 & 0 & C_{g1} \end{bmatrix}$$

The plots of the magnitudes of the transfer function in azimuth and elevation from r to T are shown in Fig. 11. The plots of the transfer functions in azimuth and elevation from $\dot{\theta}_p$ to T are shown in Fig. 12.

III. Structure Model

The structural model is derived from the finite element model of the antenna structure with free rotations with respect to the elevation and azimuth axes. The finite element model consists of the diagonal modal mass $M_m(p \times p)$, diagonal natural frequencies matrix $\Omega(p \times p)$, diagonal modal damping matrix $Z(p \times p)$, and modal matrix $\Phi(m \times p), p \leq m$, which consists of p eigenvectors ϕ_i (mode shapes), $i = 1, \cdots, p$:

$$\Phi = [\phi_1, \phi_2, \cdots, \phi_p]$$

(39)

Let the finite element model have m degrees of freedom, with s inputs $u(t)$, where u is $s \times 1$ vector, and with r outputs $y(t)$, where y is $r \times 1$ vector. If the input matrix is $B_o(m \times s)$, the output matrix for displacement is $C_{oq}(r \times m)$, and the output matrix for rates is $C_{ov}(r \times m)$, then the input–output relationship is given by the following second-order differential equation:

$$\ddot{q}_m + 2Z\Omega\dot{q}_m + \Omega^2 q_m = M_m^{-1} \Phi^T B_o u \Bigg\}$$

$$y_m = C_{oq} \Phi q_m + C_{ov} \Phi \dot{q}_m$$

(40)

Define the state variable x as follows:
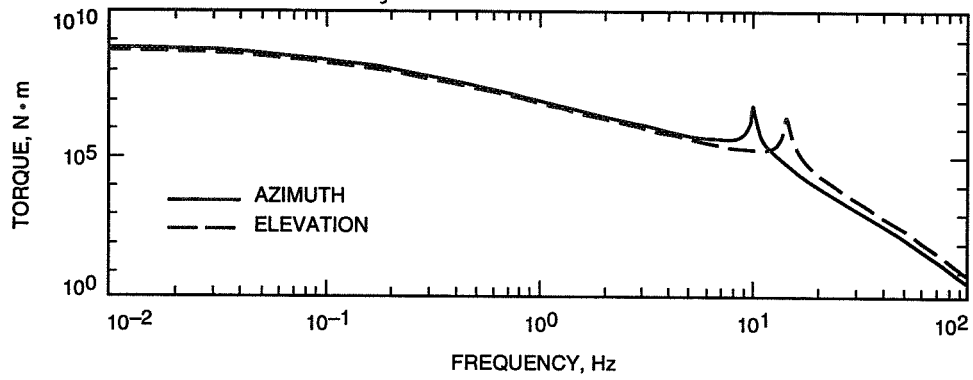
Fig. 11. Magnitude of the drive transfer function from the rate command to the output torque.
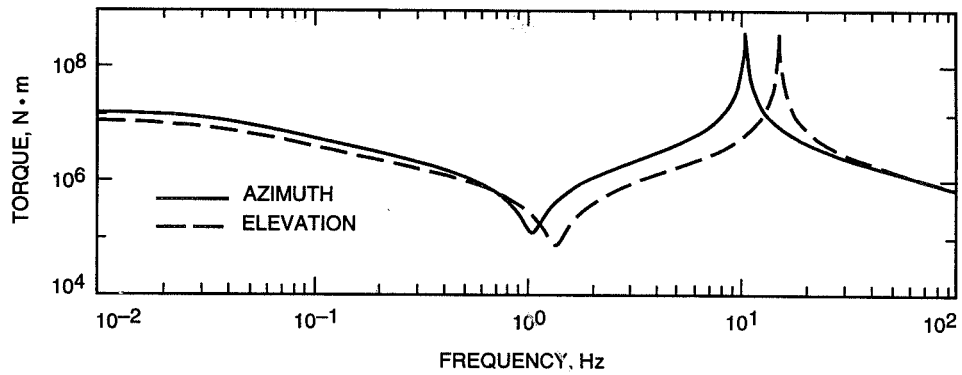
Fig. 12. Magnitude of the drive transfer function from the pinion rate to the output torque.

$$x_s = \begin{bmatrix} x_1 \\ x_2 \end{bmatrix} = \begin{bmatrix} q_m \\ \dot{q}_m \end{bmatrix} \tag{41}$$

where q_m and $\dot{q}_m$ are modal displacements and rates (such that $q = \Phi q_m; q$ is the actual displacement); then Eq. (40) can be presented as a set of first-order equations:

$$\left.\begin{aligned} \dot{x}_1 &= x_2 \\[1em] \dot{x}_2 &= -\Omega^2 x_1 - 2Z\Omega x_2 + M_m^{-1}\Phi B_o u_s \\[1em] y_s &= C_{oq}\Phi x_1 + C_{ov}\phi x_2 \end{aligned}\right\} \tag{42}$$

or in the following form:

$$\left.\begin{aligned} \dot{x}_s &= A_s x_s + B_s u_s \\[1em] y_s &= C_s x \end{aligned}\right\} \tag{43a}$$

where

$$A_s = \begin{bmatrix} 0 & I \\ -\Omega^2 & -2Z\Omega \end{bmatrix} \Bigg\}$$

$$B_s = \begin{bmatrix} 0 \\ M_m^{-1}\Phi^T B_o \end{bmatrix} \Bigg\} \qquad (43b)$$

$$C_s = [\, C_{oq}\Phi \quad C_{ov}\Phi \,] \Bigg\}$$

is the sought state–space model in modal coordinates. In our case, $u_s = [\, T_a \quad T_e \,]$, where T_a and T_e are torques at azimuth wheels and elevation pinions, respectively. The structure output consists of the elevation and azimuth encoder angles and rates, pinion angles, elevation and cross-elevation pointing errors, and other structural variables of interest. Two outputs, $\dot{\theta}_{pa}$ and $\dot{\theta}_{pe}$, the pinion rates in azimuth and elevation, are of special interest. Thus, the structural state–space equations are as follows:

$$\dot{x}_s = A_s x_s + B_{sa} T_a + B_{se} T_e \quad \Bigg\}$$

$$\dot{\theta}_{pa} = C_{pa} x_s$$

$$\qquad\qquad\qquad\qquad\qquad\qquad\qquad\qquad (44)$$

$$\dot{\theta}_{pe} = C_{pe} x_s$$

$$y = C_s x$$

The modal data obtained from the finite element model consist of 150 natural frequencies, ω_i; modes, ϕ_i; and modal masses, $m_{mi}, i = 1, \cdots, 150$. Additionally, based on the measurements, the modal damping is assumed to be 1 percent, i.e., $\zeta_i = 0.01$. Based on this information, the state matrix A_s, as in Eq. (43b), is determined by introducing the matrix of natural frequencies, $\Omega = diag(\omega_i)$, and modal damping, $Z = diag(\zeta_i), i = 1, \cdots, 150$.

The determination of matrices B_s and C_s is presented here for the azimuth wheel torque input and the azimuth wheel rate output. For the azimuth wheel torque input, consider the azimuth wheel of radius r_a and the azimuth rail of radius R_a. Let nodes n_1 be located at the contact point of the wheel and the rail. The torque applied to the wheel generates the force F_a at node n_1. The force is tangential to the azimuth rail. Assuming a rigid pinion, the force F_a applied to the wheel is

$$F_a = \frac{T_a}{r_a} \qquad (45)$$

This force has x and y components, F_{ax} and F_{ay} [see Fig. 13(a)], such that

$$F_{ax} = -F_a \cos\alpha_a = -\frac{T_a}{r_a}\cos\alpha_a \quad \Bigg\}$$

$$\qquad\qquad\qquad\qquad\qquad\qquad\qquad\qquad (46)$$

$$F_{ay} = F_a \sin\alpha_a = \frac{T_a}{r_a}\sin\alpha_a \quad \Bigg\}$$
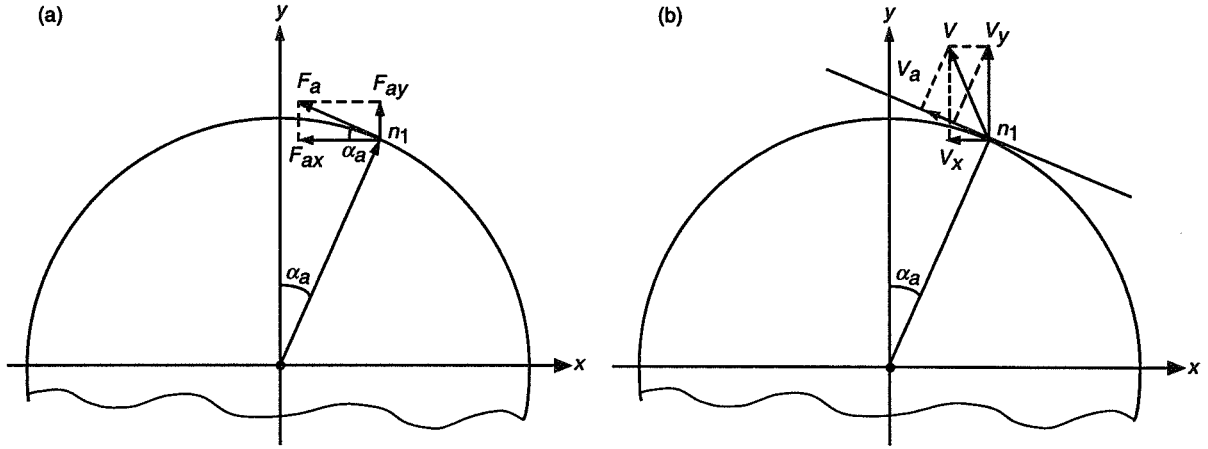
Fig. 13. Forces and rates at the azimuth pinion: (a) forces and (b) rates.

and α_a is the angle marked in this figure. Let e_x and e_y denote the unit vector (all but one component are zero, and the nonzero component is equal to one), with the unit component at the location of the x and y displacement of node n_1 in the finite element model. The input, F, to the finite element model is $F = F_{ax}e_x + F_{ay}e_y$. Therefore, B_o follows from the decomposition of F, such that $F = B_oT_a$. From Eq. (46), it follows that

$$B_o = -\frac{e_x}{r_a}\cos\alpha_a + \frac{e_y}{r_a}\sin\alpha_a \qquad (47)$$

Next, from Eq. (43b), it follows that the nonzero (lower) part of B, after introduction of Eq. (47), is

$$M_m^{-1}\Phi^T B_o = -M_m^{-1}\frac{\Phi^T e_x}{r_a}\cos\alpha_a + M_m^{-1}\frac{\Phi^T e_y}{r_a}\sin\alpha_a \qquad (48a)$$

$$= -M_m^{-1}\frac{\phi_x}{r_a}\cos\alpha_a + M_m^{-1}\frac{\phi_y}{r_a}\sin\alpha_a \qquad (48b)$$

where ϕ_x and ϕ_y are vectors of modal components of x and y displacements at node n_1:

$$\left.\begin{array}{l} \phi_x = \Phi^T e_x = [\phi_{x1},\phi_{x2},\cdots,\phi_{x150}]^T \\[3mm] \phi_y = \Phi^T e_y = [\phi_{y1},\phi_{y2},\cdots,\phi_{y150}]^T \end{array}\right\} \qquad (49)$$

where ϕ_{xi} and ϕ_{yi} are x and y displacements of mode i at node n_1. Therefore, from Eqs. (43b) and (48b), one obtains

$$B_s = \left[\begin{array}{c} 0 \\ -M_m^{-1}\dfrac{\phi_x}{r_a}\cos\alpha_a + M_m^{-1}\dfrac{\phi_y}{r_a}\sin\alpha_a \end{array}\right] \qquad (50)$$

The output matrix derivation is presented here for the wheel rate, $\dot{\theta}_{pa}$. The wheel rotation is

128

$$\dot{\theta}_{pa} = \frac{v_a}{r_a} \tag{51}$$

where v_a is the tangential velocity of the wheel at the contact point [see Fig. 13(b)]. If v_x and v_y are x and y components of v_a, and α_a is the angle marked in this figure, then

$$v_a = -v_x \cos \alpha_a + v_y \sin \alpha_a \tag{52}$$

therefore,

$$\dot{\theta}_{pa} = \left(-\frac{e_x^T}{r_a} \cos \alpha_a + \frac{e_y^T}{r_a} \sin \alpha_a \right) \dot{q} \tag{53a}$$

and in modal coordinates

$$\dot{\theta}_{pa} = \left(-\frac{\Phi e_x^T}{r_a} \cos \alpha_a + \frac{\Phi e_y^T}{r_a} \sin \alpha_a \right) \dot{q}_m = \left(-\frac{\phi_x^T}{r_a} \cos \alpha_a + \frac{\phi_y^T}{r_a} \sin \alpha_a \right) \dot{q}_m \tag{53b}$$

Finally, the matrix C_s, according to Eqs. (43b) and (53b), is

$$C_s = \left[0 \quad -\frac{\phi_x^T}{r_a} \cos \alpha_a + \frac{\phi_y^T}{r_a} \sin \alpha_a \right] \tag{54}$$

The structural model consists of $m = 150$ modes or 300 states. Modes not participating in system dynamics are eliminated. Observability and controllability properties in the balanced representation are used to determine insignificant modes. The balanced representation [9] is a state–space representation with equally controllable and observable states. The Hankel singular value is a measure of the joint controllability and observability of each balanced state variable. The states with small Hankel singular values are deleted as weakly excited and weakly observed, causing minimal modeling error.

For flexible structures with small damping and distinct poles, the modal representation is almost balanced, c.f. [10–12], and each mode is considered for the reduction separately. For a structure with m modes, matrix B_s has $2m$ rows, and C_s has $2m$ columns. Denote b_s as the last m rows of B_s, c_q as the first m columns of C_s, and c_r as the last m columns of C_s. Then b_{si} is the ith row of b_s, c_{qi} is the ith column of c_q, and c_{ri} is the ith column of c_r. Denote $\beta_{si}^2 = b_{si} b_{si}^T, \alpha_{qi} = c_{qi}^T c_{qi}$, and $\alpha_{ri} = c_{ri}^T c_{ri}$. The Hankel singular value for the ith mode is given in [11] and [12]:

$$\gamma_i^2 = \frac{w_{bi} \beta_{si} \sqrt{w_{qi}^2 \alpha_{qi}^2 + w_{ri}^2 \omega_i^2 \alpha_{ri}^2}}{4 \zeta_i \omega_i^2} \tag{55}$$

where the weighting factors $w_{bi} > 0, w_{qi} > 0, w_{ri} > 0$, and $i = 1, \cdots, m$.

Care should be taken when determining Hankel singular values. Units should be consistent; otherwise, some inputs or outputs receive more weight in Hankel singular-value determination than necessary. Consider, for example, the azimuth encoder reading in arcseconds and the elevation encoder reading in degrees. For the same angle, the numerical reading of the azimuth encoder is 3600 larger than the elevation encoder reading; hence, the elements for the azimuth output are much larger than those for elevation.

On the other hand, some variables need more attention than others: Pointing error and encoder readings are the most important factors in the antenna performance; hence, their importance has to be emphasized in mode evaluation. For consistency of units and importance of variables, the weighting factors w_{bi}, w_{qi}, and w_{ri} are introduced. Typically, weights are set to 1.

For each mode, the Hankel singular value is determined and used to decide on the number of modes in the reduced structural model. For the rigid body modes, Hankel singular values tend to infinity; hence, rigid body modes are always included in the reduced model. Hankel singular values of the 150 modes of the antenna model are plotted in Fig. 14. The reduced order model consists of 24 modes: 2 rigid-body modes and 22 flexible modes.

The plots of the transfer function in azimuth and elevation (magnitude and phase) from the wheel (pinion) torque T to the axis rate $\dot{\theta}$ are shown in Fig. 15. They show that the azimuth transfer function has low frequency resonances (about 1.2 and 2.2 Hz), which are absent in the elevation transfer function.
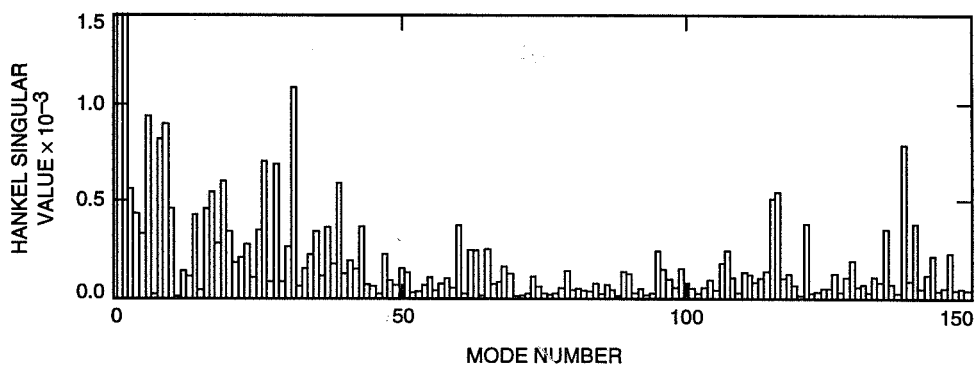
Fig. 14. Hankel singular values for the antenna structure.
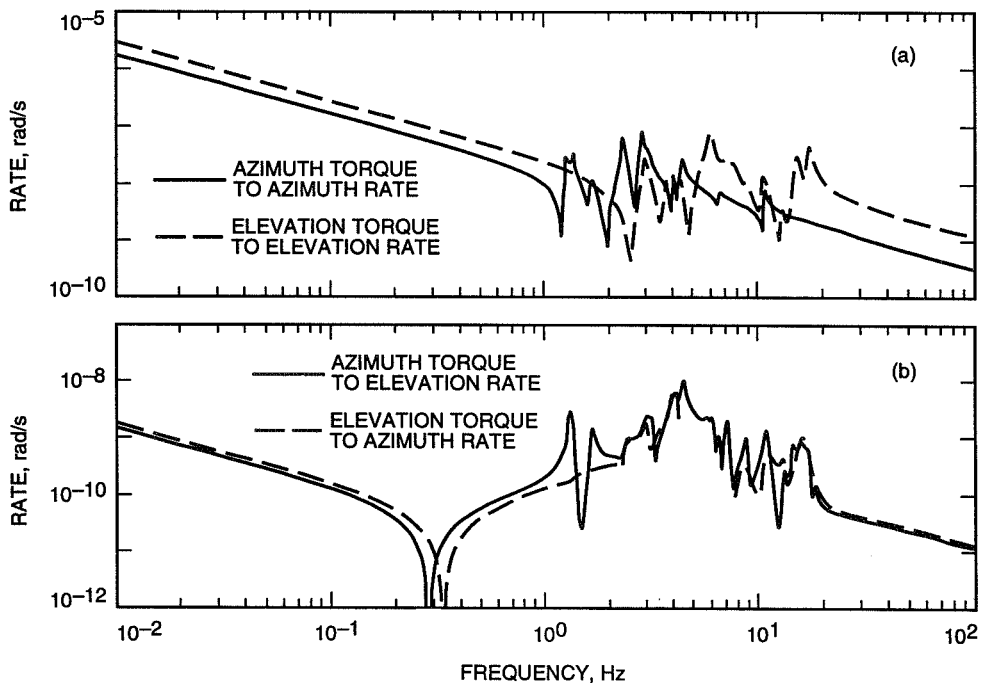
Fig. 15. Magnitude of the transfer function of the antenna structure: (a) direct coupling and (b) cross-coupling.

IV. Rate Loop Model

A rate loop block diagram is presented in Fig. 16, where T_a and T_e denote the drive torques, $\dot{\theta}_{pa}$ and $\dot{\theta}_{pe}$ denote pinion rates, and r_a and r_e are rate commands in azimuth and elevation, respectively. The state–space equations are combined from the state equations of the azimuth and elevation drives [see Eq. (38) and add subscript "a" for the azimuth drive and subscript "e" for the elevation drive] and the structure [see Eq. (44)]. Combining them, and defining the rate loop state vector x_r as $x_r = [x_{da}, x_{de}, x_s]$, where x_{da} and x_{de} are azimuth and elevation drive states, one obtains the rate-loop state–space equations:

$$\left.\begin{aligned}
\dot{x}_r &= A_r x_r + B_{ra} r_a + B_{re} r_e \\[2mm]
y &= C_r x_r \\[2mm]
\theta_a &= C_a x_r \\[2mm]
\theta_e &= C_e x_r
\end{aligned}\right\} \tag{56a}$$

where

$$\left.\begin{aligned}
A_r &= \begin{bmatrix} A_{da} & 0 & B_{dta}C_{pa} \\ 0 & A_{de} & B_{dte}C_{pe} \\ B_{sa}C_{da} & B_{se}C_{de} & A_s \end{bmatrix} \\[4mm]
B_{ra} &= \begin{bmatrix} B_{dra} \\ 0 \\ 0 \end{bmatrix} \\[4mm]
B_{re} &= \begin{bmatrix} 0 \\ B_{dre} \\ 0 \end{bmatrix} \\[4mm]
C_r &= \begin{bmatrix} 0 & 0 & C_s \end{bmatrix}
\end{aligned}\right\} \tag{56b}$$

where θ_a and θ_e are azimuth and elevation encoder readings, C_{pa} and C_{pe} are the output matrices for the azimuth and elevation pinion rates, and C_a and C_e are the output matrices for the azimuth and elevation encoders, respectively.

Figure 17 shows the magnitude of the transfer function from the azimuth rate input r_a to the azimuth encoder rate $\dot{\theta}_a$ (solid line) and the magnitude of the transfer function from the elevation rate input r_e to the elevation encoder rate $\dot{\theta}_e$ (dashed line). The figure shows that the required identity relationship for low frequencies is not acquired. The magnitude of the transfer functions for frequencies less than 0.3 Hz is 0.74, below the required 1, due to inaccuracy in the model parameters (mainly in the hydraulic part). This drawback can be removed by the experimental investigation of the parameters of the hydraulic drives, such as motors, valves, and lines. However, this inaccuracy is corrected by the position feedback loop, as will be shown later. The high-frequency peaks in azimuth and elevation (8 Hz in azimuth and 20 Hz in elevation) are the gearbox resonances.
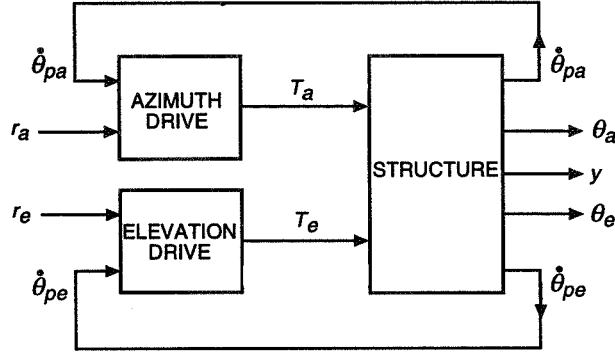
Fig. 16. Block diagram of the rate loop model.
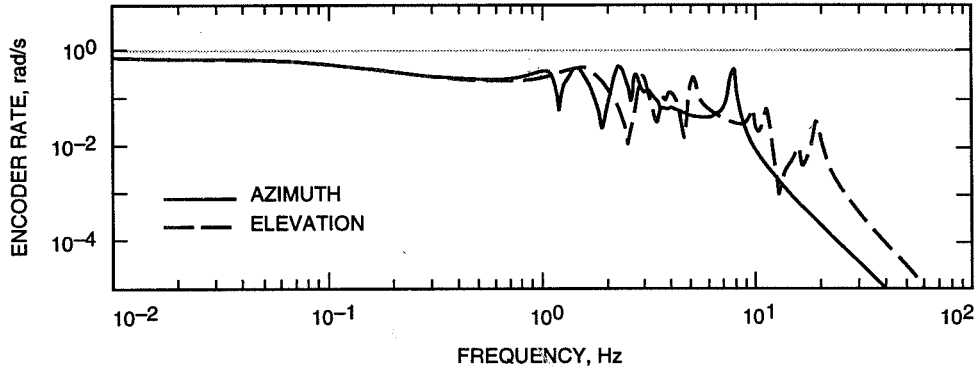
Fig. 17. Magnitude of the transfer function of the rate loop model.

V. Position Loop Model

The rate loop system with the proportional and integral (PI) controller is shown in Fig. 18, where e_a and e_e are the azimuth and elevation servo errors. For the series connection of the rate loop system and the controller, as in Fig. 18(a), define the state vector $x_o^T = [\, x_{ai} \quad x_{ei} \quad x_{rl}^T \,]$ with the new state variables x_{ei} and x_{ai} (integrals of the errors) such that

$$\left. \begin{aligned} \dot{x}_{ai} &= e_a \\[1em] \dot{x}_{ei} &= e_e \end{aligned} \right\} \tag{57}$$

The system output y is defined in Eq. (56a), the encoder output is $\theta^T = [\, \theta_a \quad \theta_e \,]$, and the input is $e^T = [\, e_a \quad e_e \,]$. The inputs to the rate loop systems are obtained from Fig. 18(a):

$$\left. \begin{aligned} r_a &= k_{pa}e_a + k_{ia}x_{ai} \\[1em] r_e &= k_{pe}e_e + k_{ie}x_{ei} \end{aligned} \right\} \tag{58}$$

where k_{pe}, k_{ie}, k_{pa}, and k_{ia} are proportional and integral parameters of the controllers. Combining the equations for the rate loop system with Eqs. (57) and (58), one obtains
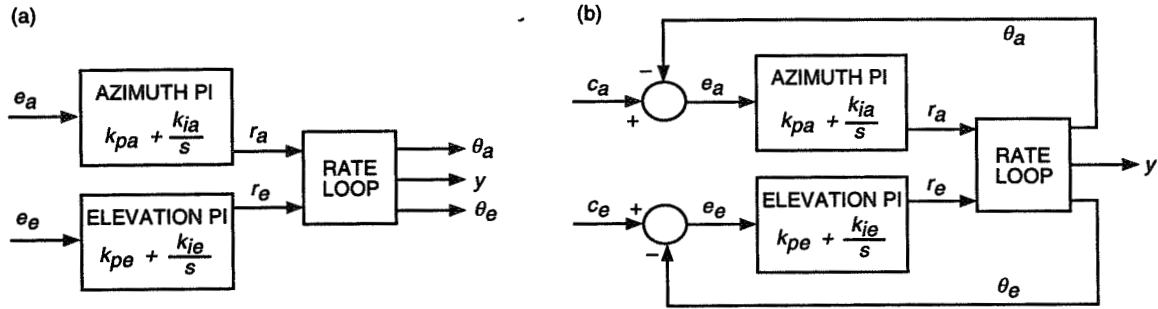
Fig. 18. Position loop: (a) open and (b) closed.

$$
\left.
\begin{aligned}
\dot{x}_o &= A_o x_o + B_o e \\[2mm]
\theta &= C_o x_o \\[2mm]
y &= C x_o
\end{aligned}
\right\}
\tag{59a}
$$

where

$$
\left.
\begin{aligned}
A_o &= \begin{bmatrix} 0 & 0 & 0 \\ 0 & 0 & 0 \\ k_{ia} B_{ra} & k_{ie} B_{re} & A_r \end{bmatrix} \\[3mm]
B_o &= \begin{bmatrix} I & 0 \\ 0 & I \\ k_{pa} B_{ra} & k_{pe} B_{re} \end{bmatrix} \\[3mm]
C_o &= \begin{bmatrix} 0 & 0 & C_a \\ 0 & 0 & C_e \end{bmatrix} \\[3mm]
C &= \begin{bmatrix} 0 & 0 & C_r \end{bmatrix}
\end{aligned}
\right\}
\tag{59b}
$$

For the closed-loop system [see Fig. 18(b)],

$$
e = c - \theta
\tag{60}
$$

where $c^T = [c_a \quad c_e]$ is a command signal in azimuth, c_a, and in elevation, c_e. Introducing Eq. (60) to Eq. (59), one obtains

$$
\left.
\begin{aligned}
\dot{x}_{cl} &= A_{cl} x_{cl} + B_o c \\[2mm]
y &= C x_{cl}
\end{aligned}
\right\}
\tag{61a}
$$

where

$$A_{cl} = A_o - B_o C_o \qquad\qquad (61b)$$

The simulations shown in Figs. 19 through 22 have two sets of assumptions: (1) a proportional gain of 1 in azimuth and elevation and an integral gain of 0.3 and (2) a proportional gain of 0.7 in azimuth and elevation and an integral gain of 0.2. The closed-loop transfer functions from azimuth command to azimuth encoder are shown in Fig. 19(a), and those from elevation command to elevation encoder are shown in Fig. 19(b). They show a bandwidth of 0.1 Hz. The cross-coupling transfer functions from azimuth command to elevation encoder and from elevation command to azimuth encoder are shown in Fig. 20. They show low-level cross-coupling. The closed-loop step responses from azimuth command to azimuth encoder are shown in Fig. 21(a), and those from elevation command to elevation encoder are shown in Fig. 21(b). They show a 20- to 30-percent overshoot and a 7- to 9-s settling time. The cross-coupling from azimuth step command to elevation encoder and from elevation step command to azimuth encoder is shown in Fig. 22. The cross-coupling is of the order 10^{-3}.
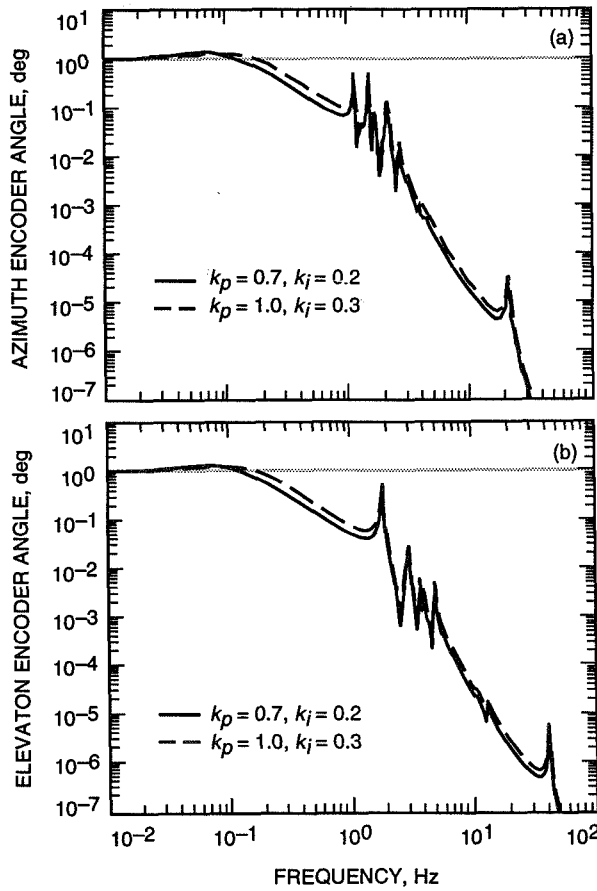
Fig. 19. Magnitude of the transfer function of the closed-loop system: (a) azimuth command to azimuth encoder and (b) elevation command to elevation encoder.
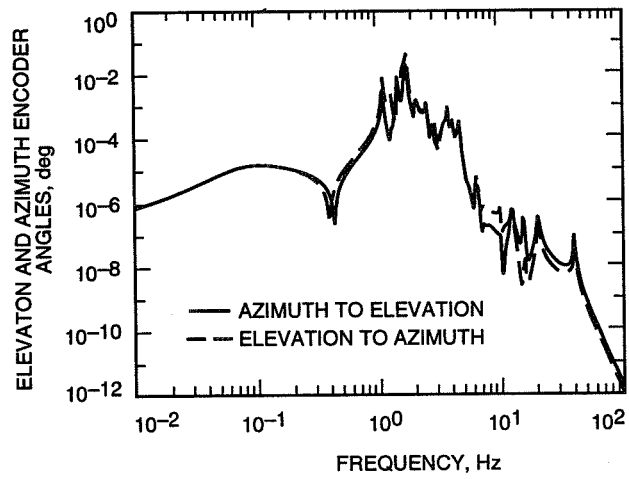
Fig. 20. Magnitude of the transfer function of the closed-loop system: azimuth command to elevation encoder and elevation command to azimuth encoder.
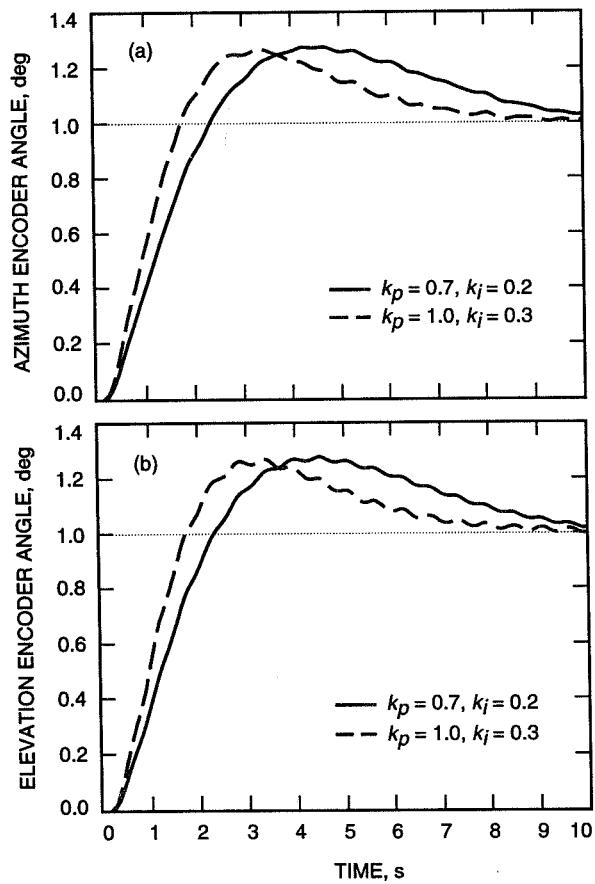
Fig. 21. Step responses of the closed-loop system: (a) azimuth command to azimuth encoder and (b) elevation command to elevation encoder.
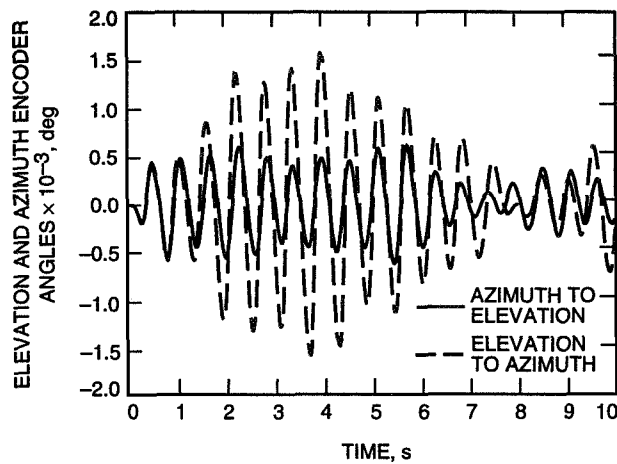
Fig. 22. Step responses of the closed-loop system: azimuth command to elevation encoder and elevation command to azimuth encoder.

VI. Wind Disturbance Simulations

Wind gust disturbances were modeled similarly to the DSS-13 antenna (see [13]) using the wind tunnel pressure distribution on the dish taken from Blaylock.[1] Their time history is generated using the wind Davenport spectrum (see [14] and [15]), determined for the Goldstone site. The simulations for the 50 km/h wind gave the results listed in Table 4 and compared with the simulation results of the DSS-13 antenna. The table shows that DSS 14 has better disturbance rejection properties (at the encoders) than has the DSS-13 antenna.

Table 4. Servo errors in mdeg (3σ rms) for 50 km/h wind gusts.

Drive	Front wind	Side wind
Elevation, DSS 14	2.6	0.7
Elevation, DSS 13	14.6	1.9
Azimuth, DSS 14	0.1	2.1
Azimuth, DSS 13	0.5	2.3

VII. Conclusions

An analytical model of the DSS-14 antenna has been developed. The rate loop model consists of the structural model (derived from the finite element model), gearbox model, hydraulic servo, and electronic boxes. The position loop was closed, and the time and frequency responses were simulated. The wind pointing errors of the DSS-14 antenna have been simulated. The model allows for detailed simulation of antenna dynamics and for modifications and improvements to the antenna control system.

The simulations confirmed that the use of encoders located at drives limits the performance of the antenna (mainly by reducing its bandwidth to 0.1 Hz). The use of the master equatorial or new encoders

---

[1] R. B. Blaylock, "Aerodynamic Coefficients for Model of a Paraboloidal Reflector Directional Antenna Proposed for a JPL Advanced Antenna System," JPL Interoffice Memorandum CP-6 (internal document), Jet Propulsion Laboratory, Pasadena, California, 1964.

located close to the axes of rotation of the antenna (similarly to the 34-m antennas) would allow expansion of the bandwidth to 0.7–1.0 Hz.

The antenna model needs further improvement. First, in this model, certain parameters of the hydraulic drive are known with rather poor accuracy, and it influences the accuracy of the antenna model. It is essential to use experimental techniques to get more precise values of the parameters. Secondly, the RF pointing errors (in elevation and cross-elevation) of the antenna should be determined in order to evaluate the precision of the antenna pointing.

Acknowledgments

References

[1] R. E. Hill, "A New State Space Model for the NASA/JPL 70-Meter Antenna Servo Controls," *The Telecommunications and Data Acquisition Progress Report 42-91, July–September 1987*, Jet Propulsion Laboratory, Pasadena, California, pp. 247–294, November 15, 1987.

[2] R. E. Hill, "Dynamic Models for Simulation of the 70-m Antenna Axis Servos," *The Telecommunications and Data Acquisition Progress Report 42-95, July–September 1988*, Jet Propulsion Laboratory, Pasadena, California, pp. 32–50, November 15, 1988.

[3] W. Gawronski and J. A. Mellstrom, "Modeling and Simulations of the DSS-13 Antenna Control System," *The Telecommunications and Data Acquisition Progress Report 42-106, April–June 1991*, Jet Propulsion Laboratory, Pasadena, California, pp. 205–248, August 15, 1991.

[4] W. Gawronski and J. A. Mellstrom, "Control and Dynamics of the Deep Space Network Antennas," *Control and Dynamic Systems*, vol. 63, edited by C. T. Leondes, San Diego, California: Academic Press, 1994.

[5] W. Gawronski and J. A. Mellstrom, "Elevation Control System Model of the DSS-13 Antenna," *The Telecommunications and Data Acquisition Progress Report 42-105, January–March 1991*, Jet Propulsion Laboratory, Pasadena, California, pp. 83–108, May 15, 1991.

[6] R. D. Bartos, "Dynamic Modeling of the Servo Valves Incorporated in the Servo Hydraulic System of the 70-Meter DSN Antennas," *The Telecommunications and Data Acquisition Progress Report 42-108, October–December 1991*, Jet Propulsion Laboratory, Pasadena, California, pp. 222–234, February 15, 1992.

[7] R. D. Bartos, "Dynamic Modeling of the Fluid Transmission Lines of the DSN 70-Meter Antennas by Using a Lumped Parameter Model," *The Telecommunications and Data Acquisition Progress Report 42-109, January–March 1992*, Jet Propulsion Laboratory, Pasadena, California, pp. 162–169, May 15, 1992.

[8] R. D. Bartos, "Mathematical Modeling of Bent-Axis Hydraulic Piston Motors," *The Telecommunications and Data Acquisition Progress Report 42-111, July–September 1992*, Jet Propulsion Laboratory, Pasadena, California, pp. 224–235, November 15, 1992.

[9] B. C. Moore, "Principal Component Analysis in Linear Systems, Controllability, Observability and Model Reduction," *IEEE Trans. Autom. Control*, vol. 26, pp. 17–32, 1981.

[10] A. Jonckheere, "Principal Component Analysis of Flexible Systems—Open Loop Case," *IEEE Trans. Autom. Control*, vol. 27, pp. 1095–1097, 1984.

[11] W. Gawronski and J. N. Juang, "Model Reduction for Flexible Structures," *Control and Dynamic Systems*, vol. 36, edited by C. T. Leondes, San Diego, California: Academic Press, pp. 143–222, 1990.

[12] W. Gawronski, *Balanced Control of Flexible Structures*, London: Springer, 1996.

[13] W. Gawronski, B Bienkiewicz, and R. E. Hill, "Wind-Induced Dynamics of a Deep Space Network Antenna," *Journal of Sound and Vibration*, vol. 174, no. 5, 1994.

[14] A. G. Davenport, "The Spectrum of Horizontal Gustiness Near the Ground in High Winds," *Journal of Royal Meteorol. Society*, vol. 87, pp. 194–211, 1961.

[15] E. Simiu and R. H. Scanlan, *Wind Effects on Structures*, New York: Wiley, 1978.

Appendix

Transfer Function Derivation

Each component of the electronics board is composed of operational amplifiers (opamps), resistors, and capacitors. The basic configuration of an inverting opamp circuit is shown in Fig. A-1. The "+" terminal of the opamp is grounded; thus, the "−" terminal voltage is zero, called a virtual ground. In this situation, the currents i_1 and i_2 flowing through impedances Z_1 and Z_2 are equal to

$$\left. \begin{aligned} i_1 &= \frac{v_{in}}{Z_1} \\[2mm] i_2 &= \frac{v_{out}}{Z_2} \end{aligned} \right\} \tag{A-1}$$

and their sum is zero; that is, $i_1 = -i_2$. Introducing them to Eq. (A-1) gives

$$v_{out} = -k v_{in} \tag{A-2a}$$

where

$$k = \frac{Z_2}{Z_1} \tag{A-2b}$$
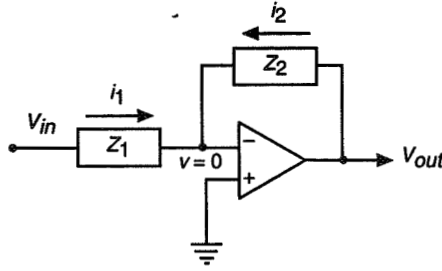
Fig. A-1. Opamp circuit.

I. Transfer Function G_{to}

A schematic for the transfer function G_{to} is shown in Fig. A-2(a), where the notation and the value of each element were taken from JPL Drawing 9479871D.[2] This schematic can be simplified to the one shown in Fig. A-2(b). In this figure,

$$R_s = \left(R_{56}^{-1} + R_{57}^{-1} + R_{58}^{-1} + R_{59}^{-1}\right)^{-1} + R_{62} = 49.5 \text{ k}\Omega \tag{A-3a}$$

where $R_{56} = R_{57} = R_{58} = R_{59} = 100$ kΩ, and $R_{62} = 24.5$ kΩ; thus, $R_s = 49.5$ kΩ. The component Z_1 is

$$Z_1 = R_{63} + \frac{R_{64}}{1 + R_{64}C_{40}s} \cong R_{63} + R_{64} = 91.1 \text{ k}\Omega \tag{A-3b}$$

where $R_{63} = 40$ kΩ, $R_{64} = 51.1$ kΩ, and $C_{40} = 0.15$ μF. The time constant $R_{64}C_{40} = 0.0077$ s is small, thus neglected. Denote $R_{mta} = 9.7$ kΩ and $R_{mte} = 7.8$ kΩ the motor resistances in azimuth and elevation, respectively, and $C_{41} = 0.15$ μF. Then, the component Z_2 for the azimuth drive is as follows:

$$Z_2 = \frac{R_{mta}}{1 + R_{mta}C_{41}s} \cong R_{mta} = 9.7 \text{ k}\Omega \tag{A-4a}$$

and for the elevation drive,

$$Z_2 = \frac{R_{mte}}{1 + R_{mte}C_{41}s} \cong R_{mte} = 7.8 \text{ k}\Omega \tag{A-4b}$$

The time constants $R_{mta}C_{41} = 0.0015$ s and $R_{mte}C_{41} = 0.0012$ s are of the order 10^{-3} s, thus considered small, and neglected.

The transfer function G_{to} for azimuth is

$$G_{to} = \frac{R_p}{R_s + R_p} = \frac{8800}{49,500 + 8800} = 0.151 \tag{A-5a}$$

and for elevation, it is

---

[2] JPL Drawing 9479871D (internal document), Jet Propulsion Laboratory, Pasadena, California.

$$G_{to} = \frac{R_p \cdot}{R_s + R_p} = \frac{7200}{49,500 + 7200} = 0.127 \qquad \text{(A-5b)}$$

where $R_p = \left(Z_1^{-1} + Z_2^{-1}\right)^{-1} = 8.8$ kΩ in azimuth and 7.2 kΩ in elevation, while $R_s = 49.5$ kΩ.
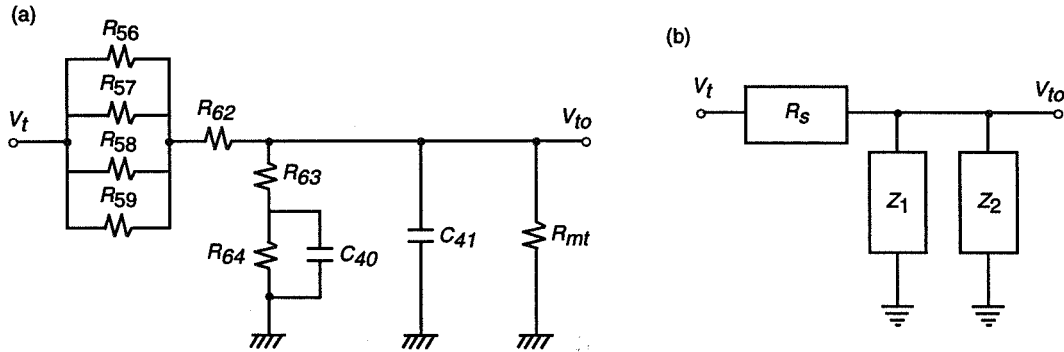
Fig. A-2. Schematic for the transfer function G_{to}: (a) full and (b) simplified.

II. Transfer Functions G_{r1} and G_{r2}

The transfer functions G_{r1} and G_{r2} are determined simultaneously. Their schematic is given in Fig. A-3(a), the parameters parameters of which are

$$
\left.
\begin{aligned}
R_{15} &= 750 \text{ k}\Omega \\[4pt]
R_{50} &= 100 \text{ k}\Omega \\[4pt]
R_{51} &= 12.1 \text{ k}\Omega \\[4pt]
R_{52} &= 442 \text{ k}\Omega \\[4pt]
R_{53} &= 442 \text{ k}\Omega \\[4pt]
R_{65} &= 909 \text{ k}\Omega \\[4pt]
R_{66} &= 90.9 \text{ k}\Omega \\[4pt]
C_{31} &= 1 \ \mu\text{F} \\[4pt]
C_{42} &= 0.1 \ \mu\text{F}
\end{aligned}
\right\} \qquad \text{(A-6)}
$$

The schematic from Fig. A-3(a) can be transformed to the form shown in Fig. A-3(b). The value of Z_3 is as follows:

$$Z_3 = R_{66} + \frac{R_{65}}{1 + R_{65}C_{42}s} \cong R_{66} + R_{65} = 10^6 \text{ k}\Omega \qquad \text{(A-7)}$$

In this variable, the small time constant $R_{65}C_{42} = 0.0909$ s was ignored.

The value Z_4 is obtained as

$$Z_4 = R_{53} + \frac{R_o}{1 + R_oC_{31}s} = 4.65 \times 10^6 \frac{1 + 0.400s}{1 + 4.205s} \tag{A-8}$$

where $R_o = (R_{50} + R_{52} + R_{50}R_{52})/R_{51} = 4205$ kΩ.

Having determined Z_3 and Z_4, the transfer functions G_{r1} (from v_r to v_s) and G_{r2} (from v_{to} to v_s) are obtained:

$$\left. \begin{aligned} G_{r1} &= \frac{Z_4}{R_{15}} = 6.20 \ G_o \\[2ex] G_{r2} &= -\frac{Z_4}{Z_3} = -4.65 \ G_o \end{aligned} \right\} \tag{A-9}$$

where

$$G_o = \frac{1 + 0.400s}{1 + 4.205s} \tag{A-10}$$

is the transfer function of a lag compensator.

(a)

(b)
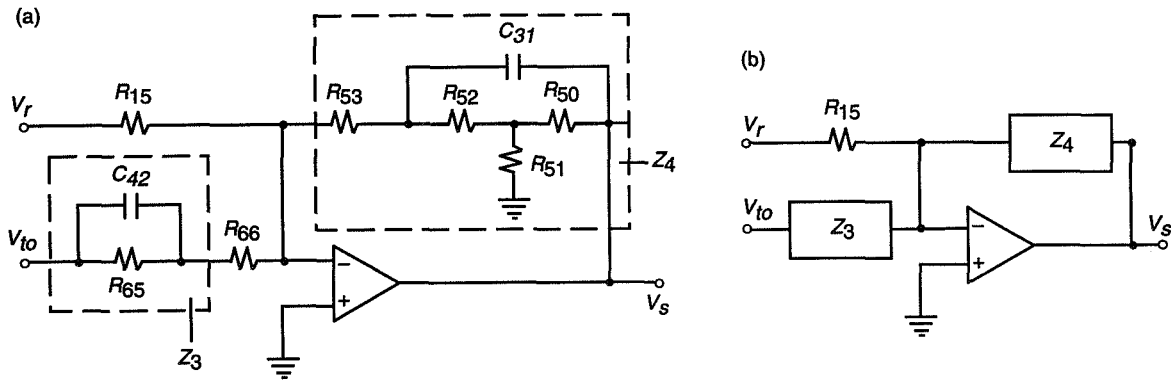
Fig. A-3. Schematic for the transfer functions G_{r1} and G_{r2}: (a) full and (b) simplified.

III. Transfer Function G_S

The transfer function G_s is determined from the schematic in Fig. A-4(a), and is shown in compact form in Fig. A-4(b). For this schematic, $R_{13} = 100$ kΩ, $R_{36} = 10$ kΩ, $R_{43} = 24.9$ kΩ, and $C_{18} = 0.1$ μF; therefore, one obtains

$$Z_5 = \frac{R_{36}}{1 + R_{36}C_{18}s} \cong R_{36} = 10 \text{ k}\Omega \tag{A-11}$$

where $R_{36}C_{18} = 0.0015$ s $\cong 0$. Since $v_1 = v_s Z_5/R_{43}$, and $i_s = v_1(Z_5^{-1} + R^{-1})$, thus,

$$G_s = \frac{i_s}{v_s} = \frac{R_{13} + Z_5}{R_{13}R_{43}} = 4.42 \times 10^{-5} \qquad \text{(A-12)}$$
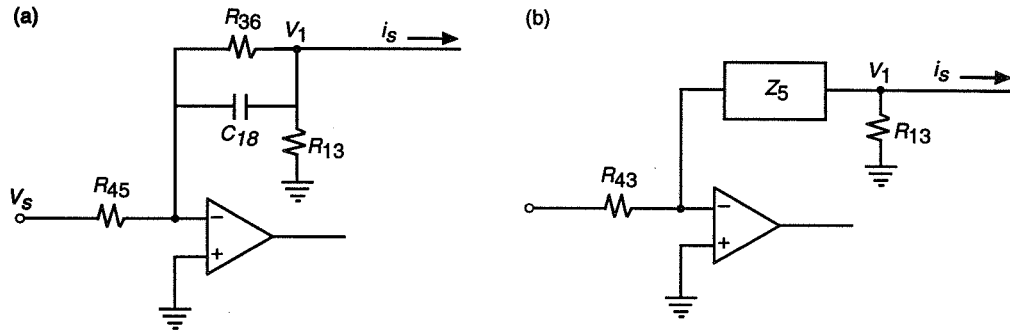
Fig. A-4. Schematic for the transfer function G_s: (a) full and (b) simplified.

A Prototype Ka-/Ka-Band Dichroic Plate With Stepped Rectangular Apertures

J. C. Chen, P. H. Stanton, and H. F. Reilly, Jr.
Communications Ground Systems Section

A prototype five-layer Ka-/Ka-band dichroic plate was fabricated and measured. This dichroic plate was designed to pass Ka-band uplink (34.2–34.7 GHz) and to reflect Ka-band downlink (31.8–32.3 GHz) for dual-frequency operation in the Deep Space Network to support the future Cassini mission. The theoretical calculation and the experimental measurement of the reflected resonant frequencies were within 0.24 percent for circular polarization. The computer program, which was used to design the dichroic plate with stepped apertures, was then verified.

I. Introduction

A dichroic plate was needed for simultaneous Ka-band uplink and downlink operation. In order to diplex two frequency bands with only a 1:1.07 ratio, stepped apertures were chosen for the Ka-/Ka-band dichroic plate design [1]. The stepped apertures, acting as resonator filters, pass the high-frequency band (Ka-band uplink, 34.2–34.7 GHz) and reflect the low-frequency band (Ka-band downlink, 31.8–32.3 GHz). The five-step aperture is a rectangular waveguide with two thin irises that divide the waveguide into three sections (Fig. 1).

II. Calculated Reflected and Transmitted Radiation Patterns and Power

The reflected and transmitted radiation patterns and power were calculated based on an incident horn pattern model at 32.0 and 34.5 GHz [2]. A 26-dB horn radiation pattern was used as the input pattern to the Ka-/Ka-band dichroic plate. The reflected and transmitted patterns were calculated at every $\phi = 12.25$-deg interval and $\theta = 1$-deg increment. The θ is the angle measured from the axis of rotation of the feedhorn (or its image in the case of a reflected pattern). The ϕ is the rotational angle around the above axis. The Cray supercomputer was used to perform this intensive calculation since 80 waveguide modes were required to ensure accuracy. The reflected and transmitted patterns are shown in Figs. 2 through 5 for the two linear polarizations that are orthogonal to each other at 32.0 and 34.5 GHz, respectively. The transmitted and reflected patterns of 32.0 GHz are similar to the incident horn pattern except that the peaks of the transmitted patterns are about −45 dB. The transmitted patterns of 34.5 GHz are similar to the incident horn pattern, while the peaks of the reflected patterns are about −20 dB.

The transmitted and reflected power can be calculated by integrating the transmitted and reflected patterns. It was found that 99.99 percent of the power is reflected and 0.01 percent leaks through the
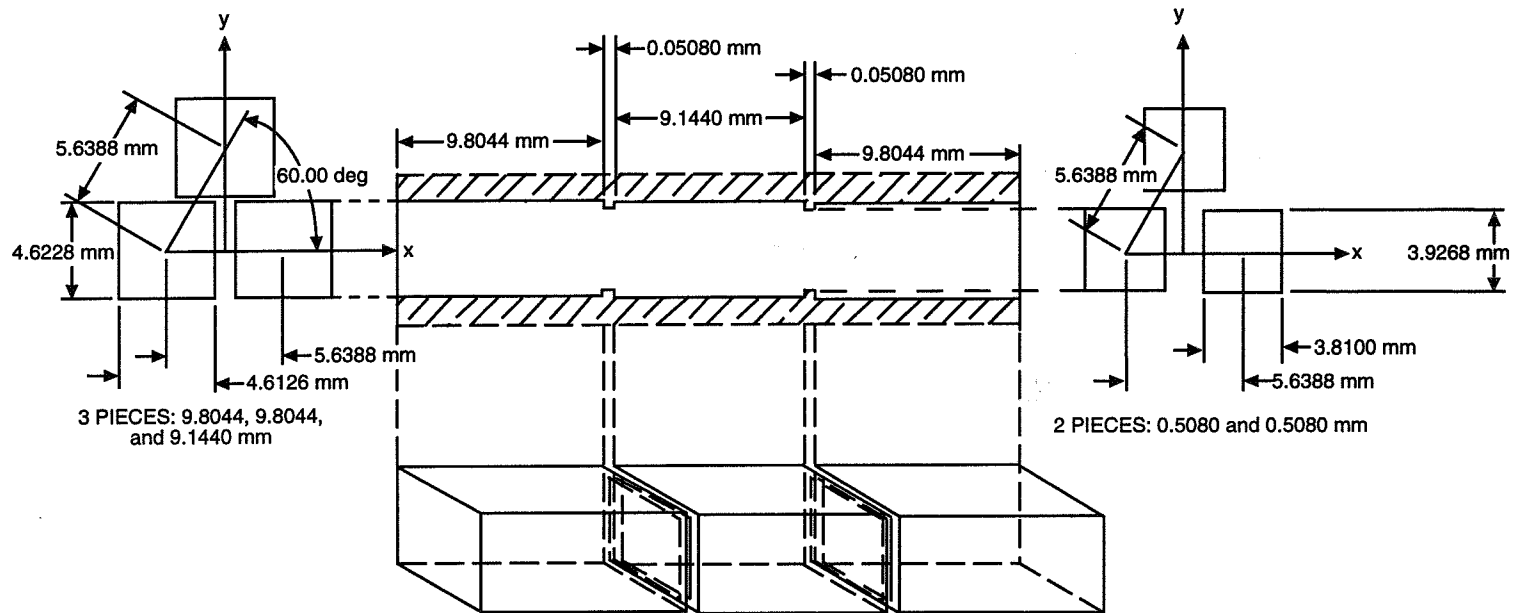
Fig. 1. Geometry of the aperture in the Ka-/Ka-band dichroic plate.

plate at 32 GHz. The power leakage may contribute 0.03 K of the noise temperature to the antenna system at DSS 13 at 34.5 GHz; 2.0 percent of the power is reflected and 98 percent is transmitted. The reflection and transmission coefficients versus frequencies were also calculated. The detailed information is in [1].
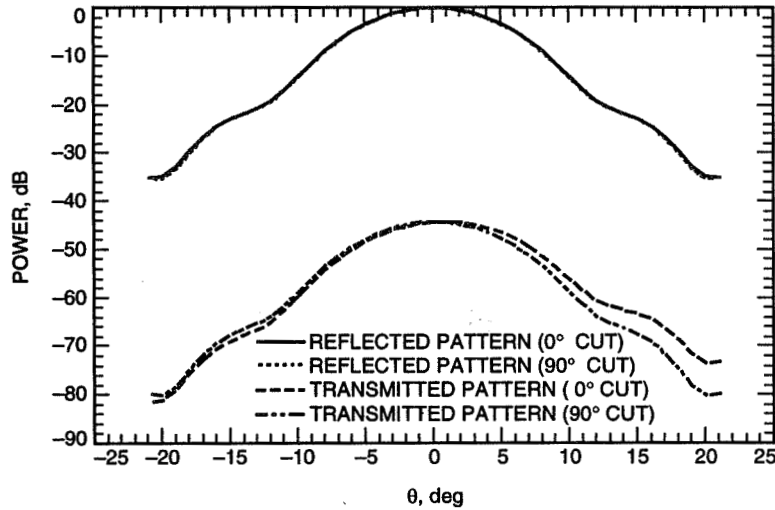
Fig. 2. Calculated reflected and transmitted radiation pattern of a Ka-/Ka-band dichroic plate at 32 GHz for linear polarization.
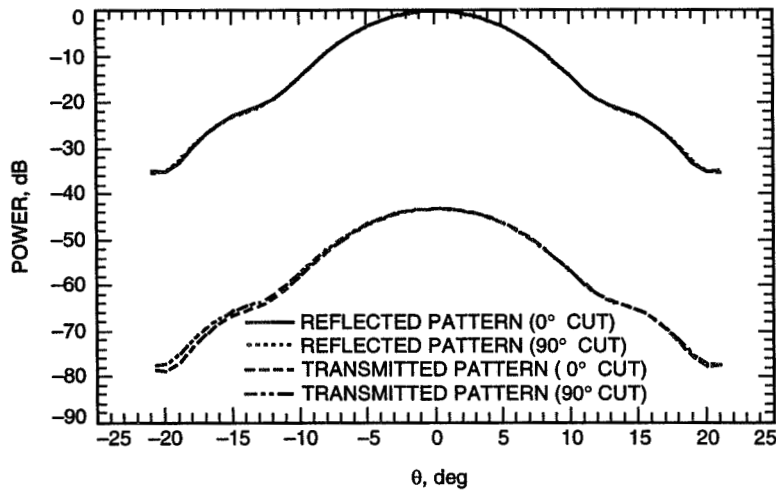
Fig. 3. Calculated reflected and transmitted radiation pattern of a Ka-/Ka-band dichroic plate at 32 GHz for the orthogonal linear polarization.
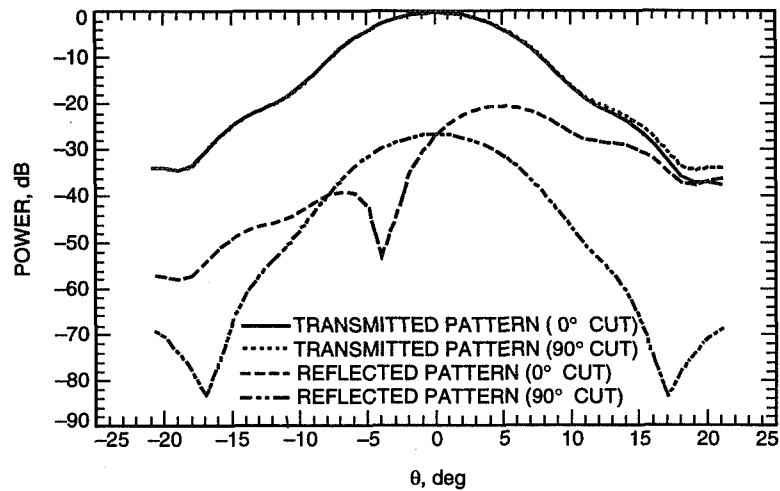
Fig. 4. Calculated reflected and transmitted radiation pattern of a Ka-/Ka-band dichroic plate at 34.5 GHz for linear polarization.
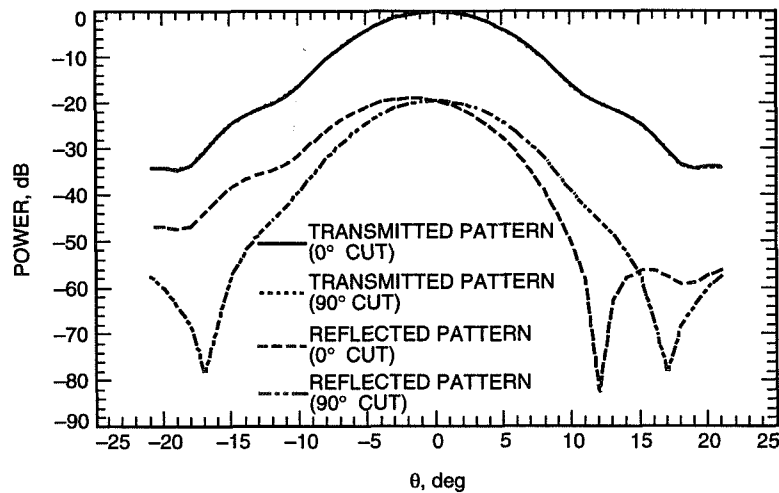
Fig. 5. Calculated reflected and transmitted radiation pattern of a Ka-/Ka-band dichroic plate at 34.5 GHz for the orthogonal linear polarization.

III. Fabrication

The prototype Ka-/Ka-band dichroic plate was a 177.8-mm-by-177.8-mm five-layer copper plate with a 152.4-mm-diameter perforated area (Fig. 6). The advantage of having only two different aperture sizes is a reduction of the fabrication cost. Since multiple metal sheets can be stacked together to be wire electrical-discharge machined when the sheets have an identical pattern, only two sets of sheets need to be run though the machine.

Previous dichroic plate fabrication dictated that, due to the tight tolerance and the cost, the wire electrical-discharge machine was the best way to fabricate rectangular apertures. The five-layer plate required a way to combine the layers into a solid structure. Holes in all four corners of the five plates were used to align the rectangular apertures and the five plates.
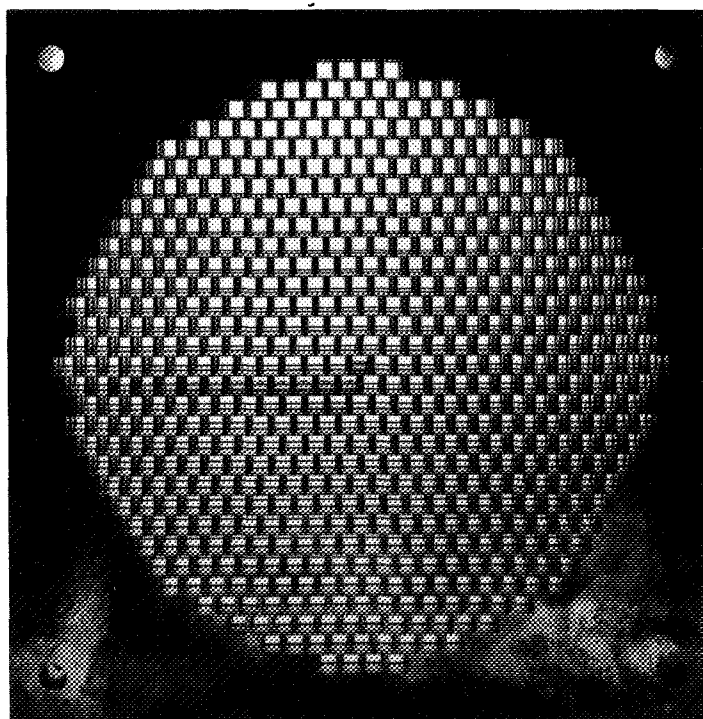
Fig. 6. Prototype Ka-/Ka-band dichroic plate.

Pure silver was deposited on both sides of the two thin plates in an electroless solution for a thickness of from 0.00508 to 0.00762 mm. The plates were then aligned with the four aligning pins originally used to locate the rectangular apertures. The fusing was accomplished in a reduced atmosphere of a hydrogen oven. A test sample made from regular copper was not adequate for this technique since the oxygen in the copper went to the surface during the brazing process. This test result dictated that only oxygen-free copper (less than 0.001 percent) was acceptable.

After visual inspection, the five-layer plate was mechanically inspected using the Monarch, Cortland, and Bafire Probe technique. Data points of the location and size of the rectangular apertures were recorded and averaged. The inspected dimensions of the apertures turned out to be 3.8331 mm by 3.9406 mm (design dimensions of 3.8100 mm by 3.9268 mm) for small apertures and 4.6200 mm by 4.6116 mm (design dimensions of 4.6126 mm by 4.6228 mm) for the large apertures. All dimensions were within a 0.0254-mm tolerance.

IV. Measurement

The reflection coefficients of the dichroic plate were measured on a Hewlett Packard 8510 network analyzer (Fig. 7). Two orthogonal linear polarizations, TE and TM, were measured. (When the electrical field of the wave is perpendicular to the plane of incidence, it is called TE polarized; if the magnetic field of the wave is perpendicular to the plane of incidence, it is called TM polarized.) A 22-dB corrugated horn was located 104-mm away from the dichroic plate along a 30-deg angle of incidence. A second horn was placed 1073 mm from the dichroic plate along the direction of the reflected beam. The reflection response curve shows two resonant frequencies for TE and TM linear polarizations, respectively (Figs. 8 and 9). The theoretical values were recalculated for the actual dimensions of the prototype dichroic plate. Results for circular polarization were computed by using the two orthogonal linear
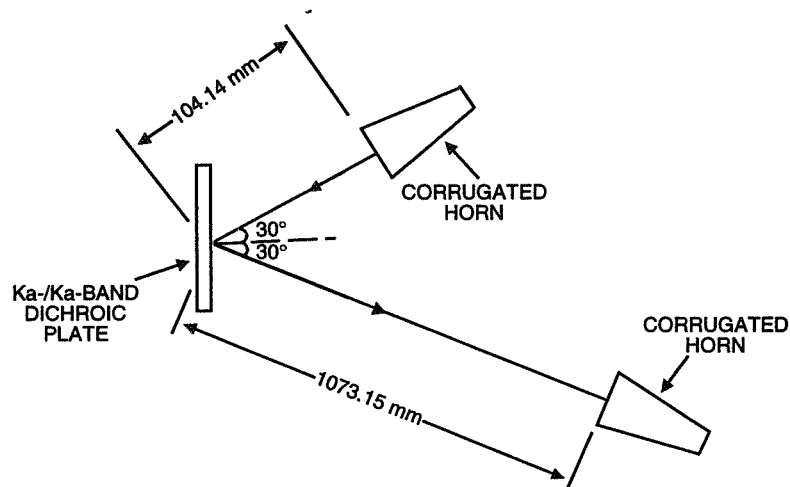
Fig. 7. Experimental setup for the reflection measurement.
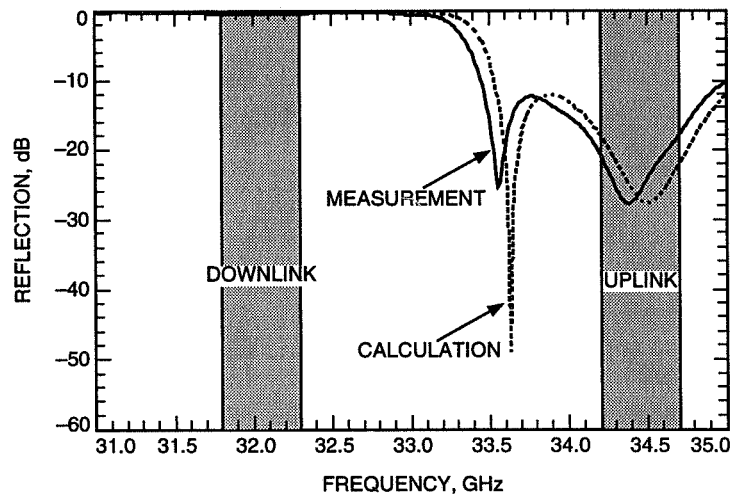
Fig. 8. Measured and calculated reflection coefficient versus
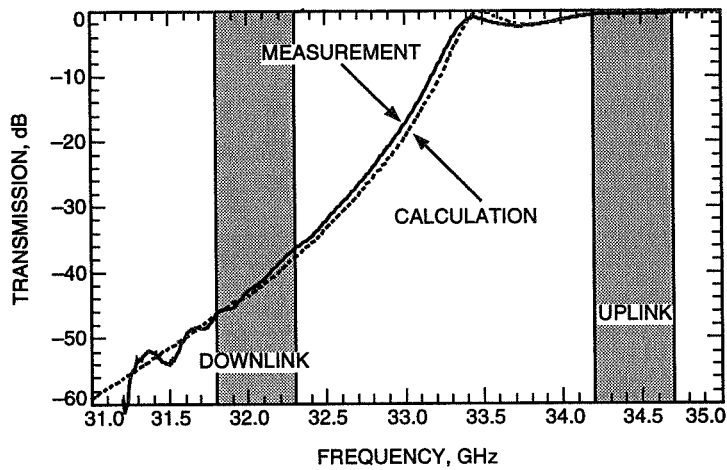frequency for TE linear polarization.

polarizations (TE and TM) and the phase difference between them (Fig. 10). The calculated and measured resonant frequencies are less than 0.25 percent in error for circular polarization (Table 1).

A transmission measurement for TE and TM polarizations was also made in order to check the performance of the reflecting band (31.8–32.3 GHz) (Fig. 11). The 22-dB transmit horn was located 127.0 mm away from the dichroic plate, which was tilted 30 deg from normal. The five-layer dichroic plate is approximately three times thicker than a one-layer dichroic plate such as the X-/Ka-band dichroic plate [3]. Therefore, the transmitted beam path was not the same as the incident beam path. Consequently, the receiving horn was offset 13.97 mm from the incident beam path. For reference, the transmission coefficients were first measured without the dichroic plate. Then the transmission coefficients were measured again with the dichroic plate between the two horns. The measured and calculated transmission coefficients showed good agreement for TE and TM polarizations, respectively (Figs. 12 and 13). The transmitted power was below −35 dB at the Ka-band downlink for circular polarization (Fig. 14).
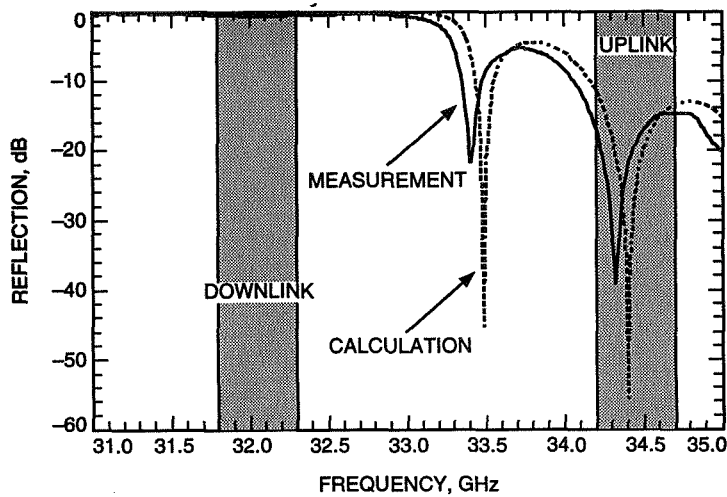
Fig. 9. Measured and calculated reflection coefficient versus frequency for TM linear polarization.
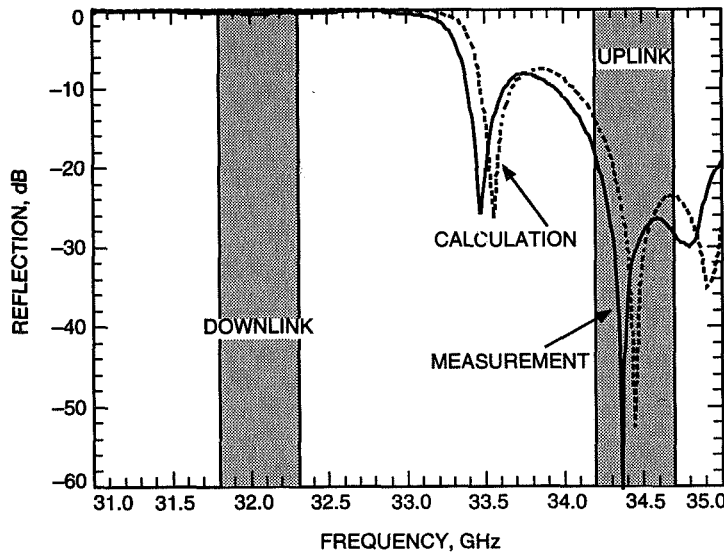
Fig. 10. Measured and calculated reflection coefficient versus frequency for circular polarization.

V. Conclusion

The prototype five-layer Ka-/Ka-band dichroic plate was successfully fabricated. The fabrication technique was proven adequate for the multilayer dichroic plate. The experimental results and theoretical predictions showed good agreement for the resonant frequency, within 0.25 percent. Furthermore, the computer code for analyzing the dichroic plate with stepped rectangular apertures was verified. A Ka-/Ka-band dichroic plate will be fabricated and implemented for an X-/X- to Ka-/Ka-band demonstration at DSS 13.

**Table 1. The measured and calculated reflection resonant frequencies
of the prototype Ka-/Ka-band dichroic plate.**

Polarization	Resonant frequency	Measurement, GHz	Calculation, GHz	Error percentage
TE linear polarization	1st	33.56	33.625	0.19
	2nd	34.37	34.5	0.38
TM linear polarization	1st	33.41	33.485	0.22
	2nd	34.32	34.40	0.23
Circular polarization	1st	33.47	33.55	0.24
	2nd	34.36	34.44	0.23
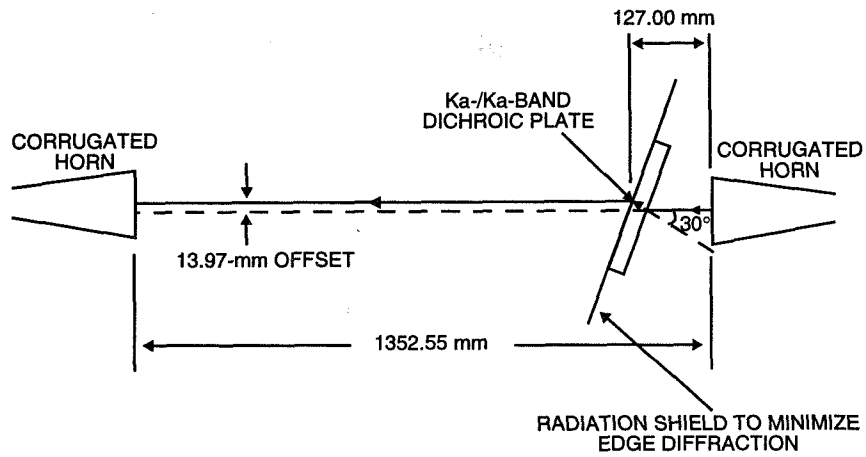
Fig. 11. Experimental setup for the transmission measurement.
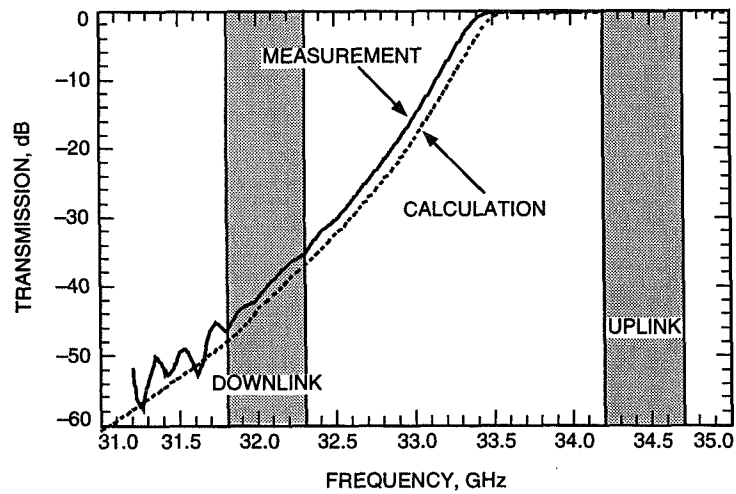
**Fig. 12. Measured and calculated transmission coefficient
versus frequency for TE linear polarization.**

Fig. 13. Measured and calculated transmission coefficient versus frequency for TM linear polarization.
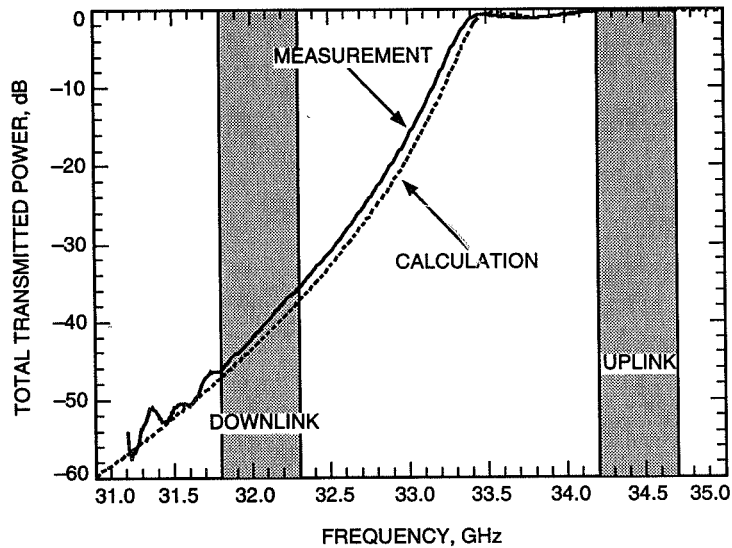
Fig. 14. Measured and calculated total transmitted power versus frequency for circular polarization.

Acknowledgment

References

[1] J. C. Chen, "Feasibility Study of a Ka-/Ka-Band Dichroic Plate With Stepped Rectangular Apertures," *The Telecommunications and Data Acquisition Progress Report 42-112, October–December 1992*, Jet Propulsion Laboratory, Pasadena, California, pp. 1–7, February 15, 1993.

[2] J. C. Chen, "Computation of Reflected and Transmitted Horn Radiation Patterns for a Dichroic Plate," *The Telecommunications and Data Acquisition Progress Report 42-119, July–September 1994*, Jet Propulsion Laboratory, Pasadena, California, pp. 236–254, November 15, 1994.
http://edms-www.jpl.nasa.gov/tda/progress_report/42-119/119N.pdf

[3] J. C. Chen, P. H. Stanton, and H. F. Reilly "Performance of the X-/Ka-/KABLE-Band Dichroic Plate in the DSS-13 Beam Waveguide Antenna," *The Telecommunications and Data Acquisition Progress Report 42-115, July–September 1993*, Jet Propulsion Laboratory, Pasadena, California, pp. 54–64, November 15, 1993.

Sequence-of-Events-Driven Automation of the Deep Space Network

R. Hill, Jr., K. Fayyad, C. Smyth, T. Santos, and R. Chen
Applications Development Section

S. Chien
Information Systems Technology Section

R. Bevan
Communications Systems and Research Section

In February 1995, sequence-of-events (SOE)-driven automation technology was demonstrated for a Voyager telemetry downlink track at DSS 13. This demonstration entailed automated generation of an operations procedure (in the form of a temporal dependency network) from project SOE information using artificial intelligence planning technology and automated execution of the temporal dependency network using the link monitor and control operator assistant system. This article describes the overall approach to SOE-driven automation that was demonstrated, identifies gaps in SOE definitions and project profiles that hamper automation, and provides detailed measurements of the knowledge engineering effort required for automation.

I. Introduction

The Voyager 1 spacecraft is cruising at 17.5 km/s toward the outer edge of the solar system. Though its onboard systems are mostly asleep during this phase of its mission, Voyager's health metrics are continually sent to Earth via a telemetry signal radiated by its 40-W transmitter. It will take 8 hours at the speed of light for the signal to reach its destination, Earth, a billion miles away. Upon arrival, the telemetry signal is received by an extremely sensitive ground communications system, NASA's Deep Space Network (DSN), where it is recorded, processed, and sent to the mission operations and Voyager project engineers, who assess the health of the spacecraft based on the contents of the signal.

The type of activity just described occurs daily for dozens of different spacecraft and projects. Though the process of sending signals from a spacecraft to Earth is conceptually simple, in reality there are many Earth-side challenges, both technical and institutional, that must be addressed before a spacecraft's signal is acquired and transformed into useful information. The purpose of this article is to identify some of these challenges and propose ways of automating the process of capturing data from a spacecraft. In particular, this article focuses on how to automatically transform a flight project service request into an executable set of DSN operations that fulfill the request. To understand in more concrete terms the processes we propose to improve, consider first the following example of the typical activities that currently occur
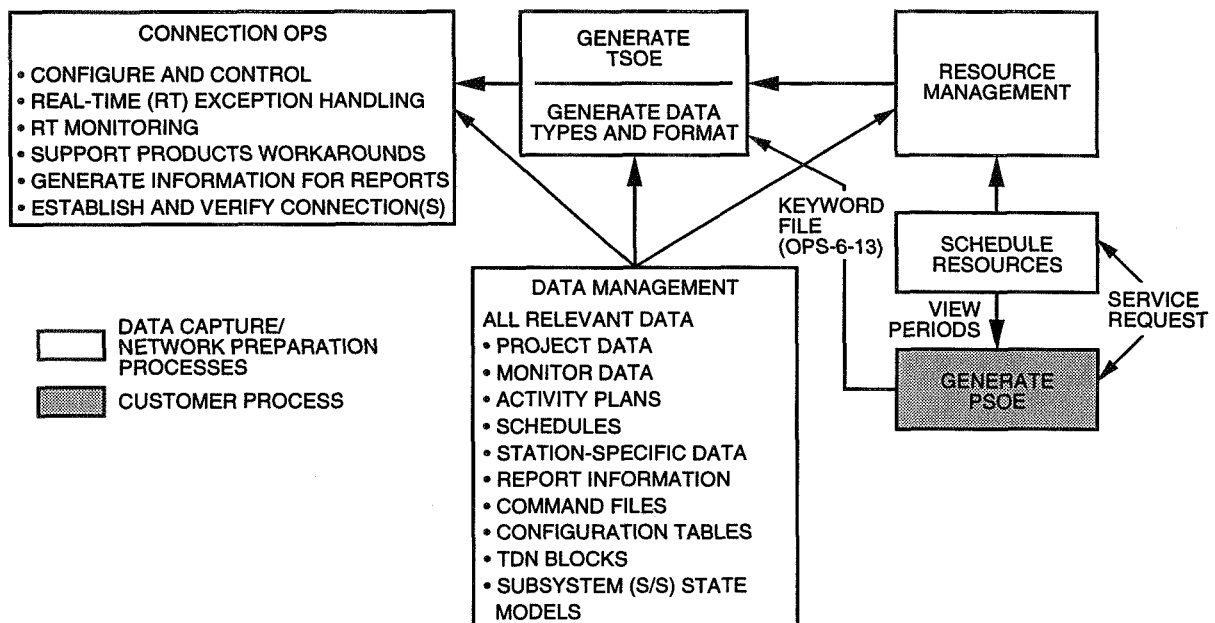
Fig. 1. Partial process map for network preparation and data capture processes.

when the DSN provides a service in response to a project request. Figure 1 shows a partial process map of the steps taken to fulfill the service request.[1]

A team within the Voyager flight project decides to perform a periodic check of the health status of the Voyager 1 spacecraft. Since the spacecraft's health metrics are sent via a telemetry signal, a project representative submits a service request to the Telecommunications and Mission Operation Directorate (TMOD) (see Fig. 1) for a telemetry downlink activity to be performed, and the time, day, and equipment are negotiated with a representative from the DSN. Once the activity has been scheduled (Fig. 1, "schedule resources"), the Voyager team develops a project sequence of events (PSOE),[2] which is a time-ordered description of the events that should take place during the activity (Fig. 1, "generate PSOE"). The PSOE is written in a high-level language[3] that provides a set of keywords and parameters to specify DSN functions and spacecraft events. Some of the keywords used in the SOE are actions that must be performed by the DSN, e.g., configure the receiver or acquire a downlink. Other keywords describe actions that will be taken by the spacecraft, e.g., a change in bit rate or the modulation index during the track activity. Once completed, the Voyager team sends the SOE to DSN operations, whose job it is to implement the requested activities.

After DSN operations receives the SOE keyword file, which is a high-level description of the events and activities that must be performed, operations personnel supplement the PSOE with additional information

---

[1] This is a modified version of the full process maps found in *Final Report of the Reengineering Team (RET) for Services Fulfillment (Operations)* (internal document), Telecommunications and Missions Operations Directorate (TMOD), Jet Propulsion Laboratory, Pasadena, California, March 14, 1995.

[2] This is a simplified description of the actual process. In reality, a project develops an integrated PSOE describing all of the activities planned for its spacecraft for a 2-week period. The integrated SOE is usually developed using the project's own language and later converted into the DSN keyword format described above. There are currently some efforts within the DSN to standardize the set of services it offers to its customers. With all of the translation required to go from the project language to the DSN keyword format, it seems desirable to develop an SOE language or tool that can be reused by multiple flight projects and that also would eliminate the need to translate into the DSN format. This is currently being addressed by the SOE reengineering team.

[3] *Flight Project Interface to the DSN for Sequence of Events Generation*, DSN Document 820-13, OPS-6-13 (internal document), Jet Propulsion Laboratory, Pasadena, California, August 31, 1995.

154

concerning resource allocation and activity-specific configuration (Fig. 1, "generate TSOE" and "generate data types and formats").[4] The TSOE (which stands for Telecommunications and Mission Operations Directorate Ground Network sequence of events) is sent to the deep-space communications complex, where operators read and transform its contents into a set of operations (ops) procedures, which, when executed, will satisfy the goals stated in the TSOE (Fig. 1, "connection ops"). Based on the keywords in the TSOE, the operator chooses procedures to accomplish the goals of the activity and executes them by manually typing and sending command directives to the subsystems in the assigned communications link. The execution of the issued directives is monitored by the operator, who closes the control loop by determining whether the directive was successful or not. By "successful" execution, we mean that the directive had its intended effect on the subsystem. Thus, to successfully transform the TSOE from a list of time-tagged keywords into an operational procedure, the following steps are performed:

(1) Determine the appropriate directive(s) and parameters to achieve the current keyword goal

(2) Determine that the necessary conditions required for the execution of the directive are satisfied (i.e., verify preconditions of the directive)

(3) Execute the directive (manual and computer-initiated activities)

(4) Verify that the directive was correctly received by the subsystem

(5) Verify that the desired subsystem state has changed (verify successful accomplishment of the postconditions of the directive)

These are the steps taken under normal circumstances. In addition, the operator monitors the overall progress of the activity and the health status of the subsystems by viewing a host of different computer displays. Exceptions must be handled in real time by the operator, who invokes recovery procedures when there are equipment anomalies or failures. Thus, from the start to the finish, the process of capturing data from a spacecraft currently involves many manual steps.[5]

II. Automated DSN Operations—The Concept

While current DSN operations are extremely labor- and knowledge-intensive, the DSN Technology Program has been investing in the groundwork for a new model of operations that automates major portions of the DSN data capture and network preparation processes. In this new model, generic services are electronically requested of the DSN by a project. These services are then provided to the project in a manner completely transparent to the project. Within the DSN services fulfillment process, routine operations will be completely automated, greatly enhancing the flexibility and responsiveness of the DSN. Furthermore, many of the costly, knowledge- and labor-intensive processes will be automated, resulting in a more efficient, streamlined DSN operations structure.

The Network Automation Work Area, funded by the DSN Technology Program, has been developing and demonstrating technology to fulfill this vision of automated data capture and network preparation. This work and these demonstrations can be described in terms of three areas (see Fig. 2): resource allocation—assignment of global DSN resources necessary to fulfill the requests; procedure

---

[4] Again, this is a simplified account of the actual process; the project SOE keyword file requires additional information before it is sent to the deep-space tracking station for implementation. The SOE also triggers the generation of predict and support data needed by various subsystems during the activity, e.g., the antenna needs pointing predicts so that it will be oriented to receive the spacecraft signal.

[5] The complete process map is in DSN Document 820-13, OPS-6-13, op cit.
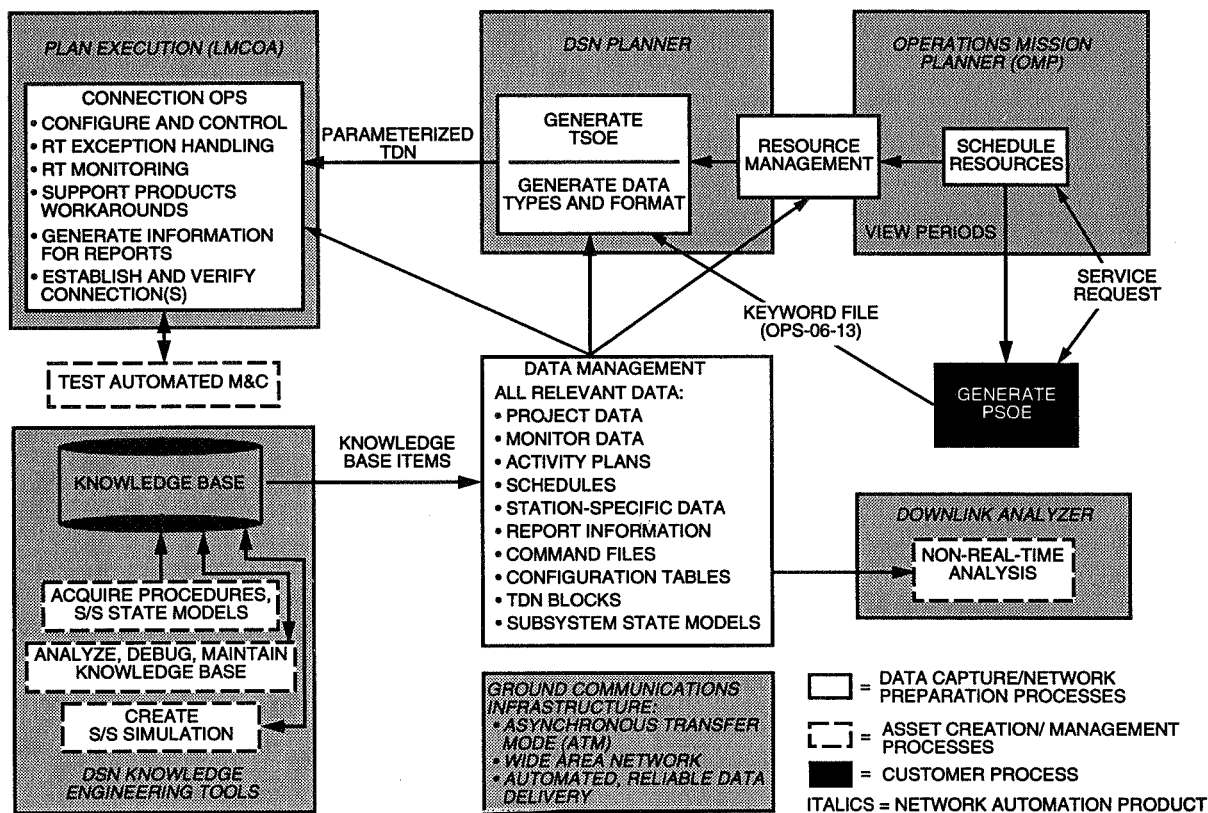
Fig. 2. Automating the DSN's data capture and network preparation processes.

generation—generation of appropriate executable procedures to fulfill specific service requests in light of the allocated equipment; and procedure execution—executing the appropriate procedure and ensuring that the appropriate services are correctly fulfilled. Below we outline in further detail ongoing efforts in each of these areas.

In the resource allocation area, the OMP-26 scheduling system has been fielded to support scheduling of the 26-m DSN antenna subnetwork. Current efforts involve extending the OMP-26 system to schedule further classes of DSN assets (extension beyond the 26-m subnet); expansion of OMP-26 coverage to the real-time area, where changing requests and equipment availability force modifications of the operational schedule; and further extension and maturation of the OMP-26 automated scheduling capability.

In the procedure generation area, we have been adapting planning technology that has been proven and fielded in science data processing applications to the problem of automated generation of antenna operations procedures. This work involves development of the DSN planner (DPLAN) system, which generates an executable antenna operations procedure, called a temporal dependency network (TDN) [3], from a high-level track specification and equipment assignment.

In the procedure execution area, the link monitor control operator assistant (LMCOA) system is being further refined and generalized to support automated tracking using DSN antennas and subsystems. The LMCOA system provides closed-loop control, execution monitoring, and error recovery to provide robust procedure execution for data capture. LMCOA has been used for the Ka-Band Antenna Performance (KaAP) experiments, the Jupiter Patrol, and the phased-array experiment at DSS 13.

III. SOE-Driven Automation Demonstration

A. Overview and Objectives

In February 1995, a comprehensive demonstration was conducted to validate the concept of end-to-end SOE-driven automation. In this demonstration, the procedure generation and procedure execution elements of automation were demonstrated by performing a Voyager telemetry downlink track using the 34-m beam-waveguide (BWG) antenna at DSS 13 in Goldstone, California. There were four major objectives to this demonstration:

(1) To demonstrate that an executable operations procedure could be generated using the DPLAN automated planning system [7].

(2) To demonstrate that the TDN generated by DPLAN could be correctly executed by the LMCOA procedure execution system to successfully perform the requested data capture process.

(3) To further understand the institutional and infrastructure difficulties in fielding technologies for (1) and (2). Specifically, what types of information are currently missing from SOEs and affiliated request information that would be needed to automatically generate, parameterize, and execute TDNs? Additionally, how much effort in knowledge engineering was required to endow DPLAN and LMCOA with the capability for this track? How much effort would it take to extend to a related track for a different project? To a different type of track?

(4) To acquire both qualitative and quantitative data on the amount of effort required to perform knowledge engineering to field systems for tasks (1) and (2) above [4,6,8,10].

The remainder of this section outlines at a high level how each of these capabilities was demonstrated and describes the interrelations between different elements of the demonstration. The remaining sections in this article describe the underlying technologies and representations.

The first goal of the end-to-end demonstration was to show automated generation of DSN operations procedures. In this element of the demonstration, DPLAN used the PSOE, equipment allocation, and a project profile file to construct a TDN that could be executed to perform the track. Generating the TDN involves

(1) Determination of the correct TDN blocks (to achieve the tracking goals in the context of the particular equipment assignment and project profile)

(2) Determination of the correct dependencies among blocks (e.g., block A must be completed before block B)

(3) Determination of the correct parameters for each block (in the context of the tracking goals, equipment assignment, and project profile)

Some elements of TDN parameterization are deferred until plan execution time (to be performed by LMCOA). DPLAN uses information about how to achieve track goals using generic TDN blocks in the context of various equipment configurations and project parameters. This modular representation of operations procedures allows for a more compact knowledge base, removing the need to maintain a complete set of complex end-to-end TDNs to cover all combinations of track types, equipment configurations, and project classes—a set that may number in the hundreds. Each TDN block is a procedure executable by

the procedure execution engine, LMCOA, and consists of a sequence of subsystem directives tailored to achieve a higher-level goal in context of a specific type of track.

The second goal of the end-to-end demonstration was to exercise the automated procedure execution capability of the LMCOA system on the TDN produced by the DPLAN. This involved demonstrating the data capture capability of the LMCOA for a series of Voyager 2 downlink telemetry passes at DSS 13. While LMCOA has been in use since the fall of 1994 for KaAP and Jupiter Patrol tracking activities, tracking Voyager 2 represented the first time LMCOA had been used to track a spacecraft. Thus, one point of the demonstration was to show the generality of the LMCOA approach to both spacecraft and nonspacecraft tracking activities.

The third goal of the end-to-end demonstration was to characterize and quantify the effort required to implement the automation architecture. This effort can be attributed to two factors. The first part of the implementation effort involved determining elements of information and infrastructure that would impede implementation of an end-to-end automation system as demonstrated. This goal was furthered by requiring all types of project, spacecraft state, and sequence-related information to be contained in the project SOE and project profile. Because the project SOE is fixed, all mission information would need to be contained in the project profile. Thus, examining the types of information in the project profile provided valuable insight into information missing from the project SOEs. The second part of the effort was to determine how much knowledge engineering was required to implement the automation architecture. A careful accounting was made of the knowledge engineering effort required to construct and validate the DPLAN knowledge base (used in generating the TDN), the TDN blocks themselves, the parameterization of the TDN blocks by both DPLAN and LMCOA, and the directives that make up the TDN blocks used in the demonstration.

We think that the labor estimates we derived in constructing the TDNs represent a realistic estimate of the true effort required to construct operation TDNs. The labor estimates reflect generation, manual evaluation, and operation validation of the TDNs. All three of these steps are required to produce a TDN capable of providing reliable operations support. Other TDNs that have been constructed by other groups, while carefully constructed and manually verified, have not yet been validated by usage in an automation system.

B. Demonstration Context: Deep Space Station 13

Located at Goldstone, California, Deep Space Station 13 (DSS 13) is the deep-space tracking station dedicated to research and development activities of the Deep Space Network. DSS 13 has functional elements (see Fig. 3) comparable to DSN tracking stations: a 34-m BWG antenna, which is controlled by the antenna pointing subsystem; feed horns for S-band (2.3-GHz), X-band (8.45-GHz), and Ka-band (32-GHz) signals; a total power radiometer (TPR) for measuring broadband signal strength; a weather subsystem for tracking wind, humidity, and other atmospheric conditions affecting signal acquisition; a microwave switch controller subsystem; and a receiver, the TP-13 telemetry processor. These subsystems are connected to a local area network (LAN) along with a monitor and control (M&C) subsystem. The subsystems communicate with the M&C subsystem via a set of communications services implemented using manufacturing message specification (MMS) protocols. The subsystems communicate with one another by setting, sending, and reading MMS-variable structures.

The TP-13 receiver was integrated into the M&C LAN to support the Voyager telemetry downlink demonstration. Since most of the recent tracking activities at DSS 13 have not involved spacecraft, the telemetry processor was not at the station. Integrating TP-13 into DSS 13 involved writing an MMS-based interface for TP-13. At the same time, the TP-13 software was ported to the OS/2 operating system, requiring reimplementation of much of the low-level communication between the TP-13 software and hardware.

STATION
MONITOR AND CONTROL

LMCOA

WEATHER
SUBSYSTEM

ANTENNA
CONTROLLER

MICROWAVE SWITCH CONTROLLER
AND TOTAL POWER RADIOMETER

IF SWITCH
CONTROLLER

TP-13
(RECEIVER)

STATION DATA RECORDER
(PROGRAMMABLE OSCILLATOR)
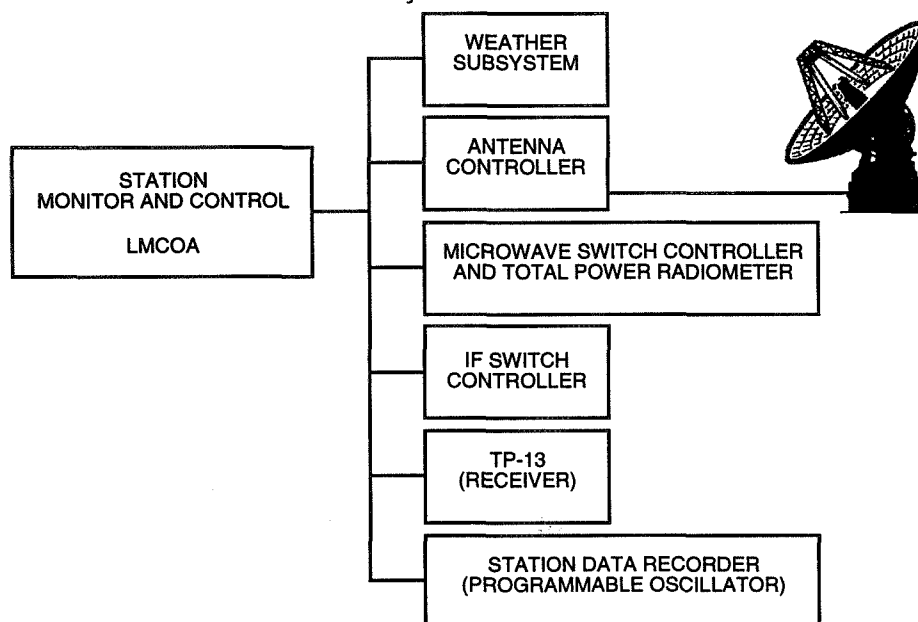
Fig. 3. DSS 13 configuration.

The station monitor and control (SMC) subsystem provides the human operator with an interface to the subsystems shown in Fig. 3. As the name suggests, the SMC subsystem is used by the operator to monitor the status of the subsystems and to exercise control over them during a track activity. The LMCOA provides the capability to automatically execute operations procedures encoded in TDNs. In the SOE-driven automation demonstration, the DPLAN automatically generated the operations procedure in TDN format, and the LMCOA executed it.

IV. Goal 1: Automated Procedure Generation

As part of the Voyager track demonstration, the capability to generate an executable operations procedure from high-level track information was demonstrated. The DPLAN planner uses high-level track information to determine appropriate steps, order constraints on these steps, and determine parameters of the steps to achieve the high-level track goals given the equipment allocation. In generating the TDN, the planner uses information from several sources:

(1) Project SOE—The project SOE specifies events from the mission/project perspective. As a result, the project SOE contains a great deal of information regarding the spacecraft state that is relevant to the DSN track, as well as a large amount of spacecraft information unrelated to DSN operations. Relevant information specified in the project SOE includes such items as the one-way light time (OWLT) to the spacecraft, notifications of the beginning and ending times of tracks, spacecraft data transmission bit-rate changes, modulation index changes, and carrier and subcarrier frequency changes. An excerpt from a Voyager SOE is shown in Fig. 4.

(2) Project profile—This file specifies project-specific information regarding frequencies and pass types. For example, the project SOE might specify a high frequency, and the project profile would specify the exact frequency used. The project profile might also specify other signal parameters and default track types. An excerpt from a Voyager project profile file is presented in Fig. 5.

159

(3) LMCOA SOE (LSOE)—Using the project profile information, the project SOE is parsed into a more manageable form specifying only the information directly relevant to the specific pass. A sample LSOE for a Voyager telemetry downlink pass is shown in Fig. 6.

(4) TDN knowledge base (KB)—The TDN knowledge base stores information on the TDN blocks available for DPLAN and LMCOA to use. This knowledge base includes information regarding preconditions, postconditions, directives, and other aspects of the TDN blocks. It also includes information on how to expand the block parameters and name into the actual flat file entry in a TDN.

(5) Equipment configuration—This details the types of equipment available and unique identifiers to be used to specify the exact pieces of equipment to be used in the track. These include the antenna, antenna controller, the receiver, etc.

```
*ID=DSNISOE52B1          S/C=032 BEG=94 360 094000     END=95 001 221500
!032 42 00022 360 201500 ACE NCT S/C ANT         STATUS, RCP/00.100/Y, HGA, RCP/00.100/Y, HGA
!032 42 00022 360 201500 ACE NCT      S/C TXR    STATUS, OFF, EXC1/TWT2/18,
LOW,EXC1/TWT2/18
!032 42 00022 360 201500 ACE NCT      S/C RCVR        STATUS, 2/S, ON
!032 42 00022 360 201500 ACE NCT      S/C RNG    MODE, OFF, OFF, ON, OFF
!032 42 00022 360 201500 ACE NCT      S/C TLM X-       MOD, 160CD, LOW, 61DG
!032 42 00022 360 201500    D42     BOT
!032 42 00022 360 201500    D42 ACD D/L, 1-WAY, X
!032 42 00031 361 095000    D42     EOT
```

Fig. 4. Sample Voyager project SOE.

```
#     switch IF3 to S-band (5), IF4 to S-band (7)
IF3 S
IF4 X
#     LOW  and HIGH subcarrier frequencies (kHz), from 870-14
SUB_LOW 22500
SUB_HIGH 360
PRED_POWER 25.6
SKY_FREQ 300000000
CARRIER_FREQ 300000000
CARRIER_UPDATE_RATE 500
CARRIER_BANDWIDTH 1
CARRIER_LOOP II
PC_NO 87.27
SUB_UPDATE_RATE 100
SUB_BANDWIDTH 1
SUB_LOOP II
PD_NO 275.42
SYMBOL_UPDATE_RATE 100
SYMBOL_BANDWIDTH 1
SYMBOL_LOOP II
ES_NO 0.871
```

Fig. 5. Excerpt from Voyager project profile file.

```
95/005/16:30:00 CONFIG: IF3=X_KA; POLAR=RCP;      SKY_FREQ=300000000;      PRED_POWER=25.6;
PO_FILE="/u/cm/lmcoa/lmcoa/src/kb/xv2_05.po";.
95/005/16:30:00 TPR_PRECAL: BAND=X;.
95/005/16:30:00 SOURCE: SRC=VGR2;.
95/005/16:30:00 CARRIER: PC_NO=87.27; FREQ=300000000;      BANDWIDTH=1.0; UPDATE_RATE=500;
LOOP=2;.
95/005/16:30:00 SUBCARRIER: PD_NO=275.42; FREQ=22500;      BANDWIDTH=1.0; UPDATE_RATE=100;
LOOP=2;.
95/005/16:30:00 SYMBOL: ES_NO=0.871;      BANDWIDTH=1.0; UPDATE_RATE=100; LOOP=2;.
95/005/16:30:00 ACQ_D/L: MODE=1-WAY; BAND=X;.
95/005/16:30:00 TELEM: BIT_RATE=160; CODE_FLAG=1; MOD_INDEX=61;.
95/005/17:15:00 TELEM: BIT_RATE=2800; CODE_FLAG=1;.
95/005/17:15:00 TELEM: MOD_INDEX=72;.
95/005/18:30:00 TELEM: BIT_RATE=160; CODE_FLAG=1;.
95/005/18:30:00 TELEM: MOD_INDEX=61;.
95/005/20:00:00 END_OF_TRACK.
```

Fig. 6. Voyager downlink telemetry pass LSOE.
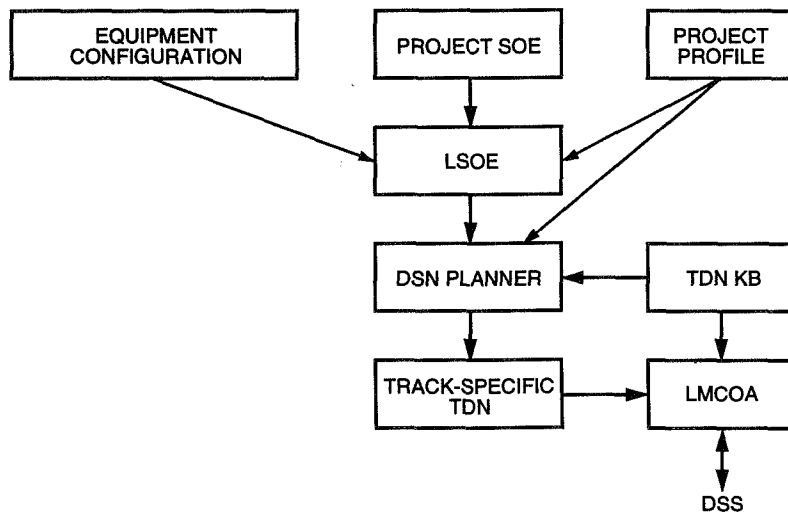
Fig. 7. SOE-driven automation architecture.

The overall flow of information in our approach to SOE-driven automation is shown in Fig. 7. In this approach, the project SOE is parsed into an LSOE that contains only that information relevant to the track of interest. DPLAN uses the LSOE and the project profile to determine the parameterized goals of the track. A sample set of track goals is shown in Fig. 8. This set of goals and a set of contextual facts derived from the LSOE are the planning inputs. The contextual facts are basically the planning system's representation of the LSOE information.

DPLAN reduces the high-level track goals into executable steps by applying knowledge about how to achieve specific combinations of track goals in the context of specific equipment combinations. This information is represented in the form of task reduction rules, which detail how a set of high-level goals can be reduced into a set of lower-level goals in a particular problem-solving context. Each task reduction rule rigorously details the scope of its expertise in terms of track and equipment combinations. This information on the scope of applicability of the rule can be considered in terms of a track goal

```
(PO_required track1)
(spacecraft_mode_changes track1)
(track_goal spacecraft_track telemetry track1)
(track_goal spacecraft_track downlink track1)
(track_goal decode_data)
(station-used track1 DSS13)
```

Fig. 8. Sample tracking goals.

hierarchy and equipment goal hierarchy, where the rule applies to all contexts below the rule in the relevant hierarchy (all specializations of its scope).

Figure 9 shows a partial tracking-goal hierarchy involving the goals for telemetry, commanding, and ranging. Figure 10 shows a partial track hierarchy for antennas. A rule might specify how to achieve a tracking goal for a particular type of antenna. For example, a rule might specify how to achieve the telemetry tracking goal for a 34-m BWG antenna. Alternatively, a rule might specify a constraint on how to achieve telemetry when using high-efficiency antennas (HEFs). For example, a rule might specify that two receiver calibration steps, A and B, might have to be ordered so that A is always before B. By representing the track, equipment, and other hierarchies, the scope of various pieces of knowledge regarding antenna track activities can be naturally and easily represented.

Using this problem specification, DPLAN then uses task reduction planning techniques, also called a hierarchical task network (HTN) [2,9], and operator-based planning techniques [11] to produce a parameterized track-specific TDN to be used to conduct the track. The actual planner used to generate the TDN is a modified version of the task reduction planning component of the multimission Video Image Communication and Retrieval (VICAR) planner system [1].[6] This track-specific TDN and the LSOE can then be used by LMCOA to operate the actual antenna to conduct the requested antenna track.

For example, the task reduction rule shown in Fig. 11 states that in the equipment context of DSS 13 and the tracking goal context of a downlink track, the abstract task of precalibration can be achieved by performing the lower-level tasks of inspecting the subsystems, connecting the subsystems, configuring the TPR, loading antenna predicts, and configuring the receiver. Furthermore, the subsystems must be inspected before connecting the subsystems, and so on. Also, some of these tasks are composite tasks and will be expanded later into more detailed tasks. For example, configuring the TPR involves configuring the IF switch, configuring the microwave switch controller (UWC)/TPR for precalibration, and performing the actual TPR precalibration.
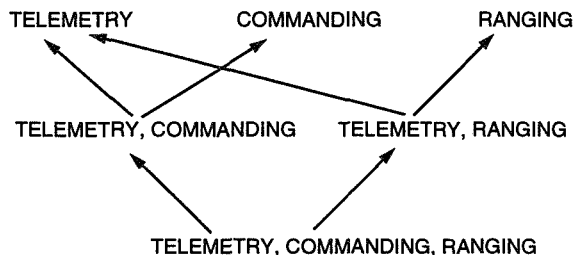
Fig. 9. Partial track hierarchy.
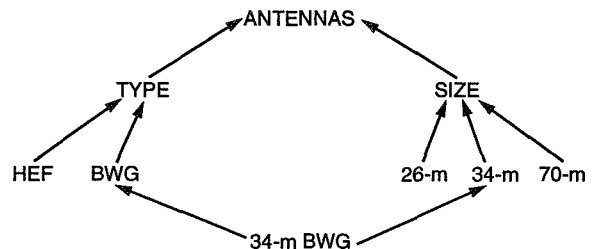
Fig. 10. Example equipment hierarchy—antenna types.

[6] S. Chien, R. Hill, and K. Fayyad, "Why Real-World Planning Is Difficult," working notes of the 1994 Fall Symposium on Planning and Learning: On to Real Applications, New Orleans, Louisiana, November 1994.

EQUIPMENT SPECIFICATION   GOÅL TO ACHIEVE   TRACKING GOAL SPECIFICATION

DSS 13   PRECALIBRATION   DOWNLINK TRACK

INSPECT SUBSYSTEMS → CONNECT SUBSYSTEMS → CONFIGURE TOTAL POWER RADIOMETER → LOAD ANTENNA PREDICTS → CONFIGURE RECEIVER
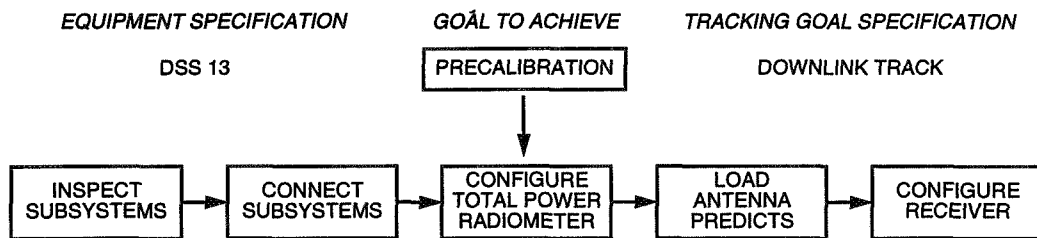
Fig. 11. Sample task reduction.

Next consider the task reduction rule shown in Fig. 12. It states that in the equipment context of DSS 13 and in any tracking goal context, the abstract goal of including a programmable oscillator (PO) can be achieved by adding the "load PO files" step followed by the "configure Doppler tuner" step. Additionally, these steps must be ordered with respect to the "connect subsystems" and "load antenna predicts" steps as indicated.

In the context of specific tracks, generic configuration blocks will be specialized as appropriate to the details of the track. For example, in the equipment context of DSS 13, if the track context is downlink, telemetry, with symbol decoding requested, the task reduction rule in Fig. 13 states the specific receiver configuration block to use to configure the receiver.

Considerable effort in computing the final TDN is devoted to determining the correct parameters (params) for blocks in the TDN. For example, Table 1 shows a configuration table used to determine the IF switch parameter for the TPR precalibration step. Depending on the communication bands used in the track, differing bands will be assigned to each of the communication pathways in the UWC/TPR. Based on the bands being used, the TPR IF switch parameter is also determined. This parameter setting is also determined during the decomposition process, so a correctly parameterized TDN can be constructed.

The application of decomposition rules continues until all of the activity blocks in the TDN are grounded–that is to say, known blocks in the TDN KB can be used to instantiate the activities. This fully instantiated TDN can then be used with the LSOE by LMCOA to perform the actual track. Shown in Fig. 14 is the TDN for a Voyager downlink telemetry track using the PO for DSS 13.

EQUIPMENT SPECIFICATION   GOAL TO ACHIEVE

DSS 13   PO REQUIRED

CONNECT SUBSYSTEMS → LOAD PO FILES → CONFIGURE DOPPLER TUNER → LOAD ANTENNA PREDICTS
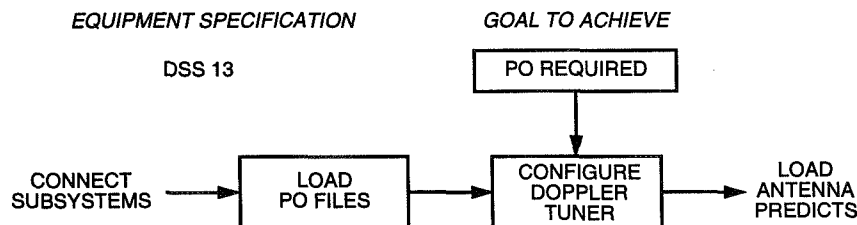
Fig. 12. Augmentation of the TDN required by an additional PO track goal.

EQUIPMENT SPECIFICATION   GOAL TO ACHIEVE   TRACKING GOAL SPECIFICATION

DSS 13   CONFIGURE RECEIVER   DOWNLINK TRACK   TELEMETRY TRACK   DECODING SYMBOLS

SPECIFIC CONFIGURE RECEIVER
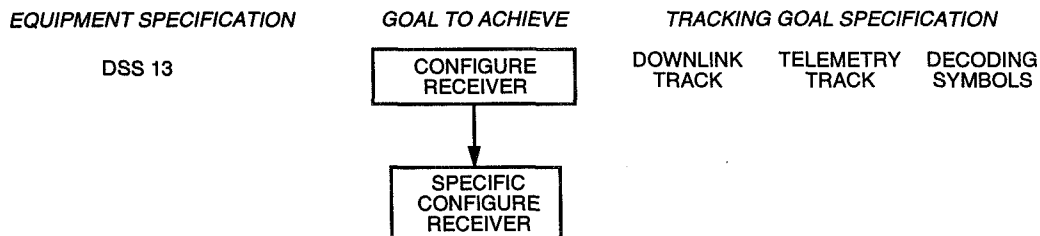
Fig. 13. A specialized task reduction.

163

Table 1. TPR IF switch parameter determination.

Frequency	IF1	IF2	Parameter
S-band	*	—	1
X-band	*	—	1
Ka-band	—	*	2
Q-band (45 GHz)	—	*	2
S- and X-band	*	*	3
X- and Ka-band	*	*	3
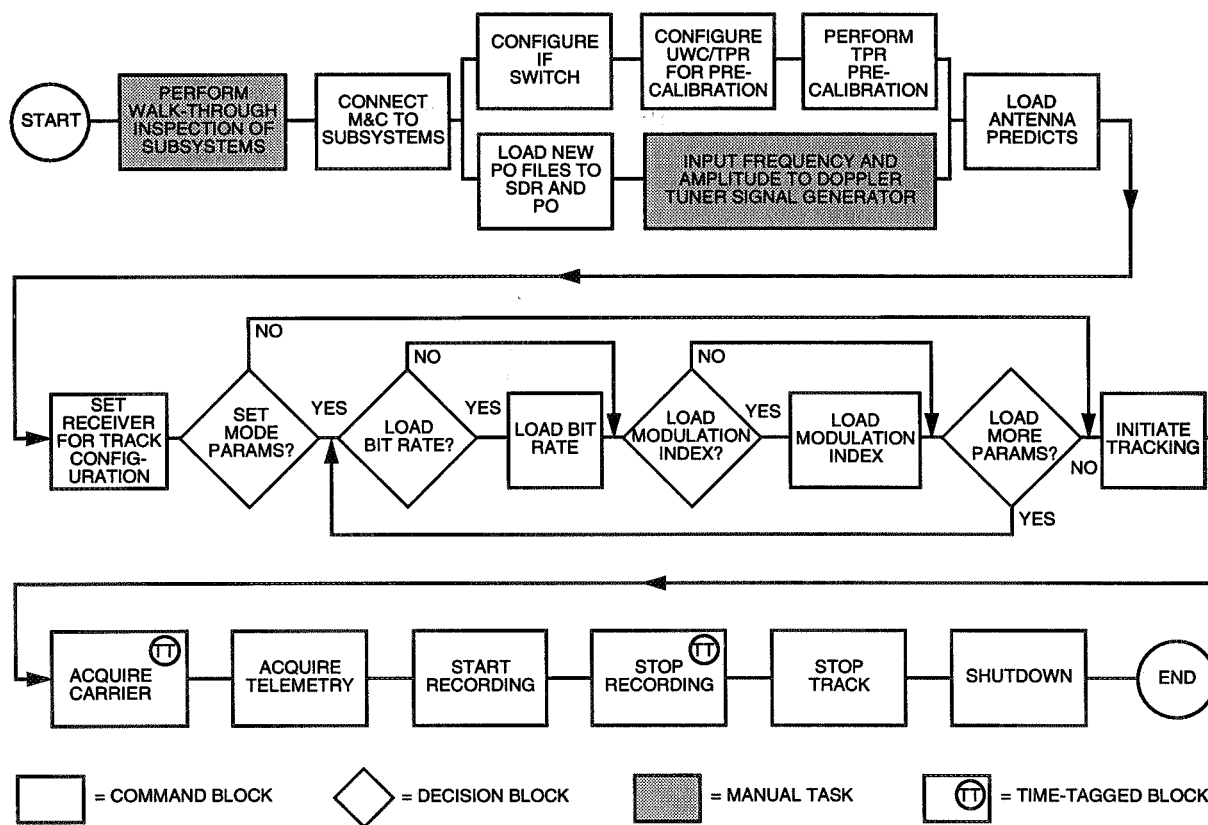
Fig. 14. The TDN for a Voyager telemetry downlink track using the DSS-13 antenna (including telemetry mode changes).

V. Goal 2: Automated Procedure Execution

The previous section described how DPLAN automatically composes a procedure, called a TDN, from a knowledge base of procedure components, called TDN blocks, based on a request for a DSN service. In this section, we describe how a TDN is executed at a deep-space tracking station, DSS 13, using the LMCOA. As the name suggests, the purpose of the Link Monitor and Control Operator Assistant is to assist DSN operators in performing tasks on the M&C subsystem. M&C tasks involve monitoring, configuring, operating, and troubleshooting deep-space communications equipment. The goal of automating the execution of procedures is to drastically reduce the amount of manual operations needed to support a DSN tracking activity by automating the execution of the operations procedures

for an activity. The benefits of achieving this goal include reducing the operator's workload, thereby allowing him or her to do other tasks, and reducing the amount of time required to perform a track.

In order to understand better how LMCOA works, a short description of the operational context in the DSS-13 M&C subsystem is given first. Then we give an overview of LMCOA's architecture along with a description of how the TDN is executed. Finally, we discuss the results of the demonstration in which LMCOA executed the TDN for the Voyager telemetry downlink activity.

A. Monitor and Control

The M&C subsystem is the centralized site for monitoring and controlling the subsystems that comprise a deep-space communications link. The M&C console displays subsystem status data to the operator and also provides a graphical user interface for controlling the subsystems; it provides all the control functions needed for an operator to perform a tracking activity. For instance, Fig. 15 shows the M&C interface for performing the boresight procedure on the antenna subsystem. The state of the antenna is displayed as a table of values for azimuth, elevation, and offset. Control over the subsystem is exercised by pressing graphical user interface (GUI) buttons, such as the "MiniCal" button shown in the display. When the M&C subsystem is used without LMCOA to perform a tracking activity, the operator manually executes a sequence of actions (i.e., pushing buttons, typing data into data entry fields, switching displays, etc.) to satisfy the requirements of the activity. All control is exercised by the operator, who must also monitor the state of the subsystems in the communications link in order to close the control loop [5].
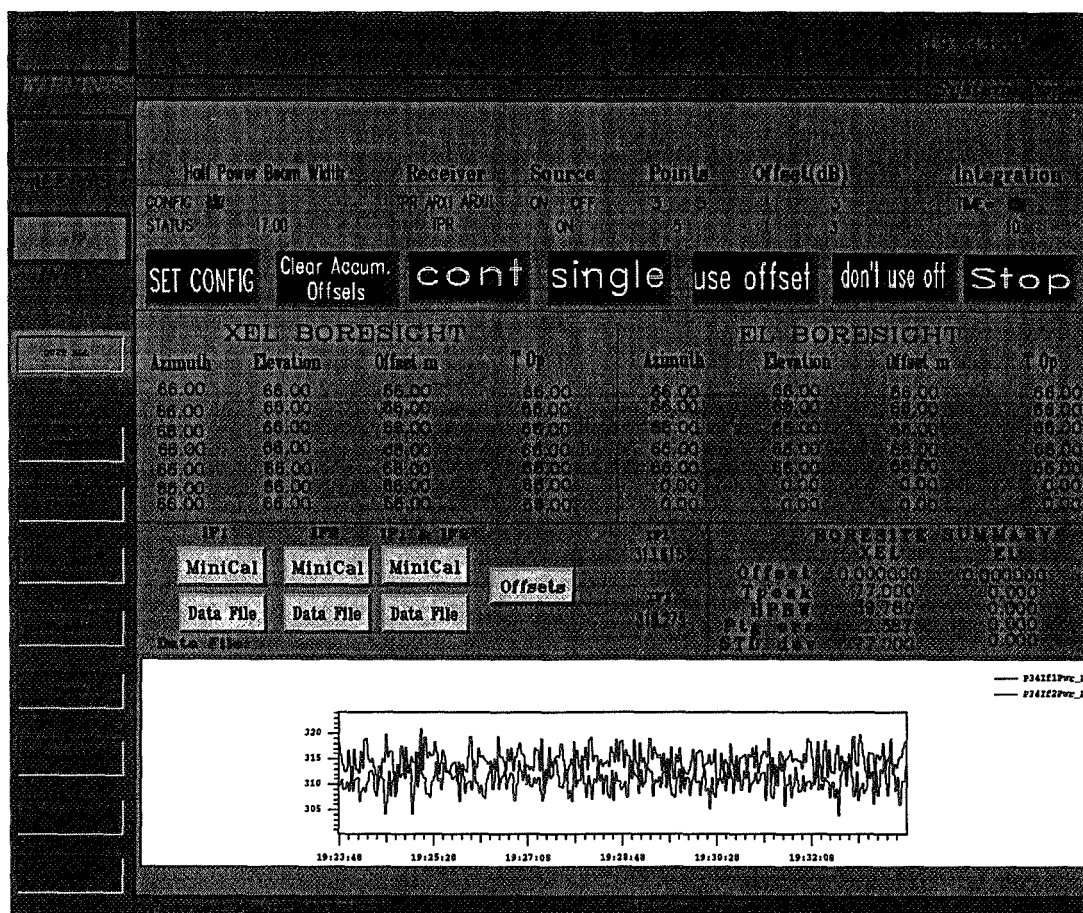
Fig. 15. The M&C subsystem user interface for the boresight procedure.

B. Link Monitor and Control Operator Assistant

There are several obvious drawbacks to operating the M&C subsystem manually. Certain DSN operations require continuous attendance by an operator over long periods of time, and some operations are highly repetitive and require large amounts of data entry. For instance, it is not unusual to conduct a KaAP track lasting 8 hours. During a KaAP track, the procedure called "load sidereal predicts" is repeated many times (see the KaAP TDN in Fig. 16 for an end-to-end view of the track); the "load sidereal predicts" procedure requires inputs by the operator each time it is conducted. We estimate that an 8-hour KaAP track requires about 900 operator inputs overall, if the track is performed manually. For this same track, under nominal conditions, LMCOA reduces the number of operator inputs to less than 10. Since people tend to be more error prone than computers on simple repetitive tasks, it makes sense to assign these tasks to LMCOA, freeing the operator for the task of handling exceptions, which requires more intelligence and knowledge.

The LMCOA performs the operations procedures for a tracking activity by executing a TDN, which is a procedure that is automatically generated by DPLAN, as described in the last section. DPLAN composes the TDN so that it contains the procedures (TDN blocks) needed for a specific tracking activity, and it orders them according to its knowledge of the dependencies that are defined among the blocks as well

RCP = RIGHT CIRCULAR POLARIZATION

☐ = COMMAND BLOCK   ▨ = MANUAL OPERATION   ▨ = SUB-TDN   ◇ = DECISION BLOCK
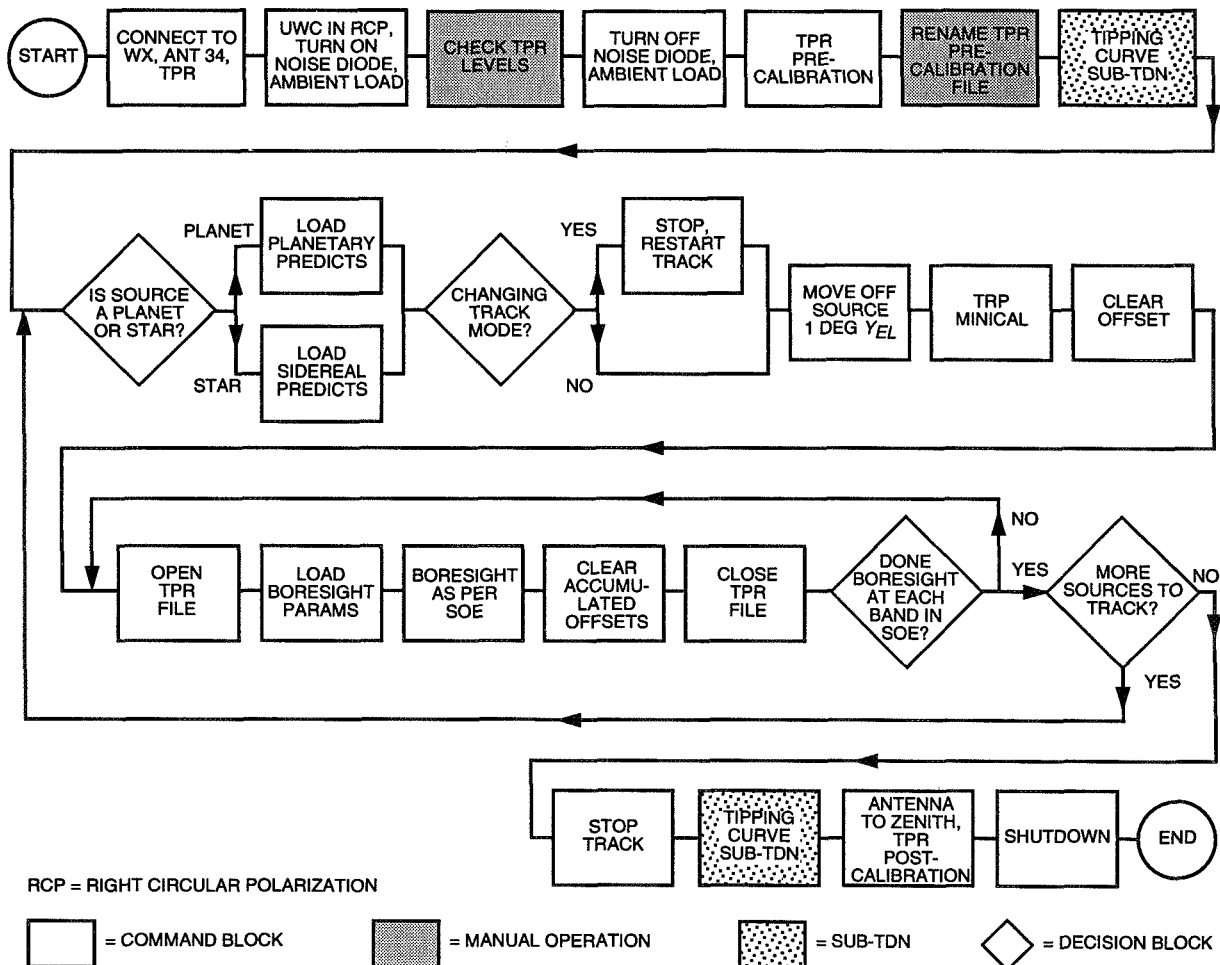
Fig. 16. A KaAP track TDN.

166

as by what it knows about the pre- and post-conditions of the blocks. The knowledge about interblock dependencies and about block pre- and post-conditions is passed to the LMCOA, whose task it is to execute the end-to-end procedure. The LMCOA receives the TDN in the form of a directed graph, where the precedence relations are specified by the nodes and arcs of the network. The blocks in the graph are partially ordered, meaning that some blocks may be executed in parallel. Temporal knowledge is also encoded in the TDN, which includes both absolute (e.g., "acquire the spacecraft at time 02:30:45") and relative (e.g., "perform step y 5 min after step x") temporal constraints. Conditional branches in the network are performed only under certain conditions. Optional paths are those that are not essential to the operation but may, for example, provide a higher level of confidence in the data resulting from a plan if performed. More details about TDNs are provided in [3].

To execute a TDN, LMCOA performs the following functions (see Fig. 17):

(1) Load the parameterized TDN into the execution manager

(2) Determine which TDN blocks are eligible for execution and spawn a process for each TDN block

(3) Check whether the preconditions of each TDN block have been satisfied

(4) Once the preconditions are satisfied, issue the TDN block commands

(5) Verify that the commands had their intended effects on the equipment

The operator interacts with the LMCOA by watching the execution of the TDN; the operator can pause or skip portions of the TDN, check the status of commands within individual blocks, and provide inputs where they are required. When part of a TDN fails, the LMCOA supports manual recovery by the operator by highlighting the point of failure and providing information about the preconditions or postconditions that failed to be satisfied.

C. Demonstration Results

Before LMCOA could perform a Voyager telemetry downlink activity, a number of steps had to be taken:

(1) Knowledge was acquired about the operations procedures for performing this type of activity. This included collecting the commands for the activity; identifying each command's parameters and its source in the SOE and project profile files; identifying each command's preconditions and postconditions and tying them to specific equipment state variables; making the commands into TDN block procedures; defining the precedence relations among the blocks; and displaying the status of the TDN's execution to the operator. Though much of this knowledge had been previously captured for the subsystems at DSS 13, some TDN blocks had to be modified because the Voyager telemetry downlink activity is different from the previously performed activities. In addition, as described earlier in this article, a new subsystem, TP-13, was installed at DSS 13 for the demonstration. Thus, a significant amount of knowledge about TP-13 had to be acquired.

(2) Portions of LMCOA had to be modified to accommodate the knowledge acquired for the Voyager telemetry downlink activity. In particular, the user interface had to be written for the new TDN, and rules were written in the situation manager. One of the long-term
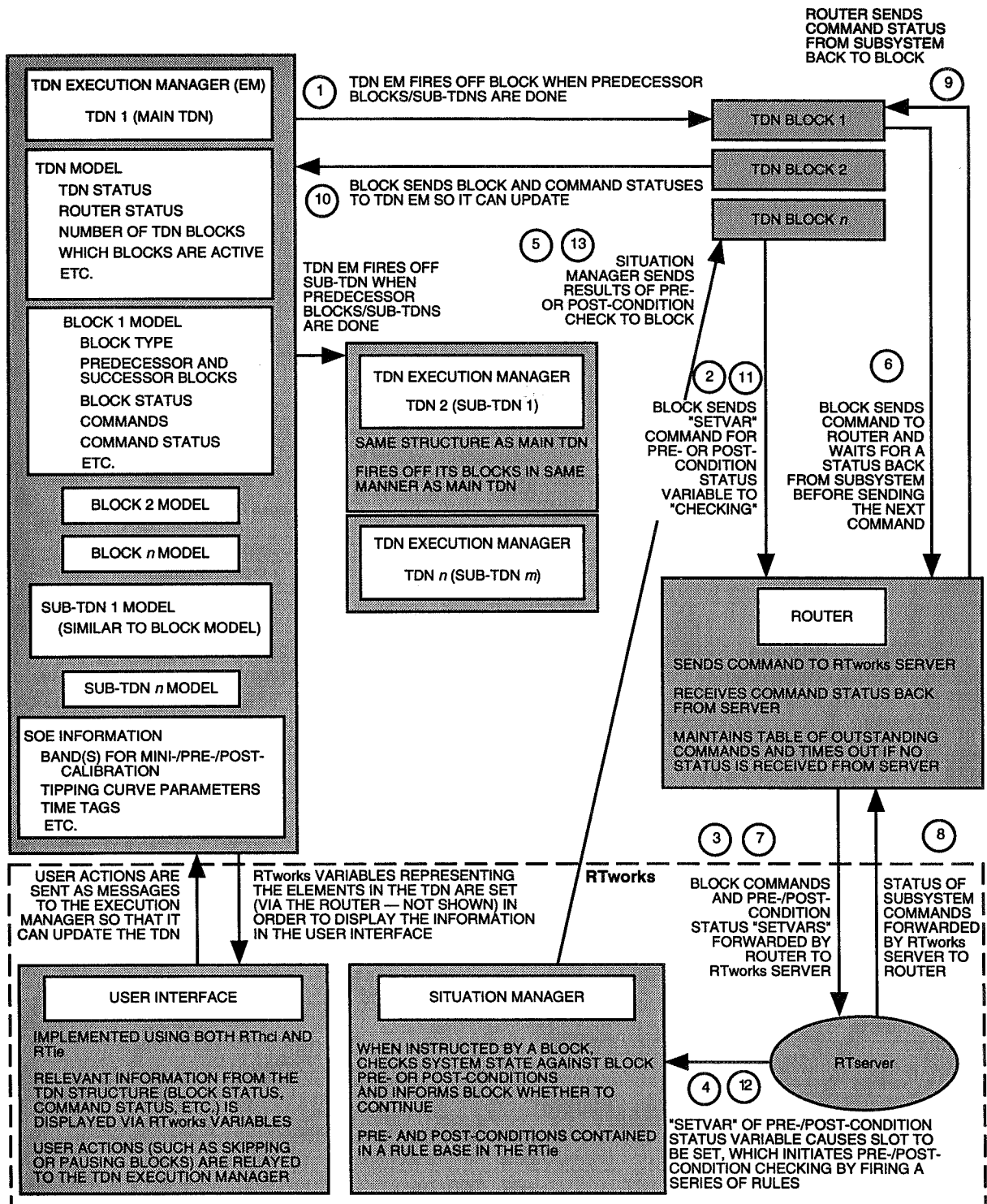
Fig. 17. LMCOA architecture.

goals for LMCOA is to generalize the architecture so that the TDN for any activity can be loaded and run without making modifications to any code, but for this demonstration, these modifications were necessary.

(3) New MMS state variables had to be defined for the TP-13 subsystem so that it could communicate with the M&C subsystem and LMCOA. The MMS variable names are used by all of the subsystems on the M&C LAN, meaning that relatively minor modifications had to be made to TP-13, M&C, and LMCOA.

(4) A TP-13 simulator was developed and installed in the network automation laboratory so that the communications interface could be tested between TP-13, M&C, and LMCOA. In addition, the TDN was debugged by executing it against the TP-13 simulator. The preconditions, postconditions, and time tags on TDN blocks often require a significant amount of testing before the TDN is validated. Such testing also helps identify missing knowledge.

Once the preceding activities had been completed, the modified versions of LMCOA and TP-13 were installed at DSS 13 and the demonstration was conducted over the course of several weeks.

VI. Knowledge Engineering

The SOE-driven automation demonstration uses a knowledge base to store data about the domain and, as such, requires that knowledge engineering be performed in order to acquire and encode the knowledge. In this section, we describe the level and types of effort required to acquire, encode, and validate the knowledge base used in this demonstration. The levels of effort can be summarized as follows and are in units of 8-hour workdays. It took about 36 workdays to acquire the knowledge, almost the same amount of time to encode the knowledge, but three times as much time to validate the knowledge base. Table 2 summarizes the knowledge engineering effort. Details about each phase of this effort are described below.

Table 2. Knowledge engineering effort.

Effort	Time, days
Acquire the knowledge	36
Background information	14
Reuse blocks from other TDNs	4
Interview experts	11
Produce TDN documentation	7
Encode the knowledge	45
Project SOE parser	10
M&C subsystem extended	11
Adapt LMCOA to Voyager TDN	15
Write, revise TDN flat file	4
Decomposition rules, syntax editor	5
Validate the knowledge base	127
TDN, pre- and post-conditions	51
M&C subsystem extensions	19
LMCOA adapted for Voyager TDN	24
Project SOE parser	7
Goldstone testing	24
DPLAN	2

A. Acquiring the Knowledge

The majority of knowledge represented in the system consists of the project SOE definition, the DPLAN knowledge base (used in generating the TDN), the TDN blocks themselves, the parameterization of the TDN blocks by both DPLAN and LMCOA, and the directives that make up the TDN blocks used in the demonstration. Much of this information comes from subsystem knowledge, for example, in defining the TDN blocks, identifying and understanding the subsystem directives within the blocks, and knowing how and when to parameterize subsystem directives within the blocks. Five subsystems were utilized for this TDN, two of which had never been used by LMCOA, and one that required more development and testing to incorporate it into the current TDN. Acquiring this knowledge took about 36 workdays.

The information was obtained by several methods, including reviewing documents and learning about the existing software systems, interviewing experts familiar with a particular part of the domain, documenting the knowledge, and participating in status meetings. Fourteen days were spent acquiring background information on DSN operations, SOEs, the M&C subsystem at DSS 13, and the LMCOA at DSS 13.

A small but very valuable amount of time was spent reviewing the existing TDNs for DSS 13. A significant amount of knowledge was directly extracted from both the Ka-Band Link Experiment (KaBLE) and KaAP TDNs for use in the Voyager TDN. The operational unit of a TDN, namely a block, has proven advantageous in our previous work on TDNs. The reuse of blocks between different operations procedures is one key advantage. Twelve of the 22 blocks, or 55 percent, in the Voyager TDN came directly from the KaBLE and KaAP TDNs. Our plans for the next generation LMCOA include the use of a relational database to store TDNs, blocks, and their contents. A block that can be used in more than one TDN needs to be represented only once in the database. Changes could be made to one or more of these reusable blocks without having to make significant, if any, changes to each TDN requiring the block. Therefore, to answer the question put forth in the overview and objectives section, the effort to extend this demonstration to a different type of track can be greatly reduced, depending on the reuse of TDN blocks from existing TDNs.

Most of the time, acquiring pre- and post-conditions occurred during the validation phase, due to the way the procedural knowledge is captured from operations personnel. Therefore, details about acquiring pre- and post-conditions are presented later in the validation section.

Eleven days were spent interviewing experts in the areas of DSN operations in general, DSS-13 operations for a spacecraft telemetry downlink pass, subsystem M&C, and project SOE definition. In addition, members of the Voyager project were interviewed in order to obtain parameters specific to Voyager that were required for parameterizing the TDN. Seven more days were spent generating graphical and written documentation of the TDN, and four days were spent participating in status meetings.

B. Encoding the Knowledge

The next step in the knowledge engineering process is to encode the knowledge into the right format in order for it to be machine readable. Due to the existing LMCOA, automated M&C subsystem, and planner, the majority of knowledge representations were designed and already used in previous efforts. In this effort, the majority of the encoding time was spent putting the acquired knowledge into a known format. Encoding the knowledge covers writing the TDN flat file, which specifies the Voyager TDN and is loaded by the LMCO; adapting the LMCOA to Voyager; writing the parser for the project SOE; extending the DSS-13 M&C subsystem to automate required subsystems; and developing DPLAN. Some highlights of the encoding effort are noted below.

The DSS-13 M&C subsystem was expanded to include two new subsystems that were not required in other TDNs developed for the LMCOA. This included developing simple subsystem simulators for testing purposes. The integration of TP-13 into the M&C environment took the most amount of time.

170

The changes made to the LMCOA for the new Voyager TDN took 15 days. Some of this time was spent extending the definition of the LSOE to account for new items in the Voyager SOE. As other types of tracks and more subsystems are handled by the LMCOA, the definition of the LSOE will broaden to include operations (e.g., boresight, modulation index changes) required by different tracks.

C. Validating the Knowledge Base

This phase of the knowledge engineering required about three times the level of effort of either the acquisition or encoding phases. This phase includes on-site testing at Goldstone in the operational environment; testing and developing simulators in the DSN advanced systems laboratory; and validating the TDN, pre- and post-conditions, and other software modules. The validation phase took 127 workdays.

Almost half of this time, 51 days, was spent validating the TDN and, especially, the pre- and post-conditions on TDN blocks. Validating the TDN involves making sure that the operations procedure is accurate. One reason this is a time-consuming task is that different experts have different ways of performing a part of the procedure or, over time, they revise and/or refine the operations procedure. This has been a constant in our experience developing TDNs. It is difficult to come to consensus on a single way to perform an operations procedure. After a TDN is in place and can be executed by the LMCOA, the operators can "see" the procedure more clearly and refine it. In any case, these reasons all point out the need to be able to modify TDN blocks and pre- and post-conditions. The format of the operations procedure must be simple so that it will be easy for developers and operations personnel to understand and maintain these procedures.

Pre- and post-conditions were extremely time consuming to validate. From our previous experience building TDNs, we have found that operations personnel do not usually think in terms of pre- and post-conditions. The need for pre- and post-conditions is much more obvious after an initial demonstration of the baseline TDN. At this time, the operators observe subsystem actions occurring automatically in the TDN and identify when some actions occur before sufficient subsystem states have been reached. These states are then implemented as preconditions. Another reason why operators are not familiar with the concept of preconditions is related to how they operate the manual M&C environment. In this environment, the operators often have a lot of equipment preconfigured. A detailed question and answer session between the TDN developer and the operator proved useful for identifying what portions of the preconfiguration are preconditions for existing blocks in the TDN. Postconditions were more difficult for the operations personnel and developers to determine.

The two main reasons for the large amount of time validating pre- and post-conditions are (1) the complexity of pre- and post-conditions and (2) subsystem support for them. Pre- and post-conditions can be very complex and, therefore, difficult to encode to have the desired effect. For example, a pre- or post-condition based on absolute or relative time can complicate the implementation of that condition. In an early version of the Voyager TDN, two TDN blocks occur in sequence, "start recording" and then "stop recording." The "start" recording block just tells the appropriate subsystem to start recording. The block then completes. The "stop recording" block does not execute until the appropriate time has been reached, according to the time in the SOE. Until this time, it appears that no blocks are executing in the LMCOA. That is true; however, the subsystems are recording data during this time. In order for the user interface to show that some activity was occurring, a postcondition was put on the "start recording" block. According to this postcondition, the "start recording" block will finish executing when the time has come to stop recording. Therefore, during the long data recording phase of the pass, the start recording block in the LMCOA remains in the executing state.

Subsystem support is also required in order to make use of pre- and post-conditions. In this and previous TDNs, one or more subsystems did not provide status information that needed to be checked by a pre- or post-condition to the M&C subsystem. For example, in the Voyager TDN, files were downloaded to the Station Data Recorder (SDR). We had to modify this subsystem to send a "finished downloading" status back to M&C so that a postcondition could automatically test when downloading was completed.

Extensions to the M&C subsystem took 19 days to complete. The majority of this time was spent incorporating TP-13, the receiver, into the M&C subsystem. New variables were added to the subsystem, and communications problems had to be overcome. This time also included writing subsystem simulators for testing M&C and the LMCOA in the DSN advanced systems laboratory.

A significant amount of time, 24 days, was spent at DSS 13. Extensive testing and debugging that could not be performed in the DSN advanced systems laboratory environment were performed at Goldstone. Much of this time was spent incorporating TP-13 into the DSS-13 M&C environment. Some of the difficulties encountered resulted in modifying sections of the knowledge base related to the M&C subsystem as well as the LMCOA.

Finally, here are the levels of effort for debugging other software modules: Debugging the SOE parser took 7 days, and debugging DPLAN took 2 days. Another 24 days were required to debug the Voyager version of the LMCOA.

VII. Discussion and Summary

At the request of the TMOD Services Fulfillment Reengineering Team, a team from the network automation work area demonstrated SOE-driven automation for a Voyager telemetry downlink track at DSS 13 in February 1995. This SOE-driven automation demonstration accomplished the following significant results:

(1) Demonstrated the ability to automatically generate procedures (TDNs) based on a project sequence of events (PSOE) using an artificial intelligence planning system called DPLAN

(2) Demonstrated the capability for automated procedure (TDN) execution using the LMCOA system; this capability has been demonstrated before but never on a spacecraft-related track

(3) Identified a set of gaps in the SOE definitions and project profiles that make it difficult to automatically generate operations procedures

(4) Produced detailed measurements of the amount of effort required for knowledge engineering for necessary DPLAN and LMCOA knowledge bases

(5) Showed that validating a TDN requires a lot of time and effort before it can be released for operational use

(6) Pointed out the need for subsystems to report their status so that postcondition checking can be done more explicitly

(7) Demonstrated that reusing TDNs can save a significant amount of effort in knowledge acquisition, knowledge engineering, and validation

Acknowledgments

172

References

[1] S. Chien, "Automated Synthesis of Complex Image Processing Procedures for a Large-Scale Image Database," *Proceedings of the First IEEE International Conference on Image Processing*, vol. 3, Austin, Texas, pp. 796–800, November 1994.

[2] K. Erol, J. Hendler, and D. Nau, "UMCP: A Sound and Complete Procedure for Hierarchical Task Network Planning," *Proceedings of the Second International Conference on AI Planning Systems*, Chicago, Illinois, pp. 249–254, June 1994.

[3] K. E. Fayyad and L. P. Cooper, "Representing Operations Procedures Using Temporal Dependency Networks," *SpaceOPS '92*, Pasadena, California, pp. 541–546, November 1992.

[4] K. Fayyad, R. Hill, and E. J. Wyatt, "Knowledge Engineering for Temporal Dependency Networks as Operations Procedures," *Proceedings of AIAA Computing in Aerospace 9 Conference*, San Diego, California, pp. 1040–1047, October 19–21, 1993.

[5] W. R. Heuser and L. Cooper, "An OSI Architecture for the DSN," *SpaceOps '92*, Pasadena, California, pp. 97–101, November 1992.

[6] R. W. Hill, Jr., K. Fayyad, T. Santos, and K. Sturdevant, "Knowledge Acquisition and Reactive Planning for the Deep Space Network," *Proceedings of the 1994 AAAI Fall Symposium on Planning and Learning: On to Real Applications*, New Orleans, Louisiana, pp. 2–4, 1994.

[7] R. W. Hill, Jr., S. Chien, C. Smyth, and K. Fayyad, "Planning for Deep Space Network Operations," *Proceedings of the 1995 AAAI Spring Symposium on Integrated Planing*, Palo Alto, California, pp. 51–56, 1995.

[8] R. Hill and W .L. Johnson, "Situated Plan Attribution for Intelligent Tutoring," *Proceedings of the Twelfth National Conference on Artificial Intelligence*, Seattle, Washington, pp. 499–505, July 31–August 4, 1994.

[9] A. Lansky, *Localized Planning With Diverse Plan Construction Methods*, Technical Report FIA-93-17, Ames Research Center, Moffett Field, California, June 1993.

[10] A. Munro, M. C. Johnson, D. S. Surmon, and J. L. Wogulis, "Attribute-Centered Simulation Authoring for Instruction," *Proceedings of AI-ED 93, World Conference on Artificial Intelligence in Education*, Edinburgh, Scotland, pp. 23–27, August 23–27, 1993.

[11] J. S. Pemberthy and D. S. Weld, "UCPOP: A Sound Complete, Partial Order Planner for ADL," *Proceedings of the Third International Conference on Knowledge Representation and Reasoning*, Boston, Massachusetts, pp. 103–114, October 1992.

Author Index,[1] 1995

The Telecommunications and Data Acquisition Progress Report

42-121, January–March 1995
42-122, April–June 1995
42-123, July–September 1995
42-124, October–December 1995

Anabtawi, A.

42-121   Computer Simulation Results for PCM/PM/NRZ Receivers in Nonideal Channels, pp. 27–53.

T. M. Nguyen and S. Million

Bar-Sever, Y. E.

42-123   A New Model for Yaw Attitude of Global Positioning System Satellites, pp. 37–46.

Bartos, R.

42-124   Modeling and Analysis of the DSS-14 Antenna Control System, pp. 113–142.

See Gawronski, W.

Belongie, M.

42-121   Enhanced Decoding for the Galileo Low-Gain Antenna Mission: Viterbi Redecoding With Four Decoding Stages, pp. 96–109.

See Dolinar, S.

42-121   Rate Considerations in Deep Space Telemetry, pp. 9–15.

See Costa, M.

---

[1] In the case of joint authorship, the reader is referred to the citation under the first author, where all the authors of the article are listed.

Benedetto, S.

42-124   Soft-Output Decoding Algorithms in Iterative Decoding of Turbo Codes, pp. 63–87.

G. Montorsi, D. Divsalar, and F. Pollara

Bevan, R.

42-124   Sequence-of-Events-Driven Automation of the Deep Space Network, pp. 153–173.

See Hill, Jr., R.

Bhaskaran, S.

42-121   The Application of Noncoherent Doppler Data Types for Deep Space Navigation, pp. 54–65.

Chen, J. C.

42-124   A Prototype Ka-/Ka-Band Dichroic Plate With Stepped Rectrangular Apertures, pp. 143–152.

P. H. Stanton and H. F. Reilly, Jr.

Chen, R.

42-124   Sequence-of-Events-Driven Automation of the Deep Space Network, pp. 153–173.

See Hill, Jr., R.

Cheung, K.-M.

42-124   Channel Capacity of an Array System for Gaussian Channels With Applications to Combining and Noise Cancellation, pp. 53–62.

V. Vilnrotter

Chien, S.

42-124   Sequence-of-Events-Driven Automation of the Deep Space Network, pp. 153–173.

See Hill, Jr., R.

Costa, M.

42-121   Rate Considerations in Deep Space Telemetry, pp. 9–15.

M. Belongie and F. Pollara

Ekroot, L.

42-121   Minimal Trellises for Linear Block Codes and Their Duals, pp. 148–158.

See Kiely, A. B.

42-121   Trellis Complexity Bounds for Decoding Linear Block Codes, pp. 159–172.

See Kiely, A. B.

42-122   Analysis of Automatic Repeat Request Methods for Deep-Space Downlinks, pp. 66–83.

See Pollara, F.

Esquivel, M. S.

42-122   Novel Solutions to Low-Frequency Problems With Geometrically Designed Beam-Waveguide Systems, pp. 138–150.

See Imbriale, W. A.

Estefan, J. A.

42-123   Sensitivity of Planetary Cruise Navigation to Earth Orientation Calibration Errors, pp. 1–29.

W. M. Folkner

Fayyad, K.

42-124   Sequence-of-Events-Driven Automation of the Deep Space Network, pp. 153–173.

See Hill, Jr., R.

Feria, Y.

42-121   Degradation in Finite-Harmonic Subcarrier Demodulation, pp. 78–86.

T. Pham and S. Townes

42-121   Testing the Performance of the Feedback Concatenated Decoder With a Nonideal Receiver, pp. 110–130.

S. Dolinar

42-121   Towards Optimum Demodulation of Bandwidth-Limited and Low SNR Square-Wave Subcarrier Signals, pp. 87–95.

W. Hurd

Lin, W.

42-121   Minimal Trellises for Linear Block Codes and Their Duals, pp. 148–158.

               See Kiely, A. B.

42-121   Trellis Complexity Bounds for Decoding Linear Block Codes, pp. 159–172.

               See Kiely, A. B.

42-123   The Trellis Complexity of Convolutional Codes, pp. 122–139.

               See McEliece, R. J.

Linfield, R. P.

42-122   A Test of Water Vapor Radiometer-Based Troposphere Calibration Using VLBI Observations on a 21-Kilometer Baseline, pp. 12–31.

               L. P. Teitelbaum, L. J. Skjerve, S. J. Keihm, S. J. Walter, M. J. Mahoney, and R. N. Treuhaft

42-124   The Effect of Aperture Averaging Upon Tropospheric Delay Fluctuations Seen With a DSN Antenna, pp. 1–7.

Lo, V. Y.

42-124   Ka-Band Monopulse Antenna-Pointing Systems Analysis and Simulation, pp. 104–112.

Lutes, G.

42-121   A High-Speed Photonic Clock and Carrier Regenerator, pp. 202–210.

               See Yao, X. S.

Mahoney, M. J.

42-122   A Test of Water Vapor Radiometer-Based Troposphere Calibration Using VLBI Observations on a 21-Kilometer Baseline, pp. 12–31.

               See Linfield, R. P.

Maleki, L.

42-122   A Novel Photonic Oscillator, pp. 32–43.

               See Yao, X. S.

Montorsi, G.

42-124   Soft-Output Decoding Algorithms in Iterative Decoding of Turbo Codes, pp. 63–87.

      See Benedetto, S.

Moon, T.

42-123   Optimum Detection of Tones Transmitted by a Spacecraft, pp. 69–98.

      See Simon, M. K.

Morabito, D. D.

42-122   Analysis of Tipping-Curve Measurements Performed at the DSS-13 Beam-Waveguide Antenna at 32 and 8.45 Gigahertz, pp. 151–174.

      L. Skjerve

Mysoor, N. R.

42-122   Performance of a Ka-Band Transponder Breadboard for Deep-Space Applications, pp. 175–188.

      J. P. Lane, S. Kayalar, and A. W. Kermode

Nguyen, T. M.

42-121   An Efficient Implementation of Forward–Backward Least-Mean-Square Adaptive Line Enhancers, pp. 16–26.

      See Yeh, H.-G.

42-121   Computer Simulation Results for PCM/PM/NRZ Receivers in Nonideal Channels, pp. 27–53.

      See Anabtawi, A.

Pham, T.

42-121   Degradation in Finite-Harmonic Subcarrier Demodulation, pp. 78–86.

      See Feria, Y.

Pollara, F.

42-121   Multiple Turbo Codes for Deep-Space Communications, pp. 66–77.

      See Divsalar, D.

Shah, B.

42-121   Residual and Suppressed-Carrier Arraying Techniques for Deep-Space Communications, pp. 173–201.

See Shihabi, M.

Shihabi, M. M.

42-121   Residual and Suppressed-Carrier Arraying Techniques for Deep-Space Communications, pp. 173–201.

B. Shah, S. Hinedi, and S. Million

42-123   Optimum Detection of Tones Transmitted by a Spacecraft, pp. 69–98.

See Simon, M. K.

Simon, M. K.

42-122   Carrier Arraying—Revisited, pp. 97–106

42-123   Optimum Detection of Tones Transmitted by a Spacecraft, pp. 69–98.

M. M. Shihabi and T. Moon

Skjerve, L. J.

42-122   Analysis of Tipping-Curve Measurements Performed at the DSS-13 Beam-Waveguide Antenna at 32 and 8.45 Gigahertz, pp. 151–174.

See Morabito, D. D.

42-122   A Test of Water Vapor Radiometer-Based Troposphere Calibration Using VLBI Observations on a 21-Kilometer Baseline, pp. 12–31.

See Linfield, R. P.

Smyth, C.

42-124   Sequence-of-Events-Driven Automation of the Deep Space Network, pp. 153–173.

See Hill, Jr., R.

Stanton, P. H.

42-124   A Prototype Ka-/Ka-Band Dichroic Plate With Stepped Rectrangular Apertures, pp. 143–152.

See Chen, J. C.

Vazirani, P.

42-121 Effects of Correlated Noise on the Full-Spectrum Combining and Complex-Symbol Combining Arraying Techniques, pp. 211–241.

Vilnrotter, V.

42-124 Channel Capacity of an Array System for Gaussian Channels With Applications to Combining and Noise Cancellation, pp. 53–62.

    See Cheung, K.-M.

Yao, X. S.

42-121 A High-Speed Photonic Clock and Carrier Regenerator, pp. 202–210.

    G. Lutes

42-122 A Novel Photonic Oscillator, pp. 32–43.

    L. Maleki

42-123 A Light-Induced Microwave Oscillator, pp. 47–68.

    L. Maleki

Yeh, H.-G.

42-121 An Efficient Implementation of Forward–Backward Least-Mean-Square Adaptive Line Enhancers, pp. 16–26.

    T. M. Nguyen

Walter, S. J.

42-122 A Test of Water Vapor Radiometer-Based Troposphere Calibration Using VLBI Observations on a 21-Kilometer Baseline, pp. 12–31.

    See Linfield, R. P.

Wilson, K. E.

42-124 An Overview of the GOLD Experiment Between the ETS-VI Satellite and the Table Mountain Facility, pp. 8–19.

42-124 Preliminary Analysis of Fluctuations in the Received Uplink-Beacon-Power Data Obtained From the GOLD Experiments, pp. 20–32.

    See Jeganathan, M.

Withington, P. M.

42-121   DSS-24 Microwave Holography Measurements, pp. 252–270.

See Rochblatt, D. J.